TECHNISCHE
UNIVERSITÄT
WIEN
Vienna University of Technology

Diese Arbeit haben beurteilt

(Univ.-Prof. Dr. F. Aumayr)

(Univ.-Prof. Dr. P. Scheier)

DISSERTATION

Erosion of Fusion Relevant Surfaces under Ion Impact

ausgeführt zum Zwecke der Erlangung des akademischen Grades
eines Doktors der technischen Wissenschaften unter der Leitung von

Univ.-Prof. Dr. Friedrich Aumayr

Institut für Angewandte Physik
Wiedner Hauptstraße 8-10 / E134
1040 Wien

eingereicht an der Technischen Universität Wien
Fakultät für Physik

von
DI Katharina Dobeš
Matrikelnummer.: 0125704
Anton-Baumgartner-Straße 125/4/30
1230 Wien

7. Jänner 2014   (Katharina Dobeš)
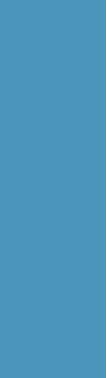
Abstract

When energetic particles impinge on solid surfaces, a multitude of phenomena is observed. Among them are erosion of material (i.e. sputtering), surface modifications, reflection or implantation of projectiles, emission of electrons photons, and other secondary particles, etc. On the one hand the observed phenomena are of basic interest with respect to questions from fundamental research. On the other they are also relevant for a multitude of applications such as semi-conductor industry, for surface analysis tools and for fusion research, as they largely contribute to the interaction of the fusion plasma with the walls of the surrounding vacuum vessel.

The international thermonuclear experimental fusion reactor ITER is currently under construction in the south of France. Its aim is to demonstrate the feasibility of using nuclear fusion as a safe and eco-friendly source for energy production. The interaction of the hot fusion plasma with the vacuum vessel walls in fact constitutes one of the major challenges in the successful realization of the ITER project. In this work, various aspects of plasma wall interaction issues relevant for future fusion devices are studied under controlled laboratory conditions mainly using a highly sensitive quartz crystal microbalance technique. A special emphasis is put on investigating the evolution of plasma facing materials under energetic particle impact of species, that will be present in the fusion machine. Experimental investigations are complimented by a thorough modeling of the observed processes. By this a unique insight into the dynamics of material mixing and particle retention, as well as basic mechanisms of erosion phenomena can be gained. Within the framework of this thesis, all of the three materials, which were originally envisaged as plasma facing components in ITER are investigated, i.e. carbon, tungsten and beryllium.

Katharina Dobeš

I

The projectiles used in the studies range from fueling species such as deuterium to impurity ions such as nitrogen, argon and neon.

In the second part of this thesis, detailed investigations on the emission of electrons from solid surfaces upon impact of highly charged ions will be presented. The studies aim at a more profound insight into the influence of the electronic structure of the target material on the neutralization and de-excitation of a highly charged ion in front, at and below the surface. An almost continuous variation of the surface properties is realized by depositing single layers of C_{60} films on a clean gold substrate, in combination with studies on clean gold and a bulk carbon surface (HOPG). In order to assess and better understand the individual contributions of electron emitting processes, total electron emission yields are determined for a wide range of projectile charge states and impact energies.

Katharina Dobeš
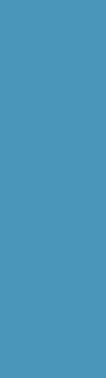
Kurzfassung

Die Wechselwirkung energiereicher Teilchen mit Oberflächen ist gekennzeichnet durch das Auftreten einer Vielfalt verschiedener Phänomene. Unter diesen wären zum Beispiel der Abtrag von Material (d.h. Zerstäubung), eine Veränderungen der Oberflächenstruktur und -zusammensetzung, Implantation bzw. Reflektion von Projektilen, Emission von Elektronen und Photonen bzw. anderer Sekundärteilchen und viele mehr zu nennen. Einerseits ist das Auftreten solcher Phänomene von fundamentalem Interesse für die Grundlagenforschung. Auf der anderen Seite haben sie eine erhebliche Bedeutung in verschiedensten Anwendungsgebieten, wie zum Beispiel der Halbleiterindustrie, für Oberflächenanalyseverfahren und nicht zuletzt auch für die Fusionsforschung, wo sie einen bedeutenden Beitrag zur Wechselwirkung des heißen Fusionsplasmas mit den Wänden des umgebenden Vakuumgefäßes liefern.

Derzeit wird in Südfrankreich der internationale thermonukleare Fusionsreaktor ITER gebaut. Er soll wesentliche Erkenntnisse zur Umsetzbarkeit von Fusion als sicherer und umweltfreundlicher Energiequelle liefern. Die Wechselwirkung des heißen Fusionsplasmas mit den Wänden des Vakuumgefäßes stellt jedoch eine der größten Herausforderungen für das Gelingen des ITER Projektes dar. In der vorliegende Arbeit werden daher verschiedene Aspekte fusionsrelevanter Plasma-Wand Wechselwirkungsprozesse mit Hilfe einer Quarzkristall Mikrowaage unter kontrollierten Laborbedingungen untersucht. Besonderes Augenmerk wird dabei auf die Veränderung von Plasmawand-Materialien unter dem Einfluss energiereicher Spezies gelegt, wie sie in einem Fusionsplasma vorhanden sein werden. Experimentell gewonnene Erkenntnisse werden durch eine ausführliche Modellierung der vorliegenden Prozesse ergänzt. Dies eröffnet einen einzigartigen Einblick in das dynami-

sche Verhalten von Mischmaterialien und Projektil-Rückhalteprozessen, aber darüber hinaus auch in grundlegende Erosionsmechanismen. Die vorliegenden Untersuchungen umfassen alle drei Wandmaterialien, die ursprünglich zur Verwendung in ITER vorgesehen waren (Kohlenstoff, Wolfram und Beryllium). Als Projektile wurden sowohl der Fusionsbrennstoff Deuterium als auch Verunreinigungs-Ionen wie Stickstoff, Argon, Neon und Stickstoff gewählt.

Der zweite Teil dieser Arbeit befasst sich mit genauen Untersuchungen zur Emission von Elektronen beim Einfall hoch geladener Ionen auf Oberflächen. Die hier präsentierten Messungen sollen einen tieferen Einblick gewähren auf den Einfluss, den die Elektronenstruktur eines Festkörpers auf die Neutralisation und Abregung eines hoch geladenen Ions bei der Annäherung, dem Auftreffen und dem Eindringen in die Oberfläche hat. Um die Oberflächeneigenschaften beinahe kontinuierlich variieren zu können, werden einzelne Monolagen C_{60} auf ein Goldsubstrat aufgebracht und mit Messungen auf reinem Gold und einer Kohlenstoff Oberfläche (HOPG) verglichen. Elektronenemissionsusbeuten werden für eine große Auswahl an Projektil Ladungszuständen und Auftreffenergien bestimmt, um den Einfluss der beteiligten Prozesse besser beurteilen und verstehen zu können.

Katharina Dobeš

Contents

Katharina Dobeš

Katharina Dobeš

1 Introduction

When energetic particles impinge on solid surfaces, a multitude of phenomena is observed. Among them are erosion of material (i.e. sputtering), surface modifications, reflection or implantation of projectiles, emission of electrons and photons, and other secondary particles, etc. The observed interaction processes are governed by a variety of properties of both the target material as well as of the projectile. These include on the one hand the surface topography (e.g. its roughness), its chemical composition, its electronic structure, and target material parameters such as the work function or transport properties. On the other hand the nature of the observed phenomena will also depend on the kinetic and potential (i.e. internal) energy, which is introduced into the surface by the impinging particle as well as e.g. its reactivity with the target atoms.

The motivation of studying the interaction of ions with solid surfaces arises from a rather ample field of applications. Investigating the physical processes involved is e.g. of genuine interest for plasma physics, as they largely contribute to plasma wall interaction. Additionally ion beams can also be used to structure surfaces on a nano-scale, which can be interesting e.g. in semiconductor technology or for various surfaces analysis methods. Apart from this, understanding the processes governing the interaction of an ion with a solid surface is also of basic interest with respect to questions from fundamental research.

A large part of the results presented in this thesis (cf. chapter 4) focuses on various aspects of plasma wall interaction issues for future fusion devices. Detailed laboratory investigations of the interaction of different fusion relevant surface - projectile combinations were conducted and will be presented. Beforehand an outline on

Katharina Dobeš

fusion research and some significant plasma material interaction phenomena for future fusion machines will be given (see chapter 2, sections 2.1 and 2.2).

Additionally, this work also covers some detailed investigations on the emission of electrons upon surface impact of highly charged ions (cf. chapter 5) and its dependency on target and projectile properties. A brief description of some basic concepts for the interaction of highly charged ions with surfaces and particle induced electron emission phenomena will be given in chapter 2, section 2.3.

Finally the experimental methods that were used in the presented investigations will be introduced in chapter 3.

List of Publications

- **K. Dobes**, V. Smejkal, T. Schäfer, F. Aumayr
  Interaction between seeding gas ions and nitrogen saturated tungsten surfaces
  International Journal of Mass Spectrometry and Ion Processes, in press
  doi:10.1016/j.ijms.2013.11.015

- **K. Dobes**, M. Köppen, M. Oberkofler, C.P. Lungu, C. Porosnicu, T. Höschen, Ch. Linsmeier, F. Aumayr
  Studies of beryllium surfaces under the impact of nitrogen and deuterium
  Proceedings of the XXI International Conference on Ion-Surface Interactions (2013)

- D. Bodewits, H. Bekker, A. de Neijs, R. Hoekstra, D. Winklehner, B. Daniel, G. Kowarik, **K. Dobes**, F. Aumayr:
  Electron emission yields from boron-like Ar ions impinging on Au(100)
  Nuclear Instruments and Methods in Physics Research B, **269** (2011), S. 1203 - 1207

- E. Bodewits, R. Hoeckstra, **K. Dobes**, F. Aumayr
  Kinetic-energy-driven enhancement of secondary-electron yields of highly charged ions impinging on thin films of C_{60} on Au
  Physical Review A, **86** (2012), S. 0629041 - 0629046

- E. Bodewits, R. Hoeckstra, G. Kowarik, **K. Dobes**, F. Aumayr
  Highly-charged-ion-induced electron emission from C_{60} thin films
  Physical Review A, **84** (2011), S. 0429011 - 0429016

Katharina Dobeš

- **K. Dobes**, P. Naderer, C. Hopf, T. Schwarz-Selinger, F. Aumayr
  Transient effects during sputtering of a-C:H surfaces by nitrogen ions Nuclear Instruments and Methods in Physics Research B, **286** (2012), S. 20 - 24

- **K. Dobes**, P. Naderer, N. Lachaud, C. Eisenmenger-Sittner, F. Aumayr
  Sputtering of tungsten by N^+ and N_2^+ ions: investigations of molecular effects Physica Scripta, **T145** (2011), S. 0140171 - 0140174

- A. Golczewski, **K. Dobes**, G. Wachter, M. Schmid, F. Aumayr
  A quartz-crystal-microbalance technique to investigate ion-induced erosion of fusion relevant surfaces
  Nuclear Instruments and Methods in Physics Research B, **267** (2009), S. 695 - 699

Conference Participation and Talks

- **K. Dobes**, F. Aumayr, M. Köppen, Ch. Linsmeier, M. Oberkofler, T. Höschen, C.P. Lungu, C. Porosnicu
  Interaction of beryllium surfaces with fusion relevant seeding impurity and fuelling ions. Hot topic talk at the XIXth Symposium on Atomic, Cluster and Surface Physics, Obergurgl/ Austria, 2014/02/11

- **K. Dobes** *Erosion of fusion relevant surfaces under ion impact*
  Seminarvortrag am Institut für Allgemeine Physik (IAP), TU Wien, 2014/01/14

- **K. Dobes**, M. Köppen, M. Oberkofler, T. Höschen, C.P. Lungu, C. Porosnicu, Ch. Linsmeier, F. Aumayr
  In-situ investigations of the interaction of beryllium surfaces with nitrogen and deuterium
  Highlight talk at the 12th annual meeting of the EU-PWI Task Force, Lisboa/ Portugal, 2013/11/28

- **K. Dobes**, M. Köppen, M. Oberkofler, T. Höschen, C.P. Lungu, C. Porosnicu, Ch. Linsmeier, F. Aumayr
  Investiagtions of the interaction of beryllium surfaces with nitrogen
  Talk at the 28th Assoziationstag, EURATOM-ÖAW, Salzburg/ Austria, 2013/10/28

- **K. Dobes**
  Investigations of the interaction of beryllium surfaces with nitrogen and deuterium
  Talk at the Midterm Monitoring Meeting WP13-IPH-A01-P2, Garching bei München/ Germany, 2013/09/11

- **K. Dobes** *Studies of beryllium surfaces under impact of nitrogen*
  Oral talk at the 22th International Conference on Ion Surface Interactions (ISI-2013), Yaroslavl/ Russia, 2013/08/22

- **K. Dobes**, E. Bodewits, R. Hoekstra, F. Aumayr
  Electron emission from HOPG due to highly charged ion impact
  Poster at the 11th European Conference of Atoms, Molecules and Photons 2013 (ECAMP-2013), Aarhus/ Denmark, 2013/06/26

- **K. Dobes**, M. Köppen, M. Oberkofler, T. Höschen, C. P. Lungu, C. Porosnicu, Ch. Linsmeier, F. Aumayr
  Erosion of beryllium under nitrogen impact - investigations of transient and steady state effects
  Poster at the 14th International Workshop on Plasma-Facing Materials and Components for Fusion Applications (PFMC-14), Jülich/ Germany, 2013/05/14

- **K. Dobes** *Sputtering of fusion relevant surfaces by seeding impurities*
  Invited talk at the 19th International Workshop on Inelastic Ion-Surface Collisions (IISC-19), Frauenchimsee/ Germany, 2012/09/19

- **K. Dobes**, E. Bodewits, G. Kowarik, R. Hoeckstra, F. Aumayr
  Electron emission due to impact of highly charged ions on C60 covered gold surfaces and HOPG
  Poster at the 19th International Workshop on Inelastic Ion-Surface Collisions (IISC-19), Frauenchiemsee/Germany, 2012/09/18

- **K. Dobes**, J. Pyszkowski, F. Aumayr
  Sputtering of tungsten by seeding impurities
  Poster at the 20th International Conference on Plasma Surface Interactions 2012 (PSI-2012), Aachen/ Germany, 2012/05/22

- **K. Dobes**, P. Naderer, F. Aumayr
  Sputtering of tungsten and a-C:H surfaces by nitrogen ions - investigation of transient and molecular effects

Katharina Dobeš

Poster at the Symposium on Surface Science 2012 (3S*12), St.Christoph/ St.Anton am Arlberg/ Austria, 2012/03/14

- **K. Dobes**, P. Naderer, A. Golczewski, K. Tichmann, T. Schwarz-Selinger, C. Hopf, F. Aumayr
Transient effects during sputtering of a-C:H surfaces by nitrogen ions
Poster at the 13th International Workshop on Plasma-Facing Materials and Components for Fusion Applications (PFMC-13), Rosenheim/ Germany, 2011/05/11

- **K. Dobes**, M. Hinterhofer, K. Tichmann, A. Golczewski, T. Schwarz-Selinger, W. Jacob, F. Aumayr
The evolution of a hydrogen-depleted surface layer on a-C:H during bombardment with N_2^+ Ions
Poster at the 37th EPS Conference on Plasma Physics, Dublin/Ireland, 2010/06/22

- **K. Dobes**, M. Hinterhofer, K. Tichmann, A. Golczewski, T. Schwarz-Selinger, W. Jacob, F. Aumayr
The Evolution of a Hydrogen-Depleted Surface Layer on a-C:H During Bombardment with N_2^+ Ions
Poster at the 5th Annual Meeting of the EU network ITS-LEIF, Alghero, Sardina/ Italy, 2010/10/12

- **K. Dobes**, A. Golczewski, T. Schwarz-Selinger, F. Aumayr
Erosion of tungsten and a-C:H surfaces by slow singly and multiply charged ions
Poster at the 12th International Workshop on Plasma-Facing Materials and Components, Jülich/Germany, 2009/06/12

Supervised Students

- **Markus Hinterhofer**
Untersuchung des Zerstäubungsverhaltens dünner Schichten mittels Quartzkristallmikrowaage, Diploma Thesis 2010

- **Paulus Naderer**
Erosion of Tungsten Surfaces by Nitrogen Ions, Diploma Thesis 2011

- **Laura Stöber** *Sputtering Investigations Using a Quartz-Crystal Microbalance Technique, Bachelor Thesis 2009*

- **Benedikt Würkner**
Userinterface and System Interconnection of the New Vacuum Control Software for the Ion-Beam-Facility AUGUSTIN, Bachelor Thesis 2011

- **Jakob Pyszkowski**
Sputtering of Tungsten and Tungsten-Nitride During Argon Bombardment, Bachelor Thesis 2012

- **Alexander Fuchs-Fuchs**
pending

- **Thomas Schäfer**
pending

- **Valerie Smejkal**
Sputtering Investigations of Fusion Relevant Materials: Erosion of Tungsten Nitride Surfaces by Argon and Neon, Bachelor Thesis 2013

- **Johannes Zlabinger**
Erosion of Tungsten Nitride Surfaces by Nitrogen Ions, Bachelor Thesis 2014

Chapter

2

Underlying Concepts of Plasma Wall Interaction & Ion-Surface Collision Processes

2.1 Fusion Research

In the 21st century humankind is confronted with the unprecedented challenge of covering its rapidly growing need for energy. The recent world energy outlook of the International Energy Agency (IEA) re-affirms that both the global energy demand as well as the CO_2 emissions continue to rise ever higher [1]. Providing sufficient electricity is crucial in guaranteeing the economic and social well-being of the worlds population. It is projected that by 2100 the global energy demand might have risen by a factor of two or even four [2].

Fossil fuels are still the dominant energy source worldwide with gas, oil and coal contributing 81% to the global energy mix [1]. Moreover it is not expected that this will substantially change in the near future. If governments realized all measures that are being currently considered to reduce energy consumption and green house gas emissions (as projected within the so-called 'new policies scenario' of the IEA), the demand for electricity would still increase by 70% until 2035 (cf. figure 2.1). This would be accompanied by a long-term average temperature increase by 3.6° C, imposing a serious impact on the climate system.

Moreover, the oil resources are probably only sufficient until 2030 (so-called 'peak oil') [1] and their abundance is concentrated to regions that are - at least in part - politically relatively unstable. Maintaining energy security additionally increases the public awareness for the need of a transition to more secure and carbon free sources for energy production.
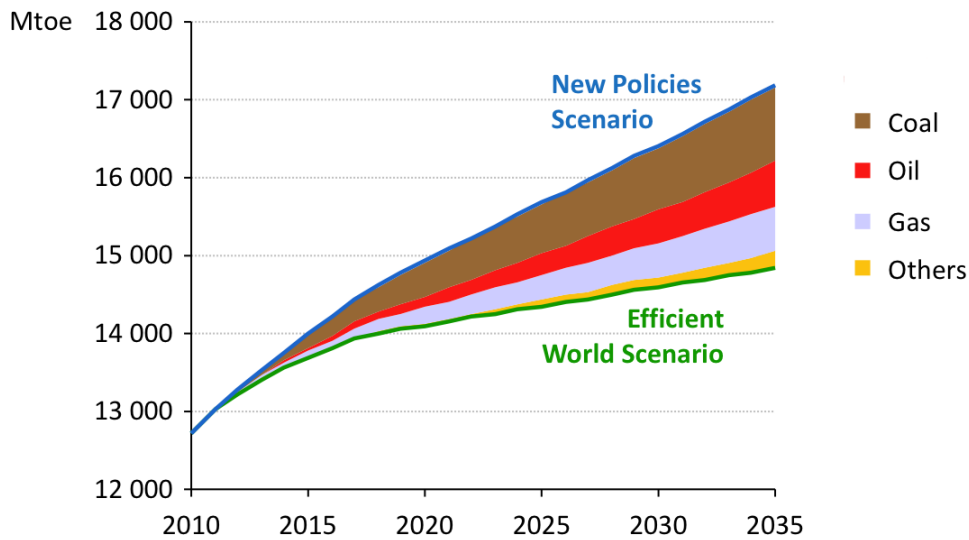
Figure 2.1: Total global energy demand as projected within the world energy outlook for two different prediction scenarios [1].

Today renewable energy production (such as hydro-power, wind, photovoltaics, geothermal, bioenergy and others) constitutes approximately 20% of the global electricity generation. The share of renewables will probably rise to 31% by 2035 [2, 3]. At the same time the amount of power generated by nuclear fission, which is in principle climate friendly, will most likely be damped, due to a lack in public acceptance of fission power plants, especially in the light of the recent nuclear accidents in Fukushima Daiichi. Alternative concepts for electricity generation are hence urgently needed to cover the electricity base load on a larger scale. In this context, nuclear fusion could fill the gap in the availability of the present mix of sustainable and secure energy sources, at least on a medium time scale.

The principle concept of nuclear fusion is based on the fact that it is energetically favorable for light nuclei to fuse into a heavier element. At the lower end of the periodic table, the strong interaction, which holds all the constituents of an atomic nucleus together, is not saturated and the binding energy per nucleon increases with atomic number. If the long-ranging repulsive Coulomb interaction between two nuclei (which are both positively charged) can be overcome and the distance between them can be reduced to below 10^{-15} m for the short-ranging strong nuclear force to become effective, they will join together to form a heavier nucleus. In this reaction the cumulative mass of the reactants is partially trans-

Katharina Dobeš

formed into kinetic energy of the end products (mass defect). This is essentially the same process that also powers our sun.

To initiate fusion on earth, the fusing nuclei will have to be heated to extremely high temperatures, in order to provide them with enough kinetic energy to overcome or at least tunnel through the Coulomb barrier so that the fusion reaction can occur. The highest fusion efficiency at the lowest possible energy is found for the two heavier hydrogen isotopes deuterium (D) and tritium (T) (cf. figure 2.2), which fuse to form a helium nucleus and a fast neutron. The net energy release in this reaction is 17.58 MeV.
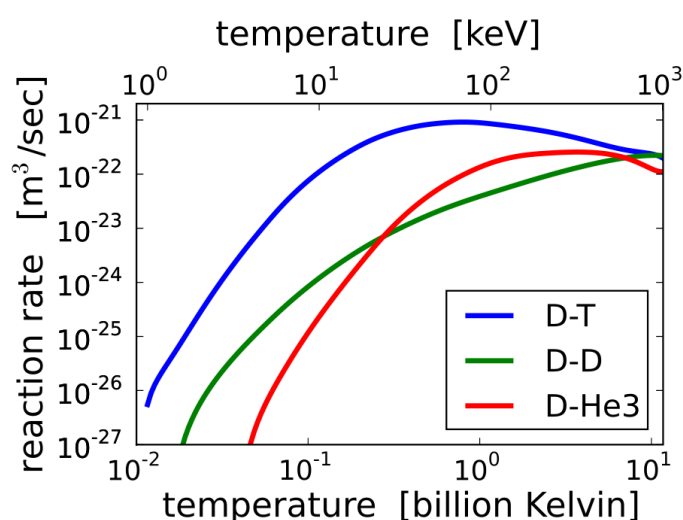
Figure 2.2: The reaction rate for different fusion reactions as a function of the plasma temperature. Picture taken from [4].

Due to the relatively high practicability of this fusion reaction, a possible fusion power plant will be powered by these two isotopes. T is however radioactive, decaying with a half life of 12.3 years. To minimize the need of handling T, it would need to be bred on site in a transmutation reaction by neutron bombardment of a lithium containing blanket within the fusion reactor.

An average fusion power plant could produce 1-1.5 GW of electrical power [5] by only consuming approximately 20 g of T and 13 g of D per operation hour [5,6]. The materials installed in a fusion reactor site will inherently exhibit comparably low levels of radioactivity [7]. Although first wall and structural materials of a power plant will be activated by fast neutron bombardment and the incorporation of T,

most or perhaps even all of the material can be regarded as non-radioactive or at least recyclable at the shut-down of the machine. The necessity for repository disposal will be restricted to less than 100 years after the decommissioning of a power plant.

Overall, thermonuclear fusion could potentially become a very attractive way of safe, clean and abundantly available energy generation for future generations.

2.1.1 ITER

The international experimental fusion reactor ITER[1] is currently being built in the south of France (cf. figure 2.3). Within the ITER collaboration, parties from all over the world are united. Conjointly the ITER partners represent over half of the world's population. The aim of the project is to demonstrate the feasibility of using nuclear fusion for electrical power generation [8]. The scientific goal is to deliver ten times the power that is needed as auxiliary heating power in order to sustain the fusion reaction (i.e. a fusion power gain of Q ~ 10) and to produce a total fusion power of 500 MW. In ITER a large part of the required plasma heating shall be provided by the α -particles that emerge from the fusion reaction. ITER will be the first fusion machine to ever produce net energy. To this day the world record for energy production from controlled thermonuclear fusion is held by the largest currently available experimental fusion reactor JET (**J**oint **E**uropean **T**orus), where scientist managed to produce 16 MW of fusion power output (which corresponded to Q ~ 0.62) [9].

According to the so-called Lawson criterion [11], there are three critical parameters which determine whether a fusion reaction becomes self-sustaining: the fuel density n_i, the plasma temperature T_i and the so-called energy confinement time τ_E, which is a measure of the insulation, for an energy loss of the system to its environment. In achieving conditions for fusion here on earth, there are several approaches, which concentrate on realizing different aspects of the Lawson criterion. Inertial fusion aims at initializing the fusion reaction by effectively heating and compressing the reactants, using high energy beams of LASER light [12]. In inertial confinement fusion both the temperature and the density of the fusing particles is driven above values typical for stellar conditions, but these conditions are only sustained for very short time intervals.

Magnetic confinement fusion on the other hand seeks to prolong the time for the fusion reaction to actually occur (i.e. to extend the energy confinement time

---

[1]The word 'ITER' is Latin for 'way' and an acronym for '**I**nternational **T**hermonuclear **E**xperimental **R**eactor' respectively.

Katharina Dobeš
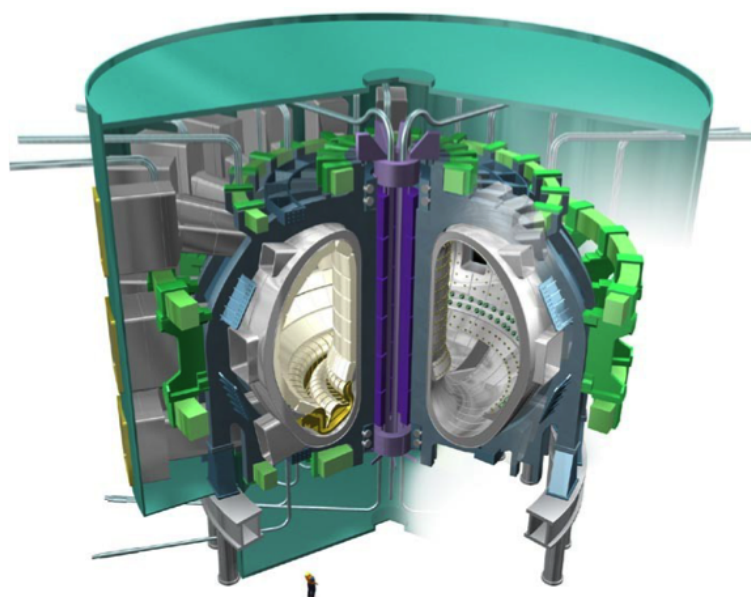
Figure 2.3: A cut-away sketch of the ITER machine [10].

τ_E). This is done by making use of the fact, that at the high temperatures that are needed for achieving a fusion reaction (cf. figure 2.2), the atomic nuclei are already stripped of all their electrons anyway. The resulting fuel plasma can then be confined in a vacuum vessel by means of a strong magnetic field, where the charged particles spiral around toroidally shaped field lines in closed orbitals (cf. figure 2.4). Thereby the interaction of the hot plasma with the vessel walls is minimized, which avoids plasma dilution and cooling.

The most advanced and therefore currently most promising magnetic confinement fusion reactor design is the so-called tokamak[2] (cf. figure 2.4). A tokamak is a machine with the shape of a torus, where the magnetic field that confines the fusion plasma is produced by coils surrounding the vacuum vessel. In addition to the resulting ring like field structure, a toroidal plasma current is induced by a solenoid located in the center of the torus. This generates a poloidal field component, which twists the field lines around the torus. In the resulting magnetic configuration, the plasma particles are constrained to orbits with constant distance to the center of the torus. Since the poloidal field component is however needed for

---

[2]The word 'tokamak' is a Russian acronym, which can be translated to something like 'toroidal chamber and magnetic coil'.
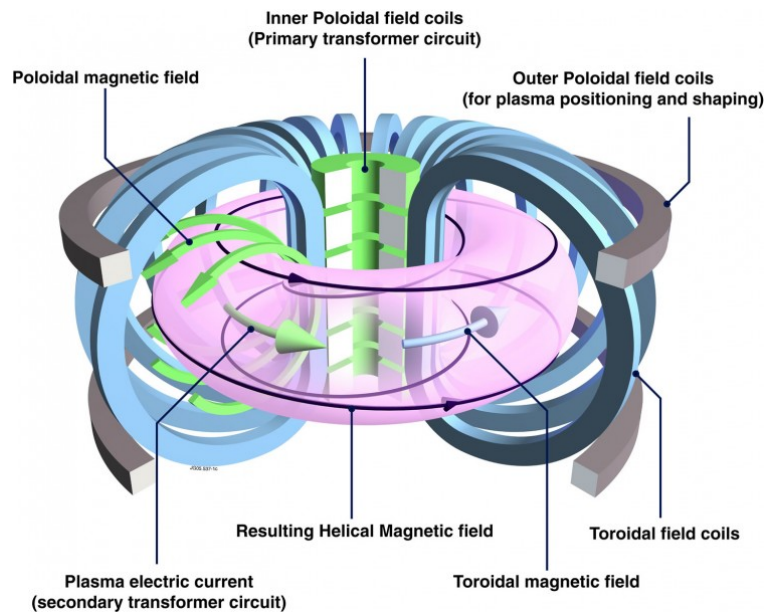
Figure 2.4: Illustration of the operating principle of a tokamak. Picture from [6].

the plasma confinement, a tokamak can by design only be operated in pulsed mode.

2.2 Plasma Wall Interaction Issues in ITER

It is foreseen that in a magnetic confinement fusion reactor, plasma temperatures of more than 100 million °C [6] will be necessary, with a confinement time of some seconds and fuel particle densities of about 10^{20} per m^3 [13]. An essential part of these particles will be exhausted via the so-called divertor. This is a component installed at the bottom of the machine, which diverts particles and also the fusion ash helium from the plasma boundary to the outer edge of the chamber, i.e. from the core region, where the plasma is confined, to a sink outside.

As a result of the rather extreme conditions, which will be encountered in a fusion machine and especially in the divertor region, one of the greatest challenges in realizing a successful reactor design will be the interaction of the fusion plasma with the wall of the surrounding vacuum vessel [14-17]. As the plasma confinement will never be perfect, plasma-material interaction issues are of major concern. Eroded wall material will have a significant influence on e.g. plasma operation and performance by diluting and cooling the fusion plasma. In addi-

Katharina Dobeš

tion, the necessity of changing in-vessel parts, will limit the availability of a possible power plant, if high wall erosion rates or degradation of materials resulting from an exposure to excessive heat loads cannot be avoided successfully. Moreover there are some safety aspects for the operation of a fusion reactor, e.g. with respect to the formation of explosive dust and the retention of radioactive tritium [14]. Any selection of plasma facing materials will have to address these very diverse design requirements.

The operation conditions of the plasma facing components in ITER will certainly be pushing the limits of what is technically realizable today, as power loads, particle and especially neutron fluxes but also tritium exposure of the materials installed in ITER will be unprecedented and beyond today's expertise. This holds especially true for the peaked power and particle loads observed during transient and off-normal events, where the plasma confinement is lost and a lot of energy (up to $\sim$ 1 - 10 GW per m^2 [18]) is deposited onto the plasma facing components. A major constraint to the life-time of the plasma wall will emanate from so-called edge localized modes (ELMs) [19] and plasma disruptions [20, 21]. While the former will occur very frequently (with frequencies of the order of $\sim$ 1 Hz) and therefore need to be controlled and mitigated by e.g. systematic triggering [22], the latter will have to be avoided altogether [16, 23], since they would result in severe melting/ablation of material, especially in the divertor region.

In the initial design of ITER, a mixture of three different plasma facing materials is foreseen to be used for the plasma facing components (cf. figure 2.5): *Beryllium* (Be) will be installed as a first wall and limiter material, i.e. for the largest area of plasma facing components ($\sim$ 700 m^2). Due to its dimensions alone, the first wall will be a source of substantial integrated particle influx to the plasma core. A material with low atomic number Z is favored here, since low Z impurities are comparably quickly ionized. As a consequence radiative losses of eroded wall material, which enters the plasma core, is less critical for a low Z material. This results in relatively high tolerable Be impurity concentrations in the plasma core of approximately 1%[3] [23]. Another advantage of Be as a plasma facing material is its ability to getter oxygen and thereby improve the vacuum conditions within the vessel. Due to its comparably low melting temperature (1550 K) and high erosion rate, the overall life-time of a Be first wall in a fusion machine will eventually become a limiting factor for the operation time of the machine [24], especially when the operation conditions are being upscaled to reactor compatible scenarios.

---

[3]This limit stems in fact from fuel dilution and not from radiative losses.
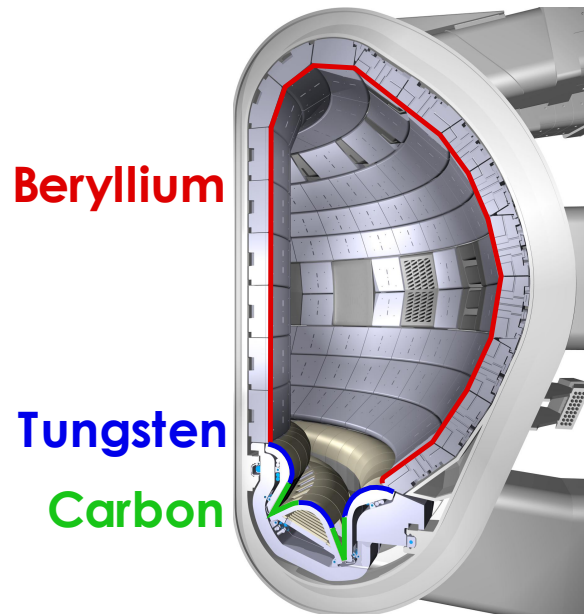
Figure 2.5: Sketch of the cross section of the ITER machine, indicating the installed plasma materials and their location in the plasma vessel [10].

Tungsten (W) will be used for the divertor baffle and dome. In this region of the machine, substantial amounts of charge exchange particles with relatively high energies of 100 - 500 eV or maybe even up to some keV [14] are expected to impinge on the plasma facing surfaces. W is comparatively resistant to physical sputtering even at these rather high impact energies (see section 2.2.1, p. 18). Hence the expected erosion rates will be comparably low and the W component lifetimes will be high. Since high Z materials such as W are however much more effective in cooling the plasma than low Z contaminations, relative W impurity levels within the core plasma will have to remain below 10^{-5} [14]. This concentration limit poses a tight restriction when compared to e.g. the tolerable amount of Be impurities. Moreover W surfaces in a fusion reactor could melt as a result of the power loads expected during transient events and disruptions, potentially resulting in irreversible material damage and excessive plasma contamination [25].

To avoid this, *carbon fiber-reinforced composites* (CFC) will be used at the divertor

Katharina Dobeš

strike points[4], where the last closed magnetic flux surface of the machine intersects the divertor plates. At this point the highest power loads are expected. CFC exhibits extraordinary power handling capabilities and does not melt. Its sublimation limit is expected to be better suited to the expected energy loads than e.g. the melting limit of tungsten. Moreover erosion of CFC components will result in the production of C impurity ions in the divertor region, which show strong radiation and thereby aid in dispersing and reducing the local power loads to highly exposed plasma facing components [27]. On the other hand C is chemically very reactive with various species, among them hydrogen [28]. Chemical erosion of C due to hydrogen isotope impact (cf. section 2.2.1, p. 23) and subsequent co-deposition in hydrogenated carbon layers will lead to high amounts of fuel (D but also T) being retained in the machine, especially in remote areas with no direct plasma contact. With the use of C in the ITER vessel, the T operation limit, which restricts the T inventory for safety considerations to $\sim$ 700 g, would be exceeded well before the end of the run-time of the machine [29]. It will therefore be necessary to remove any C containing plasma facing components before starting the actual T operation in ITER.

The above material selection allows maximum flexibility in the operation of the ITER machine [16, 17, 30]. The emphasis in this choice of materials is the development of improved operation scenarios during the initial part of the project. Before starting the actual D-T plasma however, with more knowledge on how to handle plasma wall interaction, ITER will become a full W machine. This decision was made with respect to the above-mentioned shortcomings of Be and CFC in terms of the requirements of a possible fusion power plant [23].

The use of a mixture of plasma facing materials adds significant complexity to the characteristics of the interaction of a fusion plasma with the walls of its containing vessel. When energetic particles (both neutrals and ions) impinge on the plasma wall, material is eroded (cf. section 2.2.1). The thinning of plasma facing components essentially limits their lifetime and at the same time introduces impurities into the plasma. Subsequent transport of eroded material and possible re-deposition throughout the vessel, probably combined with other species present in the machine, results in material migration and mixing (cf. section 2.2.3) as well as fuel retention (cf. section 2.2.2). Impurities and hydrogen isotopes being recycled

---

[4]To reduce the costs and due to the very positive results recently obtained with full W divertors in current fusion machines such as ASDEX-Upgrade [26], it is been currently considered to eliminate the use of carbon as plasma wall material altogether and start ITER with a full W divertor [10]. Edit in proof: the decision has been made by the Technical Advisory Committee of ITER to start operation with a full tungsten divertor.

from the plasma wall will also influence the composition, and especially the D and T content of the core plasma. All of these processes are strongly coupled in the environment of a fusion reactor.

Early tokamak experience very strongly favored the use of C based materials as plasma facing components. Hence there is only little experience for plasma operation with the material mix envisaged for ITER. Recently, a strong emphasis was put on exchanging the in vessel parts of current-day fusion machines to a mixture of ITER relevant materials to test their behavior under ITER relevant plasma conditions. ASDEX-Upgrade was equipped with a full W wall [31, 32] and has delivered very promising results on plasma operation and confinement [26] in the meantime. Only very recently JET commenced operation with an ITER-like wall [33] where both W and Be is implemented as plasma facing components. First results show clearly reduced D retention rates, W impurity levels well below the tolerable limit and acceptable plasma confinement, while at the same time wall conditioning is strongly facilitated [34].

With the transition to all-metal machines however, the intrinsic impurity levels (of e.g. C) in the divertor region of tokamaks decrease considerably. Consequently their beneficial influence on mitigation of heat loads by radiative cooling is reduced [35]. In order to maintain the desired radiated power fraction in fusion machines such as ITER, controlled injection of impurity species to replace intrinsically available coolants will be mandatory [36]. There are several candidates for this purpose [37]: Nitrogen has proven to be a valuable substitute for C in the divertor region [38, 39], due to its comparably high radiative characteristics at low electron temperatures. In addition, the use of another seeding gas with a different radiation characteristics might be necessary. For this purpose, noble gases such as Ar and Ne are considered. The presence of these externally seeded impurities will however influence the plasma wall interaction: Sputtering of high Z plasma facing materials will in fact be dominated by impurity ions [40]. In addition storage of such impurities (especially N) in the wall, will also result in a modification of the structure and composition of plasma facing surfaces [37].

Overall, current plasma experiments (like ASDEX-Upgrade and JET) are specifically designed for testing and validating plasma facing materials under the above-sketched conditions. In addition to the data being provided by these large machines, laboratory investigations can significantly aid in better understanding and modeling the underlying physical processes. In a tokamak only the superposition of all relevant effects can be observed. Under laboratory conditions however, the involved processes can be studied more independently and influencing parame-

$n_e \tau\ [10^{20} m^{-3}\ ms] = 0.1$ $n_e \tau\ [10^{20} m^{-3}\ ms] = 10$
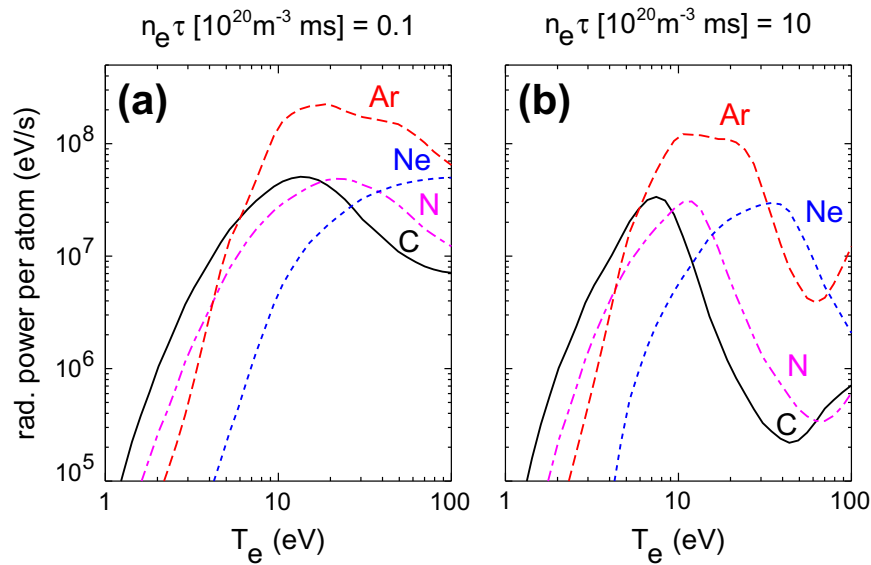
Figure 2.6: Radiated power for different seed impurities considered to be used in ITER. The depicted values were calculated for typical divertor conditions [37].

ters (like e.g. particle energies, species and fluxes, surface structure, composition and temperature and many others) may be controlled and varied separately. In this work the latter approach was chosen. Various aspects which are important in plasma wall interaction were studied under controlled laboratory conditions.

Within this chapter an outline of some of the most important plasma wall interaction issues for the operation of a future fusion power plant will be presented.

2.2.1 Erosion

In the interaction of energetic plasma particles with surfaces, material is continuously eroded. This will ultimately limit the life-time of the plasma facing components. Wall erosion is either solely driven by momentum transfer in collisions between projectiles and surface atoms (i.e. physical sputtering, cf. p. 18) or may also involve chemical reactions between the target material and the impinging particle (i.e. chemical sputtering, cf. p. 23). The charge state of the impinging projectiles does not only influence the ion impact energy due to acceleration in the plasma sheath potential, but might also enhance the sputtering yield by the release of the internal, i.e. potential energy of the ion upon surface impact (i.e. potential sputtering, cf. p. 26).
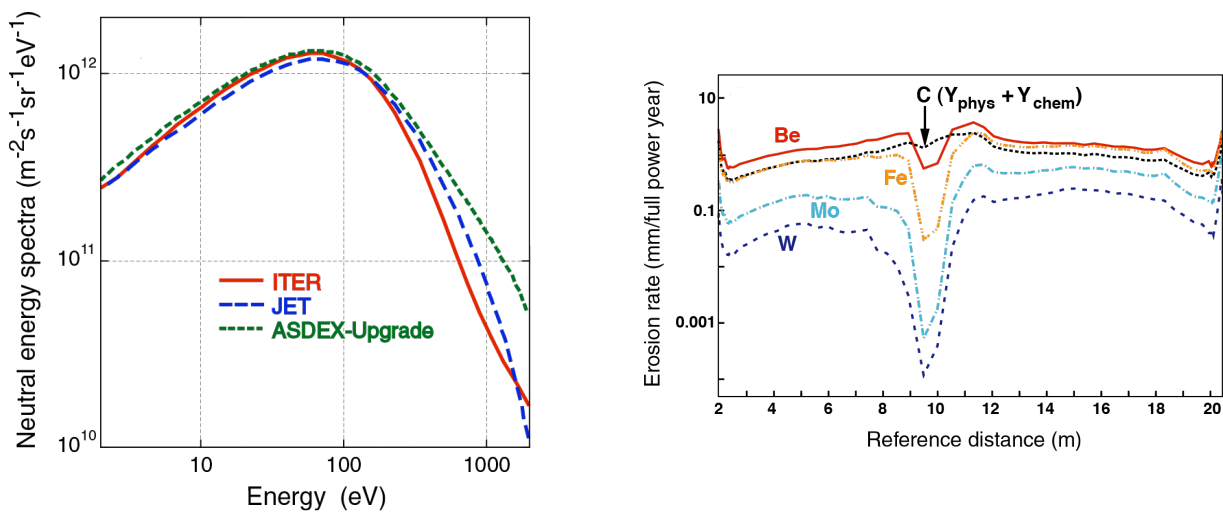
Figure 2.7: Simulated energy spectra for charge exchange neutral particles in ASDEX-Upgrade, JET and ITER (left) and resulting wall erosion rates for different materials (right) [41]. The erosion rates are simulated for one year of continuous ITER operation at full power with reference to poloidal distances ranging from the inner to the outer strike point.

The erosion rate of the ITER plasma facing components can be simulated [24, 42] with a reasonable choice for the incoming particle fluxes of all species impinging onto the vessel walls, a proper estimate of their energy spectra, and taking into account the involved erosion processes and their respective sputtering yields. Results of such simulations are shown in figure 2.7 [24]. The impact energy of the particles bombarding the walls is determined by the plasma ion temperature and the acceleration in the plasma sheath potential. Particles with higher charge states will hence impinge onto the vessel wall with higher energies. The erosion rates obtained in this simulation lead to wall thinning rates of up to $\sim$ 3.5 mm per operation year. With respect to wall erosion, W exhibits the longest life-time in a fusion reactor, with wall thinning rates about a factor of 15 lower than for low Z materials such as Be. This is generally one of the strongest arguments supporting the decision to eventually swith to a full W fusion reactor design.

Physical Sputtering

Physical sputtering is theoretically well understood and has been described in detail over the last decades [43-46]. When energetic particles bombard a surface, they transfer their energy in a series of elastic nuclear collisions to target atoms. In

Katharina Dobeš
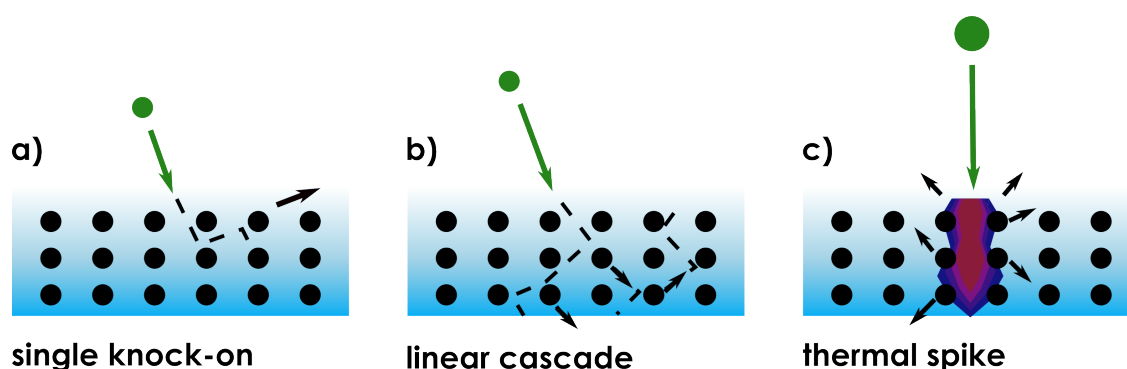
Figure 2.8: The collision regimes upon surface impact of an energetic particle can be distinguished according to the density of the collision cascade (see text).

such a collision, the projectile will be deflected in the screened Coulomb potential of a target atomic core. Furthermore, the incident particle might also induce electronic excitations within the surface in inelastic electronic collisions. Recoiling target atoms will collide with further target atoms, which will result in the creation of higher order recoils. Thus, multiple target atoms are involved in a series of energy transfers and angular deflections and a collision cascade is initiated in a near surface region of the the target material. If in such a collision cascade a target atom receives sufficient energy to overcome the surface binding energy E_s of the solid, it can be ejected, i.e. it is sputtered. The energy deposited in the ion impact will be dissipated within the collision cascade, until thermal equilibrium conditions are re-established.

Depending on the density of the collision cascade, three collision regimes are generally distinguished [47] (see figure 2.8): in the *a) single knock-on regime* the bombarding particle transfers enough energy to remove a target atom but not to initiate a collision cascade. The number of eroded particles depends on the collision cross-section between target atoms and projectile. This sputtering scheme applies to light projectiles and low impact energies.

In the *b) linear cascade regime* recoiling target atoms are energetic enough to produce higher order recoils. The collision cascade can however still be understood as a sequence of two-body (so-called 'binary') collisions between a moving particle and another particle at rest. The number of sputtered particles depends on the energy deposited per unit depth. This sputtering regime covers ion energies from the eV up to the MeV energy range.

In the limit of a very dense collision cascade, in the so-called *c) spike regime*, all atoms within a certain surface volume are set in motion. They have to be un-

derstood as a thermal ensemble, in which the temperature might even exceed the melting temperature of the solid. This will result in the evaporation of material. The spike regime applies to the impact of molecules, clusters and swift heavy ions.

A measure for the amount of eroded target material under particle impact, is the sputtering yield Y, which is defined es the average number of emitted target atoms per impinging projectile:

$$Y = \frac{\text{average number of removed particles}}{\text{number of incident particles}}$$

The above-considerations imply that the sputtering yield will depend on the energy and the angle of the impinging particle but not on the target temperature or the charge state of the projectile. In addition the energy that can be transfered in an elastic collision from the projectile to a target atom depends on the mass ratio of the collision partners. This can be expressed by the energy transfer factor γ:

$$\gamma = \frac{4m_1 m_2}{(m_1 + m_2)^2} \tag{2.1}$$

with m_1, m_2 being the mass of a target atom and the projectile respectively. There will also be a threshold energy E_{th}, below which the energy transferable in an elastic collision does not suffice to overcome the surface binding energy E_s in order to remove a surface atom [48]:

$$E_{th} = \frac{(m_1 + m_2)^4}{4m_1 m_2 (m_1 - m_2)^2} E_s \tag{2.2}$$

Below this energy threshold E_{th} no sputtering takes place. Consequently the threshold for light ions such as H isotopes and He in a fusion reactor will strongly depend on the target mass, as can be seen from the energy transfer factor γ (cf. equation 2.1). For light projectiles the threshold will not be exceeded for e.g. typical divertor energies and materials. This is illustrated in figure 2.9, where the energy dependency of the sputtering yield under D impact is shown for various fusion relevant materials. For comparison the sputtering yield obtained for C bombardment of W is included. Figure 2.9 also clearly demonstrates that the shape of the sputtering yield as a function of the ion energy is very similar for different target projectile combinations: Above the energy threshold E_{th}, the yield increases strongly with increasing projectile energy and exhibits a broad maximum at energies $\gtrsim 100$ eV, where the energy deposited in a near surface region, the so-called escape depth of sputtered particles, reaches a maximum. Above this maximum
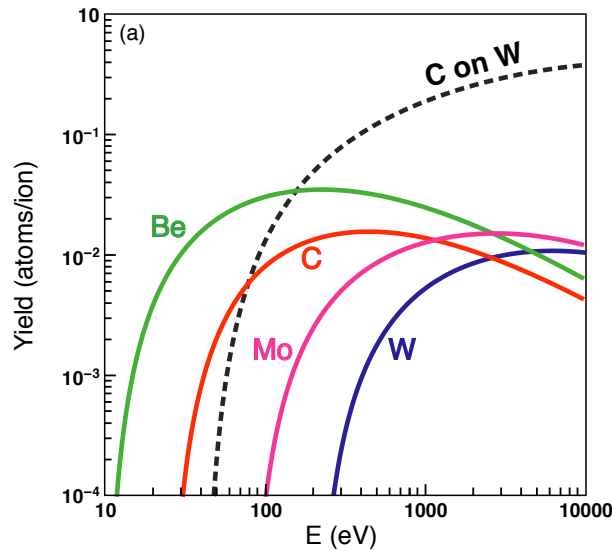
Figure 2.9: Sputtering yields for various materials being considered as plasma facing components under D incidence at normal impact. The dependency of the sputtering yield on the mass of the projectile is demonstrated by means of the sputtering yield of C impact on W. Picture taken from [41].

the sputtering yield decreases again in accordance with the cross section for nuclear collisions [49].

The dependency of the sputtering yield on the particle energy E_0 and incidence angle ϑ_0 can readily be derived within the framework of integral transport equations for atom - atom two body collisions of the particles involved in the collision cascade, as first demonstrated by Sigmund [43]. With some simple approximations for the cross section of the interacting particles, an analytical solution of these transport equations can be found [50].

Since sputtered particles originate from within a rather narrow depth below the surface, the sputtering yield must be dependent on the energy deposited per unit depth in collisions with target atoms - a quantity generally referred to as stopping power [43]. The yield can then be expressed as:

$$Y(E_0, \vartheta_0) = \Lambda F_D(E_0, \vartheta_0) \qquad (2.3)$$

with Λ being a materials constant (which for example includes the surface binding energy E_s) and F_D the so-called stopping power

$$F_D = \frac{dE}{dx} \qquad (2.4)$$

Katharina Dobeš

In a first approximation it can be assumed that the elastic interaction of the colliding particles, i.e. nuclear collisions, can be treated separately from the inelastic, i.e. electronic interaction such as e.g. excitation of target atoms. If any inelastic interaction is neglected, the average energy loss of the incident particle only depends on the nuclear stopping power:

$$\frac{dE}{dx}\bigg|_n = N \int_{T_{min}}^{T_{max}} T \, \frac{d\sigma(E)}{dT} \, dT \tag{2.5}$$

In this expression E is the energy of the incident particle, and T the energy transferred to a target atom in a nuclear collision. The probability for a collision between target atoms and projectile is determined by the nuclear cross section $d\sigma(E)$ and the atomic density of the target material N. For an analytical solution of the energy dependency of the sputtering yield in formula 2.3, the nuclear cross section can be approximated by a power cross section, as proposed by Lindhard and Scharff [51]. According to this approach, the inter-atomic interaction for a moving atom of the collision cascade with another atom at rest is described by a point charge in a screened Coulomb potential.

For low impact energies near the energy threshold for sputtering, the above-sketched analytical approach is no longer valid and fails to reproduce the experimental data [52]. In addition the influence of inelastic energy losses on the sputtering yield is more pronounced near the threshold energy [53]. Multiple attempts [44, 45, 52, 54] have been made to fit the available experimental data on sputtering yields to a universal, empirical formula. The most recent of these formulae was proposed by Eckstein and Preuss [45], who succeeded in describing the sputtering yield very accurately, especially in the near threshold region. In analogy to the analytical approach presented above, a proportionality of the sputtering yield Y to the nuclear stopping power $(dE/dx)|_n$ is proposed. To obtain this stopping power $(dE/dx)|_n$, a screening function for the free electron inter-atomic potential [55] is used. In addition the inelastic energy loss is included by a combination of two different models: Continuous energy loss, following a friction model proposed by Lindhard and Scharff [50] and local energy loss based on a model by Oen and Robinson [56]. Using these ingredients the following empirical fit formula is obtained:

$$Y(E_0) = q \, \frac{dE}{dx}\bigg|_n^{KrC} (\varepsilon) \, \frac{\left(\frac{E_0}{E_{th}} - 1\right)^\mu}{\lambda + \left(\frac{E_0}{E_{th}} - 1\right)^\mu} \tag{2.6}$$

The threshold energy E_{th}, the absolute yield q and the parameters λ and μ are fitted to the available experimental data for each target projectile combination.

The interaction of energetic projectiles with amorphous target materials can also be calculated by simulating the trajectories and collisions of all particles involved in the collision cascade with a computer program, such as the Monte Carlo codes TRIM [57] and TRIDYN [58]. From such simulations absolute values for sputtering yields, but also for ion ranges and surface damage can be inferred. Since in the linear cascade regime, the collision cascade can be understood as a series of two body collisions, these programs simulate the evolution of the collision cascade by only considering so-called binary collisions between a moving particle and another particle at rest (for details see section 3.4).

Chemical Sputtering

For some target-projectile combinations, chemical reactions between the impinging particle and the surface [28] may strongly influence the erosion behavior, resulting in both, enhanced or reduced surface removal rates. Different processes may contribute to this: Upon impact of reactive species, material compounds may be formed within a surface layer, spreading over a thickness equivalent to the range of the projectiles. This altered surface layer might in the following influence both, either the total erosion rate or the partial sputtering yield of the original surface species, e.g. due to a change in the surface binding energy E_s. Moreover, at the end of its penetration depth, the projectile might also react with a surface atom and form a molecule with a low binding energy to the substrate. These volatile molecules might then diffuse to the surface and desorb there [59].

The occurrence of such effects of course depends on the reactivity of the interacting species. In a fusion reactor chemical sputtering is most prominent for the interaction of H isotopes with C surfaces, resulting in the formation of mostly CH_3 radicals but also of higher order hydrocarbons [60]. Sputtering of any C plasma facing components will be dominated by chemical processes - especially for low ion energies and elevated surface temperatures [61].

Besides H impact, chemical sputtering is also found to occur in the presence of other reactive species such as oxygen and nitrogen. For C materials the formation and emission of CO, CO_2 [62] and C_2N_2 [63] is observed. Metal surfaces generally oxidize under O exposure. Compared to Be, an oxidized BeO surface has an increased surface binding energy, which is generally reflected in a decrease of the sputtering yield and an enhancement of the threshold energy E_{th} for BeO as compared to Be [64]. The sputtering yield of W on the other hand increases slightly due

to oxide formation such as WO_3 [65]. Only very recently the interaction of nitrogen with metals such as W and Be was investigated [66-68]. It was found that under N impact a stable nitride phase is formed in both materials, i.e. a WN [66] compound and Be_3N_2 [67] respectively. Studies on mixed material compounds such as Be-W layers are still very scarce [68, 69].
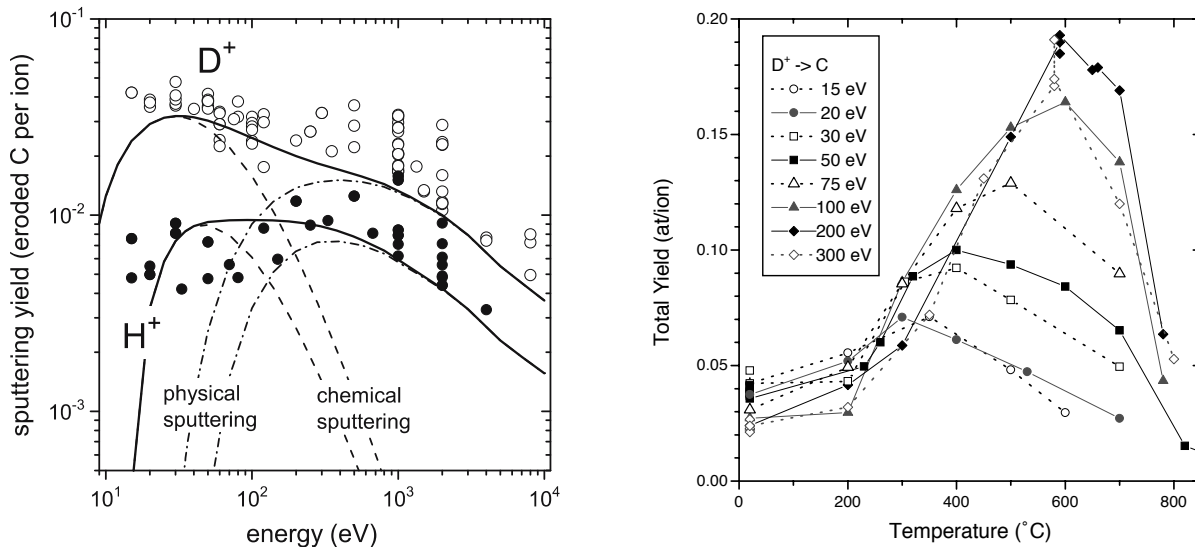
Figure 2.10: Total sputtering yield of C under D and H impact respectively as a function of the ion energy (left) and the surface temperature (right) [70].

Generally all the above processes are complex, multi-step processes that in contrast to physical sputtering (cf. p. 18) depend on a wide variety of interdependent parameters such as the surface temperature T_S, the ion flux j, the impact energy of the projectiles E_0, the surface structure and the target material composition [61]. Most progress in understanding the involved fundamental processes was made for the sputtering of C by H impact. Some experimental results on the energy and temperature dependency of the total sputtering yield of C surfaces under H and D impact are shown in figure 2.10. Apparently surface erosion induced by reactive species does not decrease towards lower energies as would be expected for physical sputtering (left graph). In addition figure 2.10 clearly shows, that the chemical sputtering yield is enhanced for elevated temperatures with a pronounced temperature maximum at a temperature T_{max}, which actually depends on the ion impact energy (right graph). Moreover an isotope effect was found, with sputtering yields for D being generally higher compared to H impact. These and other extensive studies were able to resolve the dependency of the

sputtering yield on a variety of the above-mentioned surface and projectile parameters [61, 71, 72]. As a result it was possible to realize some successful models, which describe the chemical sputtering process. By means of analytic equations, which take into account various processes and their cross-sections and activation energies [60, 73], the experimental data could be reproduced very nicely. In another approach a set of rate equations, which describe the involved mechanisms on a microscopic level [74], was used to elucidate the influence of the underlying processes.

From the cumulative data available for chemical sputtering of C under H isotope impact, the following microscopic picture could be inferred for the enhancement of the sputtering yield as compared to physical sputtering: When an H atom impinges on a C surface it creates damage along its path through the surface by displacing target atoms. At the end of its range in the surface, when the H isotope has slowed down to thermal energies, chemical reactions occur [75], in which hydrocarbons C_xH_y and H_2 molecules are formed [28]. These molecules are only very loosely bound to the surface. The chemical reaction of the H projectile with the C network is thermally activated [71], i.e. the reaction rate R follows the relation:

$$R = n_H A e^{\frac{-Q}{k_B T}} \qquad (2.7)$$

with Q being the corresponding activation energy and n_H the hydrogen concentration in the surface. As a result the chemical sputtering yield exhibits a pronounced temperature maximum T_{max} at $\sim$ 700 - 900K [76]. For temperatures beyond this maximum T_{max}, the yield decreases again, as recombination of molecular hydrogen competes the formation of hydrocarbon molecules and the available hydrogen concentration n_H therefore decreases. Hydrocarbon molecule formation is promoted by surface damage induced by preceding ion bombardment and also the intrinsic structure of the surface, since dangling C bonds in the C network of the substrate are needed as reaction sites for the impinging H projectiles [74, 77]. For this reason chemical sputtering is also found to be strongly enhanced for simultaneous bombardment of C surfaces with H and non-reactive species such as Ar [78]. In addition a threshold energy for chemical sputtering is found of $\sim$ 15 eV, which is equivalent to the energy needed for damage production E_{dam} [61, 71]. In a last step of the erosion process, the hydrocarbon molecules need to diffuse from their site of creation, i.e. the end of the ion range, to the surface where they are desorbed. This reaction step is found to be most efficient, if the ion range does not extend to large depths, i.e. if the energy deposited by nuclear collisions peaks in a region near to the substrate surface. Indeed the energy

dependency of the chemical sputtering yield is found to exhibit a similar behavior as the energy deposited by the projectile in a near the surface region [61]. In addition an elevated surface temperature facilitates the diffusion and desorption process, which contributes to the pronounced temperature dependence of the chemical sputtering yield [79](cf. figure 2.10).

Summarizing the above, the overall sputtering yield Y_{tot} for erosion of C materials under H isotope impact, including both physical and chemical contributions, can be described by the following empirical formula [71]:

$$Y_{tot} = Y_{phys} + Y_{therm}\left(1 + DY_{dam}\right) + Y_{surf} \tag{2.8}$$

In this empirical formula the total yield is basically composed of three components: The first term represents the physical sputtering yield, Y_{phys}. The second expression Y_{therm} accounts for thermally activated chemical erosion yield of thermalized H isotopes. It includes hydrocarbon formation and erosion and incorporates the T dependency of the total yield Y_{tot}. This chemical erosion yield is enhanced by a factor considering damage formation, i.e. $(1 + DY_{dam})$. Here D is an isotope dependent factor to the damage induced yield Y_{dam}. Finally the term Y_{surf} includes the sputtering of surface radicals, which too is a T dependent term. Basically the shape of the individual contributions can be described by modified versions of the Eckstein empirical formula for sputtering (cf. equation 2.6) with adapted threshold energies E_{th} for the different processes: i.e. the energy threshold for physical sputtering $E_{th} \sim$ 10 - few 100 eV (cf. equation 2.2), a threshold for surface radical desorption $E_{des} \sim$ 1 - 2 eV, and a threshold for damage production $E_{dam} \sim$ 15 eV.

Potential Sputtering

When a multiply charged ion impinges on a surface, it is generally neutralized. This processes already begins in front of the surface, when the highly charged ion quasi-resonantly captures target electrons into highly excited projectile states, while lower lying energy levels remain empty. The resulting highly excited, so-called 'hollow atom' subsequently starts to decay by a series of de-excitation processes [80-82] (see also section 2.3.1). However a large part of the potential energy of the highly charged ion (i.e. the cumulative binding energies of the electrons that have been removed in its production) is dissipated below the target surface. The ion deposits its potential energy within a very small surface volume (typically of nanometer size) and in a very short time interval ($\ll$ 100 fs) [83]. This may lead to non-linear excitation processes [84,85] and may thereby have an influence on

ion-induced phenomena such as sputtering and electron emission (see also section 2.3). Furthermore the highly charged ion might even create nanometer-sized surface modifications by depositing its internally stored energy upon target impact [86]. The characteristics of the above-mentioned phenomena strongly depend on the properties of the surface and its interaction with the projectile.
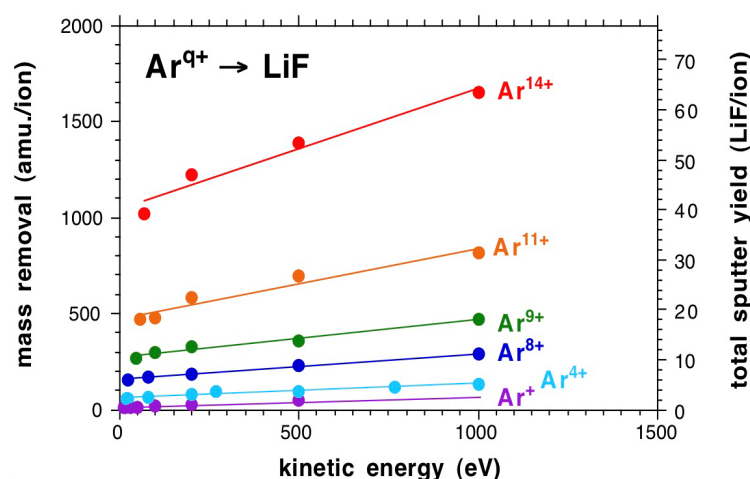
Figure 2.11: Sputtering yield of LiF [87, 88] for the impact of highly charged ions with various charge states. Even for the limit of zero kinetic energy, a finite sputtering yield is found. The potential energy stored in the projectile suffices to remove surface atoms.

While for conducting targets the sputtering yield generally only depends on the kinetic energy[5] [89, 90] of the projectile, a pronounced enhancement of the sputtering yield was found with increasing projectile charge state for a variety of insulting or semi-conducting targets [83, 91], e.g. for different alkali halides [87, 88, 92, 93], oxides [88, 94], and also hydrocarbon surfaces [95]. This phenomenon is commonly referred to as 'potential sputtering' [83, 84]. In figures 2.11 and 2.12 examples for the charge state dependency of the sputtering yield of two different surfaces (LiF and MgO_x) are shown.

Upon surface impact the potential energy of a highly charged projectile ion is transferred into excitations of the electronic system of the target. For target materials with a low charge carrier mobility, this excitation may be converted into motion of target atoms. The mechanism behind this energy transfer generally de-

---

[5]and, in some cases, also on the reactivity of target and projectile (cf. chemical sputtering, p. 23)

Katharina Dobeš

pends on the particular target material, however a strong coupling, i.e. efficient energy transfer from the electronic to the phononic system of the solid is commonly required [83]. Different effects have been identified, which may be involved in this process.

In alkali halides such as LiF or NaCl but also in some oxides like SiO_2 and Al_2O_3, the formation of self-produced lattice deformations were observed in response to excitations of valence-band electrons (i.e. electron-hole pairs created by the impinging ion). These defects, so-called 'self-trapped excitons' and 'self-trapped holes' [96], subsequently decay into different color centers, which leads to the desorption of surface atoms either directly or by a small momentum transfer from subsequent projectiles. This sputtering mechanism is called '*defect mediated sputtering*' [87, 91]. The number of sputtered particles is found to roughly depend on the number of ion induced electronic defects, i.e. on the potential energy carried by the projectile. This is reflected in the strong increase of the sputtering yield with projectile charge state (cf. figure 2.11). The minimum energy that is needed to generate a self-trapped hole by resonant electron capture form the surface, poses a potential energy threshold of $\sim$ 10 - 12 eV on this sputtering process. Such a threshold for the potential energy can indeed be confirmed by experimental results [93]. An extrapolation of the curves in the graph in figure 2.11 to zero kinetic energy of the projectile, results in a finite sputtering yield, which points to the fact that in this case no kinetic energy transfer from knock-on collisions between target atoms and projectiles is needed for the removal of surface material [83].

For other target materials such as MgO_x, an enhancement of the sputtering yield with the projectile charge state is only found in combination with the availability of ion impact velocity (cf. figure 2.12). Extrapolation to zero kinetic energy in this case, gives zero sputtering yield for all investigated charge states. The potential energy of the projectile alone does obviously not suffice to induce the potential sputtering process. This form of potential sputtering has therefore been termed '*kinetically assisted potential sputtering*' [94]. Here, the conversion of electronic excitation into target atom motion is promoted by lattice defects produced in a collision cascade of a preceding projectile impact.

Overall the above-outlined scenarios for potential sputtering can be described by a set of coupled rate equations for the different processes involved in potential sputtering phenomena [94]:

$$\frac{dY}{dt} = c_P N_{ST} + c_{KP} N_{LD} N_{ED} \tag{2.9}$$
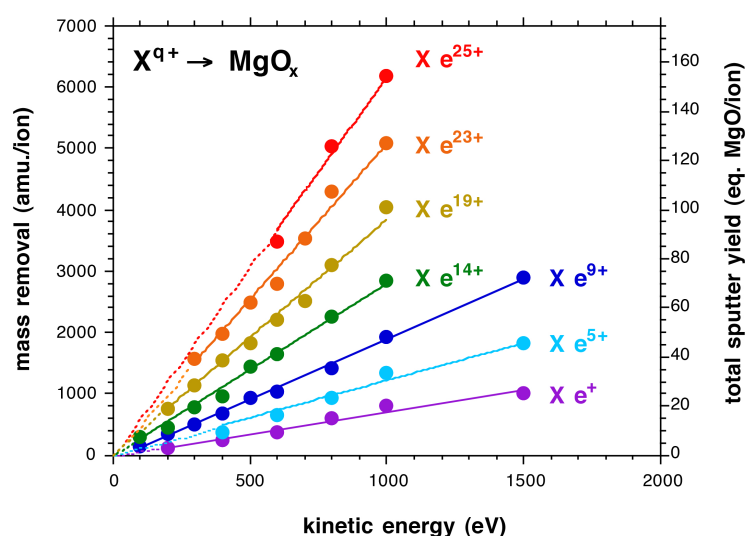
Figure 2.12: Sputtering yield of MgO_x [94] for the impact of highly charged ions with various charge states. While the sputtering yield is clearly enhanced by the projectile charge state, it extrapolates to zero for $E_{kin} = 0$. The kinetic energy of the projectile is needed to promote the observed potential sputtering phenomenon.

In this equation the first term represents 'conventional' potential sputtering, with c_P being the conversion rate of electronic defects into sputtered particles and N_{ST} representing the number of self-trapped defects. The second term in equation 2.9 describes kinetically assisted potential sputtering, with a corresponding conversion rate C_{KP} of electronic and kinetically induced defects and a proportionality to a combination of both, the number of lattice defects N_{LD} and the number of electronic defects N_{ED}.

Moreover, for some sputtering phenomena, which were observed when very highly charged ions interact for example with uranium oxide and GaAs, the so-called Coulomb explosion model may give an appropriate explanation [84,97-99]. In this model enhanced sputtering yields are attributed to strong repulsive forces introduced in the solid surface by a local electron depletion of the projectile impact zone as a result of the ion neutralization process. Lastly, extremely high densities of electronic excitations from a slow, very highly charged ion (like e.g. Th^{70+}) might destabilize the structural integrity of solids (by creating anti-bonding states). They might be responsible for enhanced sputtering yields found in some further investigations [100, 101].

2.2.2 Fuel Retention

The retention, i.e. permanent incorporation, of hydrogenic isotopes, especially of radioactive T, in the wall material of a fusion device will be one of the most constraining plasma wall interaction and operational issues for ITER. For safety and environmental reasons alone, the amount of retained T has to be restricted to ~ 700 g in ITER [29]. Recycling fuel from the plasma vessel walls will furthermore have a severe impact on plasma as well as fuel density control.
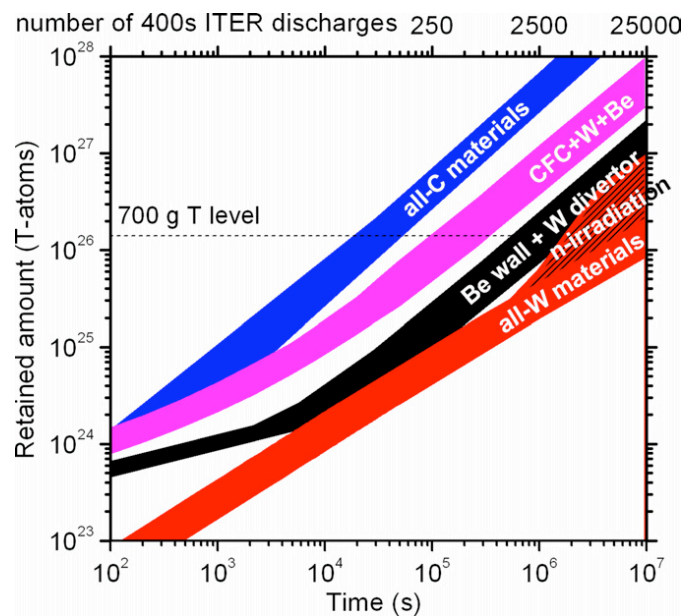
Figure 2.13: Projected T inventory for ITER with different plasma facing materials. The band width for each material option reflects uncertainties in expected particle fluxes to the wall. Picture taken from [29].

Several processes have been identified to play a role in fuel retention: Implantation of energetic hydrogen isotopes upon impact onto plasma facing surfaces, subsequent diffusion and release behavior, as well as trapping in the bulk of wall components. In addition H isotopes will be co-deposited throughout the vessel together with chemically reactive impurity species such as e.g. C. Depending on the choice of plasma facing material mix, these co-deposited layers might in fact constitute the main contribution to long-term T inventories in ITER [102].

Projections on the T inventory in ITER for different possible material mixes are shown in figure 2.13. The presented values are based on experience from existing

Katharina Dobeš

tokamak machines and sophisticated modeling of the above-mentioned fuel retention mechanisms. It is quite evident that in a full C or C containing machine (in blue and pink respectively), the maximum tolerable T level of ~ 700 g would be reached very rapidly within only a few hundred discharges, with fuel being predominantly retained in co-deposited hydrocarbon layers [29]. For a full metal W/Be machine (in black) the T safety limit would only be reached after a few thousand discharges. In this case the main contribution to retained T stems from co-deposition with Be eroded from the first wall. In an all W device (the red area in figure 2.13) more than 18 000 discharges would be possible before exceeding any safety constraints. In W T is predominantly trapped at defect sites in the bulk. Radiation damage due to neutron irradiation cloud therefore have a significant influence on the T inventory in a full W machine (see black shaded area in figure 2.13) [14, 29].

To manage the T inventory in a fusion machine, mitigation and removal techniques will be mandatory. A variety of different methods are being considered and studied (see e.g. [18, 29, 103-105]), ranging from isotope exchange in D plasma discharges, thermal desorption by surface heating, oxidative methods involving bake out procedures under high O pressure, reduction of hydrocarbon co-deposits by N seeding via the so-called Scavanger effect and many more. However, so far the obtainable removal rates and the efficiency of all of these methods generally fail to meet ITER requirements [106]. This strongly nourishes the need to abandon C in the material choice of plasma facing components, at least in the longer run.

Fuel Retention Processes

In tokamaks impinging H isotopes will have energies of up to some keV. When they penetrate into a solid surface, their kinetic energy is deposited into electronic excitation and nuclear deflections (see section 2.2.1, p. 18). On their way through the solid they will displace lattice atoms, thereby creating lattice vacancies and interstitials. At the end of their range in the solid, when the impinging particles have slowed down to thermal energies, they will be implanted. Both the depth distribution of the implanted species $n(x)$ as well as of the created defects will depend on the energy of the projectile E_0 and its atomic number Z.

Implanted H isotopes will end up in the energetically most favorable atomic configuration within the atomic lattice. For low H fluences, impinging H isotopes will at first accommodate into solution sites. Depending on the mobility of the H isotopes in the solid, implanted H may then diffuse to trapping sites. A number of trap types with different bonding strength might be present in the surface [14, 29].

Trapped H might be bound to e.g. vacancies and embedded surface impurities such as oxides. It might also agglomerate at internal surface boundaries and in voids or cavities. In addition, in some materials such as beryllium and tungsten, a stable metal-hydride phase might built up [107]. Lattice damage from ion bombardment or induced by the neutron flux generated in the fusion reaction will create further trapping sites during plasma exposure. The available trap sites are filled according to their trapping energies E_{ti}. Traps with the lowest energy are occupied first and additional H is captured such that the various trapping sites remain in thermodynamic equilibrium. The retained H concentration is distributed to the individual trap sites according to their respective enthalpies of formation. Once local saturation of all available trapping sites is reached, further H can either diffuse to surface areas of lower H concentration or is simply re-emitted.

Overall, the retention behavior of a material thus generally depends on a number of H-material interaction parameters, such as the number of trap sites N_{ti} and their trapping energies E_{ti} as well as the thermally activated, i.e. substrate temperature dependent solubility $S(T)$ and diffusivity $D(T)$ of H in the material [108]. The concentration of H in a surface is composed of an H atomic fraction in solution c_s and the individual concentrations in the trapping sites c_{ti} respectively:

$$c(x,t) = c_s(x,t) + \sum_i bdac_{ti}(x,t) \tag{2.10}$$

The individual concentrations can be determined by diffusion equations, e.g. for the solute concentration [14]:

$$\frac{\partial c_s}{\partial t} = D(T)\frac{\partial^2 c_s}{\partial x^2} + \Phi\, n(x) - \sum_i \frac{\partial c_{ti}}{\partial t} \tag{2.11}$$

In this equation Φ is the incoming H flux and $n(x)$ the corresponding depth distribution of implanted H. The exchange between individual H implantation sites c_s and c_{ti} will be governed by their enthalpy difference and corresponding rate coefficients Γ. In thermodynamic equilibrium all of these exchange terms will be zero.

In addition to trapping of H in the bulk of plasma facing materials, H isotopes might also be co-deposited together with reactive species such as C. In a fusion reactor, there will be regions of net deposition, e.g. in remote and shaded areas in the divertor [109]. In these parts of the vessel, hydrogen containing co-deposits will develop, with a layer thickness that will increase linearly with exposure time. Since in such layers the amount of retained H does not saturate, H co-deposition will constitute a dominant long-term retention source [110].

Katharina Dobeš

Hydrogen Isotope Retention in ITER Relevant Materials

In metallic material surfaces such as W and Be, H isotopes are mainly retained due to implantation and subsequent trapping in the bulk [111, 112]. It is found that in *beryllium* surfaces, H does not diffuse beyond the implantation range of the impinging H projectiles [111, 113]. Moreover the solubility of H in Be is very low [114]. The accumulated H concentration in the implantation zone therefore saturates at higher fluences, at concentrations around 0.3 - 0.4 D/Be [67, 111, 115]. Once saturation is reached, further D is re-emitted. As the ion range increases with projectile velocity, the total amount of retained H increases with H implantation energy [111]. It was also reported that the concentration of retained H isotopes decreases continuously with substrate temperature [116] and that surface impurities might strongly enhance the retention behavior [111]. Although the H atomic concentration in Be co-deposited layers is comparably small, it might still be ~ 5% [117]. This retention mechanism might in fact become a significant contribution to the overall H isotope inventory in full metal machines [29].

For *tungsten* surfaces, the solubility of H is also very small [118]. H isotopes are however very mobile and readily diffuse beyond the implantation zone [119]. H is mainly trapped at intrinsic defects or damage created by ion (and in a fusion machine also) neutron bombardment. Traps which are generated during machine operation, might overall enhance the amount of retained H by a factor of ~ 8 [29]. The retention behavior in W also strongly depends on the crystalline structure of the surface [120]. During H implantation, the H concentration might locally exceed the solubility limit, resulting in plastic deformation of the lattice and the formation of H filled voids and vacancy clusters [120]. Co-deposition of H together with W is generally not reported [117].

Due to its high reactivity towards H, fuel retention mechanisms are entirely different for *carbon* compared to Be and W. The interaction of C surfaces with H is dominated by chemical erosion (see section 2.2.1, p. 23). The emerging hydrocarbon molecules and radicals will be transported along the plasma edge and will finally be re-deposited, especially in remote areas, with no direct line of sight to the plasma [109]. Continuous growth of such layers might result in layer thicknesses of several μm and co-deposits might therefore be a dominant source for long-term H retention in a fusion reactor [110]. The H content in such layers will strongly depend on the substrate temperature during deposition and the energy of the impinging C_xH_y molecules [121, 122]. In the divertor region, low density, polymer-like, so-called 'soft' amorphous hydrogenated carbon (a-C:H) layers will

be created by deposition of low temperature plasma particles (with an incidence energy $\ll$ 100 eV). The hydrogen concentration in these soft layers might become $H/C = 0.8 - 1$ [123]. If the incident particle energy is however much higher, at temperatures near room temperature, so-called 'hard' layers with a ratio of $H/C \approx 0.4$ will form [123].

H isotopes impinging onto a C surface might also be trapped in the bulk. During H impact, a saturated surface layer is created with H concentrations at room temperature of $H/C \sim 0.3 - 0.4$ [124]. With increasing substrate temperature the saturation level decreases. From this saturated surface layer, some H might be transported deeper into the C bulk by diffusion along internal porous surfaces and grain boundaries [125].

2.2.3 Mixing of Materials

With the decision of using different materials for the first wall in ITER, the formation of mixed material layers within the vacuum vessel will be inevitable. As outlined in the previous sections, plasma facing components in ITER will be subjected to a variety of erosion processes, both due to sputtering as well as evaporation or melt layer losses. Eroded material can either be re-deposited in near vicinity to its site of origin, or will migrate over rather large distances due to long-range transport mechanisms like e.g. temperature gradient forces [41] or repeated erosion and re-deposition. While higher Z impurities tend to be re-deposited promptly [126], low Z species such as C or Be might also accumulate on surfaces rather far away from their original position in the vacuum vessel. In a fusion machine there will be areas of net deposition, where mixed material layers will grow with plasma exposure time. Whether in steady state a surface is subject to net erosion or deposition, depends on multiple parameters such as the local ion energy (i.e. plasma temperature) or the particle flux (i.e. impurity concentration). It is generally determined by the balance between surface sputtering on the one hand and implantation as well as deposition of material on the other hand [69]. In addition compositional and structural changes will be inflicted on the surfaces of plasma facing components by implantation of intrinsic impurities such as residual gas atoms (e.g. O) or eroded species, as well as due to retention of impurities which are deliberately added to the plasma for cooling purposes (e.g. Ar, Ne, N) and fueling hydrogen isotopes. As a result of all of the above, the composition of the first wall in ITER will dynamically change during operation.

The formation of mixed materials might have a severe influence on the properties of the plasma facing components. Parameters like the sputtering yield, the

melting point, fuel retention behavior, mechanical qualities, and thermal as well as electrical conductivity might potentially be significantly different for these mixed materials as compared to the designed for surfaces. It is therefore of fundamental interest to study the development and properties of such multi-component surfaces.

Under particle bombardment of a solid surface, implanted projectiles may form an altered surface layer on top of the surface substrate. This modified surface layer generally has a thickness of the order of the ion penetration depth in the solid [127]. The composition of this altered top layer will dynamically change during ion bombardment, until steady state surface conditions are established after a certain cumulative ion fluence. The exact fluence after which dynamic equilibrium is attained, and the depth to which the altered surface layer extends, will not only depend on the energy of the implanted projectiles but also on transport processes such as diffusion of particles into the bulk. The diffusivity might be enhanced by the displacement of target atoms and the creation of a highly mobile surface layer as a consequence of the particle impact (i.e. radiation enhanced diffusion) [128].

The partial sputtering yield of the individual components Y_i is generally different from the yield of the pure constituents at comparable concentration. In the collision cascade, which is initiated by the impinging particle, energy and momentum might be distributed differently to several surface constituents, due to discrepancies in their individual energy transfer factors in knock-on collisions (cf. equation 2.1). This mass effect results in an enrichment of the heavier component in the altered surface layer [128]. In addition, the chemical bonding of the surface components might differ for the individual constituents. Furthermore the escape probability of surface components will also depend on their range in the surface, which is usually larger for lighter atoms. Such bonding effects might lead to a preferential sputtering and consequently depletion of the component, which is more easily removed from the surface. Moreover, for certain high vapor pressure compounds such as oxides or nitrides, spontaneous desorption of surface molecules might be observed above a certain surface concentration [129].

Figure 2.14 shows a schematic representation of the dynamics of the formation of an implantation profile of a species A in a substrate of atomic species B with increasing projectile fluence. For low fluences, the projectile range distribution in the surface is determined by the implantation probability $n(x)$ of the impinging species. As the concentration of implanted projectiles A increases with ion fluence, both implanted atoms A and the substrate species B are being removed. The flux of sputtered atoms J_A and J_B respectively, depends on their concentration N_A, N_B in the surface and the ratio of their individual sputtering probabilities r [130]:
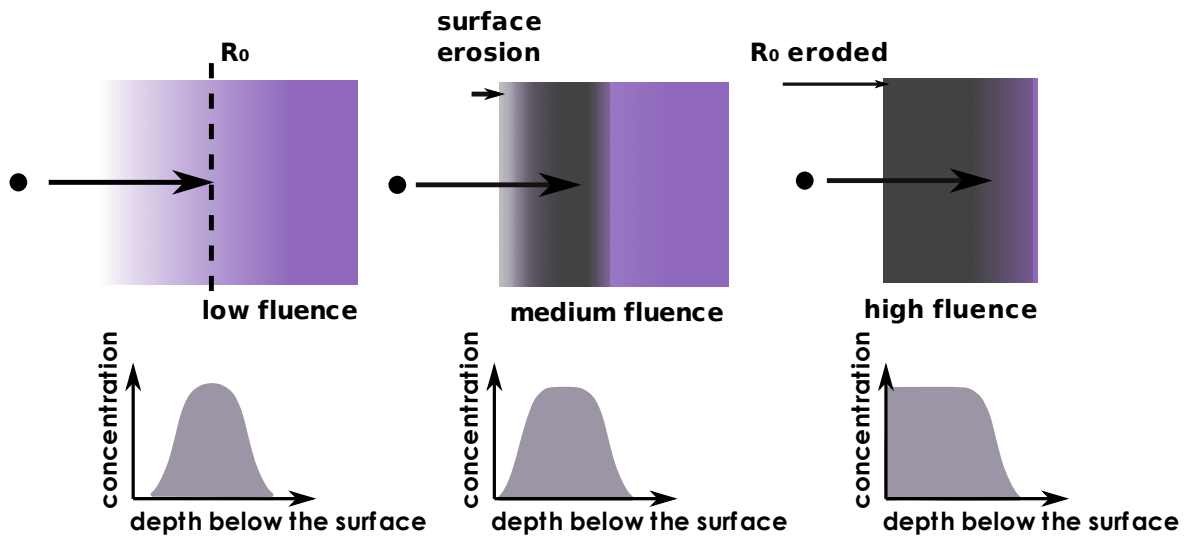
Figure 2.14: Schematics of the formation of an implantation profile. At low fluence the profile is similar to the range distribution of the projectiles. For medium fluence the implantation zone broadens and shifts towards the surface. At high fluences, when the sputtered depth becomes comparable to the ion range, steady state surface conditions are obtained.

$$\frac{J_B}{J_A} = r\left(\frac{N_B}{N_A}\right) \tag{2.12}$$

The total sputtering yield $Y = Y_A + Y_B$ is composed of the fluxes of the two species J_A and J_B,

$$(J_A + J_B) = Y\, J_i \tag{2.13}$$

if J_i is the incoming flux of species A. With increasing fluence a surface layer enriched in species A is established. As the surface is eroded from the very top (the sputtered particles emerge only from a very shallow region below the surface), the mixed material layer is shifted towards the vacuum-surface interface. Simultaneously, impinging particles are continuously implanted at their ion range R_0. This virtually results in a broadening of the A containing surface region. In steady state, after the removal of a surface layer with a thickness of the order of the ion penetration depth, the amount of retained A saturates, and an altered surface layer has established on top of the substrate. Under further ion bombardment, the erosion of this altered surface layer is in dynamic equilibrium with the modification of the underlying bulk by implantation of projectiles. The number of implanted atoms

Katharina Dobeš

is equal to the number of eroded atoms of species A, i.e. $J_A = J_i$. The surface composition does not change anymore and becomes equal to [130]

$$\frac{N_A^\infty}{N_B^\infty} = r\,(Y-1)^{-1} \tag{2.14}$$

The steady state concentrations N_A^∞ and N_B^∞ depend on the inverse sputtering yield Y and are proportional to the factor r, that determines which of the two species is more easily, i.e. preferentially sputtered.

2.3 Ion Induced Electron Emission

Particle induced electron emission is a phenomenon, which has attracted substantial interest over the last century or so (for extensive reviews on the subject see e.g. [131-133]). On the one hand it is of basic interest in elucidating fundamental aspects of the interaction of atomic projectiles with surfaces. Apart from this, it can also be used in technological applications such as particle detectors, surface analysis tools or plasma screens. In addition it has a critical influence on plasma wall interaction in fusion devices.

The emission of charged particles from plasma facing components as a result of inelastic particle-surface interaction will above all have a strong influence on plasma temperature and density in the plasma edge region of a fusion device. This in turn will affect the impact energy and particle fluxes impinging onto the first wall [134-136]. While the fraction of ionized particles in the flux of sputtered atoms is generally negligible, the emission of electrons by impact of energetic and possibly also highly charged particles will be substantial. The number of electrons, which will be ejected from plasma facing components, will determine the plasma sheath potential [134, 136]. Although in a fusion device the largest part of emitted electrons are induced by electron bombardment of plasma facing surfaces, there will also be a contribution from impact of light fueling species at sufficiently high impact energies as well as heavier (highly charged) impurity species (e.g. C, N, O, Ar) [137].

Electron emission can be described by the total electron emission yield γ, which determines the number of electrons that are emitted in a particle impact event subsumed over the total angular range $d\Omega$ and all emission energies dE:

$$\gamma = \int_0^\infty \int_{2\pi} \frac{d\gamma}{d\Omega dE} \, d\Omega dE \tag{2.15}$$

Electron emission upon surface impact is observed for different kinds of projectiles, ranging from photons to electrons and ions. In this work, only ion induced electron emission is investigated. The interaction of a charged ion with a surface is a rather complex process, as it involves a multitude of target electrons on the one hand and a (probably even highly) excited projectile on the other hand.

Two distinct electron emission regimes are commonly distinguished: Kinetic (KE, e.g. [132]) and potential electron emission (PE, e.g. [131]), i.e.

$$\gamma = \gamma_{KE} + \gamma_{PE} \tag{2.16}$$

For kinetic electron emission, the electron emission yield is mainly determined by the projectile impact velocity. Kinetic electron emission is governed by a collisional energy transfer from the projectile to an electron of the surface. If by such a collision, a target electron receives sufficient energy to overcome the surface potential barrier, it may be emitted from the surface. Potential electron emission on the other hand is caused by the potential energy, i.e. the charge state of the projectile (cf. figure 2.16). In this case the internal excitation of the projectile is converted into an electronic excitation of the target, which might result in the emission of electrons.
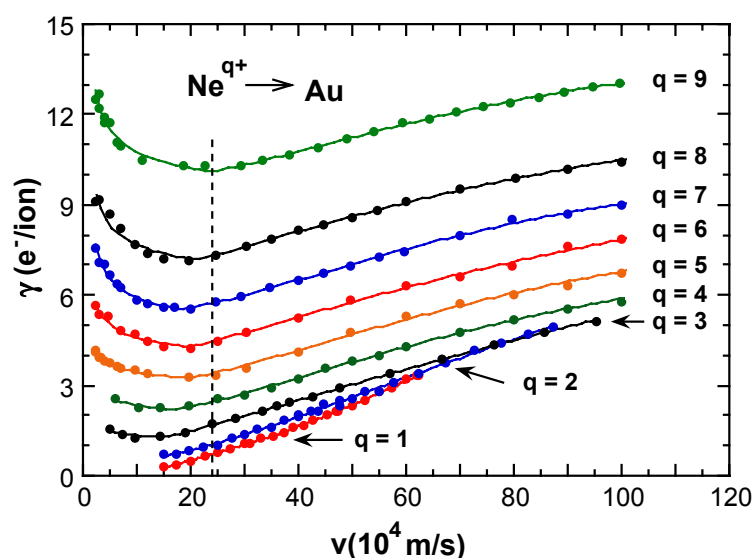

Figure 2.15: Impact dependency of total electron emission yields of neon ions with different charge states on polycrystalline gold surfaces [138]. The observed yields arise from both kinetic and potential emission. The vertical dashed line indicates the velocity threshold for kinetic emission, below which pure potential emission can be observed.

It is the rather difficult to assess these individual, but strongly interrelated electron emission regimes separately. A deeper insight can be gained by systematically varying projectile parameters such as incidence energy and also impact angle, as the influence of these two quantities on the electron emission yield is different for kinetic as compared to potential electron emission. To entirely discriminate the two contributions, it would be necessary to conduct experiments either in the limit

of very slow highly charged ion impact[6] (pure PE) or with neutral projectiles (pure KE).

Further information on the processes involved in electron emission upon surface impact of atomic particles may be obtained from investigating different target materials and thereby varying the target properties. A wide parameter range for e.g. the work function or the energy band gap can be covered by studying both conducting and insulating surfaces. This may specifically aid in understanding the influence of the above surface parameters on the observed electron emission. In addition a detailed investigation of the statistics for the number of electrons, which are emitted per ion impact event, might reveal some additional details on the involved contributions to the total electron emission yield [139-141].

Figure 2.15 gives an example for the impact velocity dependency of the electron yield of a polycrystalline gold surface bombarded with neon ions of various charge states. The observed electron yields represent a superposition of kinetic and potential electron emission. The threshold velocity for kinetic emission is indicated by a dashed line in figure 2.15. Below this threshold, pure potential emission can be observed.

In the following the fundamental concepts of particle induced electron emission will be outlined. This includes a basic description of the interaction of highly charged ions with surfaces (cf. section 2.3.1) and involved electron exchange processes (cf. p. 42). In addition the two above-mentioned emission regimes of kinetic (cf. section 2.3.3) and potential (cf. section 2.3.2) emission will be discussed in more detail.

2.3.1   Interaction of Highly Charged Ions with Surfaces

A highly charged ion can carry a lot of potential energy W_{pot}, which is determined by the sum of the ionization energies E_i, that have to be spent in its production process, i.e. for an ion with charge state q:

$$W_{pot}(q) = \sum_{n=1}^{q} E_i^{(n)} \tag{2.17}$$

For ions with very high charge states (such as in the extreme case e.g. Ar^{18+} or Xe^{52+}), this potential energy can amount to several keV and its release upon sur-

---

[6]i.e. at velocities below the threshold velocity v_{th} for kinetic emission, which is defined as the minimum velocity that is needed to eject a surface electron in a two body collision (see section 2.3.3)

Katharina Dobeš

face impact might therefore become dominant in the observed ion surface inter-action processes over e.g. the kinetic energy introduced by the projectile [85]. The increase of the potential energy of several ion species with charge state is demonstrated in figure 2.16.
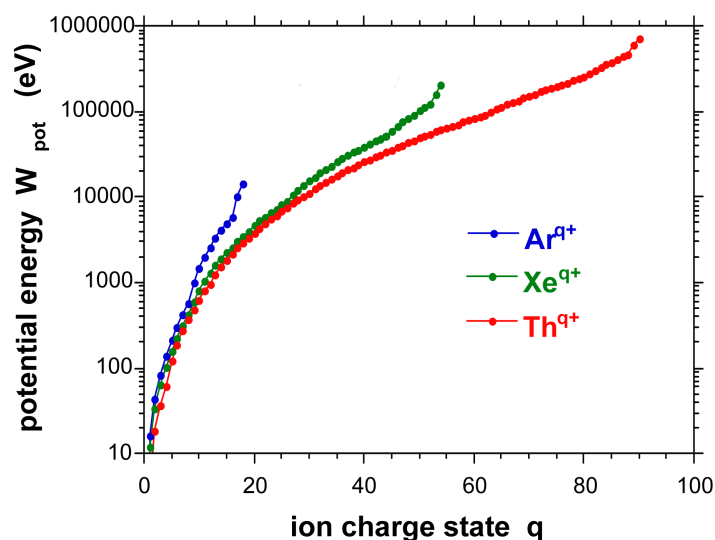

Figure 2.16: The potential energy of Ar^{q+}, Xe^{q+} and Th^{q+} as a function of the charge state q. Picture from [83].

The neutralization and de-excitation of a highly charged ion, which impinges onto a surface, can be described within the so-called hollow atom scenario [80, 83, 85, 131, 142]. The involved neutralization stages are schematically depicted in figure 2.17. At a certain distance above the surface, the highly charged ion will start to feel its image charge acceleration towards the solid. This will set a lower limit to the final impact velocity of the projectile and the interaction time above the surface. The neutralization of the highly charged ion will set in well before sur-face impact, when electrons from the conduction band of the solid are captured quasi-resonantly into highly excited target states, while lower lying energy levels of the projectile remain empty. The resulting population inversion is only short-lived and the so-formed hollow atom will start to decay as it further approaches the sur-face. With decreasing distance to the solid, increasingly lower energy levels of the atom will be populated, as the energy levels are shifted upon surface approach and resonant transitions from occupied electronic states of the solid become possi-ble. This involves a series of succeeding resonant ionization and neutralization pro-

cesses. Upon surface impact, remaining outer shell electrons of the hollow atom will be 'peeled' off, as screening of the surface electron gas becomes dominant. This results in the emission of a large number of low energy electrons. The relaxation of the excited hollow atom will proceed below the surface, where remaining inner shell vacancies of the atom finally recombine. In this process, fast Auger electrons and x-rays are emitted.
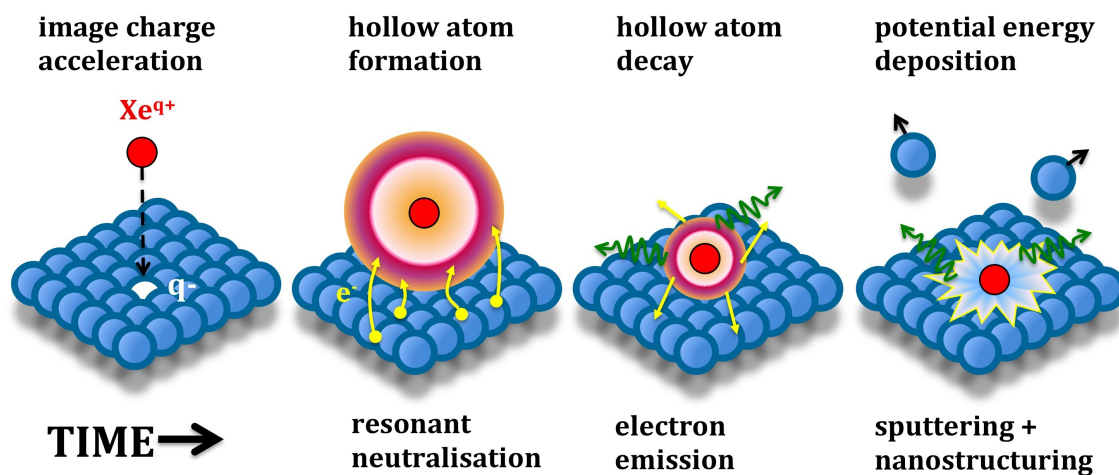

Figure 2.17: Schematic depiction of the neutralization and de-excitation scenario of a highly charged ion impinging on a solid surface. Picture from [143].

Involved Electron Exchange Processes

Within the above picture, the neutralization of a highly charged ion upon surface impact involves several charge exchange and relaxation processes [144, 145]. These are schematically shown in figure 2.18.

Already at rather large distances to the surface (some nm), *a) resonant electron transfer* from the target valence band to unoccupied projectile states will set in. These transitions will be possible, as soon as unoccupied projectile states become energetically degenerate with surface states, i.e. at crossings between the initial potential curve of ion plus target and the final configuration of neutralized projectile plus surface in figure 2.18 a). As a result highly excited Rydberg states will predominantly be populated, since they exhibit a large spatial extension and therefore a comparably large overlap. The reverse process, i.e. resonant ionization of these highly excited states into unoccupied conduction band levels, will take place as soon as the binding energies of the electrons of the hollow atom

Katharina Dobeš
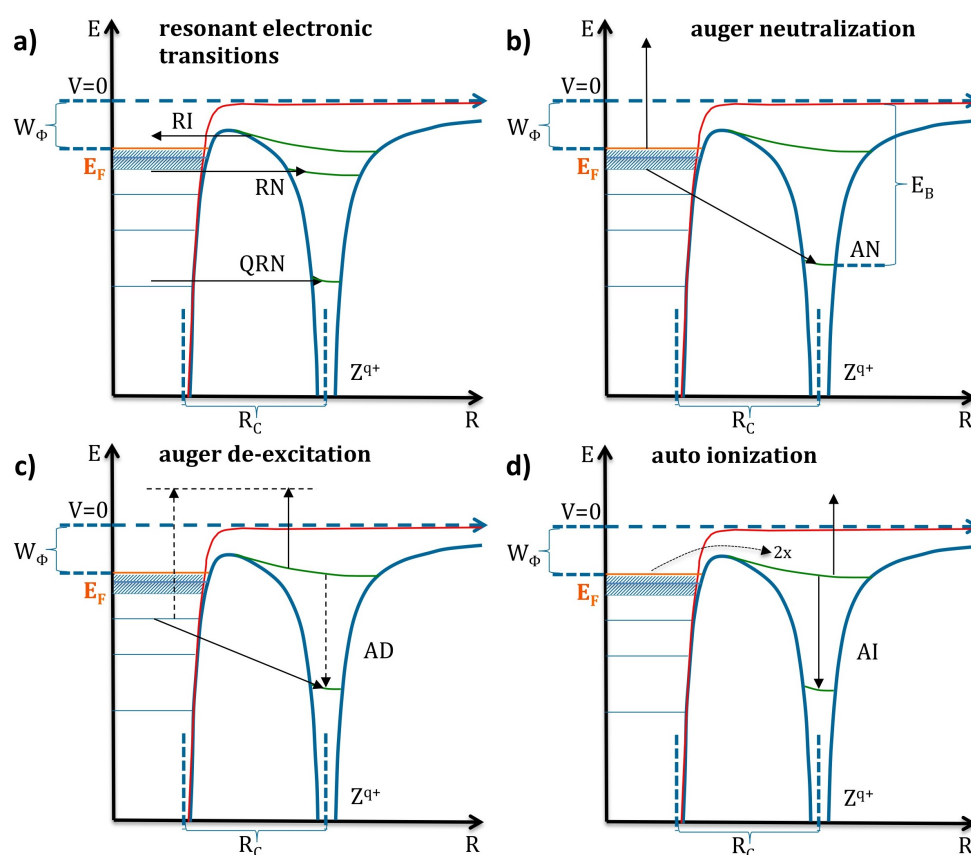
Figure 2.18: Schematic depiction the charge exchange processes, involved in the neutralization of a highly charged ion upon surface impact, i.e. a) resonant transitions, including resonant neutralization (RN), resonant ionization (RI) and quasi-resonant neutralization (QRN). b) Auger neutralization (AN). c) Auger de-excitation (AD). d) Auto ionization (AI). The potential of the solid in the absence of the ion is depicted in red and the conjoint potential in blue. E_F denotes the Fermi energy of the solid, W_Φ the target work function respectively. Picture from [143].

becomes smaller than the surface work function W_Φ. In the dynamic sequence of neutralization and ionization processes of the projectile as it approaches the surface, no electrons are emitted into the vacuum, but these one electron transitions may serve as precursors to subsequent electron emission processes, like Auger neutralization (AN), Auger de-excitation (AD) and auto ionization (cf. figure 2.18 b)-d)).

In an *b) Auger neutralization process*, two target electrons are involved. By the transition of a target electron to the projectile another electron gains sufficient energy via electron - electron interaction to be ejected from the surface. The neutralization energy has to be at least twice the work function of the solid and the kinetic energy of the ejected electron will be [85]

$$E_e \leq W_i' - 2W_\Phi \tag{2.18}$$

with W_i' being the effective neutralization energy.

c) Auger de-excitation processes will occur, as soon as the binding energy of excited projectile electrons exceeds the target work function. In this case, the excited electron can be promoted into a lower lying energy level, transferring energy to a target electron, which is then ejected from the surface. This will result in a kinetic energy for the ejected electron of

$$E_e \leq W_{ex} - W_\phi \tag{2.19}$$

if W_{ex} is the excitation energy.

Finally *d) auto-ionization* is an Auger process, which involves two (ore also more) target electrons of a multiply excited projectile. When one of these electrons decays into a lower energy level, the released energy is transferred to another electron, which is then ejected from the projectile.

A competing process in the de-excitation of hollow atoms apart from the above described electronic transitions, is photon emission. As the transition rates for radiative de-excitation scale approximately with the fourth power of the ion charge state $\sim q^4$, such processes are only significant for rather high ion charge states [146].

The Classical Over the Barrier Model

The de-excitation and neutralization dynamics of a hollow atom can be described by the so-called 'classical over the barrier model'. This description was first proposed for highly charged ion impact on metal surfaces [80, 147], later extended to non-conducting materials [82, 148, 149] and very recently also adapted to thin dielectric films on metallic substrates [150, 151].

For large distances, the collective response of the target electrons can be described by a classical image charge attraction. As the projectile approaches the surface, the potential barrier between the ion and the solid drops below the Fermi level of the solid. As a consequence, electrons from the Fermi edge of the solid

Katharina Dobeš

can then be captured classically into highly excited projectile states with hydrogenic principal quantum numbers n_c:

$$n_c \approx \frac{q^{3/4}}{W_\phi^{1/2}} \tag{2.20}$$

The critical distance R_c, at which the neutralization process sets in is

$$R_c \approx \frac{(2q)^{1/2}}{W_\Phi} \tag{2.21}$$

Both quantities depend explicitly on the charge state of the ion but also on the target work function. Consequently, the characteristics of the neutralization process will be very different for insulating targets, compared to metallic surfaces due to significant discrepancies in the valance and conduction band structure [149]. Especially the low charge carrier mobility and the wide electronic band gap of an insulator, will strongly influence e.g. the image charge attraction, but also the response of the surface due to a very localized deposition of the potential energy upon projectile impact. Related phenomena include e.g. potential sputtering (see 2.2.1, p. 26), permanent surface modifications [86, 152], but also potential electron emission [81, 131, 145, 153] (see section 2.3.2).

2.3.2 Potential Electron Emission

Potential electron emission is observed when a (highly) charged ion impinges onto a solid surface [81, 131, 145, 153]. For high charge states q the potential energy, which the ion carries as a result of the ionization process (cf. equation 2.17), may exceed the kinetic energy by far and potential electron emission might then become the dominant contribution to the total electron yield γ (cf. equation 2.16).

For exclusive potential electron emission, the dependency of the electron yield γ_{PE} on the ion impact velocity v can be approximated by an empirically derived relation of the form [81, 154, 155]:

$$\gamma_{PE}(v)\Big|_{\vartheta=\text{cons.}} = \frac{c_v}{\sqrt{v}} + \gamma_\infty \tag{2.22}$$

here, c_v and γ_∞ are parameters which depend on the investigated collision system [131]. These two parameters reflect the fact, that potential electron emission occurs both above the surface as well as at surface impact. The velocity independent contribution to the emission yield, γ_∞, considers the number of electrons

that are emitted at the surface selvedge, when outer shell electrons of the hollow atom are 'peeled-off' due to screening effects of the surface electron gas (cf. figure 2.17).

In addition, γ_{PE} depends inversely on the particle velocity v. This can be understood from the fact, that the number of ejected electrons will decrease, as the interaction time in front of the surface shortens with increasing impact velocity. The respective parameter c_v is therefore mainly attributed to auto-ionization cascades of the highly charged ion in front of the surface.

The interaction time above the surface is in fact exclusively determined by the velocity component perpendicular to the surface $v_\perp$, i.e.

$$v_\perp = v \cdot \cos(\vartheta) \qquad (2.23)$$

when ϑ is the incidence angle with respect to the surface normal. For varying incidence angles, equation 2.22 should therefore become

$$\gamma_{PE}(v, \vartheta) = \gamma_\infty + \frac{c_v}{\sqrt{v \cdot \cos(\vartheta)}} \qquad (2.24)$$

A corresponding angular and velocity dependency of the potential electron emission yield γ_{PE} was in fact confirmed by various experiments [156-158].

2.3.3 Kinetic Electron Emission

Kinetic electron emission is related to energy transfer from a projectile to the electronic system of a solid. In contrast to potential electron emission, where electrons are already ejected above the surface, kinetically emitted electrons originate from within the bulk. Therefore kinetic electron emission involves a sequence of mechanisms.

The first step in the emission of an electron by kinetic energy transfer, is the collisional excitation of the electronic system of the solid. In a first approximation, the kinetic electron emission yield will therefore be proportional to the energy, that is deposited in electronic (i.e. inelastic) collisions of the projectile as it penetrates the bulk. This can be expressed by the electronic stopping power:

$$S_e = \left. \frac{dE}{dx} \right|_e \qquad (2.25)$$

The excitation process is followed by electron transport to the surface. In a semi-empirical approach, the escape probability of an electron generated at a

Katharina Dobeš

certain depth below the surface will depend on its the mean free path λ in the surface [159]. A dependency of the kinetic electron emission yield on the mean escape depth of low energy ions could also be confirmed experimentally, when comparing yields for different orientations of an HOPG surface (i.e. ion impact perpendicular and parallel to the graphite layer orientation) [160]. Additionally, diffusing electrons may initiate cascade multiplication by collisions with further target electrons along their way through the solid. By such secondary electron generation, the electron excitation energy will be distributed among a multitude of sub-surface electrons [133].

The final step in the emission of an electron, is the escape through the surface-vacuum boundary [132]. The requirement of penetrating the surface barrier will result in a minimum projectile velocity, below which kinetic electron emission is not possible due to insufficient energy transfer to the target electrons. From energy conservation in a direct collision of a heavy projectile with a quasi-free electron at the Fermi edge of the target, this velocity threshold v_{th} can be approximated by [161, 162]:

$$v_{th} \approx \frac{v_F}{2}\left(\sqrt{1 + \frac{W_\Phi}{E_F}} - 1\right) \tag{2.26}$$

where v_F and E_F are the surface Fermi velocity and energy, respectively. W_Φ denotes the corresponding target work function. According to the above relation, the threshold velocity for kinetic electron emission will be of the order of $v_{th} \approx 10^5$ m/s, depending of course on the target under consideration.

Above this threshold velocity, the kinetic electron emission yield γ_{KE} will increase approximately linearly with increasing projectile energy E_0 up to a maximum[7], beyond which the observed electron yield decreases again [133, 161]. In general, this trend resembles the impact energy dependency of the electronic stopping power S_e (cf. equation 2.25), i.e. reflects the energy transfer from the projectile to target electrons in electronic collisions:

$$\gamma_{KE} = \Lambda^{ex} \left.\frac{dE}{dx}\right|_e \tag{2.27}$$

The proportionality factor Λ^{ex} in this equation, is a materials parameter. For heavy particle impact however, deviations from this simple relation were found [163, 164]. The observed discrepancies might e.g. originate from ionizing collisions of recoiling atoms. The resulting contribution to sub surface electron generation will introduce

---

[7]for e.g. H$^+$ this maximum is found at $\sim$ 100 keV

a dependency of the electron emission yield on the nuclear stopping power S_n (cf. equation 2.5) [163]. Additionally the effective charge state of the projectile may change along its way through the electron escape depth within the solid. As a consequence the inelastic stopping power of the bulk might in fact be an inadequate measure for the electronic energy loss of the projectile [133].

The angular dependency of the kinetic electron emission yield γ_{KE} will be proportional to the geometric path-length of the projectile within the electron escape zone of the solid. As a consequence, γ_{KE} will scale with $\cos(\vartheta)^{-1}$ [133], i.e.

$$\gamma_{KE}(\vartheta) = \gamma(0) \frac{1}{\cos(\vartheta)} \tag{2.28}$$

This condition only holds, if the ion path through the surface can be approximated adequately by a straight line and if in fact the number of ejected electrons is proportional to this path-length. Just like for the energy dependency of γ_{KE} deviations from this inverse cosine law are observed for heavy particle impact [133, 165, 166]. In a more general approach, it is found that the angular dependency of the kinetic electron emission yield can generally be fitted by the relation:

$$\gamma_{KE}(\vartheta) = \gamma(0) \frac{1}{\cos(\vartheta)^{\beta}} \tag{2.29}$$

where β is a fitting parameter, which depends on the specific target-projectile combination and the impact energy E_0. β generally varies between $0.5 \leq \beta \leq 1.5$ [133]. It considers various contributions to the electron emission yield γ_{KE}, which arise from the increased path length of the projectile within the electron escape depth for grazing incidence ions. These include e.g recoil ionization, deviations from the straight line approximation of the ion path through the surface, but also the fact that there will be a slowing down of the projectile within the electron escape depth and the electronic stopping power will therefore vary within the ion range [167].

Katharina Dobeš

Chapter

3

Experimental Methods

3.1 The QCM Technique

In this work, rates for the mass change of a variety of fusion relevant surfaces under particle impact of different species (cf. chapter 4) were investigated using a highly sensitive quartz crystal microbalance (QCM) technique, which was specifically designed and optimized at TU Vienna [168-170]. The basic working principle of a QCM is illustrated in figure 3.1. As first proposed by Sauerbrey [171], a quartz crystal can be used as a very sensitive device for determining mass changes, making use of the fact that the eigen-frequency of the quartz, which is driven at its thickness shear mode, depends on the thickness of the crystal.

According to the piezo electric effect, an AC voltage applied to the two sides of a quartz crystal induces a lateral displacement of the individual quartz layers and vice versa. The fundamental frequency of this shear vibration is determined by the thickness of the crystal with half a wavelength λ_0 across the quartz cross-section, i.e.

$$\frac{\lambda_0}{2} = t_Q \tag{3.1}$$

if t_Q is the quartz thickness. At the interface between quartz surface and vacuum, there will be an anti-node of the oscillation. As a consequence the elastic properties of the surface itself have a negligible influence on the oscillation. This is also true if a comparably thin target film of interest is deposited onto one side of the quartz, provided that it exhibits good adhesion to the substrate. Consequently any change in target film thickness and therefore any mass change of the target layer
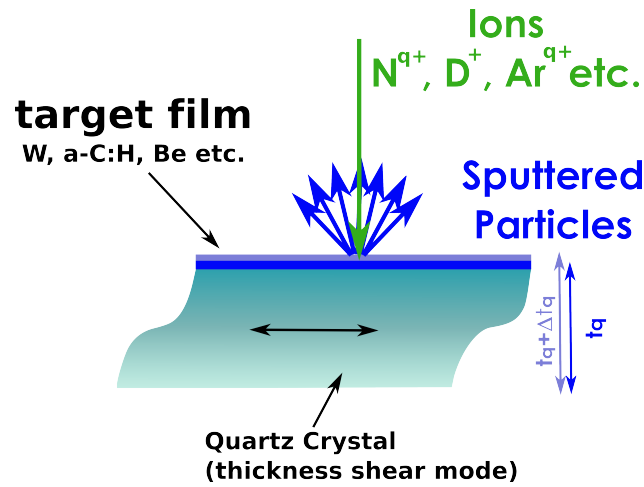
Figure 3.1: Schematic QCM principle. The thickness of the quartz crystal determines the resonance frequency in thickness shear mode. This can be used to determine mass change rates of deposited target films of interest upon particle impact.

Δm will simply be reflected in an inverse change of the resonance frequency of the quartz, i.e.

$$\frac{\Delta f_Q}{f_Q} = -\frac{\Delta t_Q}{t_Q} = -\frac{\Delta m}{m_Q} \tag{3.2}$$

The sputtering yield Y or, more generally speaking, mass changes of the target film Δm, can therefore be determined by monitoring the eigen-frequency of the crystal during particle impact, according to the relation:

$$Y = \frac{\Delta m}{\int I \cdot dt / e_0\, q} = \frac{\Delta f_Q}{f_Q} \cdot \rho_Q t_Q A_Q \cdot \frac{e_0\, q}{\int I \cdot dt} \tag{3.3}$$

Here the particle flux during the time interval Δt onto the crystal is given by the expression $\int I \cdot dt / e_0\, q$. The parameters ρ_Q. t_Q and A_Q are the quartz crystal mass density, thickness and area, respectively. If the impinging ion current density j is known, it is therefore possible to very accurately determine the areal net mass change of the target film by simply monitoring the change of the resonance frequency with time $\Delta f / \Delta t$:

$$\Delta m\,(\text{amu/ion}) = -\frac{C}{j} \cdot \frac{\Delta f_Q}{\Delta t} \tag{3.4}$$

C is a constant which subsumes quartz parameters and physical constants but does not depend on any target material properties, i.e.

$$C = \frac{\rho_Q t_Q e_0}{f_Q}$$

(3.5)

symbol	value	description
e_0	$1.602 \cdot 10^{-19}$ C	elementary charge
ρ_Q	2649 kg/m^3	quartz mass density
t_Q	$0.302 \cdot 10^{-3}$ m	quartz thickness
A_Q	$3.025 \cdot 10^{-5}$ m^2	quartz area
f_Q	5.998 MHz	quartz eigen-frequency

Table 3.1: Parameters and constants needed for determining the mass change of the target film from an observed frequency change of the quartz (cf. equations 3.4 and 3.5).

The corresponding parameters and constants are summarized in table 3.1. For determining areal net mass changes of the target film which are independent from the applied ion fluence and therefore constant in time the frequency evolution of the crystal under ion bombardment is usually linearly fitted and the mass change is evaluated with the slope of the frequency vs time curve (cf. equation 3.4). In cases where the mass change is not constant, a step wise linear approximation to the frequency change with time $\Delta f/\Delta t$ or the derivative of the frequency df/dt is determined and inserted in equation 3.4.

With the QCM method, simultaneous mass increase $+\Delta m$ (due to e.g. projectile implantation) and mass loss $-\Delta m$ (by e.g. material erosion) cannot be distinguished. By design only the balance of all processes, which result in a mass change of the target film, is observable. Additionally the QCM technique does not give any information on the actually sputtered species and their contribution to the total mass change.

The quartz crystal that is used in our experimental setup [169, 170] is a plano-convex, stress-compensated (SC) cut quartz available from *KVG Quartz Crystal Technology* (model No XA 3641). The selection of this particular quartz cut is motivated by its comparably high insensitivity to radial stress that can arise from a

non-unifrom mass removal of the target film or from the clamping of the quartz to the sample holder. The used quartz crystal has a resonance frequency of ~ 6 MHz and a diameter of 13.95 mm. It is coated with a 140 nm thick gold electrode on each side, which serves as electrical contact to the oscillator circuit that drives the crystal at its eigen-frequency. Onto one of these electrodes any target material of interest (e.g. tungsten, beryllium, amorphous hydrogenated carbon layers, etc.) can be deposited (see section 3.1.5), provided that good adhesion to the underlying gold film is guaranteed. Both, conducting as well as insulating surfaces can be investigated.
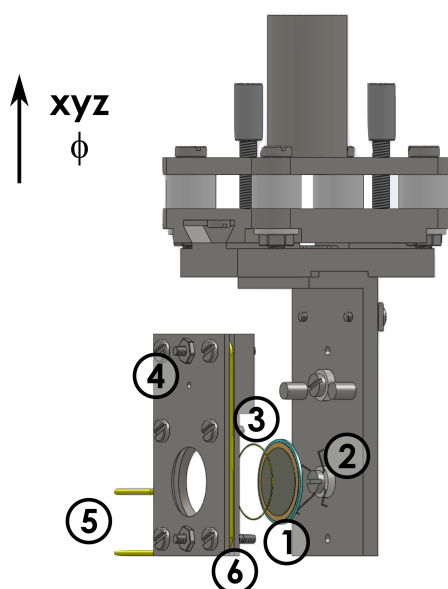

Figure 3.2: Sketch of the QCM sample holder, including: ① the quartz crystal; ② the W spring and ③ the Au ring used for clamping the quartz; ④ the Faraday cup; ⑤ the coaxial heater and ⑥ the location of the thermocouple.

The quartz crystal is mounted on a sample holder in an ultra high vacuum (UHV) chamber, usually at a background pressure of the order of ~ 10^{-10} mbar. This UHV chamber is connected to an ion source, from which energetic ions are extracted (see section 3.1.3). A sketch of the sample holder is shown in figure 3.2. The ① quartz is clamped onto the front side of the holder by a ② tungsten spring from the backside. A thin ③ gold ring is placed between quartz and sample holder front, in order to further minimize any mechanically induced stress arising form the

Katharina Dobeš

clamping. A ④ Faraday cup for ion current density determination is located at a given distance above the quartz crystal. The sample holder is connected to a rotatable, linear xyz-translation stage, which allows switching between quartz and Faraday cup position. The translation stage can be moved along all three spatial directions by stepper motors, with an accuracy of $\geq 23\ \mu m$.
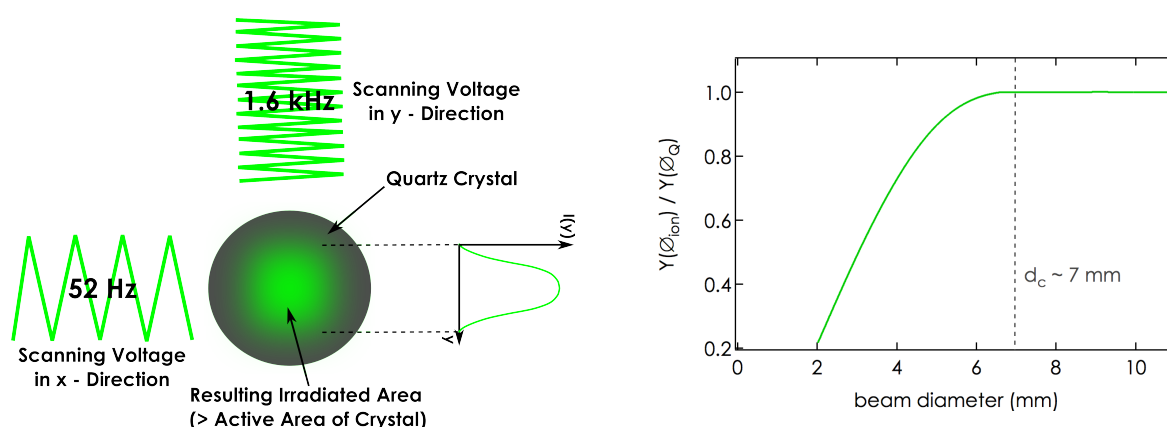

Figure 3.3: The ion beam is scanned across the active area of the crystal by applying two triangular AC scanning voltages of different frequency to a set of scanning plates in front of the quartz (left). A critical beam-diameter of 7 mm has to be exceeded during sputtering experiments (right). It is determined from the ratio of the sputtering yield determined with given beam diameter ($Y(\varnothing)_{ion}$) vs. the yield determined for a beam covering the entire quartz surface ($Y(Q)$). For detailed information see text.

For an accurate determination of any mass change of the deposited target film, the eigen-frequency change with time $\Delta f/\Delta t$ and the ion current density impinging onto the quartz crystal have to be determined precisely (cf. equation 3.4). The oscillation amplitude of the quartz decreases from its center outwards (energy trapping). On the one hand this facilitates clamping the quartz at its edge. On the other hand the decrease in oscillation amplitude also introduces a radial dependency of the sensitivity of the crystal to mass changes [171]. This effect can be eliminated by covering the whole mass sensitive inner part of the crystal (the so-called active area) with a homogeneous ion current density. In this case the areal mass change across the quartz is constant and the proportionality in equation 3.4 is in fact applicable. The diameter of the active area was determined

by step wise increasing the diameter of the ion beam impinging onto the quartz crystal by means of a set of scanning plates in front of the crystal. The scanning plates are triggered by two triangular AC voltages of different frequency (i.e. 52 Hz and 1.6 kHz, respectively). This is demonstrated in figure 3.3. Above a critical beam diameter of $d_c \sim 7$ mm, the obtained sputtering yield becomes independent from the diameter of the impinging ion beam. This critical beam diameter d_c is always exceeded in our investigations. Additionally current density variations within d_c are always kept below $\sim 10\%$, by accurately focusing and scanning the ion beam across the entire active area of the quartz crystal. The beam profile is inspected before each measurement with the Faraday cup by moving the cup step-wise through the beam in both transverse directions. Minimizing the mechanically induced stress due to ion bombardment is an additional side effect of the above described procedure.

Moreover, to keep any disturbances on the eigen-frequency of the quartz small, influences of temperature fluctuations 3.1.1 and the stability of the electronic circuit 3.1.2 and have to be considered and minimized.

### 3.1.1 Temperature Dependency and Control
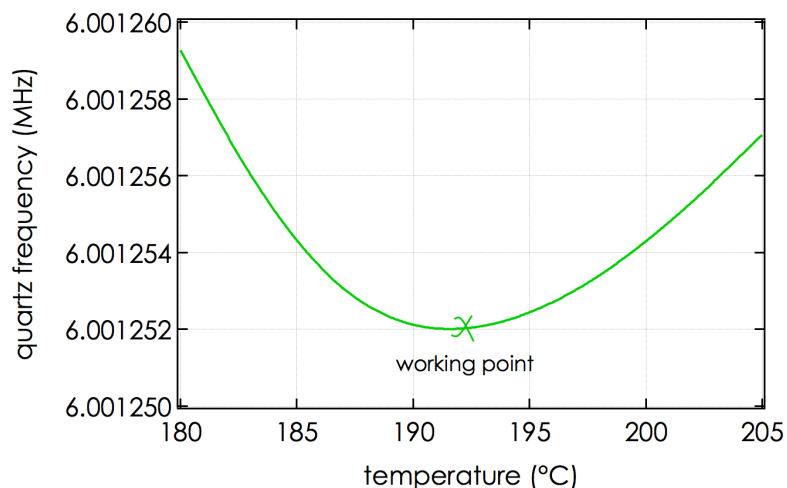
Figure 3.4: Dependency of the quartz frequency on the QCM temperature. The quartz is operated at the minimum of its frequency vs. temperature curve, where influences on small temperature changes during ion bombardment are minimal.

Katharina Dobeš

The eigen-frequency of the quartz crystal is rather sensitive to changes of the quartz operation temperature, as can be seen from figure 3.4. The observed dependency corresponds to a polynomial of cubic degree [172]. At the minimum of this polynomial function, the quartz frequency is least sensitive to temperature fluctuations. All results presented in this thesis were therefore obtained at a corresponding temperature of 465 K. It proved to be sufficient to heat the quartz with a constant heating power, as temperature changes induced by impinging ions are usually below any detectable limit. This was done by means of a coaxial heater (cf. ⑤ in figure 3.2), which is tightly clamped to the sample holder. The quartz temperature is monitored by a k-type thermocouple (⑥) which is attached to the back of the sample holder in close vicinity to the quartz. The resulting temperature stability of the quartz crystal during ion bombardment is of the order of ±0.1 K.

3.1.2 Electronic Stability

The electronic stability of the oscillator circuit, which drives the quartz at its resonance frequency, is crucial to the obtainable sensitivity of the QCM setup. The electronics used in the presented investigations is home-built [169, 173], and provides extremely high accuracy, which enables us to perform in-situ measurements on the interaction of ions with surfaces in real-time. A block diagram of the electronics is shown in figure 3.5.

In series resonance, the quartz crystal exhibits its highest admittance. In this case the voltage applied to the quartz electrodes and the current through the quartz are in phase. This is used to lock the driving frequency of the oscillator circuit to the resonance frequency of the quartz in a phase-locked loop. Any phase shift between current and voltage serves as an error signal to adjust the driving frequency to the resonance frequency.

The electronics [173] basically consists of a low noise, tunable oscillator, which generates an output signal that is fed into a voltage controlled amplifier to ensure that the vibration amplitude of the quartz stays constant. For locking the driving voltage onto the resonance frequency of the quartz crystal, the current signal through the crystal is shifted by 90° by a capacitor and forwarded to a multiplier for phase comparison with the driving voltage at the output of the oscillator. In series resonance this will result in zero output (since current and voltage are in phase). Any deviation of the driving frequency from the resonance frequency of the quartz will produce a non-zero output at the multiplier, which is then used to adjust the oscillator frequency.
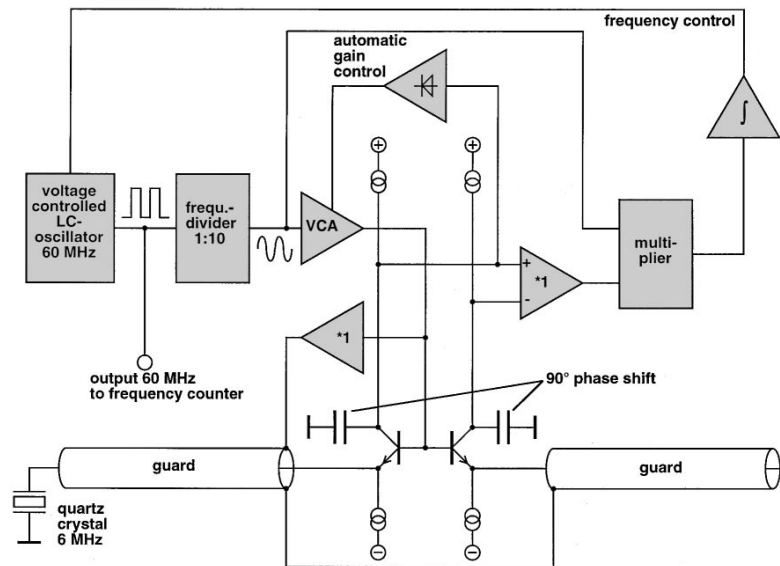
Figure 3.5: Block diagram of the electronics used in the QCM setup [173].

The electrical feedthroughs from the oscillator to the quartz crystal impose an additional parallel capacitance on the system. To actively compensate this, all electrical wiring is doubled. The two identical branches are tightly packed. One of the branches is connected to the quartz, the other serves as a dummy branch with loose ends. For phase comparison in the phase locked loop only the difference of the signals of the two branches is used. The frequency readout of the driving electronics is fed to a frequency counter and recorded with a computer in order to determine total mass changes according to equation 3.3.

3.1.3   Ion Sources and Beam Alignment

QCM investigations were conducted at different locations. Since oxidized Be is a very toxic material and handling of Be samples therefore requires specific safety precautions, experiments with Be (cf. section 4.4, 4.5) were solely performed at the *Max-Planck-Institut für Plasma Physik (IPP)* in Garching. Investigations with other target materials such as W (cf. sections 4.2 and 4.3) and a-C:H (cf. section 4.1) were conducted at the ion beam facility AUGUSTIN of the *Institute of Applied Physics* at the Technical University in Vienna. In the following a short overview on the experimental setup in these two locations is given.

Katharina Dobeš
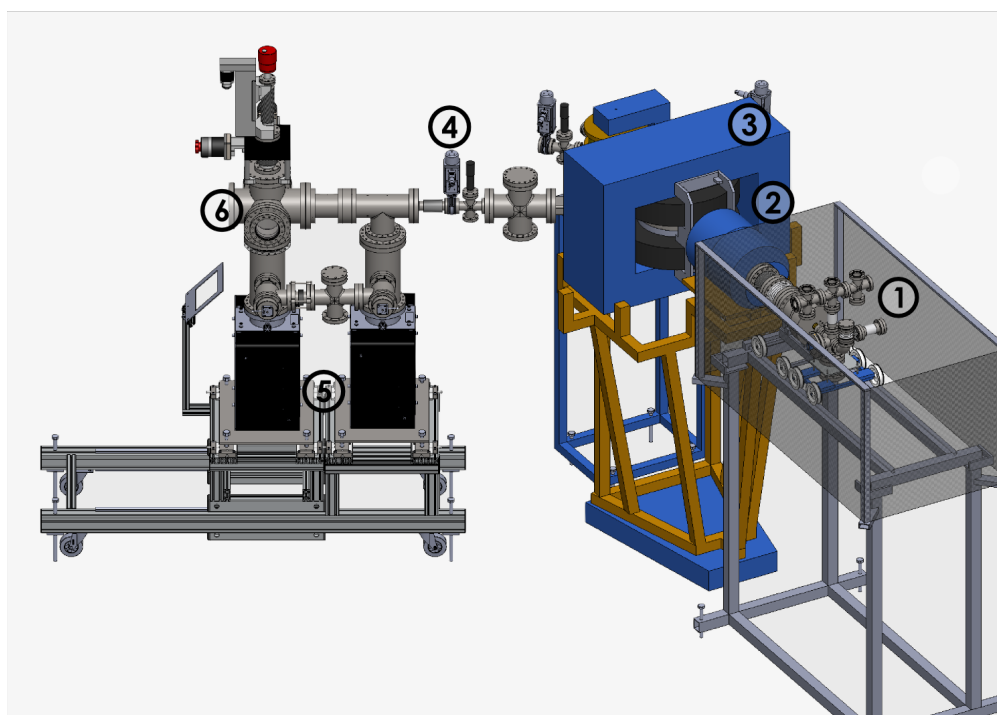
Figure 3.6: Sketch of the ion beam facility at TU Vienna, including: ① the ECR ion source; ② the quadrupole magnets; ③ the sector magnet; ④ the beamline shutter; ⑤ the ion pumps; and ⑥ the experimental chamber hosting the QCM setup (cf. figure 3.7).

... at TU Vienna

A sketch of the ion beam facility AUGUSTIN at TU Vienna is shown in figure 3.6. The ion beam facility is equipped with an 14.5 GHz electron cyclotron resonance (ECR) ion source ①, which is capable of producing singly as well as highly charged ions [174]. The plasma in the ion source is generated by resonantly heating the electrons of the working gas atoms with a microwave at their electron cyclotron resonance frequency in a magnetic field. Highly charged ions up to e.g. Ar^{14+} are generated by step-by-step ionization in a minimum-B multi mirror magnetic structure, which is used to confine the ions in the source region in order to provide enough time for multiple ionization steps. A combination of a magnetic mirror field and a hexapole is generated by a configuration of permanent magnets. The gas inlet system of the ion source allows for mixing of different gases in the source chamber, which facilitates achieving high charge states by ion impact ionization.

Katharina Dobeš

The ions are accelerated from the positive source potential to ground potential. More information on the ion source can be found in [174, 175].

After extraction, the ion beam is focused by a pair of quadrupoles ② onto the entrance of a sector magnet ③. An ion species with a specific mass over charge state ratio m/q is selected in the sector field and guided to the entrance of the beamline ④, in which the QCM setup ⑥ is mounted. The beamline is pumped by two ion pumps ⑤. A differential pumping stage reduces the pressure from 10^{-5} mbar in the source region to a low 10^{-10} mbar residual gas pressure in the experimental chamber ⑥ .
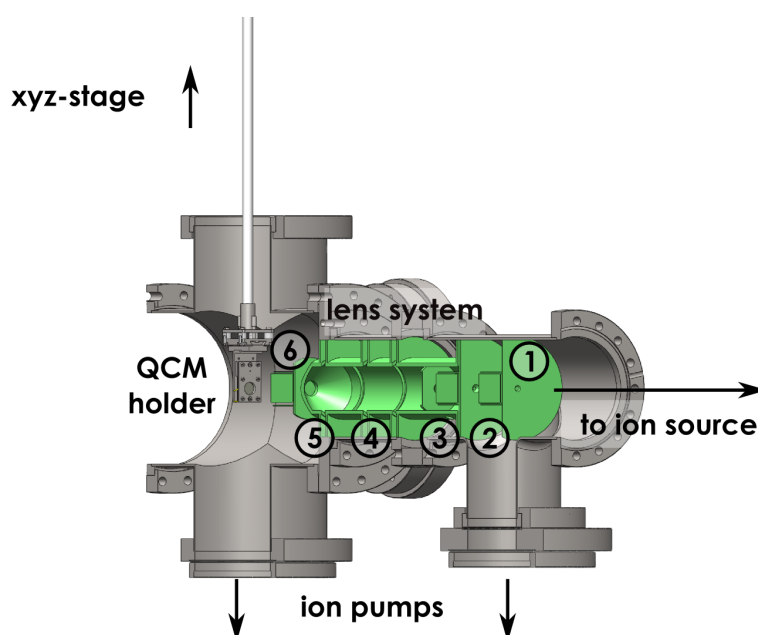

Figure 3.7: Cut-away sketch of the entire QCM beamline. The lens system used for focusing and deflecting the ion beam onto the sample position is marked in green. It includes ① an entrance aperture (5 mm); ② and ③ two sets of deflection plates; ④ an einzel lens; ⑤ a conic lens which can be used for decelerating the ion beam in front of the target; and ⑥ a set of scanning plates.

A magnified cut-away sketch of the QCM beamline is shown in figure 3.7. The beam optics that is used to collimate, focus and scan the ion beam is marked in green. It consists of an entrance aperture with a diameter of 5 mm ①, which together with a second aperture of 3 mm in diameter at ② collimates the incoming ion beam. Two sets of deflection plates ② and ③ are used to guide the ion beam through the electrostatic lens system ④ and ⑤, which basically is composed

Katharina Dobeš

of an einzel lens ④ and a conic lens element ⑤ just in front of the target, which can be used to decelerate the ion beam. This is done for investigations with low energy projectiles, typically below $E_{kin}/q \sim 500$ V. In this case, the conic lens ⑤, the scanning plates ⑥, the sample holder and all the electronics connected to it are positively biased by galvanically insulating the high potential in the target chamber from ground via an isolation transformer.

... at IPP Garching

A schematic drawing of the experimental setup in Garching, which was used in the Be experiments (cf. sections 4.4 and 4.5), is shown in figure 3.8. A sketch of the entire setup is depicted in figure 3.9. In this setup the ions are produced with a commercial electron impact ion source (SPECS IQE 12/38). The ions are extracted from the ion source by biasing the source region with a high, positive voltage. A Wien velocity filter is used to select a certain ion species from the extracted beam. The ion source and the direction of the beam when it exits the Wien filter are slightly off axis in order to keep neutral particles from passing the setup. An einzel - lens is used to focus the ion beam onto the QCM position. A pair of scanning plates in front of the sample is externally triggered with an AC voltage to scan the ion beam across the active area of the crystal. The QCM sample holder is mounted on a rotatable linear translation stage. The ion beamprofile can be determined by moving the Faraday cup which is installed on the sample holder through the ion beam along the z-axis.
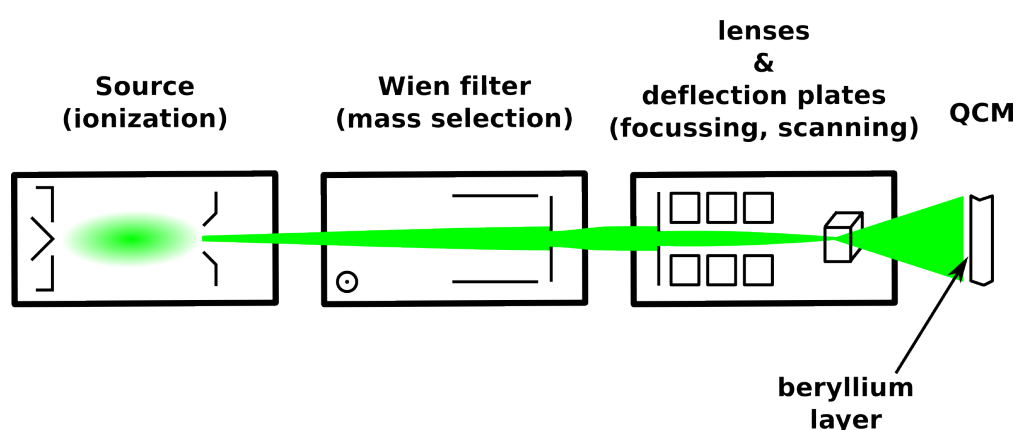

Figure 3.8: Schematic drawing of the experimental setup in Garching, including an electron impact ion source, a Wien filter for mass selection, the ion beam optics consisting of a lens system and deflection plates and the QCM.

The base pressure in the chamber during experiments is in the order of some 10^{-10} mbar. The chamber is pumped by a combination of a turbomolecular pump, a titanium sublimation pump and a cryopump, which is cooled with liquid nitrogen during the measurements. The ion source is operated at pressure of $\sim$ 1 - $5{\cdot}10^{-5}$ mbar, which results in a pressure increase to about 10^{-7} mbar in the experimental chamber during source operation.
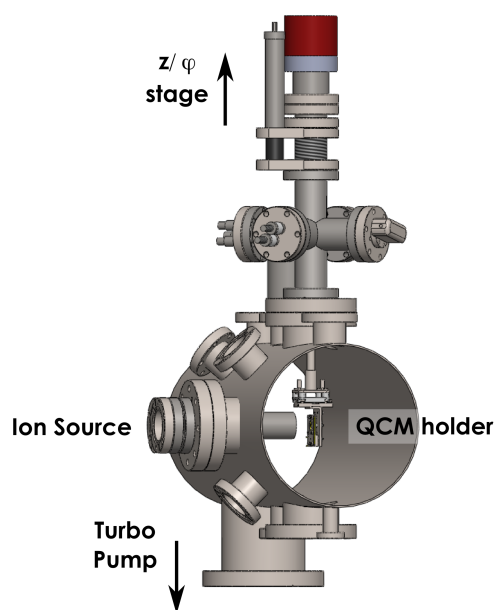

Figure 3.9: Sketch of the entire experimental setup at IPP Garching.

The working gas pressure in the ion source is controlled by flooding a small volume with the working gas. This gas reservoir is connected to the ion source via a manually adjustable valve. There is however no permanent gas supply to the high-pressure reservoir. The leakage through the valve conjoining the reservoir and the ion source itself is attenuated to the desired working gas pressure. The source pressure tends to drop over larger periods of time, as the gas reservoir on the high-pressure side gradually empties during operation. This is commonly accompanied by a decrease in ion current. Operating the ion source in a pressure regime, where the extracted ion current is least sensitive to changes of the gas pressure in the source region can minimize this effect. Therefore, prior to each measurement such a pressure regime was determined from a plateau of the dependency of the beam current density on the source pressure. A typical current vs. pressure graph obtained for this purpose is shown in figure 3.10. For long-term

Katharina Dobeš

measurements it is necessary to frequently re-adjust the valve opening during ion bombardment. Additionally the high pressure gas-reservoir has to be re-filled from time to time in order to maintain the desired pressure in the source region. This sometimes results in minor discontinuities of the extracted ion flux, which is reflected in disturbances in the frequency evolution, i.e. the mass change rate.
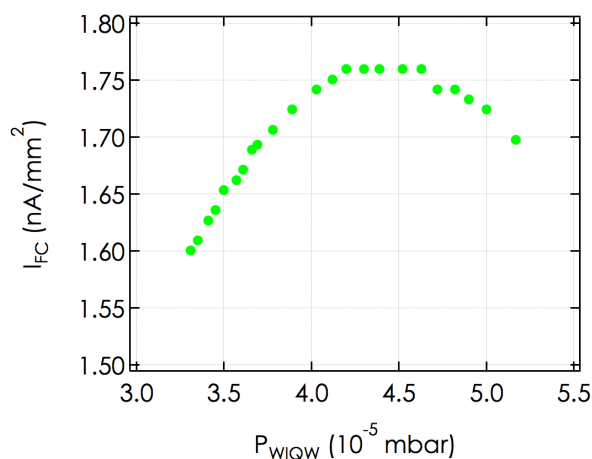

Figure 3.10: Dependency of the ion beam current density on the working gas pressure in the ion source at IPP Garching for N_2^+ ions extracted with 5000 V.

3.1.4 Estimation of the Measurement Accuracy & Sensitivity

Although the oscillator circuit which drives the quartz is very stable, the quartz crystal is still subjected to intrinsic frequency drifts, which are, at least on a medium time scale, linear (cf. figure 3.11). For small mass change rates or low ion fluxes, the quartz frequency change due to such drifts might become comparable to the ion induced frequency change, which will ultimately limit the sensitivity of the setup. In figure 3.11 the frequency behavior of the quartz crystal at rest, i.e. without ion bombardment, is shown. It exhibits an intrinsic drift of the order of 2 mHz/min, which compared to the quartz eigen-frequency of $\sim$ 6 MHz, gives a relative frequency stability of 9 orders of magnitude. The frequency readout at the frequency counter is also subjected to some noise, which is of the order of about $\sim$ 5 mHz. From this it can be concluded that the QCM technique is limited to measurements, where the product of mass change times impinging ion current exceeds 0.2 amu/ion·µA/cm^2 [169]. This is equivalent to the removal of e.g. 10^{-5}µm, which
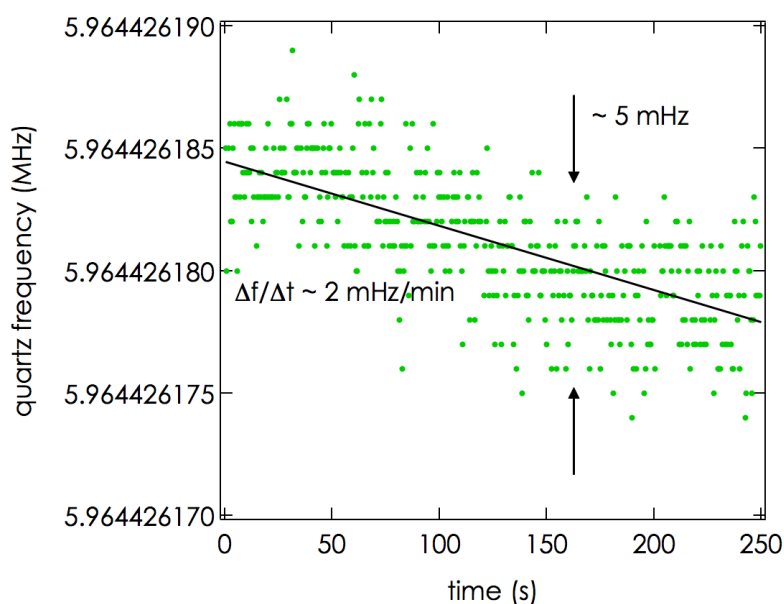
Figure 3.11: Frequency stability of the quartz crystal at rest, i.e. without ion bombardment. The intrinsic frequency drift and the noise level are a measure for the maximum attainable measurement sensitivity of the setup.

corresponds to 10^{-4} tungsten, 10^{-2} a-C:H or $5 \cdot 10^{-5}$ beryllium monolayers per second for typical ion current densities characteristic to our experimental conditions.

The experimental error of the QCM technique will not only depend on the ratio of the measured mass change rates compared to intrinsic frequency drifts of the quartz. It will also be determined by the accuracy of the ion current density determination, its intensity profile across the active area of the quartz crystal and temporal fluctuations of the impinging ion flux. To further increase the accuracy of the setup, the intrinsic frequency drift of the quartz can be subtracted from the frequency change during ion bombardment. This is done by monitoring the frequency behavior of the quartz before and after the ion irradiation, as is illustrated in figure 3.12. This procedure is only applicable if the sample surface is not subjected to any mass changes following the ion irradiation, such as surface oxidation or the outgassing of implanted projectiles. This was an issue particularly for measurements with beryllium surfaces, which show pronounced surface oxidation even at low ambient oxygen partial pressures (cf. section 4.4 and 4.5). In this case, a subtraction of the frequency behavior of the quartz, which is observed immediately

Katharina Dobeš
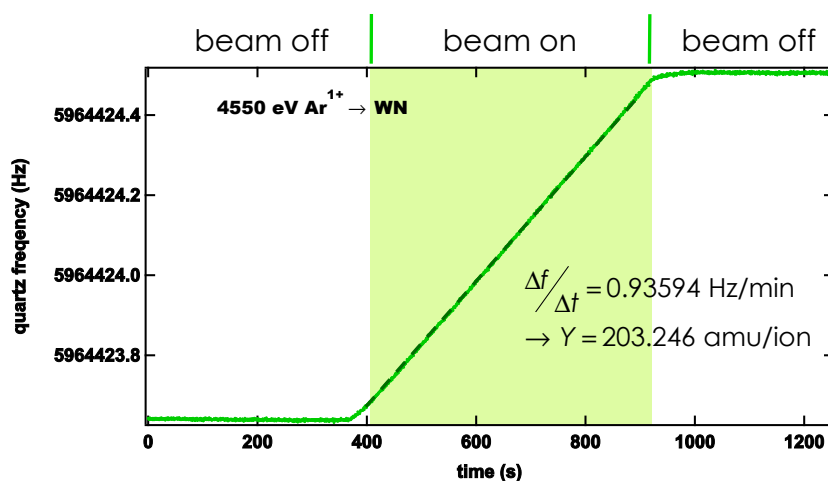
Figure 3.12: For an increased accuracy, the irradiation of the quartz crystal can be alternated with 'beam off' phases, during which the intrinsic frequency drift of the quartz is monitored. This drift can then be used for correction of the frequency change during irradiation.

after shutting the ion beam off, would actually impose an error onto determined mass change rates.

3.1.5   Sample Preparation

Tungsten

Polycrystalline tungsten films were sputter deposited on the quartz crystals at the *Institut für Festkörperphysik* of TU Vienna by Dr. Eisenmenger-Sittner. Virgin quartz crystals were installed in a mask for magnetron sputter deposition. 500 nm thick, polycrystalline W films are grown at a target temperature of 150 °C. Prior to the sputtering investigations, native oxide layers and adsorbates are removed from W surfaces by Ar sputter cleaning with fluences of some 10^{14} Ar ions per cm^2. The measured sputtering yield is monitored throughout the cleaning process. Ar irradiation was usually continued until a steady state Ar sputtering yield was obtained.

Beryllium

A schematic representation of the deposition chamber for the production of beryllium samples is shown in figure 3.13. 500 nm thick beryllium samples are produced

by a thermionic vacuum arc deposition technique at the *National Institute of LASER, Plasma and Radiation Physics* in Bucharest by Cristian Lungu and co-workers [176]. The quartz crystals are exposed to a pure beryllium vapor discharge, which is produced by melting a solid beryllium rod with a thermionic vacuum arc electron gun. Dense, bulk like beryllium layers are fabricated by accelerating the beryllium ions onto the substrate by means of a negative bias of - 750 V. The substrate temperature during deposition is 200 °C.

The beryllium coated crystals are transferred ex vacuo to the experimental chamber. Therefore, all samples, which were used in our experiments, exhibit a native surface oxide layer. X-ray photo-electron spectroscopy investigations usually also show some carbon contamination of the surface.
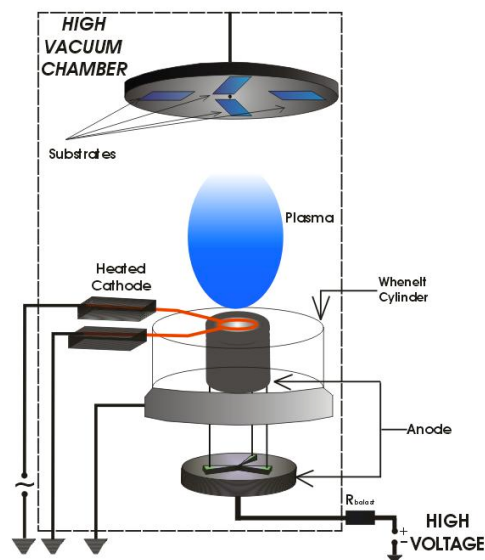

Figure 3.13: Beryllium samples are produced using a thermionic vacuum arc deposition technique [176].

Amorphous Hydrogenated Carbon (a-C:H)

Amorphous, hydrogenated carbon (a-C:H) layers are deposited onto a quartz, which is equipped with a polished gold electrode, in a low temperature methane plasma discharge at IPP Garching by Thomas Schwarz-Selinger [123,177]. A sketch of the deposition chamber is shown in figure 3.14. The film growth and characteristics can be monitored by in-situ ellipsometry during deposition. The films are

Katharina Dobeš
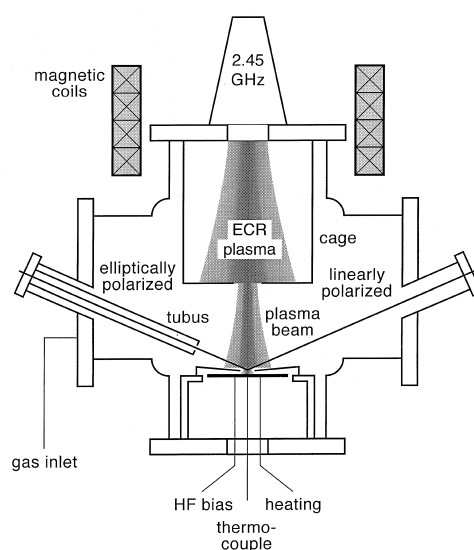
Figure 3.14: Sketch of the vacuum chamber for depositing the a-C:H layers [177].

polymer-like, so-called soft layers with an initial hydrogen content of 50 % and a density of 1.1 g/cm^3. They are deposited without any additional sample bias.

3.2   The Electron Statistics Setup

Electron statistics measurements were performed at the *Zernike Leif* facility of the *Kernfysische Versneller Institut* (KVI) in Groningen in cooperation with Erwin Bode-wits and Ronnie Hoekstra. A detailed description of the entire experimental setup can also be found in [141, 178]. The so-called *inelastic ion surface interaction station* (IISIS) was designed and constructed in order to investigate highly charged ion induced electron emission from surfaces. In this case electron emission yields of bulk surfaces such as gold and highly ordered pyrolytic graphite (HOPG) as well as thin films of C$_{60}$ deposited onto a single crystalline gold substrate were studied. Eventually the setup shall be transferred to the *HITRAP* facility at the *GSI* Helmholtz center for heavy ion research, where experiments on the interaction of surfaces with very slow (a few keV kinetic energy), highly charged ions (up to fully stripped Ur^{92+}) are planned [141].

The IISIS setup is installed in an experimental chamber connected to the central beam line of the ECR ion source at KVI in Groningen. A sketch of the setup is
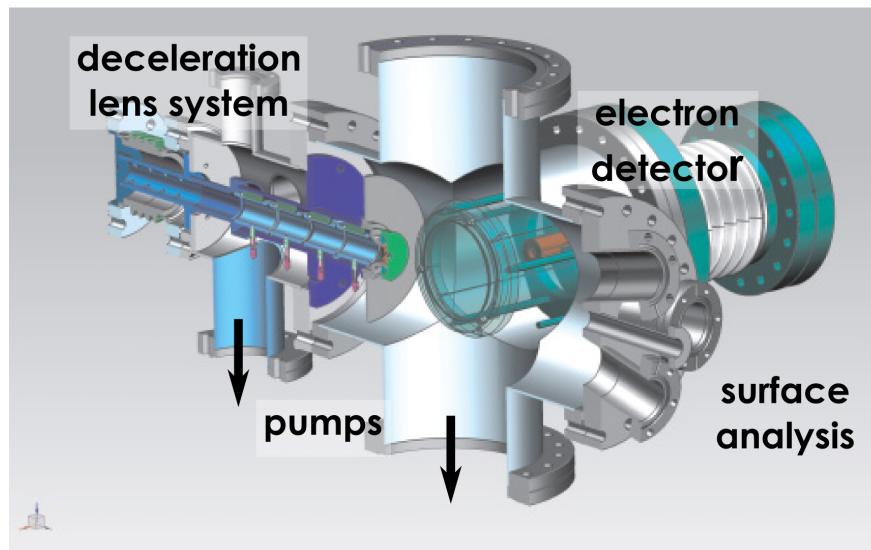
Figure 3.15: Drawing of the electron statistics setup at KVI Groningen [178], including indications on the location of the electron statistics detector, the deceleration lens system and the surfaces analysis tools.

shown in figure 3.15. The ions are extracted from the ECR ion source from a high positive potential towards ground potential. They enter the experimental chamber through a six element deceleration lens system. Apart from focusing the impinging ion beam, the lens system can also be used for step-wise deceleration when biased to a positive potential together with the experimental chamber including all parts and electronics connected to it. The chamber and all equipment necessary for performing experiments is therefore placed in a high voltage cage. In this manner, ion impact energies in a range from $\lesssim 0.1$ up to 25 keV per charge state can be provided [141]. For low ion impact energies, i.e. high deceleration voltages, the transmission efficiency of the ions passing the deceleration lens system decreases [178]. Additionally the ion beam is eventually deflected by the high positive potential at the target position. This effect has been simulated [178] by means of the SimIon[1] code [179]. The resulting incidence angle deviations $\Delta\vartheta$ are shown in figure 3.16. In the data evaluation the effective incidence angle of the ion beam is corrected accordingly for incidence energies below 1.5 keV/q.

The experimental chamber of the IISIS setup is separated from the ECR beamline by a differential pumping stage (cf. figure 3.15). An ion pump in combination

---

[1]The program SimIon is an ion optics simulation program, which is capable of calculating electric fields by solving the Laplace equation of a given geometry of electrodes.

Katharina Dobeš
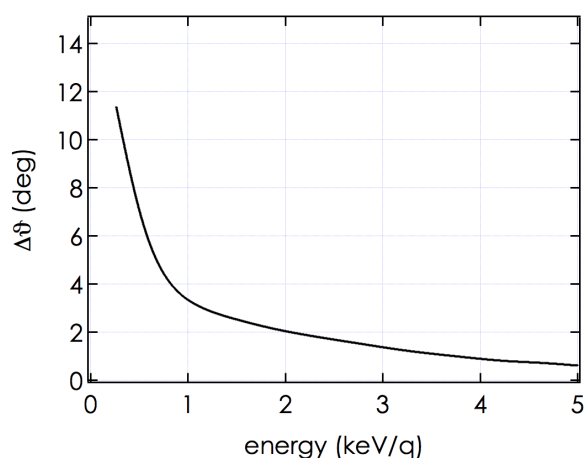
Figure 3.16: Results of SimIon [179] simulations for the deflection $\Delta\vartheta$ of the incident ion beam at low impact energies, i.e. high deceleration voltages at the IISIS setup in Groningen.

with a turbomolecular pump produces a vacuum in the low 10^{-11} mbar regime. During experiments the ion pump is switched off to prevent electrons originating from the pump from producing an undesired signal underground. An electron statistics setup [157, 180-182] is installed in the experimental chamber (cf. section 3.2.1). It is used to determine the electron emission statistics upon surface impact of highly charged ions. The electron detector itself is mounted under 90° with respect to the incoming ion beam. The target material of interest is placed on a sample holder (see figure 3.17), which is movable in all three translational directions with a precision of ~ 5 µm. Additionally it has two rotational degrees of freedom, one for varying the polar, the other for the azimuthal angle. The electrons that are emitted from the surface in an ion impact event are collected by a set of six electrodes surrounding the target. To determine total electron emission yields, they are attracted towards a detector by a positively biased highly transparent grid.

A sketch of the sample holder can be found in figure 3.17. The dimensions of the sample holder are chosen such as to ensure that the ion beam does not hit the supporting structure but only the target material. By this any contribution to the electron emission from an exposure of the sample holder material to the ion beam is avoided. The sample holder can be heated by a resistive heating, which is placed behind the target. In order to reach temperatures of up to 500 °C, the necessary heating power needs to be limited by thermally insulating the target holder from its mounting. This is done by a hole in the target holder, which limits its thermal

Katharina Dobeš
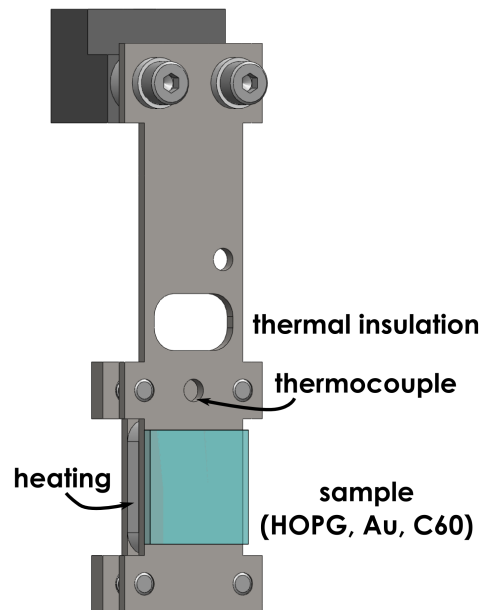
Figure 3.17: The sample holder used for electron statistics measurements. The target is mounted such as to not expose the sample holder itself to the ion beam. The holder is equipped with a heating, a thermocouple, and a bridge-like structure for thermal insulation.

conductivity. The target temperature is monitored by means of a thermocouple which is placed right above the sample.

For depositing thin target films in-situ, an UHV evaporator and a quartz crystal microbalance are attached to the experimental chamber (see figure 3.15). The target surface can be characterized by low energy ion scattering. Therefore the experimental chamber is connected to a time of flight tube under an angle of 13° with respect to the ion beam axis (cf. section 3.2.3).

3.2.1   The Electron Statistics Detector

A sketch of the electron statistics detector is shown in figure 3.18. The electrons that are emitted from the target surface are first collected by a set of six different electrodes surrounding the target. Five of these electrodes are biased negatively to push emerging electrons towards the detector. The sixth electrode, a highly transparent (geometric transmission ≈ 96%) grid is placed in front of the detector flange (marked in green in figure 3.18 and 3.19). It is on positive potential (≈ 200
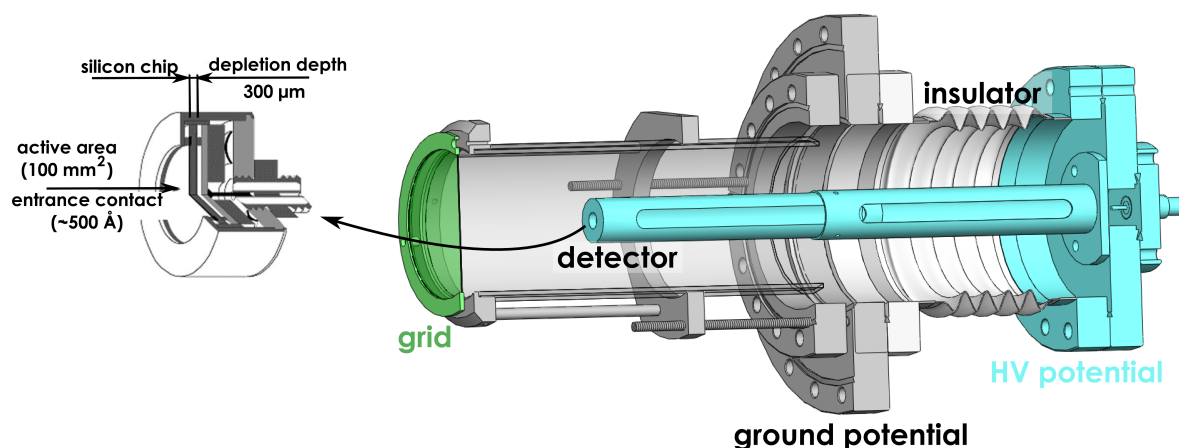
Figure 3.18: Sketch of the electron statistics detector. To collect the electrons the grid in front of the detector (green) is positively biased. The PIPS detector itself is on a high positive potential (blue) and isolated from ground by a ceramic insulator flange.

V) to collect the electrons. The voltages applied to the six electrodes surrounding the target are optimized with respect to the electron collection efficiency.

Electrons are detected by a surface barrier PIPS[2] detector, which is provided by the company *Canberra* (model BKPD100-12-300AM). To increase their impact energy E_e, they are accelerated towards the detector by a high positive potential (typically $U_{HV} \approx 30$ kV), which is applied to the detector, its supporting flange and all the electronics connected to it (marked in blue in figure 3.18). Electrons impinging on the detector surface will produce electron-hole pairs, which are separated with a bias voltage that is applied to the detector. The pulse height at the detector output is proportional to the number of generated electron hole pairs, i.e. to the energy that is deposited in the detector surface. The time scale at which electrons are emitted from a single ion impact is small (typically of the order of 10^{-12} s [80]) compared to the time resolution of the detector (which is about 10^{-6} s). Thus all n electrons generated in one ion impact will contribute to one cumulative output pulse of the detector. They will therefore be registered as a single event and the corresponding pulse height will be proportional to the number n of emitted electrons, i.e. to nE_e. The number of simultaneously impinging electrons can then be determined from a pulse height analysis of the detector output signal. To avoid pileup effects (i.e. a signal superposition of several ion impact events), multiple

---

[2]PIPS is an acronym for passivated implanted planar silicon
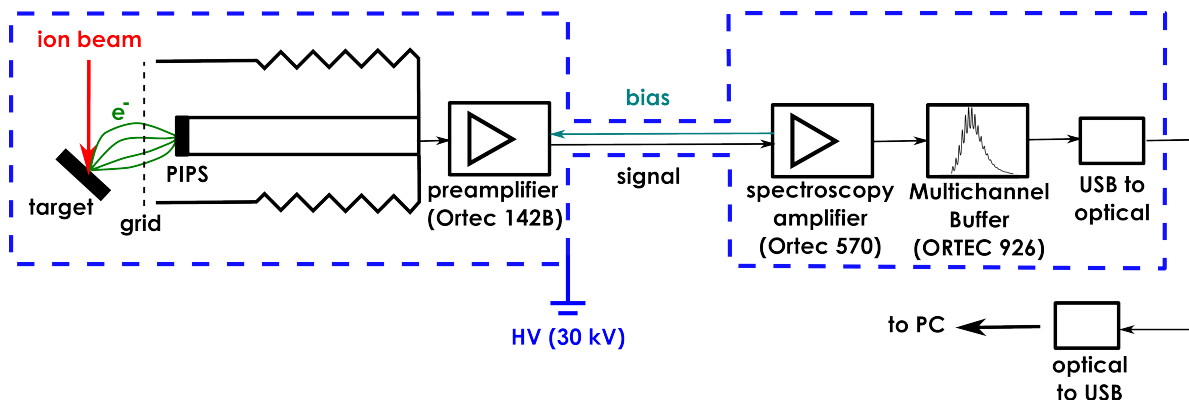
Figure 3.19: Electronics and data acquisition of the electron statistics setup. For details see text.

ion impacts within the dead time of the detector have to be avoided. This restricts the ion impact rate to $\lesssim 10^4$ per second.

A schematic drawing of the electronics that is used for data acquisition is shown in figure 3.19. The detector output is connected to a preamplifier (Ortec 142B), which is positioned just behind the detector flange. It produces mV pulses that are forwarded via a BNC connector to a spectroscopy amplifier (Ortec 570) for further amplification. The amplifier is located in a separate HV cage at some distance to the experimental setup. For pulse height analysis of the resulting signal, a multichannel buffer (Ortec 926) is used. Each channel of the buffer corresponds to a certain pulse height interval of the amplifier output signal. The buffer channels can be attributed to the detection of n simultaneously arriving electrons. The correlation between channel number and electron number has to be identified in a calibration measurement and depends on the detector voltage U_{HV} (since the deposited energy per impinging electron, i.e. the electron induced detector signal pulse height, depends on U_{HV}). Electron statistics spectra are recorded by cumulating a multitude of ion impact events in the multichannel buffer and recording them with the Maestro 32 software on a PC. The PC is connected to the multichannel buffer via two USB-to-optical adapters for electrical insulation from the high voltage potential of the detector and its electronics. In this way it is possible to record pulse height, i.e. electron emission statistics spectra for the number of electrons emitted from a solid surface as a result of a particle impact.

Katharina Dobeš

3.2.2 Interpretation of Electron Statistics Spectra

In addition to the mean number of electrons emitted in an ion impact event, i.e. the total electron yield $\gamma = \overline{n}$, it is also possible to determine the number statistics for the emission of $n = 1, 2, 3, ...$ electrons with the electron statistics setup described in this section. According to references [139, 180], the observed emission statistics of the electron yield γ is a superposition of the individual probabilities W_n for the emission of n electrons, i.e.

$$\gamma = \sum_{n=1}^{\infty} n W_n \tag{3.6}$$

with the normalization condition $\sum_{n=0}^{\infty} W_n = 1$. The probability W_0 for the emission of no electron is however not measurable. For sufficiently high electron yields the contribution of W_0 is negligible. For a correct determination of small electron yields however, it is necessary to find an adequate estimation for W_0 in equation 3.6.

For n independently emitted electrons, the probability distribution for the number of emitted electrons W_n should obey a Binomial distribution, which, for a large ensemble of involved surface electrons, will approach a Poisson distribution [139, 183], i.e.

$$P_n(\gamma) = \frac{\gamma^n}{n!} e^{-\gamma} \tag{3.7}$$

In some cases a two-parameter Polya distribution might be better suited to represent the electron number statistics of the measured data [183].

In figure 3.20 a typical experimentally obtained electron emission spectrum is shown. It is composed of several n- electron contributions (color-coded in figure 3.20). In principal the individual n- electron contributions should all be of Gaussian shape, centered around a channel corresponding to the deposition of an energy of $E_e = n \cdot e_0 U_{HV}$ in the detector surface. The width of the Gaussians is measure for the energy resolution of the detector and the data acquisition electronics [139] ($\Delta E \sim 6$ keV). Apparently there is a pronounced deviation from such a Gaussian shape in the n- electron contributions of figure 3.20. This can be attributed to the fact that there is a certain non-vanishing probability for electrons, which enter the detector surface, to be backscattered. From the shape of the electron statistics spectra it could be concluded [139] that backscattered electrons deposit about $(1-k_r) \sim 60\%$ of their initial kinetic energy in the surface before being re-emitted. Reflected electrons will promptly return to the detector due to its high potential U_{HV}. However when they return to the detector they might not hit the sensitive area of

Katharina Dobeš
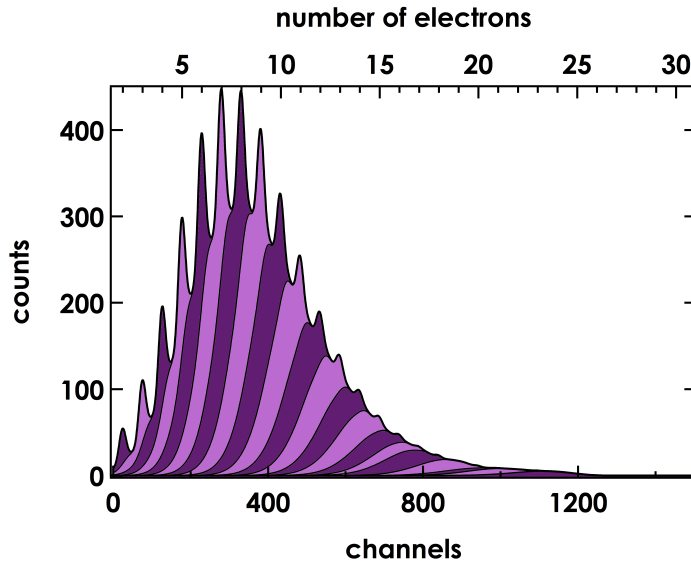
Figure 3.20: A typical electron emission statistics. The contribution of the individual n-electron probabilities including electron back-scattering are color-coded (for details see text).

the detector and might therefore be lost. As a result the n- electron peak contribution $F_n(E_e)$ to the spectrum can be interpreted as the sum of m individual peaks $f_n(E_e, E_m, \Delta E_m)$ which include m-fold electron backscattering from the surface. E_m and ΔE_m are the corresponding energy and halfwidth, of the m backscattered electrons [139, 180]:

$$F_n(E_e) = \sum_{m=0}^{n} P_n(m) f_n(E_e, E_m, \Delta E_m) \tag{3.8}$$

If the probability for backscattering of an electron is p_r, the functions $P_n(m)$ follow a binomial distribution:

$$P_n(m) = \binom{n}{m} p_r^m (1-p)^{n-m} \tag{3.9}$$

The probability for backscattering p_r can be determined from fitting the n- electron contributions in an electron statistics spectrum (cf. figure 3.20). It is usually of the order of $p_r \sim 18\%$ in our case. The total electron yield upon ion impact can now be determined from equation 3.6 by fitting the electron number statistics (cf. equation 3.7) to the observed electron spectrum. For higher electron yields, i.e. $\gamma \gtrsim$

Katharina Dobeš

20, the contribution of backscattered electrons will increasingly suppress the characteristic single electron peak structure in the statistics spectrum, which then can be fitted appropriately by a Gaussian instead to the number statistics in 3.6. The center of this Gaussian is related to the average yield γ [155, 184], with a correction factor α which accounts for the shift of the spectrum due to electron backscattering,

$$\alpha = \frac{1}{1 - p_r \, (1 - k_r)} \tag{3.10}$$

3.2.3   Sample Preparation and Characterization

Different samples were used to study electron emission by highly charged ion impact and its dependency on various surface parameters (cf. section 2.3.1). To characterize the surface composition before conducting electron emission measurements, low energy ion scattering by means of time of flight (TOF) was used. The TOF tube is connected to the beamline under 13° with respect to the beam axis. A channeltron for particle detection is mounted at the end of the tube.

In a binary collision of an ion with a surface atom, the energy of the reflected projectile will depend on the ratio of its mass compared to the mass of its collision partner. This can be used to determine the target surface composition by recording the time of flight of the scattered projectiles from the surface to the detector at the end of the TOF tube. For this purpose a set of chopper-sweeper plates is installed at the entrance into the experimental chamber at a well defined total distance to the detector. The chopper is used to generate a pulsed ion beam with a well-defined reference timing signal. The energy loss of the projectile as a result of scattering from the surface, i.e. its particular collision partner, can then be determined from the exact time at which the ion arrives at the detector. For more details on this particular TOF setup see [178].

In the presented electron statistics measurements, the targets are precisely positioned with respect to the ion beam spot. This was done to avoid irradiating the sample edge or any other component in the experimental chamber, which is installed close by. The sample position was optimized in both lateral directions by step-wise changing the sample position and identifying a plateau in the observed electron yield.

Gold

In the presented investigations, a single crystal Au(100) target was used. It was cleaned by cycles of sputtering with 7 keV Ar$^+$ ions under grazing incidence angles, followed by annealing at temperatures of up to 500 °C. This was repeated until an atomically clean surfaces was obtained. The surface composition was determined in between consecutive sputtering and annealing cycles by means of time of flight (see p. 73).

C$_{60}$

Thin films of C$_{60}$ were produced with a commercially available electron beam evaporator (*Omicron* model no. EFM3), which is installed at the IISIS target chamber. It can be used to deposit films with thicknesses ranging from less than a monolayer up to bulk material. The C$_{60}$ layers were produced by heating a powder containing crucible by electron impact from a tungsten filament with electron currents of up to 3 A. The deposition rate of the material can be determined with a quartz crystal microbalance (*Tectra* MTM-EK), which is also installed in the experimental chamber. Target exposure times were chosen with respect to the desired C$_{60}$ layer thickness. The C$_{60}$ layers were deposited onto a clean Au(111) substrate at an elevated temperature of 180 °C. A single monolayer of C$_{60}$ can be prepared by depositing several monolayers of C$_{60}$ on the Au surface and subsequent annealing to 400 °C, which leaves only the C$_{60}$ molecules which are adsorbed on the Au substrate behind [185]. The (sub) monolayer growth of the films can be examined with low energy ion scattering (see p. 73).

Highly Ordered Pyrolytic Graphite (HOPG)

In our investigations we used a highly ordered pyrolytic graphite (HOPG) sample with a graphite layer orientation parallel to the surface plane. Prior to installation in the vacuum chamber, the HOPG sample was cleaved with an adhesive tape. This produces an atomically flat, clean surface as could be confirmed by atomic force microscopy (AFM). In figure 3.21 two AFM pictures of the freshly cleaved HOPG surface are shown. The image section on the left hand side shows an area of 2×2 μm^2. Several terraces are visible in the displayed area. When zooming in onto one of those terraces, an atomically flat surface is revealed, as can be seen from the 470×470 nm^2 section to the right. The root mean square of the surface roughness within the scanned area in figure 3.21 is ≈ 0.06 nm.

Katharina Dobeš
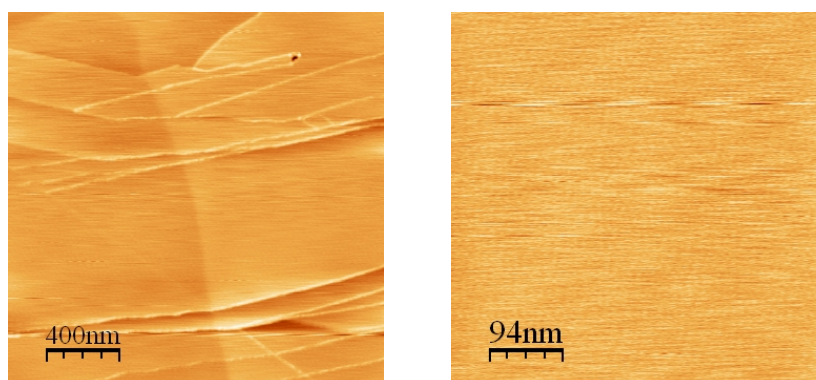
Figure 3.21: AFM images of freshly cleaved HOPG surfaces used in our experiments. In the left graph an area of 2×2 μm^2 is shown. Several terraces are visible in the displayed section of the surface. The right graph shows a zoom in onto an area of 470×470 nm^2, displaying an atomically flat surface, with 0.06 nm RMS roughness.

3.3   Nuclear Reaction Analysis

Total amounts of retained deuterium and nitrogen projectiles in beryllium samples (cf. sections 4.4 and 4.5) were determined using nuclear reaction analysis (NRA). The beryllium surfaces were irradiated with mono-energetic helium projectile ions that were produced in a tandem accelerator located at IPP Garching. At a certain incidence energy, the helium ions undergo nuclear reactions with the constituents of the surface. The resulting reaction products can then be detected to determine the areal density of the involved reactant in the surface (cf. table 3.2). In this way, beryllium, nitrogen and deuterium areal concentrations were quantified.

The energy of the incident ions was chosen such as to provide ions at an energy where the reaction cross-section of the observed nuclear transmutation does not vary much with the incidence energy. Hence the cross-section can be considered constant for the projectile as it slows down within the information depth in the sample. In this way the areal densities of the particular elements could be determined by comparing the count-rate of the reaction products to the respective count-rate obtained with standard reference samples of a well-defined composition and atomic density. The reference samples and the nuclear reactions that were used in our investigations are summarized in table 3.2.

element	nuclear reaction	incidence energy	reference
Be	$^9Be(^3He,p)^{11}B$	2 MeV	Be
D	$D(^3He,p)^4He$	2 MeV	a-C:D
N	$N^{14}(^4He,p)^{17}O$	4.94 MeV	CN_x ZrN

Table 3.2: Nuclear reactions and reference samples used to determine areal densities of beryllium, nitrogen and deuterium in beryllium samples after nitrogen and deuterium irradiation (cf. sections 4.4 and 4.5).

3.4   Computer Simulations - TRIM and TRIDYN

The interaction of atomic projectiles with amorphous surfaces can be simulated by means of Monte Carlo codes, which calculate projectile and recoil trajectories in the limit of a linear collision cascade (cf. section 2.2.1, p. 19). Such simulations can be used to determine ion ranges, partial as well as total sputtering yields, collision cascade damage, surface compositional changes etc.

For this purpose, the codes TRIM[3] [57] and TRIDYN [58,186] were used in this work. While TRIM calculates the interaction of the projectile with the surface disregarding any compositional changes or defect formation due to projectile implantation and high fluence irradiation, TRIDYN is capable of including such dynamic alterations of the surface during ion bombardment. High fluence phenomena as well as non-noble gas surface bombardment was therefore simulated with the TRIDYN code.

Both programs treat the collision cascade, which is initiated by the surface impact of a projectile, in a binary collision approximation (BCA). The trajectory of the projectile and the recoiling atoms is simulated as a sequence of nuclear collisions between two collision partners. Both the recoils as well as the projectile are followed in their slowing-down process until their kinetic energy drops below a certain threshold energy, the so-called cut-off energy, which is usually of the order of a few eV [57]. All generations of recoils including the projectile itself are sequentially treated in this way.

---

[3]TRIM - TRansport of Ions in Matter

Katharina Dobeš

Moving particles are characterized by their energy and their direction of motion. In between subsequent collisions they travel a distance λ, which is defined as the mean atomic distance of the substance

$$\lambda = n^{-1/3} \qquad (3.11)$$

if n is the atomic density of the target. In this way, the crystalline structure of the sample is neglected. The impact parameter for the two body collision is chosen as a random parameter. The energy transfer in the collision and the scattering angle are calculated with a proper inter-atomic potential, such as the free electron Kr-C inter atomic potential [55]. Electronic energy loss can be taken into account either non-locally by a continuous slowing down along the entire particle trajectory [50, 187], locally whenever a collision occurs [56] or by a 50:50 superposition of both approaches [188]. Each full projectile history n_H, i.e. so-called 'pseudo projectile' represents a fluence increment $\Delta\Phi$ by Φ_{tot}/n_H. For a sufficiently large number of trajectory calculations, the output data like e.g. sputtering yields, ion ranges etc. are obtained with a suitable statistical quality.

Surface atoms are treated as 'sputtered' whenever they are able to penetrate the surface at the coordinate x = 0. The surface barrier is treated as a planar potential. Sputtered particles have to overcome a certain surface binding energy E_s, i.e. the particle energy component perpendicular to the surface $E_0 \cos^2 \vartheta_0$ has to fulfill the following condition:

$$E_0 \cos^2 \vartheta_0 > E_s \qquad (3.12)$$

If the above-condition is not met, the particular particle will be reflected back into the solid. The choice of the surface binding energy E_s will therefore have a critical influence on the obtained sputtering yields. Usually the enthalpy of formation $\Delta_f H^0$ is used for E_s in the presented calculations.

TRIM can also be used to estimate radiation damage of the surface, i.e. permanent displacement of lattice atoms using the TRIM code. However the code is inherently limited to treating collisional effects. Thermal migration or recombination of displaced atoms, as well as defect interaction (e.g. clustering) are neglected in this approach. A stable defect, i.e. a Frenkel pair consisting of a vacancy at the original atomic site and an interstitial atom at its final position, is created if the final distance between interstitial and vacancy is sufficiently large. This is implemented by a displacement threshold energy E_d, which, depending on the target material, is of the order of $\sim$ 1 - 30 eV.

TRIDYN is an extended version of TRIM, which is able to account for a dynamic compositional changes of the surface due to high fluence surface irradiation. This is done by slicing the surface into $i = 1, ... N$ discrete, equidistant depth intervals Δx_i, each of which is characterized by a total atomic density n_i and a fractional composition of all $j = 1, ... M$ surface constituents q_{ij}. By the ion impact, surface atoms might be removed due to sputtering or recoil relocation and projectiles might be implanted. This changes the areal densities of the surface components $a_{ij} = q_{ij}n_i\Delta x_i$ in the individual depth intervals Δx_i. Subsequent to calculating a full pseudo-projectile history and before the next pseudo-projectile is simulated, the surface slabs are allowed to relax according to [58]:

$$\Delta x_i = \sum_{j=1}^{M} \frac{a_{ij}}{n_{0j}}$$

(3.13)

In this way the initial nominal density n_{0j} is restored.

target surface	element	n_{0j} [Å^{-3}]	E_s [eV]	E_d [eV]
a-C:H	C	0.05089 [1]	2.8 [1]	13 [2]
	H	0.05089 [1]	2.8 [1]	13 [2]
W	W	0.0632 [3]	8.68 [3]	38 [4]
WN	W	0.0632 [3,5]	8.68 [3,5]	38 [4]
	N	0.0632 [5]	8.68 [5]	38 [4]
Be	Be	0.12347 [3]	3.36 [3]	15 [4]
Be$_3$N$_2$	Be	0.12347 [6]	3.36 [6]	15 [4]
	N	0.21022 [6]	4.9 [6]	15 [4]

Table 3.3: Input parameters that were used in the presented TRIM and TRIDYN simulations: n_{0j} - target material atomic density, E_s - surface binding energy, and E_d - displacement energy. The above input parameters are derived from: [1] [189], [2] [190]; [3] [191], [4] [192]; [5] [66]; [6] [193]

The maximum concentration of implanted projectiles will usually be limited due to local saturation in the surface, which is reached as soon as either all solute and trapping sites are filled (cf. section 2.2.2) or the stoichiometric concentration of a

Katharina Dobeš

compound of the surface constituents is attained. To account for this, the maximum concentration of the involved particle species in the surface can be limited in a TRIDYN simulation. Excess atoms will then either effuse out of the surface immediately ('re-emission' model) or will be deposited in the nearest, non-saturated surface slap (incorporating a simple 'diffusion' model in the simulation).

The input parameters which are needed in the above-described simulations can readily be derived from textbooks (e.g. [191]). Table 3.3 summarizes the main input parameters that were used in this work to simulate the target materials of interest.

4

Results I
Ion Surface Interaction of Fusion Relevant Target - Projectile Combinations

4.1 Transient Effects During Sputtering of a-C:H Surfaces by Nitrogen Ions

Part of the following has been published in [194] and [195].

In present fusion experiments carbon is still often used as first wall material because of its advantageous thermal properties. Carbon as a plasma facing material however, poses a serious problem on future fusion devices. Co-deposition of eroded carbon with hydrogen isotopes leads to the formation of hydrogenated amorphous carbon (a-C:H) layers which contain tritium (cf. section 2.2.2). The thickness of these co-deposited layers will grow with operation time of the machine and will therefore constitute the major contribution to tritium retention in carbon containing machines [110]. As a consequence a tritium inventory within the fusion vessel builds over time and under reactor-like conditions is expected to rapidly exceed required safety limits [102].

Nitrogen seeding is presently used in fusion devices to reduce local power loads on highly exposed surfaces by enhanced radiative cooling [196] (cf. section 2.2, p. 17). This is why the interaction of nitrogen ions with a-C:H films is of considerable interest. It has recently been shown [189, 190] that a-C:H layers bombarded by molecular nitrogen N_2^+ ions exhibit an erosion rate which is enhanced by the chemical reactivity of the nitrogen projectiles especially at ion energies below the threshold for physical sputtering. By this, apart from radiatively cooling the plasma edge, the use of nitrogen as a seeding gas could also have a positive effect on the tritium inventory by eroding re-deposited a-C:T layers within the fusion device.

Hopf et al. [77] were able to model the energy dependence of chemical sputtering processes of hydrocarbon films on the basis of the following microscopic picture (cf. also section 2.2.1): when penetrating the a-C:H layer, energetic ions break C-C bonds, which are eventually passivated by consecutive projectiles. In the case of chemically reactive projectiles, this leads to the formation of volatile species, which can diffuse to the surface and desorb there. Hopf et al. showed [77] that the chemical sputtering yield is thus proportional to the bond breaking density, i.e. the number of carbon displacement events per depth interval $y_{bb}(x,E)$, and the ion implantation depth profile $n(x)$.

According to the above mechanism chemical sputtering requires the presence of chemically reactive species such as hydrogen or (in our case) nitrogen, while physical sputtering does not. Since chemical sputtering only takes place at sites where reactive atoms (i.e. hydrogen or nitrogen) are present, the corresponding yield is thus assumed to be proportional to their respective atomic fractions within the target, while physical sputtering is proportional to the complementary fraction, i.e. the number of 'pure' carbon sites, where no reactive species is available in the vicinity. By this the authors in [77] were furthermore able to describe the dependence of the sputtering yield on the incoming ion flux.

Total sputtering yields of so-called 'soft' a-C:H layers under N_2^+ bombardment were determined using the highly sensitive quartz crystal microbalance technique introduced in section 3.1 Soft a-C:H layers are characterized by a relatively high hydrogen content of 50%, which is why they exhibit the characteristics of an insulating layer. 'Hard' a-C:H films on the other hand contain less hydrogen (typically 30%) and are better conducting surfaces. When exposing a fresh a-C:H layer to a nitrogen ion beam, it is found, that the erosion yield at first decreases exponentially with ion fluence until a steady stat value is reached after applying some 10^{15} N_2^+ atoms to the surface (see section 4.1.1). The above-described chemical sputtering model by Hopf et al. [77] can be used to explain the measured steady state sputtering yields. In addition the transient development of the sputtering yield can be understood in more detail by simulation calculations based on the code TRIDYN (see section 4.1.2).

4.1.1 Experimental Results

Total sputtering yields of 'soft' a-C:H layers under nitrogen bombardment are investigated at TU Vienna under controlled laboratory conditions with the QCM setup that was introduced in section 3.1. All experiments were performed at a quartz temperature of 460 K.

Katharina Dobeš
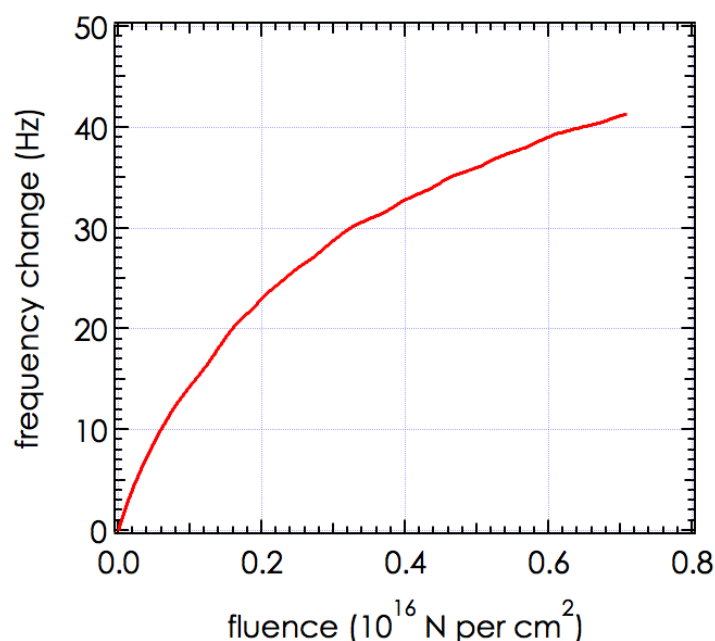
Figure 4.1: Evolution of the quartz frequency during 1 keV N_2^+ ion bombardment of a 'soft' a-C:H surface as a function of the applied ion fluence. At the beginning of the irradiation, a strong non-linear change of the resonance frequency of the quartz is observed.

Soft, polymer-like a-C:H layers with a hydrogen content of 50% were deposited onto a polished gold electrode of a quartz in an ECR methane plasma discharge (cf. section 3.1.5) [123]. The film growth and characteristics of the layer was monitored by in-situ ellipsometry. The thickness of the films was determined to be about 370 nm. The a-C:H samples are transferred ex vacuo to the UHV experimental chamber at TU Vienna (cf. section 3.1.3, figures 3.6 & 3.7). N_2^+ projectiles are extracted from the Vienna ECR ion source. The total mass change of the target film is determined from the Eigen-frequency change of the quartz crystal according to equation 3.4. From the slope of a fit to the frequency change-curve, only total mass changes per incident projectile (in atomic mass units) can be determined. To investigate the evolution of non-constant sputtering yields, consecutive measurements can be re-joined to one single curve. By this only total mass changes, i.e. net erosion or net deposition, can be determined while no information on the actually sputtered species is obtained.
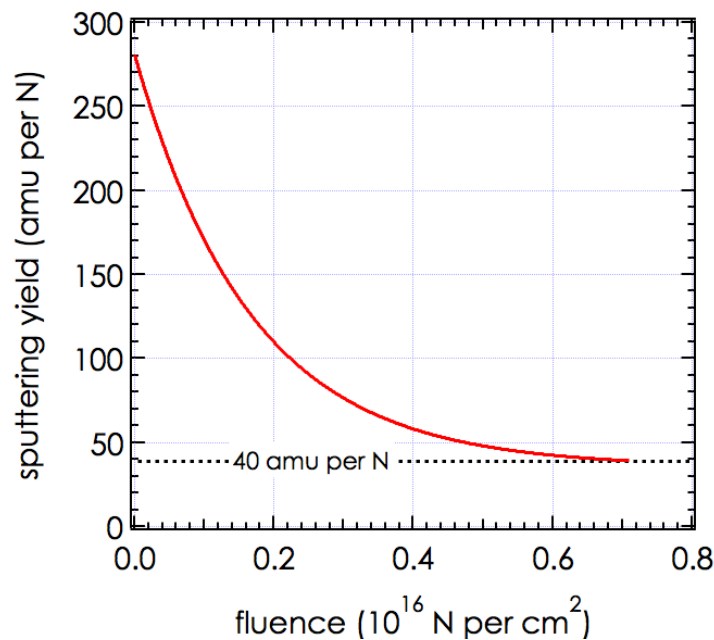
Figure 4.2: Total sputtering yield of the a-C:H surface under N_2^+ ion bombardment (in atomic mass units per incident N-atom) as a function of the ion fluence. Data are evaluated from the slope of the frequency curve in figure 4.1. For high fluences, the observed sputtering yield approaches a steady state value of $\sim$ 40 amu per N (indicated by the dashed line).

Figure 4.1 shows, how the QCM frequency measured for the impact of 1keV N_2^+ ions (i.e. 500 eV per N-atom) changes its slope with increasing ion fluence, indicating a significant change in erosion yield during the course of the entire measurement. The corresponding evolution of the sputtering yield as a function of the ion fluence is shown in figure 4.2. The measurements started with a virgin, i.e. freshly deposited 'soft' a-C:H layer. Fluences and sputtering yields are given per incident nitrogen atom (not N_2 molecule). At the beginning of the ion irradiation an elevated sputtering yield is observed that decreases exponentially with fluence to approximately 1/5 of its initial value. After approximately $7 \cdot 10^{15}$ N atoms per cm^2 have been applied to the surface a steady state value of the sputtering yield is finally reached (marked by the dashed line in figure 4.2). At this fluence about 4 nm of target material have been removed, as can be estimated from the observed sputtering yield and with a target density of 1.1 g/cm^3 [189]. A similar behavior was

Katharina Dobeš
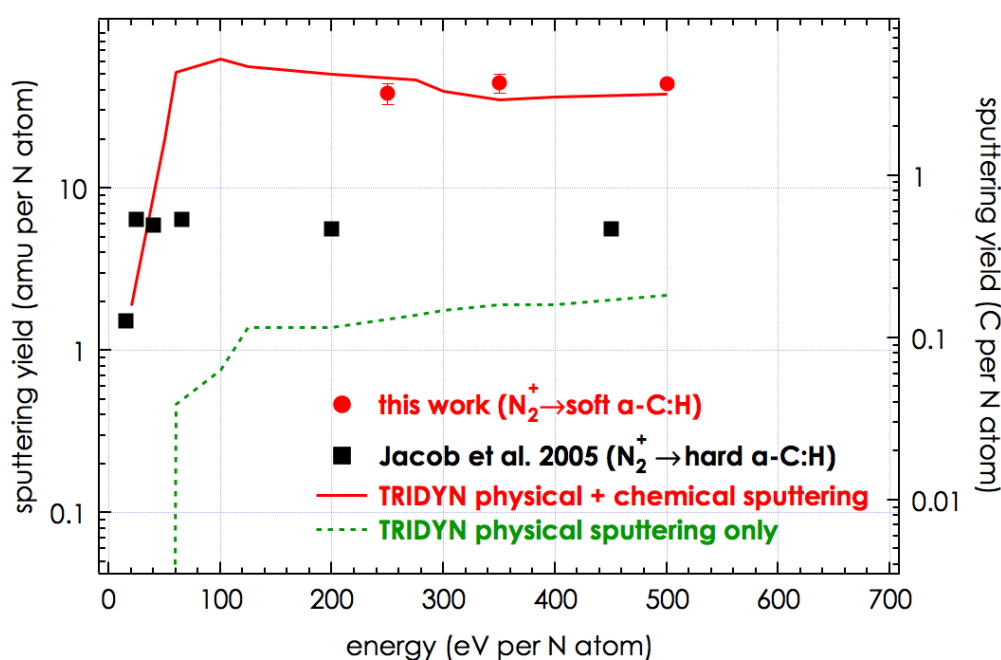
Figure 4.3: Comparison of the obtained steady state sputtering yields (full red circles) for the impact of N_2^+ ions on 'soft' a-C:H films with previous data and TRIDYN calculations. QCM results are given in atomic mass units per incident N-atom. Black squares show experimental data by Jacob et al. [189] for bombardment of 'hard' a-C:H surfaces. Their sputtering yields are given in C atoms per incident N atom. Steady state sputtering yields are calculated by TRIDYN [186] using the model proposed by Hopf et al. [77] (full red curve) and are compared to calculations, which consider physical sputtering only (broken green curve). For details see text.

also found for other impact energies (500 eV and 700 eV N_2^+ projectiles), always starting with a fresh a-C:H film of course.

Figure 4.3 summarizes the steady state sputtering yields obtained at the end of each measurement series. For comparison data by Jacob et al. [189] for bombardment of 'hard' a-C:H layers are shown. These data were obtained for a-C:H layers of lower hydrogen content (30%) than in our case. Mind also that in [189] the number of eroded carbon atoms per incident N-atom is determined from an a-C:H film thickness change, which is determined by real time ellipsometry. The observed thickness change can then be converted into an C erosion yield due to a strong correlation between the physical properties of the a-C:H layer and the

carbon density in the film [122]. With our measurement technique on the other hand, the total mass removal (including hydrogen, nitrogen, and heavier compounds such as different kind of hydrocarbons C_xH_y and other volatile molecules) is obtained. Both, the different actually accessible measurement quantities and the discrepancy in the hydrogen content of the investigated surface layer might explain the deviations between the data presented in this work and those of [189].

The code TRIDYN [186] (cf. section 3.4) has been used to perform simulations of the interaction of nitrogen with a-C:H (also see section 4.1.2). In these simulations the molecular nitrogen ion is treated as two separate atomic nitrogen projectiles at the same velocity or equivalently at the same specific energy (i.e. half the impact energy). TRIDYN is in principle only capable of reproducing physical processes (like e.g. physical sputtering but not chemical sputtering). Just taking physical sputtering into account(see green dashed line in figure 4.3) TRDIYN delivers steady state sputtering yields which clearly underestimate the experimentally observed values. Evidently it is essential to also include the chemical sputtering yield mechanism proposed by Hopf et al. [77] in order to adequately reproduce the observed steady state sputtering yields. This will be described more throughly in the following section.

4.1.2 Modeling

Steady State Sputtering Yields

In the following a model shall be introduced, aiming to qualitatively describe both the transient as well as the steady state sputtering behavior observed in our experiments. It is based on a model proposed by Hopf et al. [77]. Within the framework of this model, some simplified physical and chemical sputtering processes describe the interaction between target and projectile. They are used to establish a set of rate equations, which are able to reproduce the measured data. The model presented here, shall make the experimental results plausible and give a qualitative picture of the involved physical processes. For a more detailed and complete description of the system, an atomistic-level simulation by e.g. molecular dynamics would be more favorable as e.g. realized in [197].

Within the simplified picture proposed here, chemical sputtering is described as a result of the following multi-step process (cf. also 2.2.1): Impinging nitrogen ions (with an incidence energy of E) break C-C bonds with a bond breaking yield density of $y_{bb}(x, E)$, which is equal to the number of events along the ion penetration path (in the direction of the x-coordinate), in which the recoil atom in a binary col-

Katharina Dobeš

lision receives an energy bigger than the bond breaking energy E_{bb}. It was found that thirteen electronvolt is a reasonable value for E_{bb} [190] in order to adequately describe the interaction of nitrogen projectiles with an a-C:H surface. Subsequent nitrogen projectiles then passivate the resulting dangling bonds by forming volatile species. This process is dependent on the availability of nitrogen ions, which in turn is determined by the ion implantation depth profile $n(x, E)$. The so-formed volatile species diffuse to the surface with a probability which decreases exponentially with their depth of origin, i.e. $e^{-x/\lambda}$ and desorb there. Herein the decay length λ is set to 0.4 nm [77]. The total sputtering yield Y_{tot} will then be given by [77]:

$$Y_{tot}(E) = Y_{phys}(E) + Y_{cs}(E) = Y_{phys}(E) + a \int y_{bb}(x, E) n(x, E) dx \qquad (4.1)$$

with a being a proportionality factor and Y_{phys} and Y_{cs} denoting the physical and the chemical sputtering yield, respectively. Chemical sputtering only takes place at sites where either hydrogen or nitrogen is present, while carbon sites are assumed to be physically sputtered. The proportionality factor a takes uncertainties into account such as how many nitrogen or hydrogen atoms are needed on average for one chemical sputtering event.

The surface can now be subdivided into concentrations Θ_H and Θ_N of sites were either hydrogen or nitrogen is present in the vicinity of a carbon atom, and the complementary fraction Θ_C of 'pure' carbon sites, i.e.

$$\Theta_C = (1 - \Theta_H - \Theta_N) \qquad (4.2)$$

Hydrogen and nitrogen sites are chemically sputtered with a maximum yield of

$$Y_{cs}^{max} = Y_{cs}(\Theta_H + \Theta_N = 1) \qquad (4.3)$$

Here it is assumed for simplicity that the chemical sputtering yield of nitrogen and hydrogen is equal. Carbon sites on the other hand are physically sputtered with a maximum yield of

$$Y_{phys}^{max} = Y_{phys}(\Theta_C = 1) \qquad (4.4)$$

Y_{phys}^{max} and Y_{cs}^{max} are regarded as limiting cases for zero and maximum hydrogen and nitrogen concentration in the target. The total sputtering yield can then be written as:

$$Y_{tot} = Y_{cs}^{max} \cdot \left(\Theta_1^H + \Theta_1^N\right) + Y_{phys}^{max} \cdot \left(1 - \Theta_1^H - \Theta_1^N\right) \qquad (4.5)$$

Here, the concentrations Θ_1^H and Θ_1^N are equipped with an index '1' to indicate that sputtered species originate only from within a very narrow depth below the

Katharina Dobeš

surface (cf. section 2.2.1). To describe the observed steady state sputtering yields shown in figure 4.3 in a first step Y_{tot} is calculated from equation 4.5 with TRIDYN for the case of 1 keV N_2^+ ions, which are assumed to be equal to two separate atomic nitrogen projectiles with half the energy. The TRIDYN input parameters used to simulate the interaction are summarized in table 3.3 on page 78. As initial target, an a-C:H film with a relative hydrogen concentration of $H/C = 1$ is used. The target density is set to 1.1 g/cm^3. The surface binding energy for carbon and hydrogen ions is set to $E_S \sim 2.8$ eV, the surface binding energy of nitrogen is taken to be $E_S \sim$ 1.9 eV [189]. Both the physical as well as the chemical sputtering yield are determined at a fluence of $7 \cdot 10^{15}$ N atoms per cm^2, which corresponds to steady state conditions in our measurements. The resulting TRIDYN curve depicted in figure 4.3 (red solid line) is then obtained using a proportionality factor of $a = 5$ in equation 4.1. As demonstrated in figure 4.3 a good agreement with our experimental data is obtained for all investigated energies.

Fluence Dependence of the Sputtering Yield

The observed dependency of the sputtering yield on the applied ion fluence (see figure 4.1) reflects the modification (i.e. the change of the composition) of the a-C:H layer with increasing ion fluence. Modeling this process tended to be more difficult. In a first step the evolution of the atomic fractions of hydrogen, nitrogen and carbon under ion bombardment were calculated from a balance of various processes: Hydrogen and nitrogen are removed from the surface by either ion-induced depletion due to momentum transfer with a yield of Y_{depl} or by chemical sputtering Y_{cs}. Impinging nitrogen projectiles are additionally implanted at C-C sites with an implantation yield of Y_{imp}.

As the surface is eroded, bulk material with atomic concentrations different from those in the top surface layer emerges into the ion range. To account for this, the target is sliced into four different 2 nm thick sub-layers and an underlying bulk with fixed atomic concentrations corresponding to the initial surface conditions (cf. table 3.3). The distinct yields for the above-mentioned processes is calculated for each individual layer separately using values obtained from TRIDYN at a simulated fluence of $7 \cdot 10^{15}$ N atoms per cm^2. By using TRIDYN instead of TRIM, compositional changes of the surface as a result of projectile implantation and continuous surface erosion are taken into account too. Hereby Y_{depl} is determined from the number of displaced atoms in a collision cascade within such a surface sub-layer minus the number of recoil atoms, which come to rest in this sub-layer. Y_{imp} is derived from the nitrogen implantation depth profile of $n(x)$, which is shown in figure

Katharina Dobeš
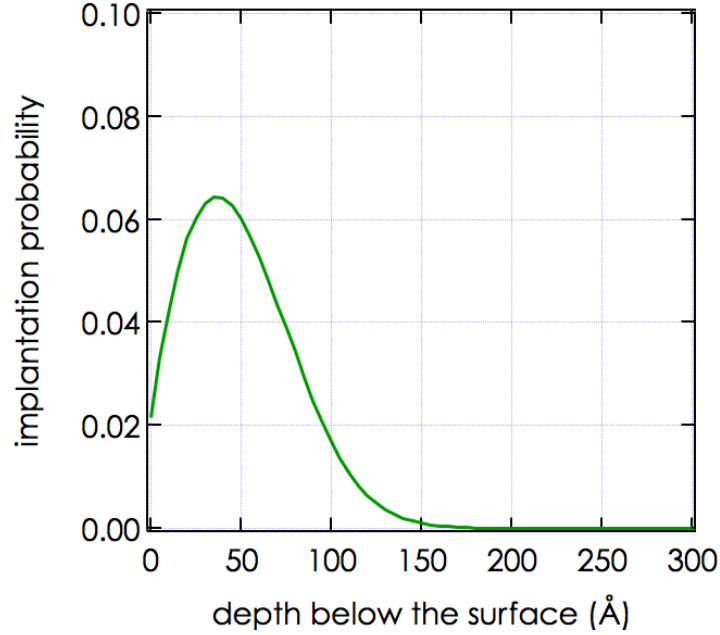
Figure 4.4: Implantation probability obtained from TRIDYN [186] of 1 keV N_2^+ ions impinging on a soft a-C:H surface.

4.4. Y_{cs} is determined from equation 4.1. The evolution of the surface concentrations in the four sub-layers $i = 1 - 4$ is then given by the following rate equations, which calculate the balance between the above-mentioned processes:

$$n_0 \frac{d\Theta_i^H}{dt} = -j_N \left(Y_{depl}^H + Y_{cs}^H \right) \Theta_i^H + j_N Y_{tot} \; \Theta_{i+1}^H \qquad (4.6)$$

for the hydrogen concentrations Θ_i^H in the surface sub-layers and

$$n_0 \frac{d\Theta_i^N}{dt} = -j_N \left(Y_{depl}^N + Y_{cs}^N \right) \Theta_i^N + j_N \left(1 - \Theta_i^N - \Theta_i^H \right) Y_{impl} + j_N Y_{tot} \; \Theta_{i+1}^N \qquad (4.7)$$

for the nitrogen concentrations Θ_i^N. With the term $j_N Y_{tot} \; \Theta_{i+1}^X$ ($X = H, N$) the particle exchange of a particular sub-layer with its individual subjacent layer as a consequence of surface erosion is included. The composition of the undermost sublayer $i = 4$ corresponds to the initial bulk concentrations.

In figure 4.5 the resulting concentrations of carbon, hydrogen and nitrogen in the top-most sub-layer are depicted as a function of the ion fluence. From the rate equations in 4.6 and 4.7, one finds that under ion bombardment a nitrogen
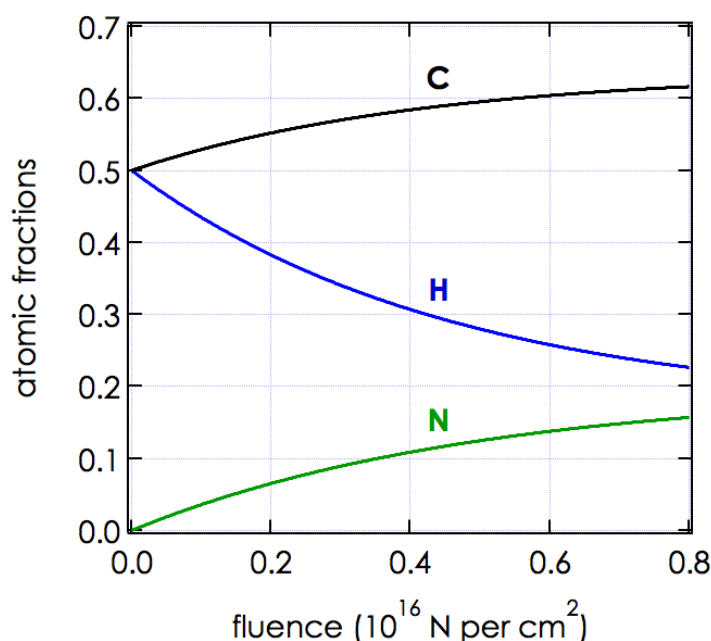
Figure 4.5: Fluence dependency of the atomic fractions of C (θ_1^C, black curve), H (θ_1^H, blue curve) and N (θ_1^N, green curve) in the top most layer of the a-C:H surface under N bombardment. The curves are obtained from the set of rate equations (cf. equations 4.6 and 4.7) describing the interaction of the projectiles with the surface.

concentration builds up within the surface, while the hydrogen concentration decreases with the impinging ion fluence.

From the evolution of the surface composition under ion bombardment, the number of removed particles per incident nitrogen atom due to the respective sputtering processes in equation 4.5 can be calculated. For a comparison with the experimental data from figure 4.2, however, a total mass removal (in amu per nitrogen atom) has to be deduced from these yields, since this is the quantity accessible with the QCM experimental technique. In doing so, somewhat arbitrary assumptions in the masses of the volatile compounds formed and subsequently desorbed from the surface in the chemical sputtering processes Y_{cs}^H and Y_{cs}^N have to be made. In an attempt of bringing the measured total sputtering yields from figure 4.2 into agreement with Y_{tot} as obtained from equation 4.5, typical masses were used for eroded molecules according to those reported in the literature such as CN, HCN, C_2N_2 [198] and different kinds of hydrocarbons C_xH_y, respectively.

Katharina Dobeš
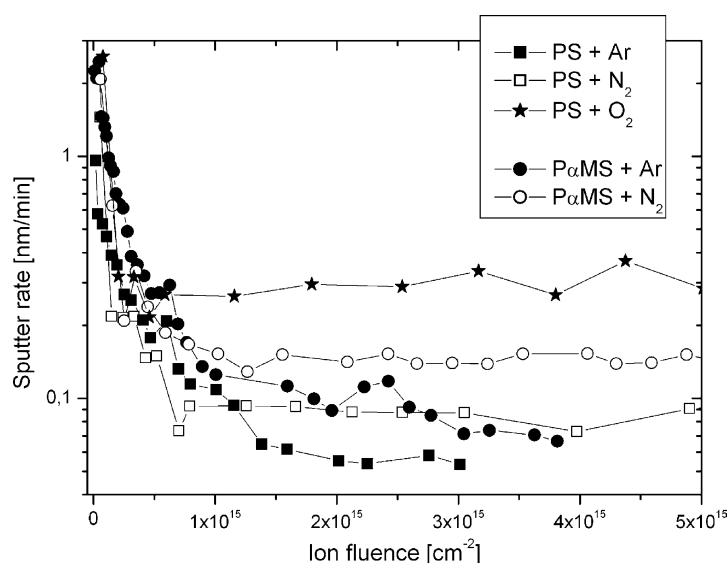
Figure 4.6: Evolution of the sputtering yield of different polymers (i.e. PS - polystyrene; PαMS - poly(α-methylstyrene) under the impact of various ions (i.e. argon, nitrogen and oxygen) [199]. A strong fluence dependency of the sputtering yield is observed followed by a saturation behavior for prolonged ion-beam exposure. The characteristics of the sputtering yield evolution depends on the target-projectile combination, i.e. on the chemistry of the interaction process.

However regardless of the applied molecule mass, the evolution of the total sputtering yield with ion fluence was inconsistent with the measured data. Especially the model failed to describe the substantial difference between the experimentally observed initial sputtering yield and the yield under steady state conditions.

When investigating sputtering rates of different polymers under ion irradiation with a QCM technique, Zekonyte et al. [199] observed a dynamic change in the total mass removal with ion fluence which is very similar to the one found in the experiments presented here. This is demonstrated in figure 4.6, where the evolution of the sputtering yield for two different polymers, i.e. polystyrene and poly(α- methylstyrene) is shown for the impact of various ion species, both chemically reactive and inert. The authors in [199] observe a distinct decrease in sputter rate up to fluences of $\sim 5 \cdot 10^{15}$ ions per cm^2. At prolonged ion beam exposure a saturation in the sputtering yield is reported, whereas the specific characteristics of this transient behavior depends on the target-projectile combination, i.e. the chemistry of the interaction process. It could be shown by x-ray photoelectron spectroscopy that

Katharina Dobeš
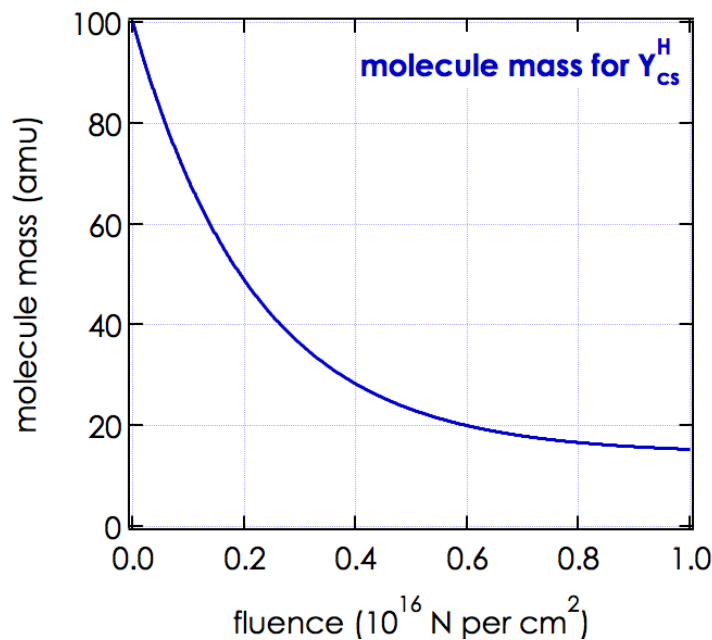
Figure 4.7: Evolution of the molecular mass of the C_xH_y species chemically sputtered at H-sites, which had to be assumed to correctly model the evolution of the sputtering yield with ion fluence.

the observed transient effect in the sputtering yield is linked to a chemical modification of the target film, which is induced by the ion bombardment. The decrease in the sputtering yield with ion fluence was additionally enhanced by a substantial reduction of the occurrence of higher molecular weight fragments in the sputtered species (as confirmed by secondary ion mass spectrometry measurements [200]).

The formation of a modified surface layer of an a-C:H film under ion bombardment was also found by von Keudell et al. [201]. These authors investigate the properties of an a-C:H film during deposition using in situ ellipsometry. They observe a densification of the target film under ion bombardment, which they attribute to the ion bombardment induced creation of dangling bonds and the displacement of bonded hydrogen in the surface, which is followed by the formation of new C-C bonds in the carbon network.

The findings in [199, 201] strongly suggest that assuming a constant mass for the chemically sputtered species constitutes an oversimplification of the problem and that it is necessary to introduce a change of the eroded molecule mass with im-

Katharina Dobeš
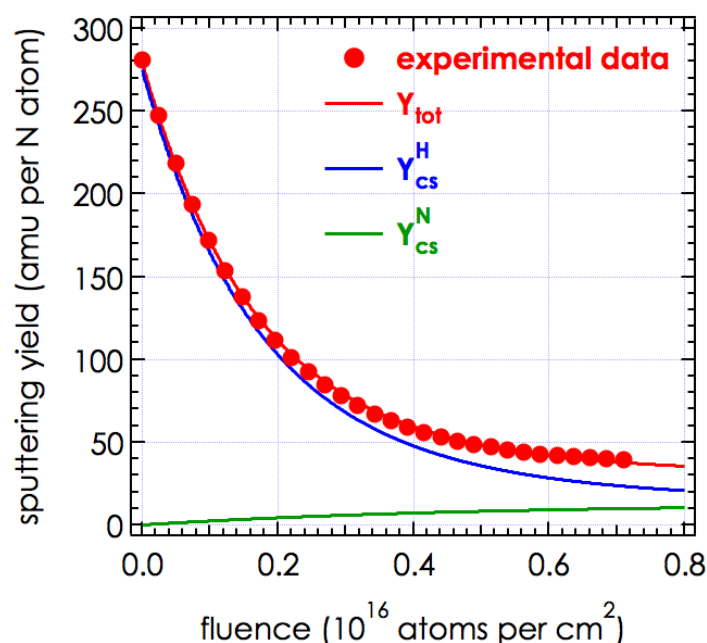
Figure 4.8: Comparison of the modeled total sputtering yield (red solid line) with results obtained from the experiment (red circles). The evolution of Y_{cs}^H (blue solid line) was obtained assuming that the sputtered molecule masses change with ion fluence (cf. figure 4.7), while for Y_{cs}^N (green solid line) the sputtered molecules were assumed to be of constant mass. In the total sputtering yield Y_{tot} a constant physical sputtering yield is also included (cf. figure 4.3). This Y_{phys} is not explicitly depicted.

pinging ion fluence to our model, in order to describe the transient sputtering yield observed in the experiment appropriately.

Since the above-described processes are governed by a modification of the chemical structure of the target film, it is suggested here to account for the change of the molecule mass by varying the mass of the eroded C_xH_y molecules only. This, of course, will strongly affect the evolution of the chemical sputtering yield at hydrogen sites Y_{cs}^H and consequently also of the total sputtering yield Y_{tot}. It is therefore assumed that the mass of the sputtered C_xH_y species decreases with ion fluence and eventually reaches a steady state value. The function dependency was adapted in a way to optimally reproduce the yield evolution found in the experiment (see figure 4.2). The such determined evolution of the molecular mass of the eroded C_xH_y species is depicted in figure 4.7. Initially molecule masses around

100 amu are eroded per incident nitrogen atom. This value decreases exponentially until under steady state conditions molecules with a mean mass of 15 amu (corresponding to e.g. a CH_3 molecule) per incident nitrogen atom are sputtered. With this assumption the modeled evolution of the total sputtering yield with ion fluence is in very good agreement with the experimental findings. In figure 4.8 both the experimental results (red dots) as well as the modeled evolution of the total sputtering yield (red line) are depicted. Additionally the underlying evolutions of the chemical sputtering yields at hydrogen sites Y_{CS}^H (blue line) and at nitrogen sites Y_{CS}^N (green line) are also shown.

4.1.3   Summary & Concluding Remarks

The sputtering of 'soft', polymer-like a-C:H layers under N_2^+ ion bombardment up to energies of 1 keV was investigated. It was found that the total sputtering yield observed, at first decreases strongly with ion fluence and reaches a steady state value after some 10^{15} N_2^+ ions per cm^2 have been applied to the surface.
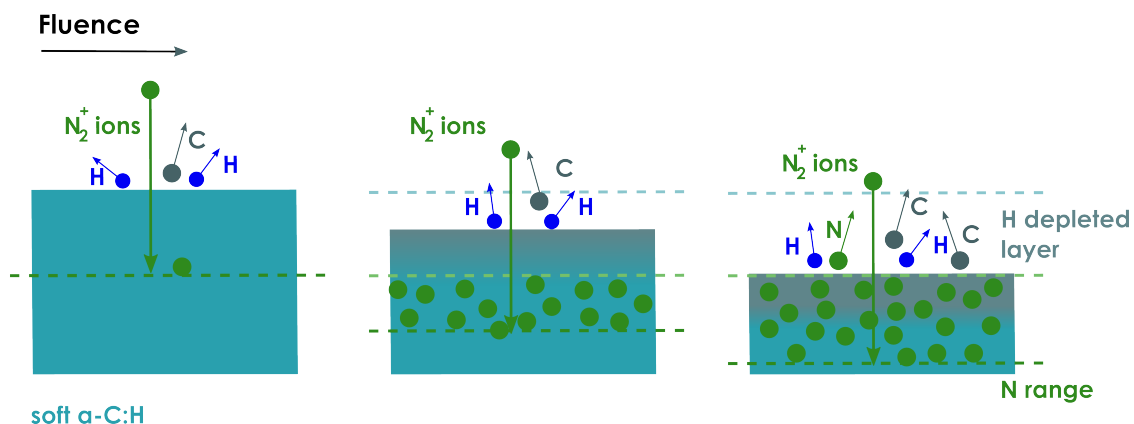

Figure 4.9: Scheme of the sputtering process of the a-C:H surface under nitrogen impact. The evolution of the surface is depicted for increasing ion fluence from a virgin surface (left) to the transient behavior (center) and steady state conditions (right). For details see text.

Qualitatively this evolution can be understood in the following way: nitrogen projectiles impinging on an a-C:H surface at first preferentially abstract hydrogen from the surface leaving behind dangling C bonds. This leads to a restructuring of the carbon network and generally a densification of the target film within the ion penetration depth. This process is accompanied by the implantation of nitrogen

projectiles in the surface. The creation of a hydrogen depleted, nitrogen containing top surface layer is reflected in a transient behavior of the sputtering yield for low ion fluences. This could be observed both in the experiments presented here as well as in investigations from other groups [199, 201].

In order to understand the transient behavior of the sputtering yield, a set of rate equations for the atomic composition of the target material was considered, which takes into account various interaction processes between projectiles and target. The rates for the underlying processes were obtained from TRIDYN. A change in surface composition due to the sputtering yield alone is, however, not able to explain the strong decrease in the observed sputtering yield with ion fluence. Good agreement between model and experimental data could only be obtained by assuming that the average mass of the hydrocarbon molecules eroded in the chemical sputtering processes also decreases with ion fluence. With a similar approach also the observed steady state sputtering yields as a function of the impact energy could be reproduced nicely.

4.2 Sputtering of Tungsten by N^+ and N_2^+ Ions: Investigations of Molecular Effects

Part of the following has been published in [202]

In 2007, ASDEX Upgrade was the first fusion machine to operate with a full tungsten wall [38]. Also in future fusion devices like ITER, tungsten is foreseen as a divertor target [20] (cf. section 2.2, page 14). In order to reduce the power load to the divertor target plates to acceptable values, radiation cooling is essential [196]. Since the elimination of carbon from these fusion machines, radiation due to intrinsic impurities is no longer sufficient and has to be replaced by seeding of additional impurities (also cf. section 2.2, page 17) [196]. At ASDEX Upgrade nitrogen seeding with feedback control has meanwhile matured into a standard operational scenario [38]. The divertor target power flux could be mitigated by high radiation levels to technically acceptable values using nitrogen, and the performance of the plasma was even increased compared to discharges without seeding [38].

It is therefore of considerable interest to study the interaction of nitrogen containing plasmas with tungsten surfaces. Schmid et al. recently studied the sputter erosion of tungsten by high fluences of N_2^+ projectiles and observed the formation of a tungsten-nitrid surface layer within the ion penetration depth [66]. As a result of the nitrogen accumulation in these layers a reduced partial sputtering yield of tungsten as compared to a pure tungsten surface was found [66].

In both modeling as well as experiments it is often assumed that the impact of an X_n^+ molecule ion on a solid surface has the identical effect as n X^+ ions at the same velocity (i.e. that generally no molecular or non-linear sputtering effects are observed for the impact of molecular projectiles). The high accuracy of the QCM experimental technique previously introduced in section 3.1 allows a detailed investigation of possible differences in the sputtering yield due to bombardment by atomic and molecular nitrogen projectiles.

4.2.1 Experimental Results

To measure the total sputtering yield for nitrogen ion bombardment of tungsten, the highly accurate QCM setup developed at TU Vienna [169, 170] was used (cf. section 3.1). 500 nm thick, polycrystalline tungsten films (cf. section 3.1.5) are bombarded by atomic and molecular nitrogen ions. The tungsten films are deposited onto the quartz crystals prior to installing them in the experimental chamber at TU Vienna by vapor deposition (cf. section 3.1.5). The ions are extracted from the
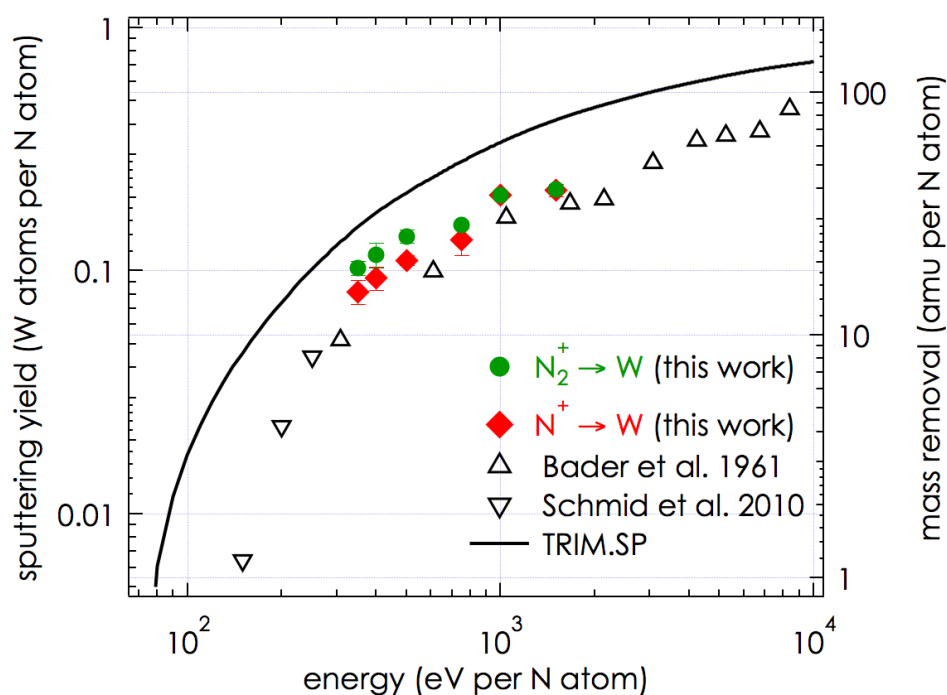
Figure 4.10: Sputtering yield per incident nitrogen atom of polycrystalline tungsten bombarded by molecular N_2^+ ions (full circles) and by atomic N^+ ions (full diamonds) versus projectile energy per nitrogen atom. Experimental data published earlier are included for comparison: ($\triangle$) [203] and ($\triangledown$) [66]. The black solid line represents a fit to TRIM.SP [57].

Vienna ECR ion source in an energy range of some hundred eV up to 2000 eV per nitrogen atom. The molecular and the atomic fraction of the extracted beam is separated by mass to charge state selection in the sector magnet of the facility. During the measurements the QCM temperature is held constant at 460 K. The mass change of the target film during ion bombardment and therefore the sputtering yield is derived from the measured change in the quartz crystal frequency in the usual way, by using equation 3.4.

Prior to nitrogen bombardment the tungsten surfaces were sputter cleaned in situ with Ar^+ ions. About 10^{15} argon ions per cm^2 were applied to the surface, while the resulting sputtering yield was monitored. At first an elevated sputtering yield is observed, which most likely results from an adsorbate or oxide layer. Ar^+ bombardment was continued until a steady state sputtering yield was reached. With a sputtering yield of about 0.7 tungsten atoms per argon projectile at 1 keV

impact energy, this corresponds to the removal of a few monolayers of tungsten only. This procedure was then repeated with nitrogen ions, where again typically 10^{15} nitrogen ions per cm^2 were necessary to reach a steady state sputtering yield value.

Figure 4.10 shows measured sputtering yields of polycrystalline tungsten for both the impact of molecular N_2^+ (full green circles) and atomic N^+ (full red diamonds) ions. For comparability the projectile energy as well as the sputtering yield are normalized to the number of nitrogen atoms in the projectile. In this way projectiles of equal velocity are compared and possible non-linear sputtering effects due to the impact of diatomic molecular projectiles should become visible. To avoid systematic errors as much as possible, the results shown in figure 4.10 for N^+ and N_2^+ projectiles have been obtained in random order on different days and sometimes even with different quartz crystals. Every data point shown is the result of at least five individual measurements usually carried out the same day on the same quartz crystal. In some but not all cases the measurements have been repeated on a different day, sometimes even on several different days and also on a different quartz crystal. The error bars shown correspond to the standard deviation of the mean value of all the individual measurements. For this reason some data points carry much smaller statistical error bars than others.

The experimental data in figure 4.10 is also compared to results of previous measurements by Schmid et al. [66] and Bader et al. [203] as well as a TRIM.SP fit [57]. The TRIM.SP data are noticeably higher than all the experimental data points and correspond to the 'static' TRIDYN [58] calculations presented by Schmid et al. [66], where a dynamic surface composition change due to ion impact is suppressed (cf. section 3.4). To explain the difference between their experimental data and those of the 'static' TRIDYN simulations, Schmid et al. [66] argued that during the bombardment of tungsten with high fluences of nitrogen ions, the accumulation of nitrogen leads to the formation of a tungsten-nitride phase within the ion penetration depth, thus reducing the sputtering yield as compared to a pure tungsten surface. Their data points were obtained by bombardment with ions from a nitrogen plasma (composed of $\sim$ 90% N_2^+ and 10% N^+) with a fluence of some 10^{19} ions per cm^2, after which they found that the implantation of nitrogen in the surface layer had saturated. Their arguments were supported by dynamic TRIDYN calculations, which also showed a significant reduction of the tungsten erosion due to nitrogen implantation.

The effect of nitrogen implantation on the sputtering experiments presented here was estimated with a dynamic TRIDYN [58] simulation. Since experiments were performed at ion fluences of less than $3\cdot10^{15}$ N ions per cm^2 only a very small

Katharina Dobeš
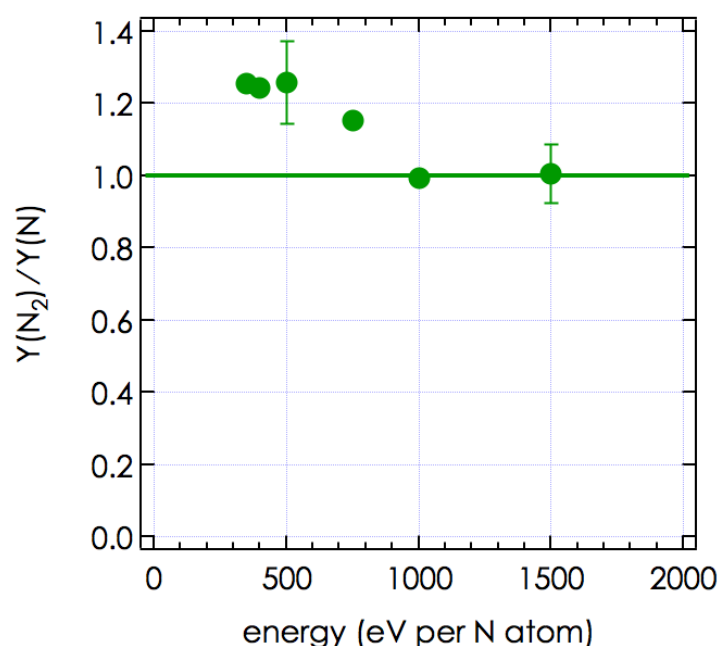
Figure 4.11: Ratio between the sputtering yield per nitrogen atom for the bombardment of tungsten with molecular vs. equally fast atomic nitrogen projectiles (full symbols). The horizontal line corresponds to the linear case, where N_2^+ acts as two independent N^+ projectiles.

reduction of the total sputtering yield (within the experimental error of $\sim 10\%$) can be expected. The results shown in figure 4.10 therefore represent sputtering of a pure tungsten surface.

4.2.2 Discussion

Taking a closer look at the differences between N^+ and N_2^+ sputtering yields in figure 4.10, one finds that for energies above 1000 eV per nitrogen atom the sputtering yields per incident nitrogen constituent in the projectile coincide well for atomic and molecular ions. Below 1000 eV per nitrogen atom however, the amount of sputtered tungsten atoms per incident nitrogen constituent in the projectile is clearly higher for the impact of a N_2^+ molecular ion than for N^+ atomic ion bombardment. In this energy range a N_2^+ ion can obviously not be considered equivalent to two independent nitrogen atoms impinging on the surface (i.e. a so-called 'molecular effect' is observed).

Katharina Dobeš

This enhancement becomes even more clear by plotting the ratio between the sputtering yields per atom for bombardment with molecular and atomic nitrogen ions for equally fast projectiles as demonstrated in figure 4.11. At energies between 350 and 500 eV per nitrogen atom the *sputtering yield per atom* is about 25% higher for molecular than for atomic projectiles. Towards higher impact energies this enhancement diminishes and vanishes above 1000 eV per atom with the ratio between the two yields approaching one.

At first glance such a pronounced molecular effect seems somewhat surprising. At high energies (typically 50 keV or higher) molecular effects are well investigated and attributed to nonlinear effects in the collision cascade [204-206]. In the linear cascade regime of sputtering (cf. section 2.2.1, page 19), i.e. for impact energies of typically 1 - 50 keV, the sputtering yield per atom of a molecular ion should equal that of an atomic ion at the same impact velocity (i.e. the same energy per atomic constituent) [206]. Very little is known, however, about molecular effects close to the sputtering threshold (for impact energies < 1 keV). Yao et al. [207] have reported the first observation of a sputtering enhancement for molecular projectiles as compared to atomic ions at very low projectile energies. They investigated the sputtering yield from a polycrystalline gold surface under the impact of molecular and atomic nitrogen and oxygen ions. The main results of their studies are shown in figure 4.12. Below a certain impact energy threshold (500 eV in the case of nitrogen, 100 eV for oxygen bombardment) they observe a noticeable divergence of the molecular (i.e. N_2^+ and O_2^+ respectively) sputtering yield from the corresponding atomic (i.e. N^+ and O^+ respectively) yield. Yield enhancements of up to almost a factor of four have been found for kinetic energies of 50 eV [207]. A similar molecular effect has also been reported for chemical sputtering of graphite by low energy atomic and molecular hydrogen and deuterium projectiles [208] and was also attributed to differences in the elastic binary collision energy transfer of molecular compared to two independent atomic ions. In addition a molecular size effect for the sputtering of a-C:H surfaces by hydrogen and deuterium projectiles was reported by Harris et al. [209], who observed that the methane production per incident H constituent was clearly enhanced for molecular ion impact.

For a qualitative explanation of the observed molecular effect, the arguments presented by Yao er al. [207] will be followed. On the basis of a simple energy transfer model, the energy transferred to a target atom in a binary elastic collision by a diatomic molecule is determined by an *effective projectile mass m**, which varies between the two limiting cases, that the diatomic molecule can either be

Katharina Dobeš
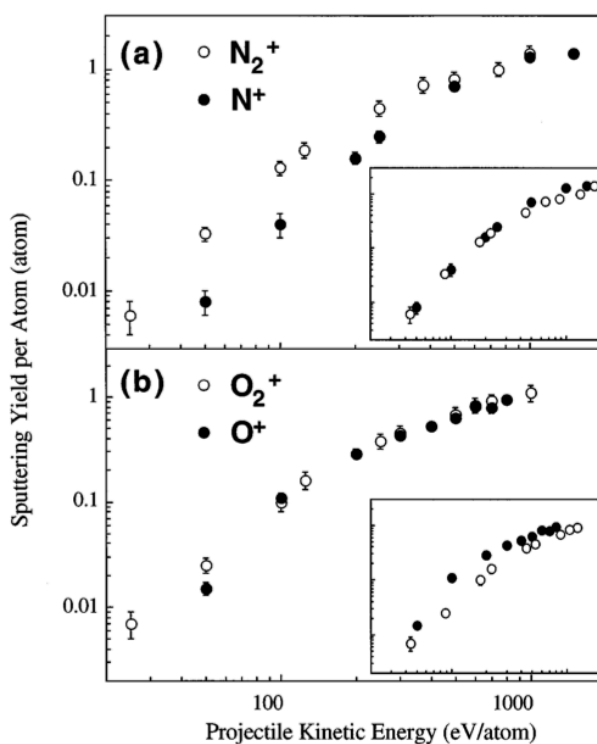
Figure 4.12: Sputtering yield of gold bombarded by molecular and atomic oxygen and nitrogen projectiles as a function of the projectile impact energy [207]. In the insets the sputtering yield is shown vs. the energy transfer per atom in the unified atom limit. For more information see text.

understood as two independently impinging atoms, or one rigid particle with twice the mass than its atomic constituents, i.e.

$$m \leq m^* \leq 2m \tag{4.8}$$

Yao et al. argue that the effective projectile mass in the collision with a surface atom will depend on the relation between the vibrational frequency of the molecule and the collision time (i.e. the projectile velocity). Two extreme cases can be considered: in the limit of a very large bond stiffness of the molecule (i.e. a high vibrational frequency/ a low impact energy) the N_2^+ projectile can be treated as a single particle with twice the mass of a nitrogen atom, while in the limit of a weak bond (at high impact energies) the two nitrogen atoms of the molecule act more

or less independently. In an elastic head-on collision, the maximum energy transferable for a projectile with mass m and kinetic energy E_0 onto a target atom with mass M is given by (cf. equation 2.1):

$$\Delta E = \frac{4m \cdot M}{(m + M)^2} \cdot E_0 \tag{4.9}$$

For a ^{14}N atom of energy E_0 colliding with a ^{184}W target atom this energy transfer amounts to

$$\Delta E_{atom} = 0.263 \cdot E_0 \tag{4.10}$$

In the limiting case that the incident nitrogen molecule can be interpreted as one single rigid particle with a mass of 28 amu and a kinetic energy of $2E_0$, the energy that is transferred to a surface atom is increased to

$$\Delta E_{molecule} = 0.459 \cdot 2E_0 \tag{4.11}$$

or 0.459·E_0 per incident nitrogen constituent. From this simple estimate one finds that at very low impact energies up to 1.7 times more energy per atom can be transferred to a tungsten surface atom by a molecular nitrogen projectile than for atomic nitrogen bombardment. For collision times shorter than half the vibrational period of the N_2 molecule, i.e. for higher kinetic energies, the molecule will behave more like two single atoms and the energy transferred per incident nitrogen atom will become equal for both projectiles.

4.2.3   Summary & Concluding Remarks

Total sputtering yields of polycrystalline tungsten surfaces bombarded by molecular and atomic nitrogen ions were presented. The obtained yields are in good overall agreement with data from the literature. When comparing the molecular with the atomic sputtering yield at projectile energies below 1000 eV per nitrogen atom, however, it was found that the sputtering yield per nitrogen atom under impact of N_2^+ ions is approximately 25% higher than that of two equally fast N^+ ions. This molecular effect can be explained qualitatively with an energy transfer model assuming an effective mass for the molecular projectile, which depends on the time scale of the molecular vibration as compared to the collisional interaction.

Katharina Dobeš

4.3 Interaction of Seeding Gas Ions with Nitrogen Saturated Tungsten Surfaces

Part of the following is being published in [210].

Carbon is increasingly being replaced by metallic plasma facing components in fusion machines. On the one hand, its chemical reactivity with hydrogen isotopes results in unacceptably high erosion rates due to chemical sputtering (cf. section 2.2.1), which ultimately limits the lifetime of carbon containing materials in a fusion reactor vessel. On the other hand the formation of hydrogenated carbon layers by co-deposition of carbon impurities with hydrogen isotopes throughout the fusion machine (cf. section 2.2.2) would drive the tritium inventory in the vacuum chamber beyond operation limits within only a comparably small number of discharges [29].

The transition to all-metal machines however, involves dismissing the benign cooling effect of radiating carbon species in the plasma edge (cf. section 2.2 and figure 2.6). To mitigate the heat loads to plasma facing components by radiative power dissipation, it will therefore be necessary to replace intrinsic carbon impurities by the injection of seeding gases. Potential seeding species (cf. figure 2.6) involve noble gases like argon or neon but also nitrogen, which has proven to be a valuable substitute for carbon in the divertor region [38]. In ASDEX Upgrade nitrogen seeding with power feedback has already matured into a standard operational scenario [38].

The erosion of high Z plasma facing components will be dominated by these externally seeded impurity species (cf. p. 17) [40]. Moreover, implantation of nitrogen into the plasma facing materials will result in a dynamic modification of the surface structure and composition during the operation of the fusion reactor (cf. section 2.2.3). Mixing of materials might severely influence physical properties of the plasma facing components, such as the sputtering yield, the melting point or the electrical and thermal conductivity. It is therefore of fundamental interest to fusion research to study the formation and the properties of such multi-component surfaces.

In a recent study by K. Schmid et al. it was found that for high fluences of energetic nitrogen ions impinging onto tungsten surfaces, a tungsten-nitride surface layer is developed within the ion penetration depth [66]. Dynamic equilibrium conditions for the surface composition are established, after the removal of a surface layer with a thickness of the order of the ion range. The authors also report that

Katharina Dobeš

due to the accumulation of nitrogen in the surface, the partial tungsten sputtering yield is reduced as compared to sputtering of a pure tungsten surface. From this point of view the formation of tungsten nitride mixed material layers in a fusion reactor could in fact be beneficial by decreasing the tungsten impurity release into the plasma.

It was also found [211] that the resistivity of tungsten nitride films varies with the deposition conditions. It increases with the nitrogen content in the surface and can be as high as 3000 - 5000 $\mu\Omega\cdot$cm for as-deposited, nitrogen rich films. While for conducting targets the sputtering yield generally only depends on the kinetic energy of the projectile [89, 90], a pronounced enhancement of the erosion rate with the charge state of the impinging ion, i.e. so-called potential sputtering ([83] and references therein) was found for some insulating and semi-conducting targets (cf. section 2.2.1), like alkali halides [87, 93], oxides [89, 94] and also hydrocarbon surfaces [95]. As already outlined in section 2.2.1 potential sputtering is mainly observed for target materials with a strong electron-phonon coupling, where the electronic excitation, which is introduced into the surface by the deposition of the potential energy (i.e. the sum of the ionization energies) of the highly charged ion during surface impact, can efficiently be converted into motion of target atoms.

In a fusion reactor, elevated sputtering yields of nitrogen containing wall material due to potential sputtering by highly charged impurity ion impact, would give rise to undesirably enhanced wall erosion rates and core plasma contamination by high Z impurities. The study presented in this section therefore aims at testing whether nitrogen saturated tungsten surfaces are prone to potential sputtering under subsequent impact of highly charged noble gas species such as argon or neon (Ar^{q+} and Ne^{q+}, respectively), which are both considered to be used as seeding impurities in future fusion reactors like ITER. The presented study was conducted under controlled laboratory conditions, which enables an investigation of the sputtering yield for mono-energetic particle impact of a single ion species with a well-defined charge state.

4.3.1 Experimental Results & Discussion

Total sputtering yields of a tungsten nitride surface under the impact of seeding ions were determined using the highly sensitive quartz crystal microbalance technique introduced in section 3.1 at the ECR ion source facility in 3.1.3. The experiments were conducted at a base pressure on the low 10^{-10} mbar regime in the UHV chamber and at an elevated target temperature of 465 K. The beam facing side of the quartz crystal is coated with a 500 nm thick, polycrystalline tungsten film

Katharina Dobeš

(cf. section 3.1.5), which is deposited onto one of the gold electrodes by vapor deposition in a separate preparation chamber and transferred to the experimental chamber ex vacuo. The total mass change of the target film is determined from a change of the resonance frequency of the quartz according to equation 3.4.

N^+. Ar^{q+} and Ne^{q+} ions (q = 1 - 9) are produced in the ion source SOPHIE at the ion beam facility in Vienna (cf. section 3.1.3). The ion current density impinging onto the sample is determined by means of a faraday cup, which is located at at a given distance above the quartz crystal on the sample holder (cf. figure 3.2). Ion current measurements are conducted before and after each sputtering yield measurement.
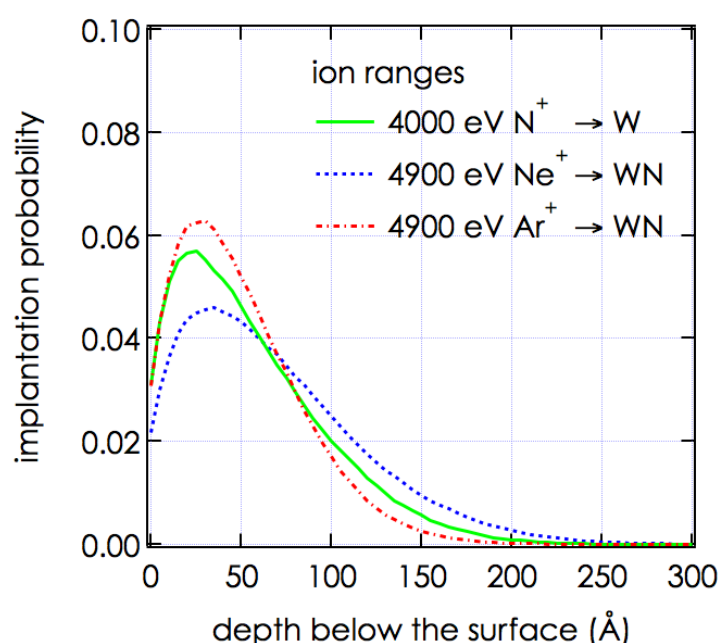
Figure 4.13: Ion ranges of the highest utilized projectile energies as obtained from static TRIDYN [58] simulations. The range of nitrogen projectiles in a pure tungsten surface is compared to the range of argon and neon projectiles in a tungsten nitride surface at the highest energy, which was used in the sputtering experiments.

Nitrogen saturated tungsten surfaces are prepared by implanting energetic nitrogen ions into a freshly deposited tungsten surface. The nitrogen impact energy and the saturation fluence were chosen such, as to ensure that the Ar^{q+} and Ne^{q+} projectiles used in the subsequent investigations, predominantly interact with the nitrogen saturated surface layer along their path through the surface.

Katharina Dobeš

For this purpose ion ranges of all three projectiles were estimated with the Monte Carlo code TRIDYN [58]. TRIDYN is in principle capable of also considering compositional changes of the surface, resulting from the applied projectile fluence (cf. section 3.4). For estimating the projectile ranges however, static simulations were performed in this case, i.e. any compositional changes of the surface were suppressed. The implantation profile of nitrogen was estimated for a pure tungsten surface; ranges of neon and argon were determined on the resulting tungsten nitride surface. For this purpose an atomic fraction of W/N=1 was assumed in the calculations, which is in accordance with the surface composition found in the studies by Schmid et al. [66]. The surface binding energy of both, the simulated tungsten and the tungsten nitride surface was set to the value generally used for pure tungsten, i.e. 8.68 eV [191]. The entire set of input parameters used in the simulations is summarized in table 3.3.

The energy of the nitrogen ions, which were used for saturating the tungsten surface, was adapted with respect to obtaining a similar nitrogen implantation profile as compared to the ion range profiles of the noble gas ions (argon and neon) at the highest energy subsequently investigated in the sputtering experiments. Consequently a N^+ ion impact energy of 4000 eV was chosen and the sputtering investigations for neon and argon projectile ions were conducted only below an impact energy of 4900 eV. In figure 4.13 the implantation profile as obtained from TRIDYN of 4000 eV N^+ ions in tungsten (in green) is compared to the profiles of Ar+ (in red) and Ne+ (in blue) in a tungsten nitride surface at the highest investigated impact energy of 4900 eV.

For obtaining a nitrogen saturated tungsten nitride surface, the nitrogen irradiation was continued up to a cumulated ion fluence of ~ $3.5 \cdot 10^{17}$ N per cm^2. The mass change of the tungsten surface under ion impact was monitored throughout the entire saturation process. With increasing ion fluence, the QCM detected a minor decrease in the total mass removal rate. Nitrogen bombardment was stopped after an integrated surface recession of approximately 70 Å, which clearly exceeds the mean ion range in the surface as estimated by TRIDYN (cf. figure 4.13). By this it was ensured that nitrogen saturation conditions were obtained.

Surface erosion under the impact of argon ions of various charge states (q = 1 - 9) was determined for both, a pure tungsten as well as a tungsten nitride surface. The experimental results are shown in figures 4.14 and 4.15, respectively. The depicted sputtering yields were obtained in a sequence from high to low impact energies. Thereby the ion range in the surface was gradually decreased in the course of the investigations, which was done in order to keep the compositional changes induced by preceding ion bombardment at a minimum for all investigated ion en-
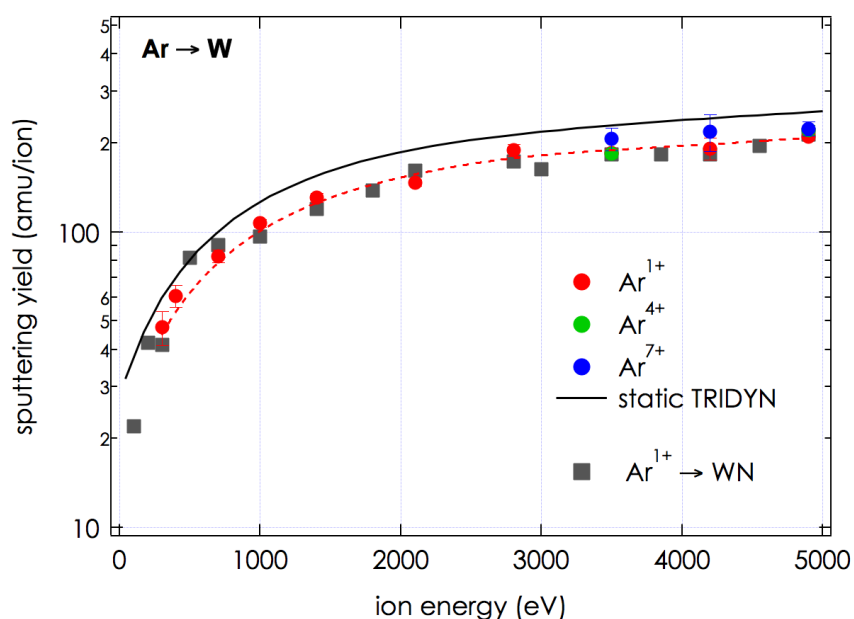
Figure 4.14: Sputtering yield of a pure tungsten surface under Ar^{q+} (q = 1- 7) ion impact as a function of the ion energy. Within the given error bars, no dependency of the sputtering yield on the charge state of the ion is found. The data compare well with a static TRIDYN simulation for the sputtering of pure tungsten (black solid line). In addition total sputtering yields obtained on a nitrogen saturated tungsten nitride surface (grey squares) are also shown for comparison.

ergies. The total argon fluence applied to the tungsten nitride surface remained below $1.8 \cdot 10^{15}$ ions per cm^2, which resulted in a cumulative surface recession of less than 1.5 Å. Therefore, from a comparison with the nitrogen implantation profile used for saturating the surface (cf. figure 4.13), the conclusion can be drawn that the influence of the argon ion bombardment on the composition of the surface should be comparably small.

Neither for the pure tungsten surface, nor for the tungsten nitride surface a dependency of the sputtering yield on the charge state of the impinging projectile is found within the experimental accuracy. In figures 4.14 and 4.15, TRIDYN results for the total sputtering yields (including both the partial sputtering yield of nitrogen and tungsten from the surface) are also included (black solid line). They compare well with the experimental results in both cases. It is therefore concluded that kinetic sputtering is by far the dominant contribution to the erosion yield, while po-
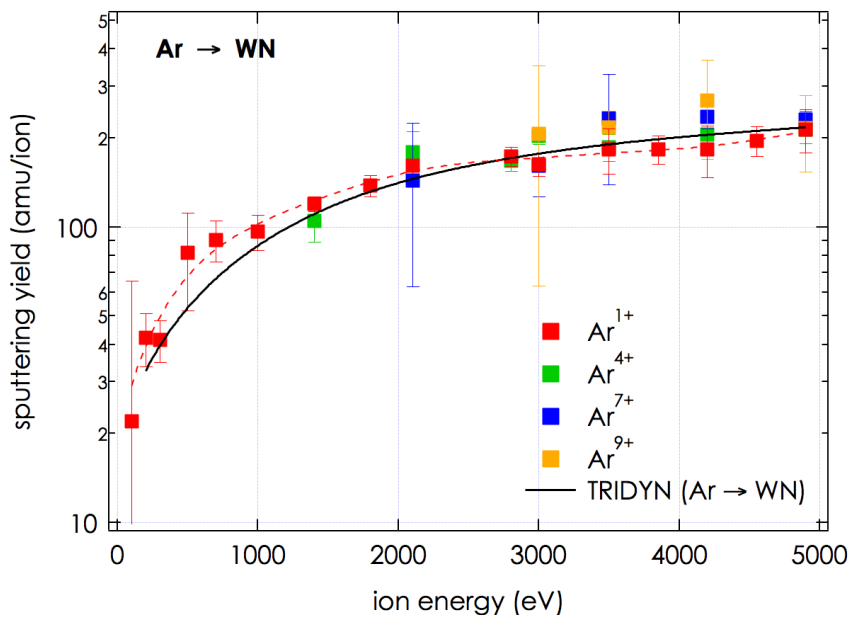
Figure 4.15: Sputtering yield of a nitrogen saturated tungsten nitride surface under Ar^{q+} (q = 1-9) ion impact as a function of the ion energy. Within the given error bars, no dependency of the sputtering yield on the charge state of the ion is found. The data compare well with a static TRIDYN simulation of the total sputtering yield (i.e. partial sputtering yield of tungsten and nitrogen combined) of a W/N = 1 tungsten nitride surface (black solid line).

tential sputtering mechanisms are negligible even in the case of tungsten nitride surfaces.

For direct comparison of the total yield of the tungsten surface with sputtering from tungsten nitride, the sputtering yield data obtained for Ar^+ impact on the tungsten nitride surface is also included in figure 4.14. There is no substantial difference in the total sputtering yields of the two surfaces. The reduction of the mass removal rate due to a decrease of the partial sputtering yield of tungsten from the tungsten nitride surface, is apparently overall balanced by nitrogen erosion from the surface. This is supported by the observation that the erosion rate of the surface barely changed during the entire nitrogen saturation process.

Similar investigations were conducted for the impact of neon on tungsten nitride. The experimental results are shown in figure 4.16. In this case, a possible charge state dependency of the sputtering yield was only tested for one single impact energy, where again no difference for sputtering by Ne^{4+} compared to

Katharina Dobeš
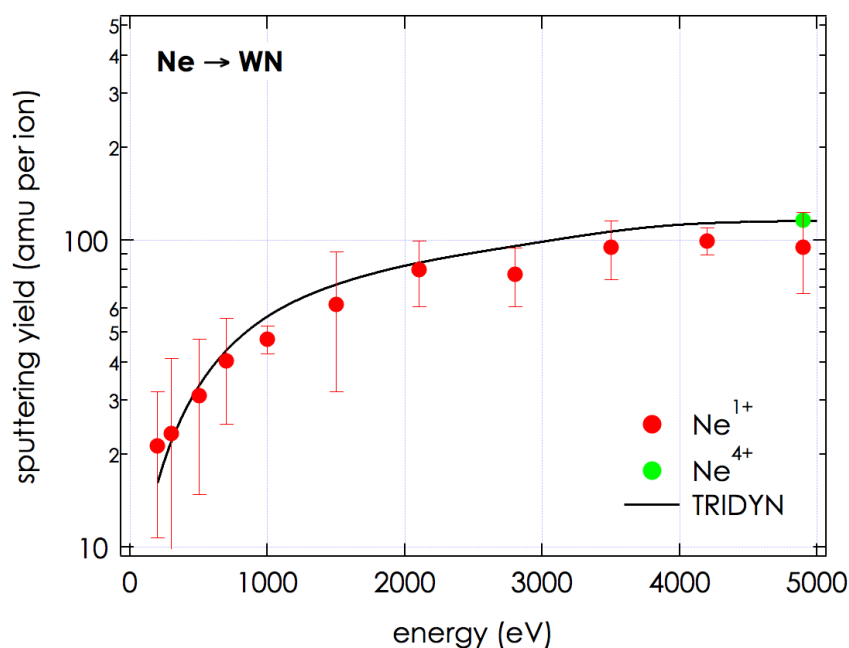
Figure 4.16: Sputtering yield of a nitrogen saturated tungsten nitride surface under Ne⁺ ion impact as a function of the ion energy. For reference the sputtering yield of a neon ion with charge state q = 4 is also shown. Again, no dependency of the sputtering yield on the charge state of the ion is found. The experimental data are compared to a static TRIDYN simulation of the total sputtering yield (i.e. partial sputtering yield of tungsten and nitrogen combined) of a W/N = 1 tungsten nitride surface (black solid line).

Ne⁺ impact was found. The total sputtering yield of the tungsten nitride surface due to neon impact is generally smaller than under argon impact, as can be expected from the purely kinetic nature of the sputtering process and the less efficient energy transfer in a binary collision of neon projectiles with the much heavier tungsten atoms.

4.3.2   Summary & Concluding Remarks

Sputtering of tungsten and tungsten nitride surfaces was investigated for seeding impurity ion impact (i.e. argon and neon). The observed sputtering yields were found to be independent of the charge state of the projectiles for both surfaces. From this, no enhancement of wall erosion rates in fusion machines due to potential sputtering of nitrogen saturated tungsten surfaces has to be expected. In

previous studies [211] it was found however that for tungsten nitride surfaces the electrical conductivity, which is a determinant factor in the occurrence of potential sputtering, depends on the deposition conditions. The absence of potential sputtering in a fusion machine might therefore still depend on parameters like the wall temperature, the nitrogen impact energy and generally the actual nitrogen content in mixed, nitrogen tungsten surfaces in a future fusion reactor.

Erosion of tungsten nitride surfaces was found to be smaller for neon impact than for argon impact, as can be expected from the purely kinetic nature of the sputtering process. Additionally the total sputtering yield of tungsten nitride surfaces is found to be comparable to the sputtering yield of pure tungsten, with nitrogen erosion apparently balancing the reduction of the partial tungsten sputtering yield. This on the other hand means that the release of tungsten from tungsten nitride is decreased compared to erosion of pure tungsten, which is in agreement with the results reported in [66].

4.4 Erosion of Beryllium under Nitrogen Impact - Investigations of Transient and Steady State Conditions

The largest part of the vacuum vessel wall of the fusion experimental reactor ITER, will be covered by beryllium (cf. section 2.2). Beryllium is chosen as a plasma facing material in fusion research primarily due to its low atomic number Z. Compared to e.g. tungsten, the energy loss from the plasma by radiating beryllium species is comparably small and hence the maximum tolerable beryllium concentration in the plasma core is of the order of several percent compared to only about 10^{-5} for tungsten [20]. In addition beryllium is an excellent oxygen getter material and will thereby aid in improving the vacuum conditions in the fusion reactor vessel.

As carbon is increasingly replaced as a plasma facing component in today's fusion experiments, the benign cooling effect of intrinsic carbon impurities by radiative power dissipation in the divertor region and the plasma edge is being dismissed. To keep the heat load to the plasma facing components below the maximum acceptable limit, it will be necessary to introduce additional seeding impurities into the plasma edge. Among such seeding gases, nitrogen is strongly favored due to its comparably high radiative characteristics at low electron temperatures [37] which is responsible for its capability of replacing the radiating carbon species in the divertor region of the tokamak (cf. section 2.2). Nitrogen seeding is already successfully implemented in today's fusion experiments such as ASDEX Upgrade [34] and JET [212].

With the introduction of nitrogen into the fusion plasma vessel, the formation of nitrogen containing mixed material layers is expected. Dynamic implantation of nitrogen in the vessel walls or co-deposition with eroded species will result in a modification of the surface structure and composition of plasma facing materials during the operation of a fusion reactor. The formation of such mixed material layers might have a severe influence on surface properties such as the melting point of the material, its thermal as well as electrical conductivity, its erosion rate, the plasma control due to recycling of implanted species and also the fuel retention and release behavior.

When bombarding a beryllium surface with energetic nitrogen ions, Oberkofler and co-workers [67] recently observed the formation of a beryllium nitride phase within the ion penetration depth (cf. figure 4.17). They report that the amount of retained nitrogen increases with applied nitrogen fluence and saturates at a fluence, at which a surface layer with a thickness of the order of the projectile penetration depth is eroded. In accordance with this, a pronounced beryllium ni-
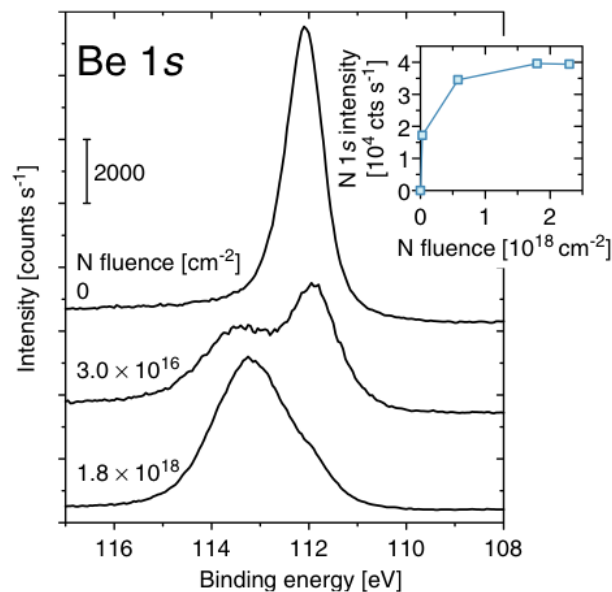
Figure 4.17: XPS spectra of a beryllium surface after different fluences of nitrogen to the surface. The inset shows the saturation of the integrated N 1s intensity as a function of the fluence. Picture from [67].

tride peak appears in the x-ray photoelectron spectra of the surface, which grows in intensity with the surface nitrogen content, whereas the metallic beryllium peak is increasingly attenuated. The integrated atomic nitrogen fraction of the corresponding XPS peaks points to the formation of a stoichiometric Be_3N_2 compound within the ion penetration depth.

In this section, investigations on the interaction of energetic nitrogen projectiles with beryllium surfaces will be presented. The experiments were performed under controlled laboratory conditions. For a better understanding of the interaction and mixing dynamics of beryllium surfaces with nitrogen projectiles, a mono-energetic nitrogen N_2^+ ion beam was used. Total mass changes of the beryllium surface were investigated using the quartz crystal microbalance technique presented in section 3.1, providing a unique in real time insight into the transient saturation dynamics of the surface. It shall be stressed here that the applied experimental approach is restricted to observing total mass changes, i.e. that only the balance between any simultaneous mass loss (e.g. erosion) and mass increase (e.g. implantation of projectiles) can be observed.

Apart from the transient saturation behavior of the beryllium surface under nitrogen impact (see section 4.4.1), erosion under dynamic equilibrium conditions

Katharina Dobeš

was also investigated (cf. section 4.4.2). Additionally the influence of the nitrogen saturation level on the oxidation behavior of the surface was studied (see section 4.4.3).

As dealing with highly toxic beryllium samples requires special safety precautions, the experimental investigations presented in this section were performed at IPP Garching instead of TU Vienna. The beryllium samples were provided by C. Lungus group from Bucharest. 500 nm thick beryllium layers were deposited at an elevated temperature of 200°C in a pure beryllium vapor discharge by a thermionic vacuum arc deposition technique (cf. section 3.1.5) [176]. The beryllium samples exhibit a native oxide surface layer, which builds during transport and storage in air. Apart from this, x-ray photoelectron spectroscopy measurements performed on the virgin samples also revealed some carbon contamination of the surface.

The projectile ions used in the presented studies were produced in an electron impact ion source (SPECS IQE 12/38, cf. section 3.1.3). The ion source is equipped with a Wien filter, which is used to select the molecular fraction of the ion beam. The projectiles are extracted from the ion source in an energy range between 375 eV and 2.5 keV per constituent nitrogen atom. An ion optics is used to deflect and focus the ion beam onto the quartz crystal's position in the experimental ultra high vacuum chamber. The experiments were performed at a residual gas pressure in the low 10^{-9} mbar regime. The ion current density impinging onto the sample is frequently determined in between ion beam exposure of the surface by means of the Faraday cup, installed on the sample holder (cf. figure 3.2). The quartz crystal was always kept at 460 K, both during as well as in between experiments, to minimize the influence of temperature fluctuations due to the ion impact on the resonance frequency of the quartz and consequently on the sensitivity of the setup.

4.4.1 Nitrogen Saturation

The transient saturation behavior of a beryllium surface under nitrogen impact was investigated for the impact of N_2^+ projectiles at an energy of 2500 eV per nitrogen constituent (i.e. 5000 eV per projectile ion). In figure 4.18 the evolution of the observed quartz resonance frequency, Δf (left), and the corresponding total mass change rate $\Delta m/\Delta\Phi$ (right), are shown as a function of the applied nitrogen fluence.

The curve in figure 4.18 summarizes the nitrogen saturation behavior of the beryllium sample from an as-received to a nitrogen saturated surface, with a steady
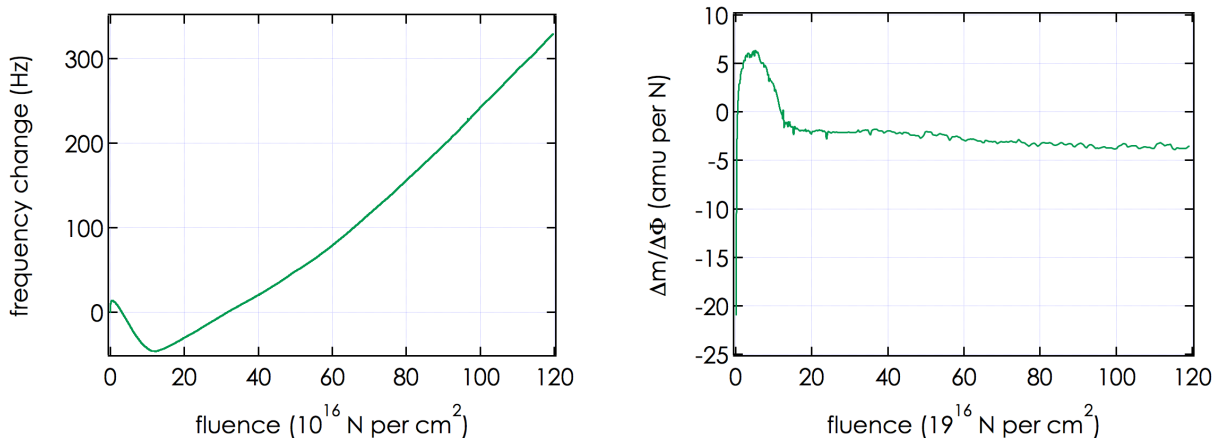
Figure 4.18: Evolution of the quartz frequency (left graph) and resultant total mass change rate (right) observed when saturating a virgin beryllium surface with N_2^+ ions at an impact energy of 5000 eV (i.e. 2500 eV per N).

state surface composition. Upon close inspection, the saturation curve can be sectioned into four different sub-parts:

1. $\Phi \lesssim 4 \cdot 10^{15}$ N/cm² an initially very pronounced mass removal rate, which slows down quickly with increasing fluence.

2. $4 \cdot 10^{15} \lesssim \Phi \lesssim 1.2 \cdot 10^{17}$ N/cm² a regime of net mass increase (i.e. positive Δm).

3. $1.2 \cdot 10^{17} \lesssim \Phi \lesssim 8.3 \cdot 10^{17}$ N/cm² a regime of net mass loss, where the erosion rate still changes with the ion fluence (i.e. negative Δm).

4. $\Phi \gtrsim 8.3 \cdot 10^{17}$ N/cm² steady state erosion, where the observed erosion rate furthermore remains constant with increasing ion fluence.

The total observed mass change rate represents the balance of different processes, which occur simultaneously as the surface is bombarded with nitrogen projectiles (cf. section 2.2.3):

Impinging nitrogen projectiles are implanted at their ion penetration depth. Generally it can be expected that the diffusivity of implanted projectiles is low and that most of them will hence remain at the depth at which they come to rest in the surface. With increasing projectile fluence, this will result in the built-up of a nitrogen containing mixed material layer at the ion penetration depth.

Katharina Dobeš

In addition material is simultaneously eroded from the surface. As the projectile concentration in the surface increases with applied ion fluence, both the implanted nitrogen atoms as well as the beryllium substrate will be sputtered. The partial sputtering yield of the two species will depend on their individual near surface concentrations (Θ_N^s and Θ_{Be}^s respectively), since eroded particles predominantly originate from only within a very shallow sub-surface region (cf. section 2.2.1). As the surface is gradually eroded, the mixed material layer is increasingly shifted towards the vacuum-surface interface and implanted nitrogen projectiles will emerge into the near surface zone, from which sputtered atoms originate. This will result in an increased partial nitrogen sputtering yield. Eventually, after a surface layer presumably with a thickness of the order of the ion penetration depth has been eroded, dynamic equilibrium conditions for simultaneous nitrogen erosion and implantation are established. At this point the total amount of retained nitrogen saturates and additional ion bombardment has no further effect on the surface composition. The above-sketched interaction scheme is in fact reflected in the observed evolution of the mass change rate (cf. figure 4.18) as will be discussed in the following.

Removal of Loosely Bound Surface Adsorbates ($\Phi \lesssim 4 \cdot 10^{15}$ N/cm^2)

Initially a very efficient mass removal is observed, which decreases rapidly with applied ion fluence. This can be attributed to the removal of loosely bound surface adsorbates from the fresh, un-irradiated surface. X-ray photoelectron spectroscopy investigations performed on a comparable, virgin beryllium sample suggest that initially the surface is covered by some carbon contamination and a native beryllium-oxide layer, originating from the storage of the samples in air between their production and the installation in the experimental UHV chamber. The corresponding XPS data is shown in figure 4.19.

A rough estimate of the adsorbate coverage of the surface can be deduced from a closer inspection of the initially observed mass change rate. This is shown in figure 4.20, where the adsorbate coverage is inferred from the respective mass change rate at the very beginning of the ion bombardment (left graph) and from a TRIDYN simulation of the initial sputtering behavior (right graph).

The shape of the mass change rate initially resembles an exponential function. This is most obvious when plotting the logarithm of the mass loss rate vs. the applied nitrogen fluence, as it has been done in figure 4.20 (left). ln ($\Delta m/\Delta \Phi$) is linearly dependent on the applied fluence Φ, suggesting that the observed process is a
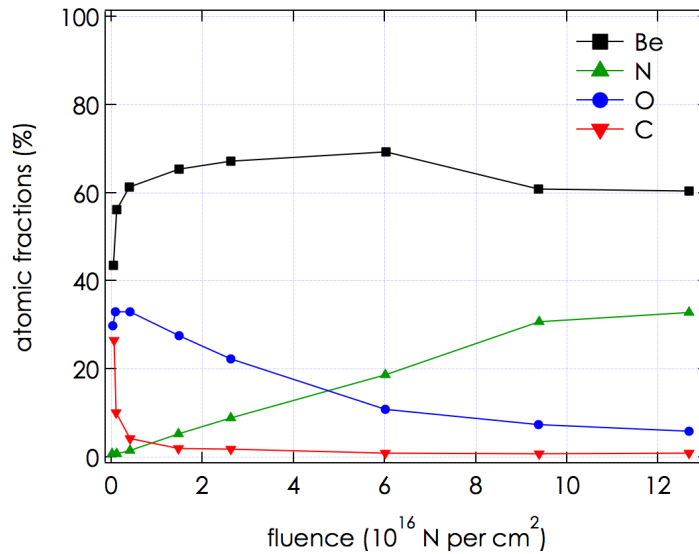
Figure 4.19: Atomic concentrations of beryllium, nitrogen, oxygen and carbon on the surface of an as-received beryllium sample as determined by XPS [213]

first order reaction, i.e. that to a first approximation the removal rate $Y(\Phi)$ is proportional to the adsorbate surface coverage Θ:

$$Y(\Phi) = \frac{d\Theta}{d\Phi} = \Gamma\Theta \tag{4.12}$$

if Γ is a rate coefficient for the respective sputtering process. This results in an exponential dependency of the form:

$$Y(\Phi) = \frac{\Delta m}{\Delta\Phi} = Y_0 \cdot e^{-\Gamma\Phi} \tag{4.13}$$

and correspondingly:

$$\Theta = \Theta_0 \cdot e^{-\Gamma\Phi} \tag{4.14}$$

From a linear fit of the curve in figure 4.20, the initial adsobrate coverage Θ_0 can then be estimated:

$$\Theta_0 \sim 8.5 \cdot 10^{16} \text{ amu per cm}^2$$

which corresponds to e.g. $\sim$ 2 monolayers of a typical beryllium oxide coverage. Within the above approach, the curve trend in figure 4.20 has to be extrapolated over a comparably wide range (cf. dotted line in figure 4.20), which gives rise to

Katharina Dobeš
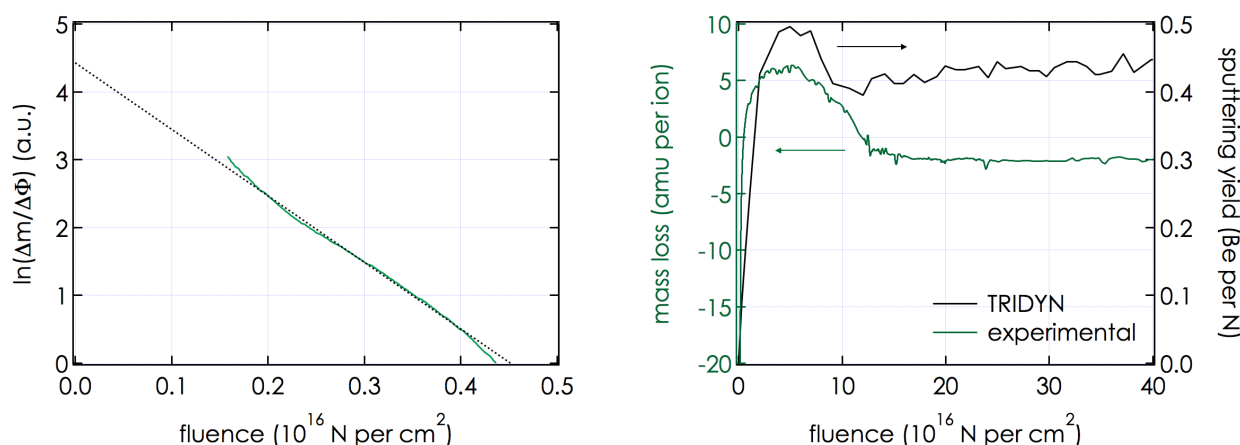
Figure 4.20: The adsorbate coverage can be estimated either from the observed erosion rate (left) by fitting a first order reaction, or from a TRIDYN simulation (right) with a layered structure of a 3 Å carbon layer and 3 nm of beryllium oxide on top of the beryllium bulk.

quite some uncertainty in the evaluation of Θ_0. This is why the resulting value should only serve as a rough estimate.

The above estimation is however supported by a TRIDYN [58, 186] simulation for the evolution of the partial sputtering yield of beryllium from the surface (see figure 4.20, right). In this simulation the surface is approximated by a layered structure of 3 Å of carbon on top of a 3 nm thick beryllium-oxide layer covering the beryllium bulk. The general input parameters used in the TRIDYN simulation are summarized in table 3.3. In the right graph of figure 4.20, the total mass change observed in the measurement (in green) is compared to the beryllium sputtering yield (in black) as obtained from TRIDYN. The shape of the simulated sputtering yield as a function of the applied nitrogen fluence, resembles the measured data very nicely, implying that such a surface coverage could in fact be a reasonable estimate for the actual initial surface composition.

Implantation Dominated Regime ($4 \cdot 10^{15} \lesssim \Phi \lesssim 1.2 \cdot 10^{17}$ N/cm^2)

Following this initially very efficient mass removal, a regime of net mass increase is observed for a nitrogen fluence ranging from $\Phi \sim 4 \cdot 10^{15}$ to $\Phi \sim 1.2 \cdot 10^{17}$ N per cm^2 (cf. figure 4.18). In the balance of nitrogen implantation (Y_{imp}) and simultaneous surface erosion of both, implanted projectiles and the beryllium substrate (Y_N and

Y_{Be}, respectively) the mass increase rate due to implantation initially exceeds the total sputtering yield, i.e.:

$$Y_{imp} > Y_{Be} + Y_N \qquad (4.15)$$

From a static TRIDYN simulation the implantation probability $n(x)$ of the nitrogen projectiles in the beryllium surface, i.e. the depth below the surface at which the nitrogen containing, mixed material layer is formed, can be estimated. The obtained implantation probability $n(x)$ is shown in figure 4.21. From the maximum of the resulting range profile, it can be expected that the nitrogen content in the surface will peak at a depth below the surface of about ~ 86.5 Å .
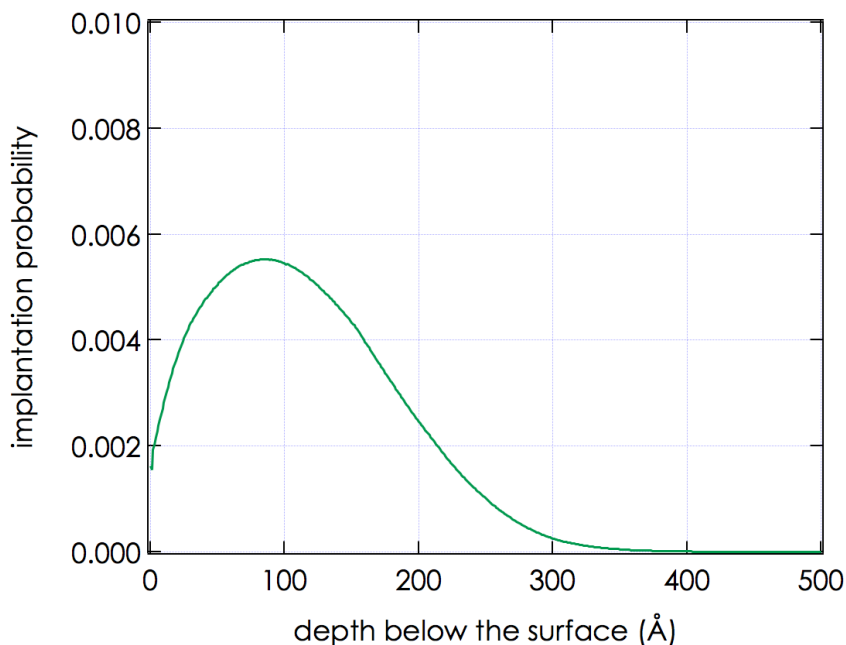
Figure 4.21: Nitrogen range in beryllium at 2500 eV impact energy obtained from TRIDYN. The most probable range of the projectiles is ~ 86.5 Å.

Upon closer inspection it is found that initially in the balance of nitrogen implantation and surface erosion, the observed mass increase is about constant over a rather large fluence interval. While this is not so obvious from the trend of the curve in figure 4.18, it becomes much more clear when taking a look at the cumulative mass change Δm, i.e. the integrated mass change rate, which is shown in figure 4.22. For fluences $\lesssim 7.6 \cdot 10^{16}$, it is found that the cumulated mass change is linearly proportional to the applied ion fluence, i.e. increases at a constant rate with applied fluence. Neglecting any simultaneous mass loss due to surface erosion,

Katharina Dobeš
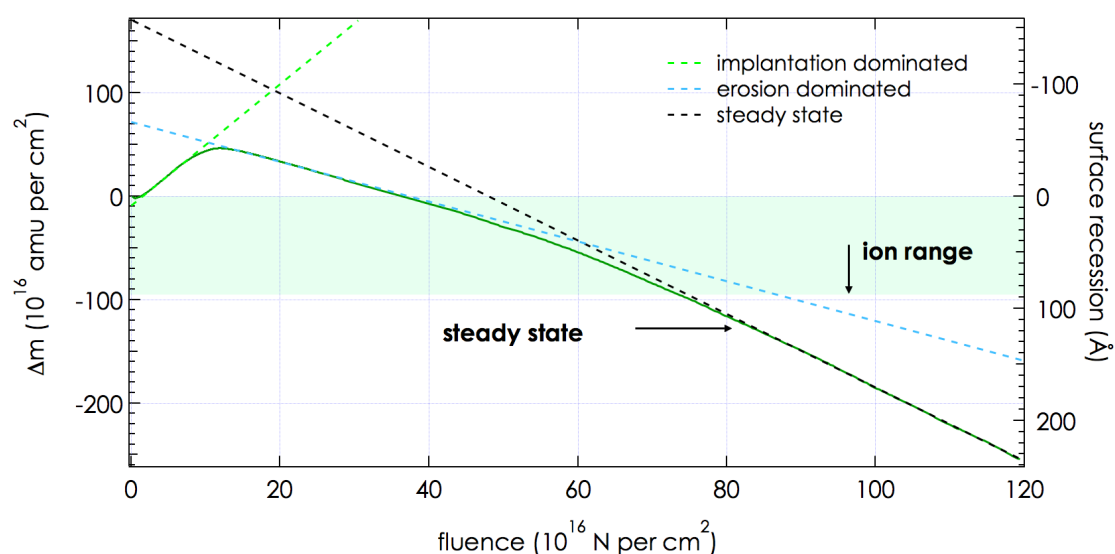
Figure 4.22: Cumulative mass change Δm and corresponding surface recession during nitrogen saturation of a beryllium surface as a function of the applied nitrogen fluence. For low fluences the mass change is dominated by projectile implantation (green dashed line). In the sputtering dominated regime two fluence intervals of about constant mass loss are observed (blue and black dashed lines, respectively). The ion range as estimated by TRIDYN is also indicated (shaded area). For details see text.

a lower estimate for the initial implantation probability can be deduced from the slope of the corresponding linear fit to the experimental data (as demonstrated by the green dashed line in figure 4.22), i.e. $Y_{imp}^0 \gtrsim 40\%$.

The actual implantation probability is however concealed by the simultaneous mass loss due to surface erosion and will in fact be higher. For a more accurate estimation of Y_{imp}^0, the total surface erosion rate ($Y = Y_N + Y_{Be}$) has to be included. Since implanted nitrogen projectiles predominantly accumulate at a depth well below the surface (see figure 4.21), it can be assumed that initially, the erosion of retained nitrogen does not substantially contribute to the total sputtering yield, i.e. $Y_N^0 \sim 0$. To a first approximation only sputtering of beryllium atoms has to be considered.

The corresponding sputtering yield, Y_{Be}^0, can be deduced from the mass loss rate observed in steady state, i.e. when finally nitrogen implantation exactly balances nitrogen erosion and the nitrogen surface content does not change anymore. In this case the observed surface erosion rate is solely due to beryllium sput-

Katharina Dobeš

tering, i.e. $Y^\infty \equiv Y_{Be}^\infty$. It has to be taken into account though, that at this point the surface is composed of both nitrogen and beryllium, which ultimately reduces the availability of beryllium and consequently its partial sputtering yield. For a constant beryllium erosion rate Γ_{Be} the observed beryllium sputtering yield however depends on its surface concentration Θ_{Be}^s according to the simple relation:

$$Y_{Be}(\Theta) = \Gamma_{Be}\Theta_{Be}^s(\Phi) \tag{4.16}$$

Consequently the initial beryllium sputtering yield can be estimated from the steady state sputtering yield by scaling it with an appropriate beryllium surface concentration $\Theta_{Be}^s(\Phi_{eq})$. In accordance with previous investigations [67] for the interaction of nitrogen projectiles with beryllium surfaces, $\Theta_{Be}^s(\Phi_{eq})$ is approximated by the atomic nitrogen concentration of a stoichiometric beryllium-nitride Be_3N_2 compound, i.e. $\Theta_{Be}^\infty \sim 0.6$. From this a more realistic initial implantation probability is obtained, i.e.

$$Y_{imp}^0 \sim 84\%$$

Erosion Dominated Regime ($\Phi \gtrsim 1.2 \cdot 10^{17}$ N/cm^2)

Eventually the local nitrogen saturation concentration is reached and additional nitrogen projectiles are implanted less efficiently into the beryllium substrate. Excess nitrogen projectiles are re-emitted from the surface. At some point the mass increase due to projectile implantation is then outbalanced by the erosion of the surface. In the experiment this is reflected by a transition to a regime of net mass removal for fluences $\gtrsim 7.6 \cdot 10^{16}$, which can be seen both in figure 4.18 as well as 4.22.

A dynamic TRIDYN simulation has been performed in order to verify the above-sketched implantation characteristics. A summary of the utilized TRIDYN input parameters is given in table 3.3. It is assumed that the maximum nitrogen content in the surface is restricted to 40%, i.e. to a concentration according to stoichiometric beryllium-nitride. The dependency of the resulting retained atomic nitrogen fraction on the applied nitrogen fluence is shown in figure 4.23. Initially the implantation probability is 1, i.e. essentially all impinging projectiles are retained. At a fluence of approximately $1 \cdot 10^{17}$ nitrogen atoms per cm^2, the nitrogen saturation concentration is reached, which results in a drastic reduction of the retained atomic fraction to approximately $Y_{imp}^\infty \sim 18\%$.

In comparison with the experimental data, TRIDYN is capable of reproducing the fluence at which local nitrogen saturation is reached, very accurately. The
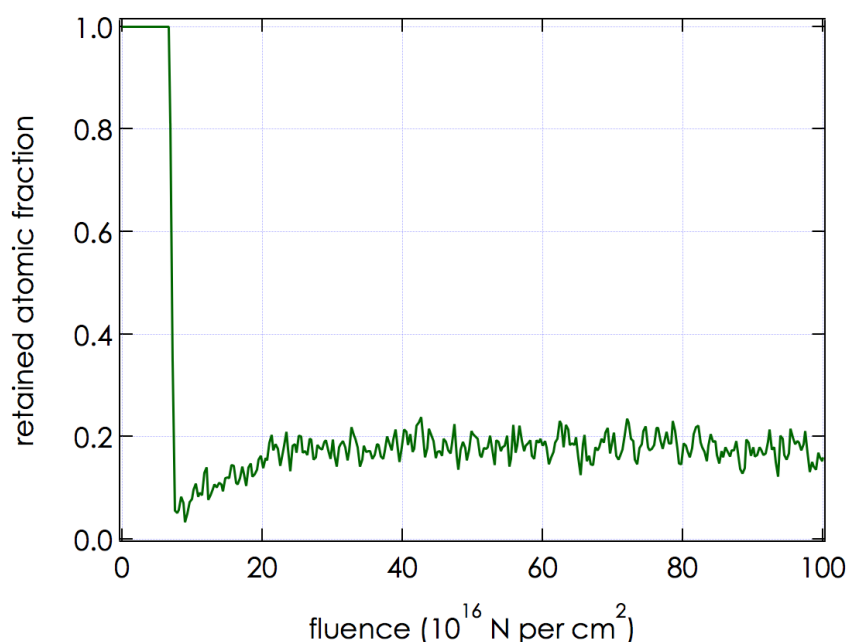
Figure 4.23: Results of a dynamic TRIDYN simulation for the fraction of retained nitrogen projectiles as a function of the applied ion fluence. Initially all nitrogen projectiles are implanted. At a fluence of $\sim 1 \cdot 10^{17}$ N per cm^2 local saturation sets in, which reduces the implantation probability to about 18%.

predicted implantation probability of initially 100%, is however slightly higher than what is expected from the experimental data (i.e. ~84%, see above). However, TRIDYN only simulates the slowing down of the projectile and the equilibration of the initiated collision cascade and therefore only considers the kinetics of the interaction process. Any chemical reaction or compound formation (from beryllium to beryllium nitride in this case) is not included in the simulation, which possibly might be the reason for this discrepancy.

Based on the TRIDYN simulation alone, one would assume that as soon as the nitrogen concentration saturates, dynamic equilibrium conditions are attained too. In the simulation the implantation rate Y_{imp} but also the partial sputtering yields of the involved species (Y_N and Y_{Be}) become constant at this point. From the experimental data (cf. figure 4.22) it is found however, that although the implantation dominated regime is followed by a regime of about constant mass loss (blue dashed fit in figure 4.22), this initially constant erosion rate of approximately $Y_{trans} \sim 2.04$ amu per nitrogen is surpassed by a transition region around a fluence

of roughly $6 \cdot 10^{17}$ nitrogen atoms per cm^2. At this point the observed sputtering yield starts to gradually increase again (the measured curve deviates from the linear fit in figure 4.22). Steady state surface conditions are finally reached only after a total fluence of $8.3 \cdot 10^{17}$ nitrogen atoms per cm^2 have been applied to the surface. The observed sputtering yield becomes constant and from this point onwards does not change anymore with increasing ion fluence (black dashed line in figure 4.22).

In steady state the number of implanted projectiles is exactly balanced by the number of eroded nitrogen atoms ($Y_{imp} = Y_N$). Therefore, the observed erosion rate arises from beryllium sputtering only, i.e.:

$$Y^\infty = Y_{Be}^\infty = 0.4 \text{ Be per N}$$

The nature of the two separate regimes of constant sputtering yield is not entirely clear. In figure 4.24 the experimentally obtained cumulative mass change (in green, cf. figure 4.22) is compared to the mass change as predicted by TRIDYN (in black). The TRIDYN curve combines the simulated mass change rates due to projectile implantation and sputtering of all involved species (beryllium as well as nitrogen). The shape of the two curves in figure 4.24 is similar, but there are some distinct differences. As stated above, TRIDYN would expect a higher initial nitrogen retention rate (Y_{imp}^0), which is reflected in a steeper increase of the mass change in the implantation dominated regime at fluences below $\Phi \lesssim 1 \cdot 10^{17}$ nitrogen projectiles per cm^2. After the nitrogen saturation concentration of 40% has been reached in the implantation zone of the surface, TRIDYN predicts a net surface erosion, with a constant erosion rate of in total $Y^\infty \sim 0.5$ beryllium atoms per nitrogen projectile. In the TRIDYN simulation the transition to net erosion also coincides with achieving steady state surface conditions. Although the steady state sputtering yield obtained from TRIDYN is very similar to the steady state sputtering yield observed at the end of the experimental curve, the intermediate regime of constant erosion succeeding the implantation dominated regime in the experiment, is not reflected in the simulated data.

As the diffusivity of implanted nitrogen projectiles in the beryllium bulk is expected to be small, the nitrogen concentration in the surface will be localized around the ion penetration depth of about ~ 87 Å (cf. $n(x)$ in figure 4.21). This is supported by the observation [67] that upon interaction of energetic nitrogen projectiles with a beryllium surface, the thickness of the resulting beryllium-nitride layer is of the order of the ion penetration depth. In this case a surface layer as thick as the ion range has to be eroded before the nitrogen-rich mixed material layer emerges to the surface and steady state conditions are obtained. From the

Katharina Dobeš
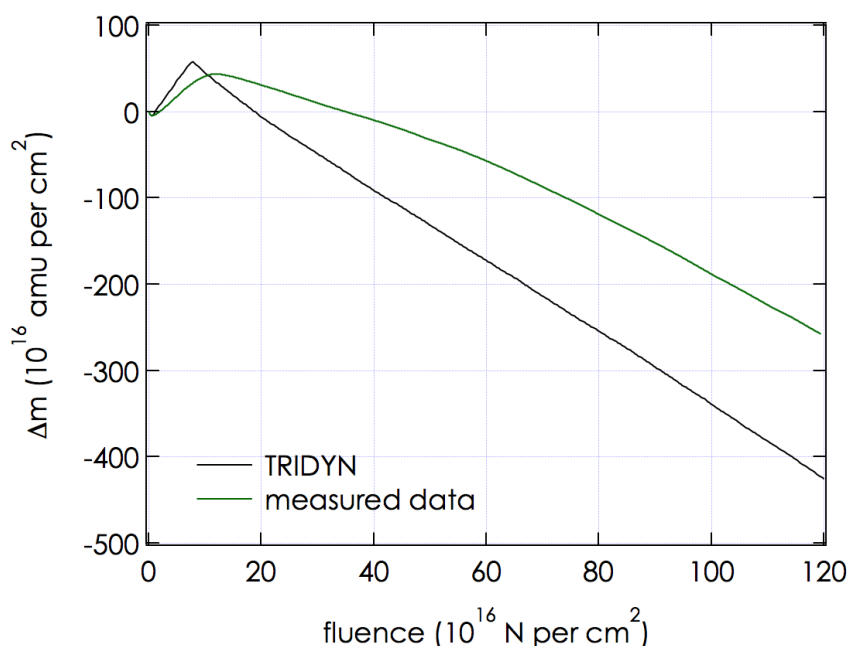
Figure 4.24: Comparison of the cumulative mass change during N saturation obtained from the experiment (green) to results from a TRIDYN simulation (black). The mass change of the TRIDYN curve incorporates erosion of beryllium and nitrogen species as well as projectile implantation.

cumulative mass loss in figure 4.22 and an appropriate value for the surface density, the total surface recession can be estimated. In figure 4.22 the cumulative mass change (left axis) is converted into a surface recession (right axis), using a linear interpolation between the density of beryllium, i.e. $\rho_{Be} \sim 1.8$ g/cm^3, and beryllium nitride for higher fluences, i.e. $\rho_{Be_3N_2} \sim 2.7$ g/cm^3. In order to estimate at which point in the nitrogen saturation curve, a surface layer of the order of the ion penetration depth has been eroded, the ion range as predicted by TRIDYN is also indicated in figure 4.22 by the green shaded area.

According to this estimation, the experimentally observed surface recession exceeds the ion penetration depth of ~ 87 Å only at a fluence of about $7.4 \cdot 10^{17}$ nitrogen projectiles per cm^2, i.e. slightly below the fluence that is needed to obtain steady state surface conditions in the experiment. In this case local nitrogen saturation at the ion penetration depth might indeed be reflected in the experimental data by the transition from net mass gain to net erosion, as at this point the implantation probability is strongly reduced and the erosion of the surface starts to

dominate the observed mass change. It might however take much longer until the resulting nitrogen saturated sub-surface zone is shifted towards the vacuum interface by continuous erosion and finally extends towards the escape depth for sputtered atoms. The about constant total erosion rate, which is observed following local saturation of the nitrogen content, i.e. for fluences $2 \cdot 10^{17} \lesssim \Phi \lesssim 4 \cdot 10^{17}$ N per cm^2, suggests an about constant near surface composition. This probably implies that initially, implanted nitrogen does not contribute much to the total erosion rate as the surface layer from which sputtered particles originate is mainly composed of beryllium. At a fluence of about $4 \cdot 10^{17}$ nitrogen atoms per cm^2 the nitrogen-rich layer finally starts to contribute to the surface erosion and the partial nitrogen sputtering yield gradually increases, which is marked by the observed relatively broad transition region to steady state erosion conditions in figure 4.22. Once the surface recession exceeds the initial ion penetration depth, dynamic equilibrium conditions are obtained and the surface composition within the ion penetration depth becomes constant.

In this simplified picture the three regimes of about constant mass change, which are observed in the experiment (cf. figure 4.22) could then be explained and summarized in the following way: first a constant implantation rate until local saturation is reached (implantation dominated regime), second a constant erosion rate as the nitrogen saturated sub-surface layer does not yet contribute to erosion (erosion dominated regime) and third steady state conditions at which the nitrogen saturated layer has finally emerged to the surface and the composition in both, the implantation zone as well as the layer from which sputtered particles originate become constant (steady state). In the erosion dominated regime, one would then mainly observe the balance between beryllium sputtering and the steady state nitrogen implantation rate Y_{imp}^{∞}, since in the implantation depth the saturation concentration is already reached. With the steady state beryllium sputtering yield Y_{Be}^{∞}, an estimate for Y_{imp}^{∞} could then be made in the same way as for Y_{imp}^{0}, i.e.

$$Y_{imp}^{\infty} \sim 28.5\%$$

This agrees quite well with the value predicted in the TRIDYN simulation (cf. figure 4.23).

A different explanation for the observed saturation dynamics could be found in the surface morphology. In figure 4.25 a scanning electron microscopy picture of the nitrogen saturated surface (left) is compared to an unirradiated, as-received surface (right). Obviously the nitrogen exposure results in a roughening of the

Katharina Dobeš
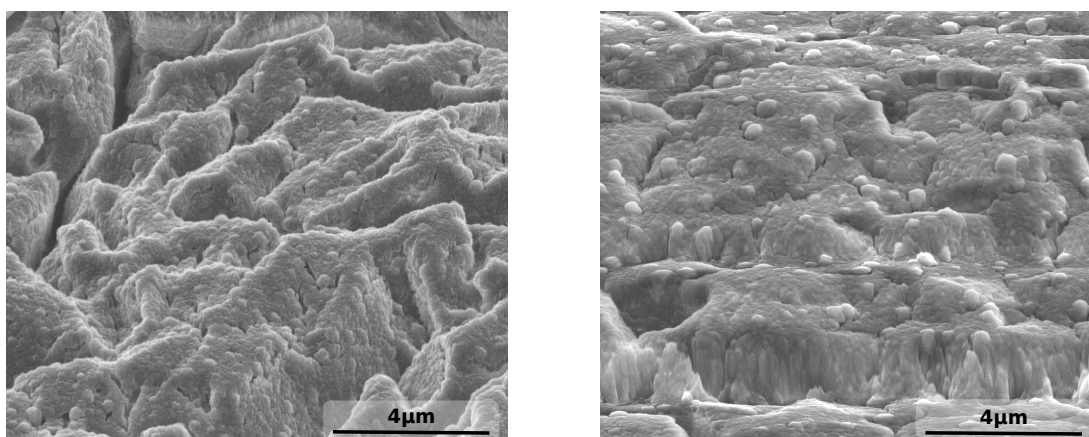
Figure 4.25: SEM images comparing the morphology of a nitrogen saturated beryllium surface (left) to a virgin, as-received beryllium sample (right) for a comparable image scale (as indicated at the bottom). Both images are obtained at a surface tilting angle of 52°.

surface. Generally the sputtering yield will increase with surface roughness [43]. Based on the evolution of the mass change rate alone, the transition from the initial erosion dominated regime to steady state sputtering in figure 4.22 could also be due to an alteration in the surface morphology at this fluence.

Following the nitrogen saturation of the surface, post mortem nuclear reaction analysis (NRA) measurements were performed with nitrogen projectiles at an energy of 4.94 MeV (see table 3.2). To estimate the total amount of retained nitrogen, the protons from the reaction $^{14}N(^4He, p)^{17}O$ were detected. From the observed reaction rate, the integrated areal density of nitrogen is approximately $1.4 \cdot 10^{17}$ atoms per cm^2. It is not straightforward to convert this value into an atomic concentration of implanted nitrogen projectiles within the surface, since the thickness to which the nitrogen saturated surface layer is confined, i.e. from which the NRA signal originates, cannot be assessed easily. Although the nitrogen range profile in figure 4.21 suggests that the nitrogen concentration will peak at a depth of roughly 87 Å, a significant amount of nitrogen will be implanted beyond this depth. In an attempt of making a rough estimation for the nitrogen concentration in the surface, the nitrogen range profile can be cut-off somehow arbitrarily at e.g. 20% of its maximum value, by which it is assumed that a representative integration depth for the observed nuclear reaction is ~ 250 Å. If the integrated areal nitrogen density determined in the NRA measurement is then compared to the density of beryllium-

nitride, i.e. 0.148 at/Å^3 [193], this would imply a nitrogen content of on average $\Theta_N \sim 0.37$.

4.4.2 Steady State Erosion

As soon as steady state surface conditions are reached, the interaction of the nitrogen projectiles with the beryllium surface is marked by a constant erosion yield. Subsequent to saturating a beryllium target with a total fluence of $1.2 \cdot 10^{18}$ nitrogen projectiles per cm^2, the sputtering yield of the resulting beryllium-nitride surface was determined for various nitrogen impact energies in the range of 375 eV per N to a maximum kinetic energy of 2500 eV per N. These measurements were performed without any further treatment or analysis of the surface. To keep projectile induced surface modifications small for all investigated impact energies, the impact energy of the projectiles and as a consequence the projectile penetration depth was gradually decreased.
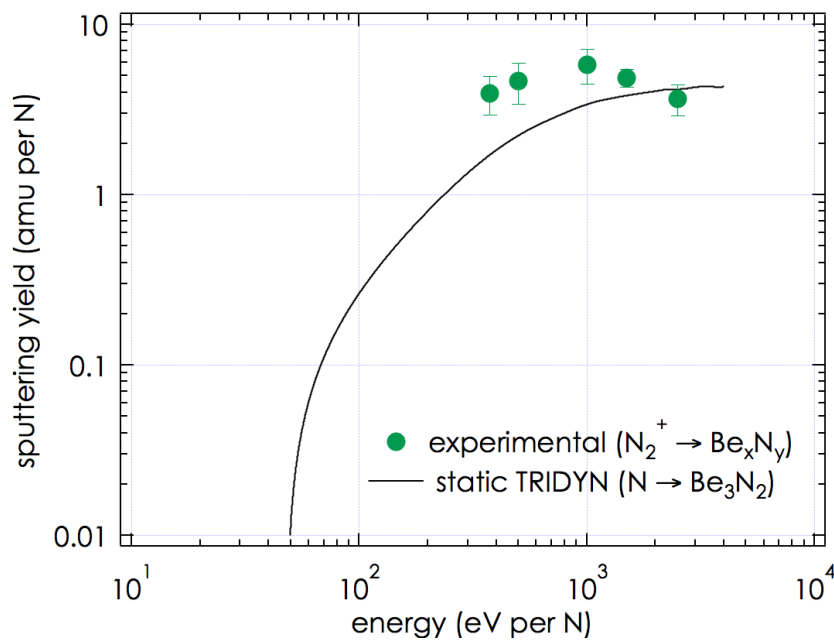
Figure 4.26: Steady state nitrogen sputtering yield of the nitrogen saturated beryllium surface as a function of the projectile impact energy. Experimental data (green symbols) is compared to data from a static TRIDYN simulation for sputtering of a Be_3N_2 (black solid line).

Katharina Dobeš

In figure 4.26 the experimentally obtained total erosion yields are shown and compared to a static TRIDYN simulation for sputtering of a beryllium nitride Be_3N_2 surface (black solid line). The input parameters used for the TRIDYN simulation are listed in table 3.3.

4.4.3 Oxidation of Beryllium Nitride

One of the advantages of using beryllium as a plasma facing material is its affinity to oxygen, which might aid in reducing the impurity concentration in the ITER vessel. When interrupting the nitrogen bombardment in the experiments, indeed a distinct mass increase is observed, which can be attributed to the formation a surface oxide from an exposure to the residual oxygen pressure in the vacuum chamber.

Remarkably it is found that the characteristics of the observed oxidation curve strongly depends on the nitrogen saturation level of the surface. When interrupting the nitrogen bombardment at a comparably low cumulative nitrogen fluence, the observed mass increase is much more pronounced than it is for a surface with an almost saturated nitrogen content. This is shown in figure 4.27, where two different oxidation curves, i.e. the mass accumulation rate observed right after interrupting the nitrogen bombardment, are compared. In the graph to the left the nitrogen bombardment was stopped after a cumulative fluence of $2.4 \cdot 10^{17}$ nitrogen per cm^2, i.e. during the initial erosion dominated regime of the saturation curve in figure 4.22. The curve on the right was obtained during an interruption at a much higher fluence of $7.5 \cdot 10^{17}$ nitrogen per cm^2, i.e. almost towards steady state surface conditions. In both cases the respective nitrogen fluences were applied without any intermediate interruption. Both oxidation curves were obtained at a comparable residual gas pressure in the low 10^{-9} mbar regime.

With an enthalpy of formation for Be_3N_2 of $\Delta_f H^0 \sim 6.1$ eV/at, compared to $\Delta_f H^0 \sim 5.5$ eV/at for BeO [191], the formation of beryllium nitride is energetically only a little less favorable than surface oxidation. From the experimentally observed oxidation behavior it seems as if the formation of beryllium nitride on top of the beryllium substrate effectively passivates the surface towards oxidation.

The clear difference in the two oxidation curves shown in figure 4.27 also implies that at a fluence of $2.4 \cdot 10^{17}$ nitrogen atoms per cm^2 (left graph), the nitrogen saturation level at the surface is lower than after a cumulative fluence of $7.5 \cdot 10^{17}$ nitrogen per cm^2 (right graph). This strongly suggests that during the initial part of the erosion dominated regime, where a constant erosion rate is first observed (i.e. at fluences $2 \cdot 10^{17} \lesssim \Phi \lesssim 4 \cdot 10^{17}$), the nitrogen content at the surface has not yet
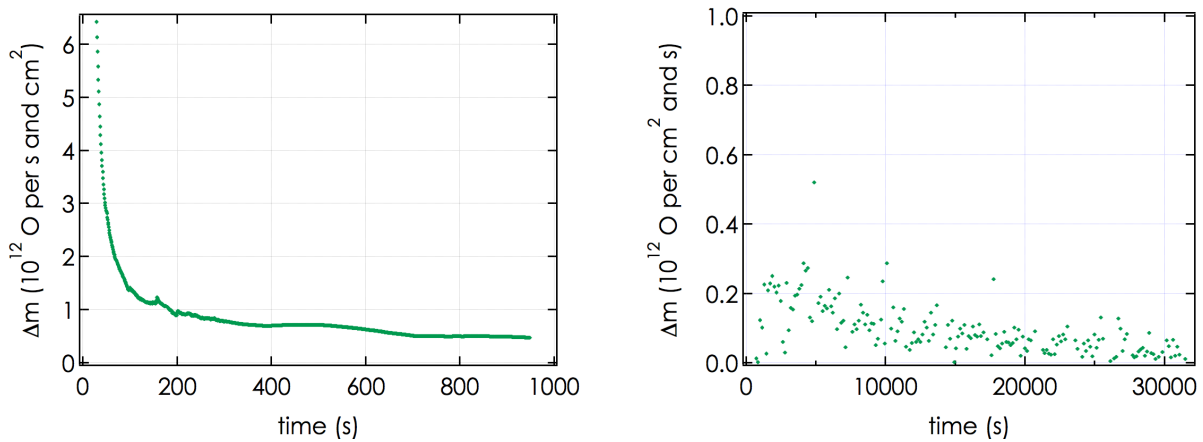
Figure 4.27: Comparison of the observed surface oxidation for two different nitrogen saturation levels. In the left graph the surface has been saturated up to a total nitrogen fluence of $2.4 \cdot 10^{17}$, in the right to a total fluence of $7.5 \cdot 10^{17}$ nitrogen projectiles per cm^2. Both fluences were applied without intermediate interruption.

saturated. The two individual regimes of constant erosion yield in the saturation dynamics of the surface therefore have to be at least partially linked to the evolution of the nitrogen concentration at the surface.

The mechanisms involved in the *initial* kinetics of the oxidation of a beryllium surface was studied by Zalkind and co-workers [214], who propose two possible kinetics models to describe surface oxidation: a *random Langmuir type, two site chemisorption process* and a *clustering and island formation model*. In the latter case, first oxide islands are formed on the surface, which then laterally spread with time until they coalesce and finally cover the entire surface. Both models can be fitted to a kinetics equation for the surface coverage Θ [214], which for the clustering and island growth model is given by:

$$-\ln(1 - \Theta) = k \cdot t \tag{4.17}$$

and for the chemisorption process by:

$$\frac{\Theta}{(1 - \Theta)} = k \cdot t \tag{4.18}$$

The coefficient k in the above expressions represents the oxidation rate, which depends on the specific oxygen exposure.

The surface oxide coverage Θ can be determined as the relative coverage in comparison to a reference value for maximum coverage. In a first approximation
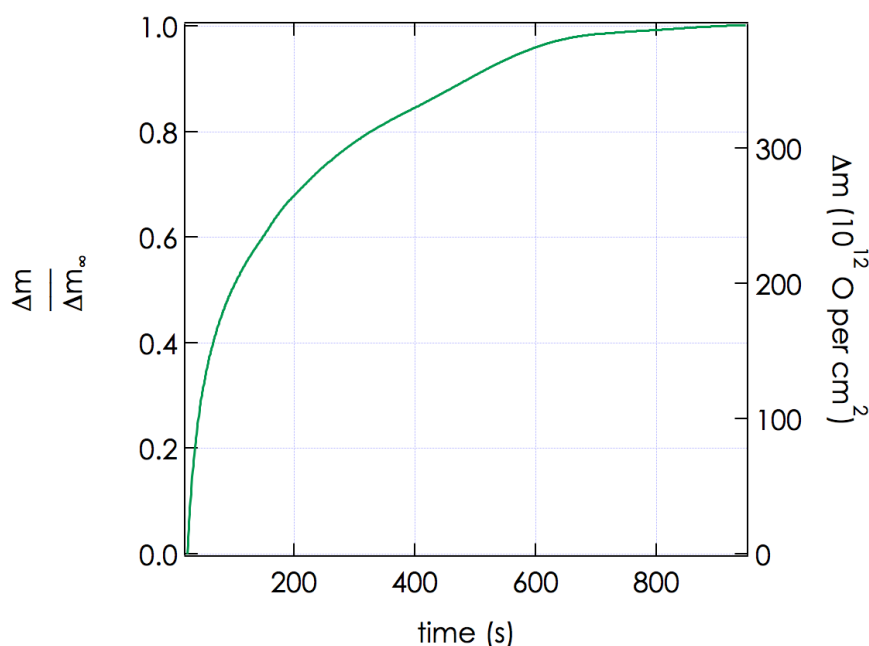
Figure 4.28: Integrated mass change of the beryllium surface due to oxidation after a total nitrogen fluence of $2.4 \cdot 10^{17}$ N per cm^2. From the cumulative mass change at the end of the observation interval Δm_∞ a normalized ratio of oxide surface coverage $\Theta = \Delta m / \Delta m_\infty$ can be estimated.

the cumulative mass increase at the end of the investigation interval has been used for this purpose, i.e.

$$\Theta(t) = \frac{\Delta m(t)}{\Delta m_\infty} \tag{4.19}$$

By this it is assumed that at the end of the observation interval the surface oxidation is overall completed. Given that in this first investigation of the surface oxidation of nitrogen containing beryllium surfaces, the observation intervals were rather limited, this assumption might introduce quite some imprecision and the presented data are therefore only used to give a general idea of the observed dynamics. In figure 4.28 the corresponding relative oxide coverage as a function of the exposure time is shown for the oxidation dynamics observed after a total fluence of $2.4 \cdot 10^{17}$ N per cm^2 (cf. left graph in figure 4.27).

To test the applicability of the two above described models to the observed oxidation dynamics, the left-hand side of the individual kinetics equations (cf. equations 4.17 and 4.18) is plotted in figure 4.29. For consistency with either of the pro-

Katharina Dobeš
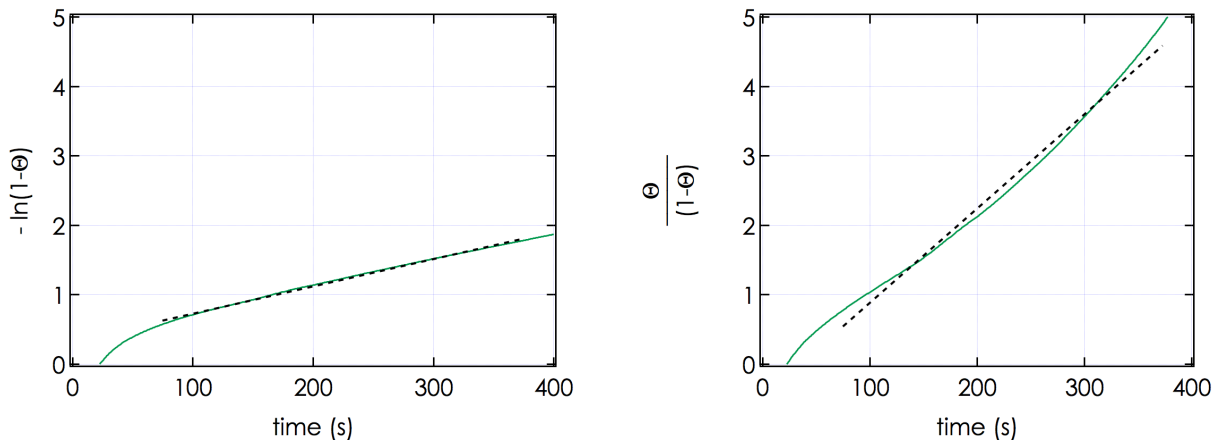
Figure 4.29: From the initial oxidation dynamics the oxidation kinematics and especially an oxidation rate coefficient can be fitted according to two different models for island formation and growth (left) and a two site chemisorption process (right) [214]. The oxide coverage Θ is extracted from figure 4.28.

posed models this should result in a linear relationship of the respective kinetics to the elapsed time *t*. Evidently the island formation and growth model (left graph) fits the experimental data much better. At the very beginning, the observed oxidation dynamics somewhat deviates from a linear dependency though. To this point, the reason for this is not clear. From the slope of the corresponding curve, the oxidation rate coefficient *k* can in principle be determined, which in this case amounts to: $k \sim 3.9 \cdot 10^9$ O/s.

If the nitrogen bombardment is repeatedly interrupted during the saturation of the surface, the passivation towards oxidation is apparently retarded by an intermediate formation of an oxide layer, which then has to be removed again upon resuming the exposure to nitrogen projectiles. After the oxidation curve displayed in figure 4.27 (left), the nitrogen bombardment was interrupted for a second time at a total fluence of $7.6 \cdot 10^{17}$ N per cm^2. While the observed oxidation is clearly reduced to $k \sim 1.8 \cdot 10^9$ O/s, this is nevertheless in clear contrast to the virtually entirely suppressed surface oxidation observed when continuously irradiating the surface with nitrogen up to a comparable fluence (cf. figure 4.27, right).

Katharina Dobeš

4.4.4 Summary & Concluding Remarks

The saturation dynamics of a beryllium surface under the impact of energetic nitrogen projectiles has been studied in real-time and in situ. By this a unique insight into the involved processes could be gained. From the characteristics of the saturation curve and supported by TRIDYN simulations, the contribution of the involved mechanisms to the total observed mass change can be disentangled and their individual rates can be estimated.

The overall saturation dynamics of the surface can be subdivided into 3 sections: an implantation dominated regime, an erosion dominated regime and finally steady state conditions. After a fast removal of surface adsorbates, the interaction of the beryllium surface with the nitrogen projectiles is at first marked by a net mass increase, due to dominant projectile implantation. Within this implantation dominated regime, a constant mass increase rate is observed for fluences in the range of $1 \cdot 10^{16} \lesssim \Phi \lesssim 7 \cdot 10^{16}$ N per cm^2. The initial nitrogen retention rate can be estimated from the slope of this constant mass increase and is expected to lie between 40% (if any simultaneous mass loss due to erosion is neglected) and 84% (as determined with an appropriate estimation for the surface erosion yield). At a fluence of $\sim 1.2 \cdot 10^{17}$ N per cm^2 a transition from dominant implantation to dominant surface erosion is observed, most likely due to a local saturation of the nitrogen content at the ion penetration depth, which results in a reduction of the N implantation rate.

The erosion dominated part of the saturation curve is composed of two regimes of about constant mass loss rate which are separated by a transition region. Initially a constant erosion yield of approximately 2 amu per N is observed, which at a fluence of $\sim 4 \cdot 10^{17}$ N per cm^2 starts to slightly increase again. At a total fluence of $\sim 8.3 \cdot 10^{17}$ N per cm^2 steady state surface conditions are finally reached, i.e. the mass change per impinging projectile is furthermore independent from the applied ion fluence and the nitrogen content in the surface becomes constant. In steady state nitrogen implantation is exactly balanced by the partial nitrogen sputtering yield from the surface. The observed sputtering yield can be attributed to beryllium sputtering only, i.e. amounts to ~ 0.4 Be per N. While the above-described, two individual net erosion regimes are not reflected in the TRIDYN simulation, they are still most likely linked to the nitrogen saturation dynamics of the surface. They probably arise from the fact that different N fluences are needed to saturate the surface at the implantation depth (transition from implantation dominated to erosion dominated) and in the near surface zone, from which sputtered particles originate (transition to steady state), respectively. However, some of a

change in surface morphology on the erosion yield cannot be excluded. From a comparison of the mass change rate for the two regimes of constant erosion rate, an estimate for the steady stat N implantation yield can be derived, i.e. ~ 28.5%. This value is in fairly good agreement with the TRIDYN simulation (18%).

Moreover, the dependency of the surface oxidation rate on the nitrogen saturation level of the surface was studied. It was found that the oxidation rate of the surface decreases strongly with the nitrogen content. Towards steady state conditions, surface oxidation is almost entirely suppressed and the observed mass change virtually falls below any detectable limit. As the formation of beryllium-nitride is energetically only a little less favorable than surface oxidation, nitrogen saturation of the beryllium surface seems to be an effective passivation towards oxidation. Using nitrogen as a seeding gas in ITER might therefore reduce the expected ability of the beryllium first wall to actually getter oxygen.

Katharina Dobeš

4.5 Interaction of Deuterium with Beryllium and Beryllium-Nitride Layers

As demonstrated in the previous section, the introduction of nitrogen into the vacuum vessel of ITER will result in the formation of nitrogen containing beryllium mixed material layers. An important question that arises in this context is whether the resulting surface compound will have an influence on the fuel retention and recycling behavior of the ITER first wall.

In general it is observed (e.g [111, 119] and references therein) that hydrogen isotope retention is influenced by material parameters such as the diffusivity and the hydrogen solubility, but also on the specific material type and the availability of defects, which can serve as trapping sites for implanted hydrogen isotopes (see section 2.2.2). In ITER radiation damage due to neutron bombardment will therefore have a severe influence on the amount of retained fuel in the wall materials [111]. Lattice displacements introduced by the impact of energetic particles such as nitrogen impurity ions may serve as an additional precursor for hydrogen isotope trapping.
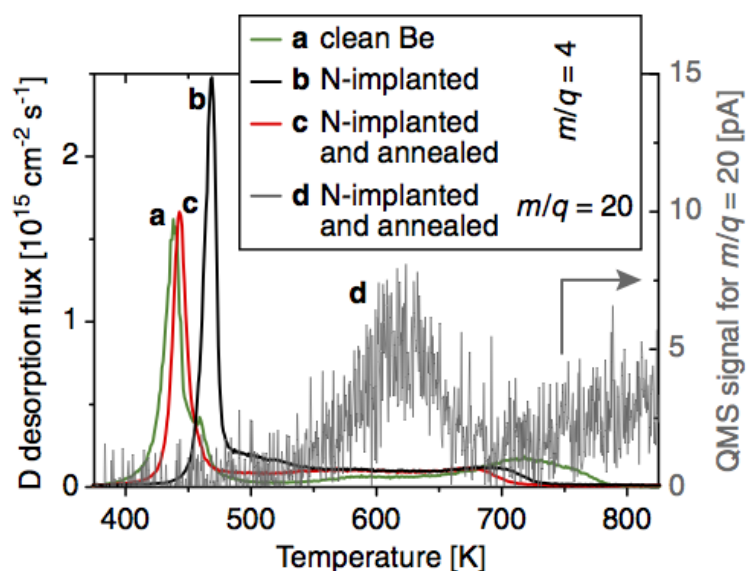
Figure 4.30: TPD spectra of D_2^+ from clean and nitrogen implanted beryllium after implantation of deuterium at 600 eV to $2.8 \cdot 10^{17}$, $2.1 \cdot 10^{17}$ and $1.9 \cdot 10^{17}$ D per cm^2. Picture taken from [67].

Oberkofler and co-workers [67] observed that for low deuterium fluences, the retained projectile fraction is slightly reduced in nitrogen saturated surfaces compared to pure beryllium. They attribute this to an increased reflection rate of deuterium projectiles by the heavier nitrogen atoms in the surface as compared to the beryllium substrate. At high fluences however, the authors report that the amount of retained deuterium is overall not affected by the presence of nitrogen. For disordered, i.e. not-annealed surfaces, they find that implanted deuterium is released at noticeably different surface temperatures (see figure 4.30), which they ascribe to a reduced diffusivity of deuterium through the disordered beryllium nitride layer.
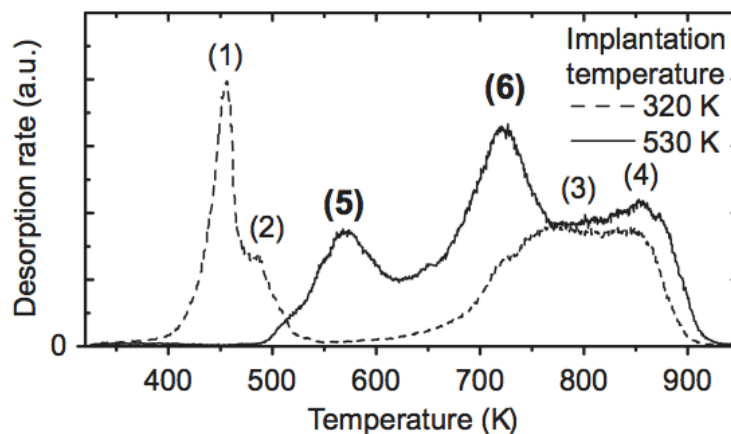
Figure 4.31: TPD spectra of a beryllium surface implanted with deuterium at 320 and 530 K. Various trap sites are identified: (1-2) supersaturated binding sites, (3-4) trapping to lattice defects, (5) BeD_2, (6) release from oxidized surface. Picture taken from [115].

The general retention mechanisms of deuterium projectiles in pure beryllium surfaces has been studied in various investigations so far (cf. section 2.2.2). Commonly it is found that at low fluences, essentially all deuterium is retained [215,216]. At fluences of about $\sim 1 \cdot 10^{17}$ deuterium per cm^2, the deuterium content in the surface usually starts to saturate. The resulting deuterium saturation concentration within the saturation zone is of the order of $D/Be \sim 0.35 - 0.4$ [67,216]. The overall inventory and the exact fluence at which saturation is observed depends on the projectile energy, i.e. the projectile range in the surface. By means of temperature programmed desorption investigations, several binding sites for retained deuterium could be identified [67,115,215,217]. For low fluences, implanted deuterium is mainly bound to defects in the surface, which are either intrinsically present or

induced by preceding projectile impact. In this case the thermal desorption spectrum is dominated by high temperature deuterium release peaks at around 770 - 840 K. For fluences beyond the local saturation fluence of about $1 \cdot 10^{17}$ D per cm^2, all available defect sites are occupied and additional deuterium is retained at supersaturated binding sites. This is usually accompanied by structural surface changes, like the formation of bubbles which are filled with molecular D$_2$ [218] and generally a porous structure in the implantation zone [111]. Desorption of deuterium from these supersaturated zones usually occurs at lower temperatures in the range of 440 - 470 K, implying that the respective binding sites are energetically less favorable. At elevated implantation temperatures (i.e. above the low temperature release stage of 440 - 470K), these low temperature binding sites are suppressed as they cannot be occupied [115, 219]. Instead deuterium above the bulk saturation concentration is retained at sites, which desorb at somewhat higher temperatures around ~ 550 - 700 K. These can be attributed to a thermally activated formation of a beryllium-hydride or hydroxide phase in the implantation zone of the surface.

This section presents the results from in real-time studies of the dynamics of deuterium retention in beryllium. The presented investigations were performed using the quartz crystal microbalance technique introduced in section 3.1. The influence of the presence of implanted nitrogen projectiles on the retention behavior of beryllium surfaces was studied by performing comparable experiments on clean, as-received beryllium and on a nitrogen saturated sample. The nitrogen saturated beryllium surface was prepared by applying ~ $1 \cdot 10^{18}$ N per cm^2 at an impact energy of 2500 eV per N. The thus established surface was used for the subsequent investigations without further treatment (like e.g annealing). Both during N and D bombardment as well as in between, the surface temperature was kept at 460 K, which is expected to be a typical ITER first wall operation temperature [220]. At this temperature it is anticipated that implanted deuterium will continuously desorb from the surface, as in this temperature region a deuterium release peak usually is observed in thermal desorption spectroscopy.

Deuterium projectile ions were produced in an electron impact ion source (cf. section 3.1.3) and accelerated by an extraction voltage of 5000 V. The molecular part of the beam was selected with a Wien filter resulting in a surface impact energy of 2500 eV per deuterium constituent. As the nitrogen saturated surface was prepared with nitrogen projectiles at the same impact energy, it can be expected that the majority of the deuterium ions will penetrate the nitride layer and be implanted in the underlying beryllium bulk. This is confirmed by a static TRIDYN simulation for the respective implantation profiles as demonstrated in figure 4.32.
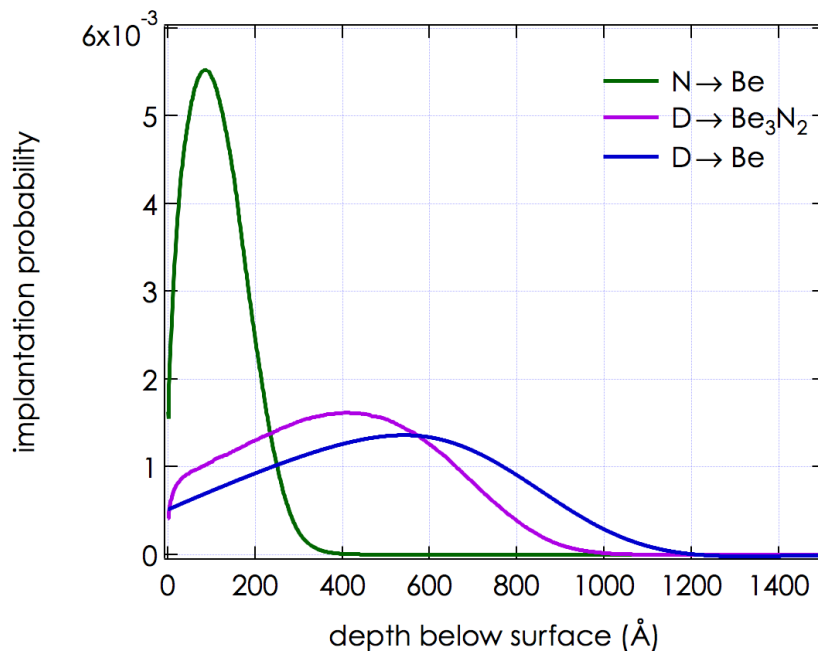
Figure 4.32: Comparison of the TRIDYN implantation probabilities for all investigated target-projectile combinations (N on beryllium, D on beryllium-nitride, D on beryllium).

While the nitrogen implantation profile in beryllium (green) has its maximum at a depth below the surface of ~ 9 nm, the deuterium projectile range is expected to be much higher, i.e. ~ 54 nm in pure beryllium and ~ 42 nm in stoichiometric Be_3N_2. The utilized TRIDYN input parameters are summarized in table 3.3.

4.5.1 Deuterium Saturation

On a previously nitrogen saturated beryllium surface, the saturation behavior for the impact of 2500 eV per D molecular deuterium ions was studied. The observed cumulative mass change as a function of the deuterium fluence and the elapsed time respectively is shown in figure 4.33. During the entire surface irradiation the ion flux to the surface was about constant at $4.3 \cdot 10^{13}$ D per cm^2 and second. As the fluence which is required to establish steady state surface conditions was rather high, the saturation curve in figure 4.33 was recorded in two consecutive measurements, interrupted by a break of roughly 30,000 seconds. This is indicated in figure 4.33 by the blue shaded area. During the entire interruption a continuous
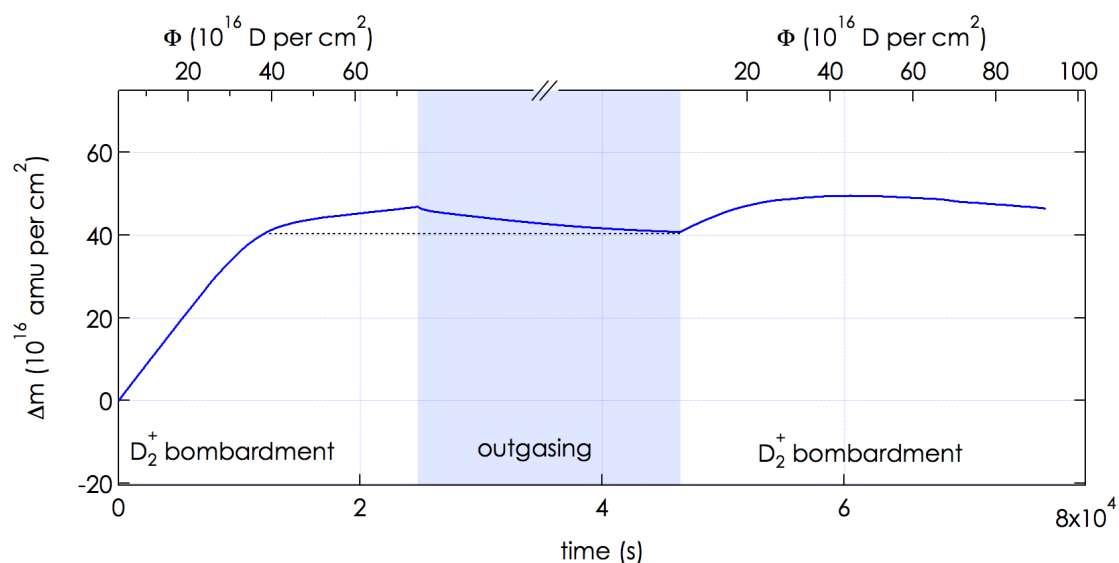
Figure 4.33: Cumulative mass change Δm during deuterium saturation of a nitrogen saturated beryllium surface as a function of the applied deuterium fluence and elapsed time, respectively. The deuterium bombardment had to be interrupted once, which is indicated by the blue shaded area. During this interruption a continuous D release is observed. The saturation dynamics is marked by a high retention rate in the beginning, which starts to saturate at a fluence of $\sim 2.5 \cdot 10^{17}$ D per cm^2. In steady state a minor surface erosion rate is observed. For details see text.

mass decrease could be observed, which can be ascribed to thermal desorption of implanted deuterium, as the surface temperature of 460 K corresponds to a deuterium desorption peak usually observed in thermal desorption spectroscopy (see section 4.5.2).

The continuous mass loss observed during the interruption also implies that the second part of the deuterium saturation curve cannot be considered to be a smooth continuation of the previously observed mass change. This is indeed reflected in the discrepancy of the trend of the two sub-curves. The indicated fluences of the two consecutive deuterium irradiations (top axis) are therefore not added to a combined total fluence. In an attempt of merging the two sub-parts of the deuterium saturation curve, the effective cumulative deuterium fluence for the second irradiation can be determined by correcting the total fluence by a value corresponding to the deuterium fluence overall released during the intermediate interruption. This is indicated in figure 4.33 by the dashed line, which shows to
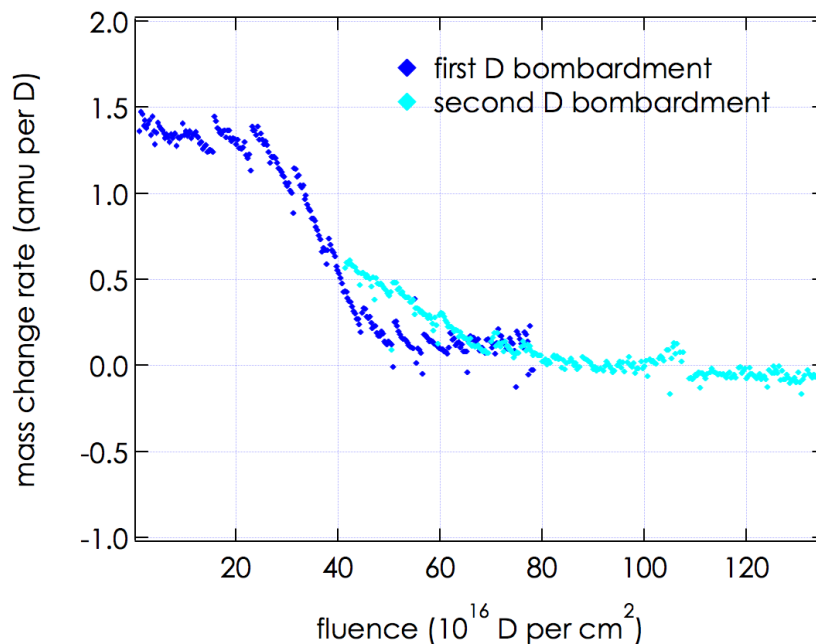
Figure 4.34: Mass change rate of the nitrogen saturated beryllium surface during D bombardment. The graph combines the two consecutive D irradiations by correcting the effective deuterium fluence for the second sub-part by a value corresponding to the total deuterium fluence overall released during the intermediate interruption (see figure 4.33).

which point in the saturation curve the deuterium content in the surface is seemingly reversed by the continuous release during the interruption. By this approach it is assumed that the observed mass change is solely due to deuterium desorption, i.e. any simultaneous processes resulting in a mass change such as e.g. surface oxidation are neglected. On a nitrogen saturated surface, the oxidation rate is however expected to be small (cf. section 4.4.3). Additionally the surface composition might also be changed due to e.g. diffusion of implanted deuterium beyond the implantation zone, which too is not taken into account here.

In figure 4.34 the resulting total mass change rate is shown as a function of the thus obtained 'effective' deuterium fluence applied to the surface. Obviously, the two sub-parts of the deuterium saturation curve connect very nicely. Still, the observed curve trend upon resuming the deuterium irradiation (light blue) is slightly different at first compared to before the interruption (dark blue). The reason for this might be that the above-mentioned processes (surface oxidation, deuterium

Katharina Dobeš

diffusion) do indeed have some influence on the evolution of the surface during the interruption.

For low fluences (i.e. $\Phi \lesssim 2.5 \cdot 10^{17}$ D per cm^2) the interaction of energetic deuterium ions with a nitrogen saturated beryllium surface is marked by a mass increase which is constant with fluence pointing to predominant deuterium retention with a constant retention probability (cf. figures 4.33 and 4.34). Above a fluence of $2.5 \cdot 10^{17}$ D per cm^2 a transition to a reduced mass increase rate is observed, which is again constant up to a cumulative fluence of about $\Phi \sim 8 \cdot 10^{17}$ D per cm^2. At this point the observed mass increase starts to gradually decline. Only for fluences above $\Phi \gtrsim 1 \cdot 10^{18}$ D per cm^2 a small net surface erosion is detected, which becomes constant at a fluence of $\sim 1.2 \cdot 10^{18}$ D per cm^2 with a total erosion yield of $Y_{tot}^{\infty} \sim 0.12$ amu per D.

It is generally not straightforward to estimate the rates of all the processes involved in the deuterium saturation dynamics of the nitrogen saturated surface. In comparison with the nitrogen saturation dynamics the observed mass change is an even more complex superposition of a variety of different processes. Apart from erosion of the involved species, i.e. of nitrogen (Y_N) and beryllium (Y_{Be}) but also implanted deuterium (Y_D), deuterium projectiles are simultaneously implanted (Y_{imp}). In addition at a surface temperature of 460 K, retained deuterium projectiles are continuously desorbed from the surface (Y_{des}). In the observed mass change these processes are all superimposed. The respective rates depend on the concentration of the related species and will therefore change with the applied deuterium fluence.

From the mass change rate observed for low deuterium fluences, a lower estimate for the initial deuterium implantation rate can be deduced, i.e. $Y_{imp}^{0} \gtrsim 0.65$ if to a first approximation simultaneous deuterium desorption and mass removal due to surface erosion is neglected. Looking at the erosion rate at the end of the saturation curve, where in dynamic equilibrium deuterium release from the surface (due to either sputtering or desorption) is balanced by the implantation rate, it can be expected that the mass loss due to erosion is rather small ($Y_{tot}^{\infty} \sim 0.12$ amu per D). This is also supported by TRIDYN, which estimates an initial surface erosion yield of $Y_{Be} + Y_N + Y_D \sim 0.3$ amu per D. Accordingly a more realistic estimate for the overall initial deuterium retention rate (i.e. deuterium implantation and desorption rate combined) would then be $Y_{ret}^{0} = Y_{imp}^{0} - Y_{des}^{0} \sim 0.7$.

At a fluence of $\Phi \sim 2.5 \cdot 10^{17}$ D per cm^2 the deuterium content in the surface starts to saturate which is reflected in a transition to a reduced retention rate. This is in good agreement with the observation reported in the literature [67, 115, 216]

for reaching the local saturation concentration in the implantation zone at comparable deuterium fluences. In the mass change rate in figure 4.34 a second regime of about constant mass change is subsequently observed for fluences up to $\sim 8 \cdot 10^{17}$ D per cm^2. This can be ascribed to retention of deuterium in supersaturated surface zones, and at an elevated surface temperature of 460 K probably also to the thermally activated formation of a beryllium hydride phase in the surface [67, 115, 215]. Taking the erosion rate observed at the end of the saturation curve (see above) into account, the mass change rate in this second regime corresponds to an overall retention rate upon reaching local saturation of $Y_{ret} \sim 0.22$ amu per D (i.e. $Y_{ret}^{sat} \sim 0.11$).
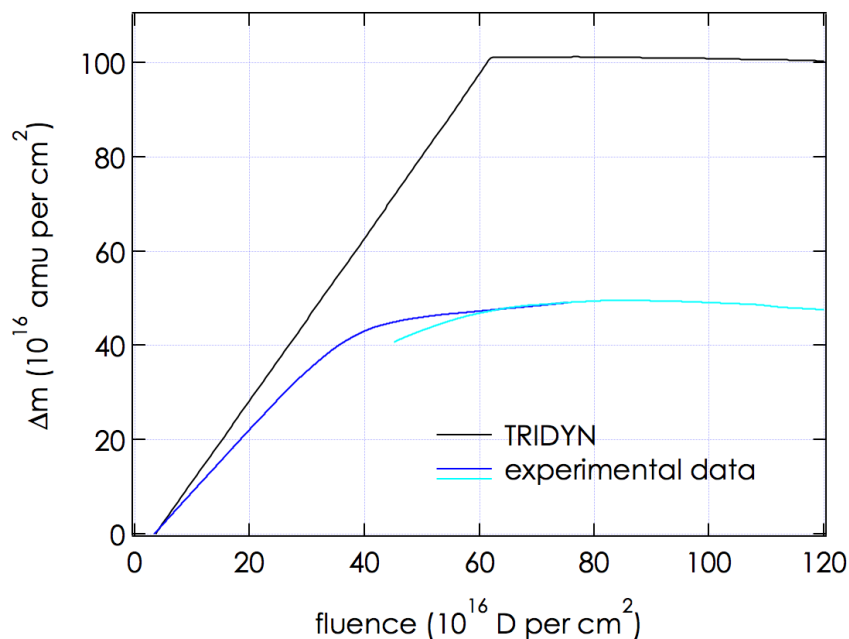
Figure 4.35: Comparison of the cumulative mass change during D saturation of Be$_x$N$_y$ observed in the experiment (blue) to results from a TRIDYN simulation (black). The mass change of the TRIDYN curve incorporates erosion of beryllium, nitrogen and deuterium, as well as projectile implantation.

Following these two individual regimes of about constant retention probability, at a fluence of $\sim 8 \cdot 10^{17}$ D per cm^2 the observed mass increase starts to gradually decline. Finally, at a fluence of $\Phi_{eq} \sim 1.2 \cdot 10^{18}$ D per cm^2 steady state surface conditions are obtained. From this point onwards the surface is gradually eroded with a constant total sputtering yield of (see above) $Y_{tot}^{\infty} \sim 0.12$ amu per D. In this

case the deuterium content in the surface is in equilibrium, i.e. deuterium release due to thermal desorption and self-sputtering is balanced by the implantation of projectiles.

The evolution of the observed mass change during deuterium saturation can be compared to a TRIDYN simulation. In the simulation a stoichiometric Be_3N_2 surface compound was assumed. The maximum deuterium content in the surface was limited to 35% according to values reported in the literature [67, 115]. The full set of input parameters is listed in table 3.3. The most severe shortcoming of this simulation is its lack of incorporating thermally induced desorption of deuterium from the surface. In addition, possible chemical reactions like the formation of a beryllium hydride phase [115] are not reproduced by TRIDYN.

In figure 4.35 the total mass loss observed in the measurement (in blue) is compared to the total mass change derived from TRIDYN. The TRIDYN data includes erosion of deuterium, beryllium and nitrogen as well as projectile implantation. In addition, figure 4.36 shows the fraction of retained deuterium as obtained from the TRIDYN simulation.
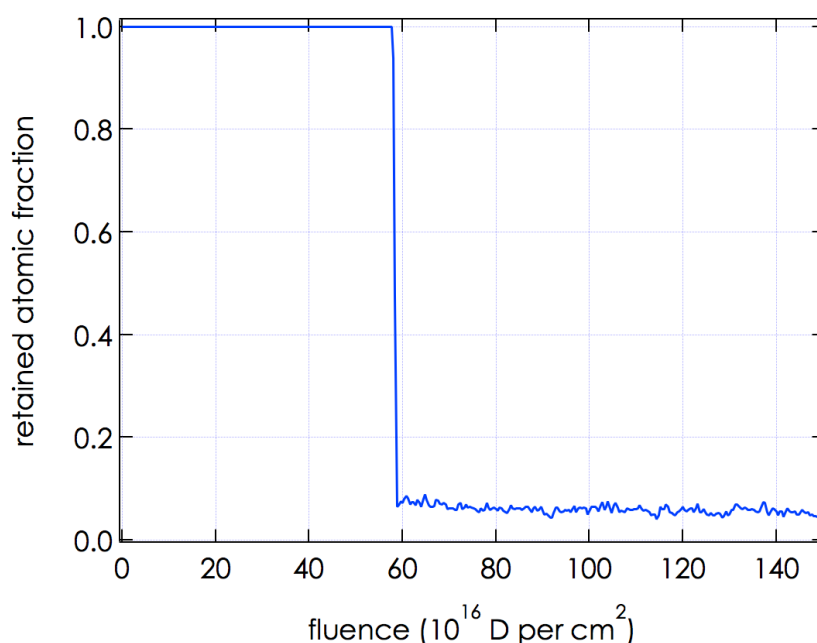
Figure 4.36: Results of a dynamic TRIDYN simulation for the fraction of deuterium projectiles retained in Be_xN_y as a function of the applied ion fluence. Initially all deuterium projectiles are implanted. At a fluence of $\sim 6 \cdot 10^{17}$ D per cm^2 the content saturates and the retention rate is reduced to $\sim 5\%$.

In the very beginning TRIDYN predicts a mass change which is mostly dominated by deuterium implantation with an initial retention rate of 100% (cf. figure 4.36). The resulting total mass change (cf. figure 4.35) is a bit higher than the mass increase actually observed in the experiment. Given that thermal desorption of deuterium from the surface is not reproduced by the simulation, this discrepancy is within the expectable limits. According to TRIDYN, the deuterium content in the surface saturates at a fluence of $\sim 6 \cdot 10^{17}$ D per cm^2. At this point the retention rate reduces to approximately 5% and steady state conditions are established. According to TRIDYN, the deuterium bombardment henceforward results in a minor erosion rate of 0.02 amu per D, which compared to the experimental data ($Y_{tot}^{\infty} \sim 0.12$ amu per D) is again a slight underestimation.

Obviously, the constant deuterium retention rate in local supersaturation as it is observed in the experiment for fluences of $2.5 \cdot 10^{17} \lesssim \Phi \lesssim 8 \cdot 10^{17}$ D per cm^2 cannot be accounted for in the simulation. In line with this, in the experiment steady state conditions are reached only at $\sim 1.2 \cdot 10^{18}$ D per cm^2, i.e. at about twice the fluence expected from the TRIDYN simulation.

Immediately after the measurement curve in figure 4.33 was finished, the sample was removed from the vacuum. Post mortem nuclear reaction analysis was performed with 2 MeV deuterium projectiles. From the reaction $D(^3He, p)^4He$ (cf. table 3.2), the areal density of retained deuterium was determined to be $\sim 2.5 \cdot 10^{17}$ D per cm^2, which corresponds to $\sim 18\%$ of the effectively applied deuterium fluence (i.e. of the applied D fluence corrected by the total D fluence released during the interruption).

4.5.2 Deuterium Desorption

From the mass change observed upon interrupting the deuterium irradiation at a fluence of $\sim 7.5 \cdot 10^{17}$ D per cm^2 (cf. figure 4.33), the dynamics of the deuterium release can be studied. In figure 4.37 the observed mass loss rate is depicted as a function of the time elapsed after shutting the deuterium beam off. The data recording was started ~ 400 seconds after shutting the ion beam off. For the entire observation interval of almost 30,000 seconds a pronounced mass loss can be observed. At first, the detected desorption rate, which corresponds to approximately $2 \cdot 10^{13}$ D per cm^2 and second (estimated by extrapolation to 0 on the time axis), decreases very quickly. After about 3000 s the slowing down of the desorption rate moderates and from this point onwards is not as fast as in the very beginning. It shall be noted here that any surface oxidation will in principle lead to a simultaneous, counteracting mass increase and will therefore result in an underestimation of the

Katharina Dobeš
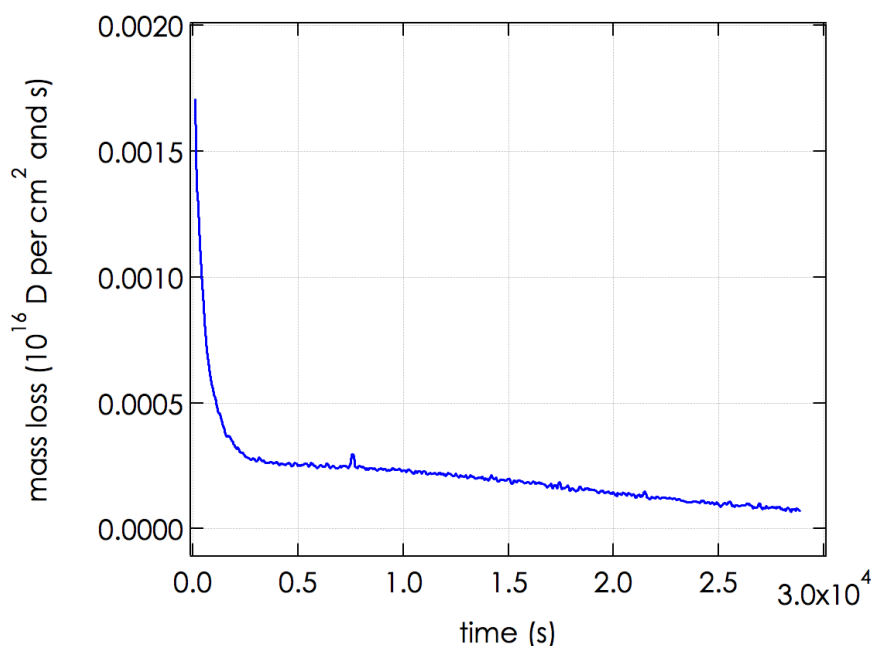
Figure 4.37: Observed mass loss rate of the nitrogen saturated beryllium surface as a function of the elapsed time after a cumulative D fluence of $7.8 \cdot 10^{17}$ D per cm^2. A continuous mass loss due to D outgasing is found, which is much more distinct in the beginning and then decreases for longer waiting times.

observed deuterium desorption rate. However, for a nitrogen saturated beryllium surface it was found that surface oxidation is suppressed to below any detectable limit (see 4.4.3). It is therefore assumed that the surface oxidation rate only plays a minor role here.

The amount of released deuterium is connected to the deuterium content in the surface Θ_D. The actual reaction kinetics depends on the rate limiting step of the deuterium release process. The initial part of the deuterium desorption curve in figure 4.37 can best be fitted according to a second order process, i.e. the desorption rate Y_{des} is proportional to Θ_D^2:

$$Y_{des} = \Gamma_{des} \cdot \Theta_D^2 \tag{4.20}$$

if Γ_{des} is the respective reaction coefficient. In this case the following relation between desorption rate Y_{des} and surface content Θ_D should apply:

$$\frac{1}{Y_{des}} = \frac{1}{\Gamma_{des}\Theta_D^2} + \frac{2}{\Theta_D} \cdot t + \Gamma_{des} \cdot t^2 \qquad (4.21)$$

In figure 4.38 a fit (in light blue) of the initially observed inverse desorption rate (in dark blue) according to equation 4.21 is shown. The fact that the initial part of the observed deuterium desorption curve (cf. figure 4.37) follows the kinetics of a second order process, implies that the rate limiting step in the desorption of deuterium from the surface requires the presence of two deuterium atoms. In this case the deuterium desorption rate is most likely limited by the D_2 recombination preceding the release from the surface. From the desorption rate observed at this point of the deuterium saturation curve, it can be estimated that about half of the impinging deuterium flux during surface irradiation is re-emitted due to thermal desorption.
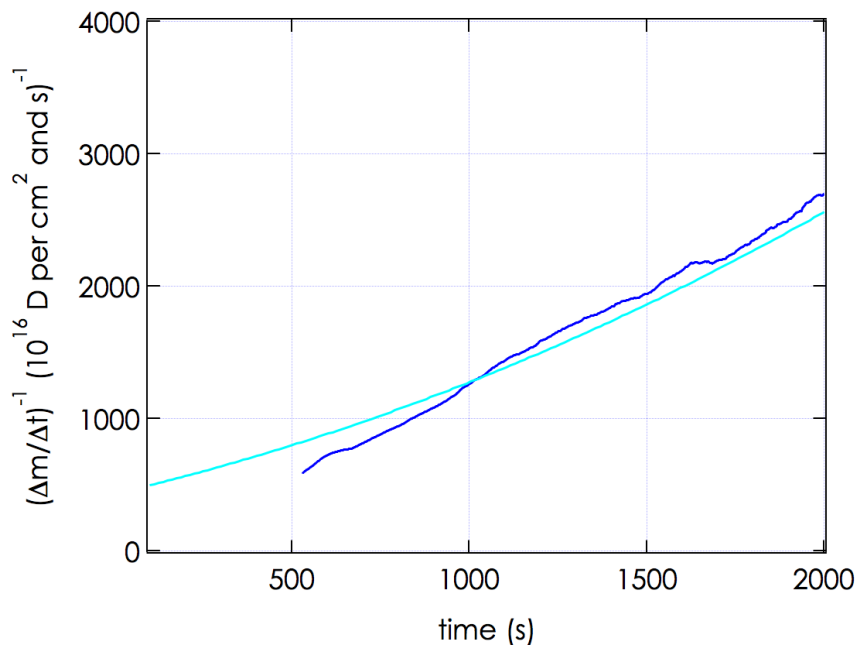
Figure 4.38: The initial D release curve (dark blue) (cf. figure 4.37 can be fitted according to a second order process (light blue), indicating that the observed release rate is limited by D_2 recombination. For details see text.

For longer observation times ($t \gtrsim 3000$ s) the kinetics of the desorption process clearly changes. The second part of the desorption curve in figure 4.37 rather

Katharina Dobeš

follows e.g. a square root dependency, which would indicate that after some time the deuterium desorption rate is limited by deuterium diffusion to the surface.

4.5.3 Comparison Beryllium-Nitride and Pure Beryllium

Deuterium Saturation

To compare the deuterium saturation dynamics of the nitrogen saturated surface with a pure beryllium surface, similar experiments were also performed on an as-received, pure beryllium sample. In figure 4.39 the cumulative mass change as a function of the applied deuterium fluence is shown and compared to the corresponding measurement curve on the nitrogen saturated surface (cf. figure 4.33). For the deuterium irradiation of the pure beryllium surface, the ion flux to the surface was slightly higher, than in the case of the nitrogen saturated surface, i.e. at $\sim 4.6 \cdot 10^{13}$ (compared to $\sim 4.3 \cdot 10^{13}$) D per cm^2 and second. To account for this and to make the two curves in figure 4.39 actually comparable, the saturation dynamics obtained on beryllium-nitride was scaled by a factor of $4.3/4.6 \sim 0.93$. The fluence axis (top) corresponds to the deuterium saturation curve on pure beryllium but matches the scaling of the curve obtained on nitrogen saturated beryllium.

Figure 4.40 depicts the mass change rate observed on the pure beryllium sample as a function of the applied ion fluence (to be compared with figure 4.34). For the presented measurements, the deuterium irradiation of the surface was again interrupted once in the course of saturating the surface, which is marked by a shaded area in figure 4.39. Just like it was done for the measured data on beryllium-nitride, the two individual sub-parts of the entire measurement curve can be merged into one single curve by correcting the cumulative fluence of the second sub-part of the measurement according to the total deuterium fluence, which is released during the intermediate interruption. The total deuterium fluence applied during the second irradiation evidently just seems to suffice to balance the intermediately desorbed deuterium amount. In contrast to the nitrogen saturated surface, it can be expected that pure beryllium is subjected to a pronounced surface oxidation (cf. sections 4.4.3 and 4.5.3). For the pure beryllium surface the corrected effective deuterium fluence might therefore constitute an underestimation of the total deuterium amount actually released during the interruption. This might explain the somewhat increased mass change rate observed after resuming the deuterium irradiation. Additionally by diffusion of implanted deuterium into the beryllium bulk beyond the projectile implantation zone, the deuterium surface content might actually be reduced during the interruption.

Katharina Dobeš
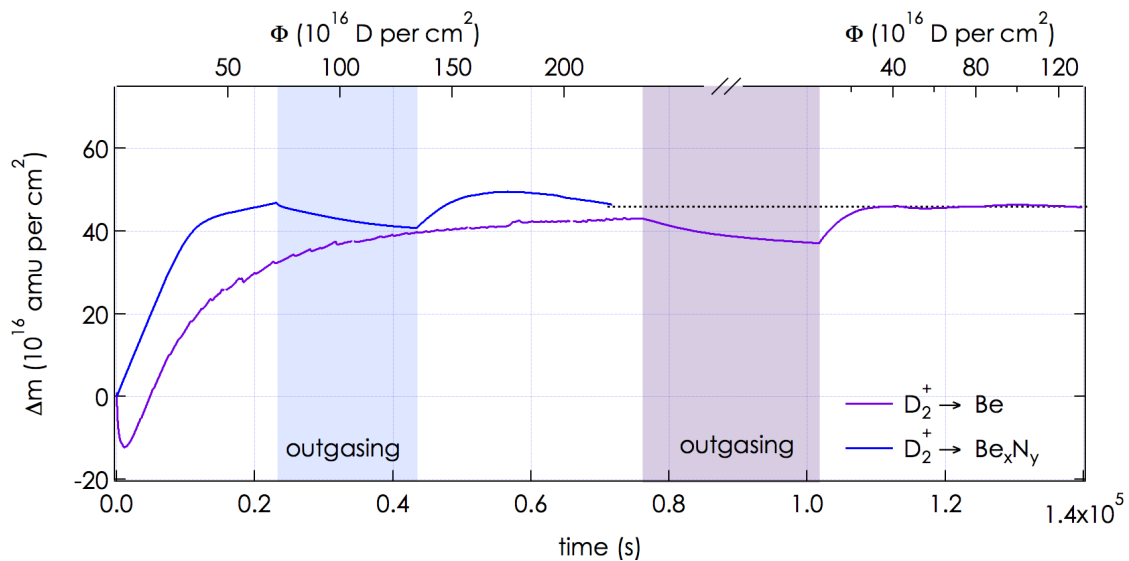
Figure 4.39: Cumulative mass change Δm during deuterium saturation of a beryllium surface (in purple) compared to a nitrogen saturated surface (blue), respectively. The the two curves are scaled according to their slightly different projectile fluxes to make the dynamics of the deuterium saturation comparable. The indicated deuterium fluences (top) correspond to the measurement on pure beryllium. Interruptions of the D irradiation are indicated by the shaded areas. For details see text.

At first glance the shape of the cumulative mass change observed on the pure beryllium surface in principle resembles the corresponding curve for the bombardment of the nitrogen saturated beryllium surface with deuterium projectiles (cf. figure 4.39). In contrast to the nitrogen saturated surface, the deuterium saturation curve on pure beryllium is at first marked by a pronounced mass removal. This can be attributed to the remova ofl loosely bound surface contaminants (such as C) and the native beryllium oxide from the as-received surface. For fluences in between $1 \cdot 10^{17} \lesssim \Phi \lesssim 2.5 \cdot 10^{17}$ D per cm^2, a constant mass increase rate is observed. From the total mass change at the end of the investigated fluence interval it can be expected that the erosion rate of the surface will be negligible. Therefore the detected mass increase is a suitable measure for the overall retention rate at this point, i.e.

$$Y^0_{ret} = Y^0_{des} + Y^0_{imp} \sim 1.15 \text{ amu per D}$$

Katharina Dobeš
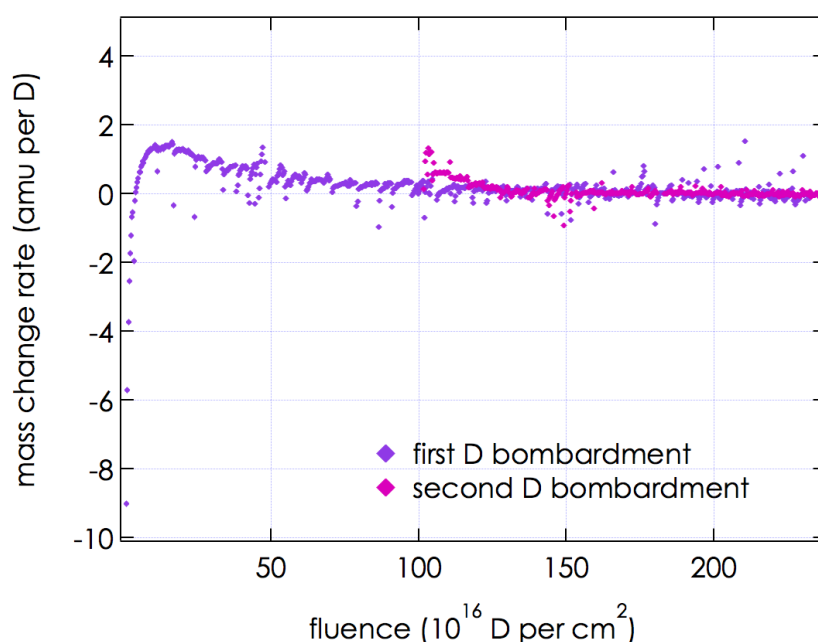
Figure 4.40: Integrated mass change of the pure beryllium surface during D bombardment. The graph combines the two consecutive D irradiations by correcting the effective deuterium fluence for the second sub-part by a value corresponding to the total deuterium fluence overall released during the intermediate interruption (see figure 4.39).

which corresponds to a retention probability of ~ 0.58. Compared to nitrogen saturated beryllium ($Y_{ret} \sim 65 - 70\%$), the initial deuterium retention probability is a bit smaller on pure beryllium. For fluences $\gtrsim 2.5 \cdot 10^{17}$ D per cm^2 a deviation from this constant mass increase is observed. Similarly to the saturation dynamics on nitrogen saturated beryllium, this can be attributed to establishing the local deuterium saturation concentration in the deuterium implantation zone. The fluence at which this initially constant implantation rate starts to saturate compares well for the two surfaces. In contrast to the nitrogen saturated surface, establishing the local saturation concentration is not followed by a second regime of about constant implantation rate on pure beryllium. Instead a slow and gradual decrease of the observed mass change rate is found.

After a total effective fluence of $\Phi_{eq} \sim 2.3 \cdot 10^{18}$ D per cm^2, finally steady state conditions are reached. This amounts to about twice the fluence that is needed for establishing dynamic equilibrium when bombarding a nitrogen saturated surface

with deuterium. While for beryllium nitride a minor surface erosion was observed in steady state, on pure beryllium all involved processes seem to balance each other and the observed mass change rate from this point onwards is zero. Using post mortem nuclear reaction analysis performed on the deuterium saturated surface, the areal density of retained deuterium was determined. With $\sim 1.7 \cdot 10^{17}$ deuterium per cm^2 it is noticeably lower than for the nitrogen saturated surface ($\sim 2.5 \cdot 10^{17}$ D/cm^2).
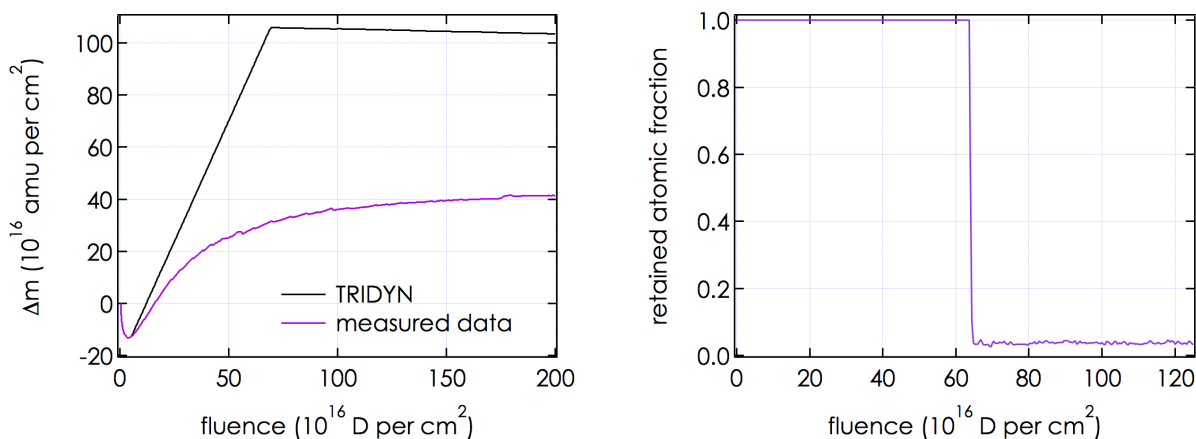
Figure 4.41: Comparison of the cumulative mass change during D saturation of Be (left) and corresponding retained D fraction (right) according to a dynamic TRIDYN simulation. For details see text.

Just as for the nitrogen saturated surface, for pure beryllium the deuterium saturation dynamics observed in the experiment can be compared to a TRIDYN simulation. The corresponding total cumulative mass change (left) and the retained fraction of applied deuterium (right) are shown in figure 4.41. In this simulation, the maximum deuterium content in the surface was again limited to 35%. For the complete set of input parameters see table 3.3.

All in all the TRIDYN curve is very much the same as for the simulation on beryllium nitride. In the beginning, again all of the deuterium projectiles are retained in the surface. The resulting total mass change (including erosion and retention) amounts to ~ 1.8 amu per D, which is again higher than observed in the experiment. However, thermal desorption of implanted deuterium is again not included in the simulation. According to the simulation, the deuterium content in the surface saturates at a fluence of $6.4 \cdot 10^{17}$ D per cm^2 and steady state conditions are reached. Thus the simulation agrees with the experiment concerning the fact that

higher deuterium fluences are needed to establish the saturation concentration in the surface, although the predicted difference is not as severe as observed in the experiment. From TRIDYN, in steady state a minor surface erosion is expected, with a sputtering yield, which is of the order of ~ 0.02 amu per D. This is about the same as for the beryllium-nitride surface.

	Be_3N_2	Be
D range (TRIDYN)	42 nm	54 nm
atomic density[1]	0.21216 at/$Å^3$	0.12347 at/$Å^3$
surface binding energy[1]	4.9 eV/at	3.4 eV/at
Y_{ret}^0 (measurement)	0.65 -0.7	0.58
Φ_{eq} (measurement)	$\sim 1.2 \cdot 10^{18}$ D/cm^2	$\sim 2.3 \cdot 10^{18}$ D/cm^2
Y_{tot}^{∞} (measurement)	~ 0.1 amu/D	~ 0 amu/D
retained D density (NRA)	$\sim 2.5 \cdot 10^{17}$ D/cm^2	$\sim 1.7 \cdot 10^{17}$ D/cm^2

Table 4.1: Comparison of the main differences of the deuterium saturation dynamics on the two investigated surfaces. [1] [193].

The pronounced discrepancy in the fluence, after which dynamic equilibrium conditions are established on the two surfaces in the experiment, but also the general trend of the observed differences for the deuterium saturation dynamics can be understood on the basis of some fundamental considerations. The atomic density of pure beryllium ($\rho_{Be} \sim 0.12347$ at/$Å^3$) is lower than the density of a stoichiometric beryllium-nitride ($\rho_{Be_3N_2} \sim 0.21216$ at/$Å^3$) [193]. Consequently the expected deuterium ion range is higher in beryllium than it is in beryllium nitride as confirmed by a static TRIDYN simulation (cf. figure 4.32). Therefore in pure beryllium the deuterium saturated surface zone will extend further into the bulk than in a nitrogen saturated surface. From this it could be expected that the total amount of retained deuterium saturates at a higher value for pure beryllium than for the nitrogen saturated surface. Contrary to this, post mortem nuclear reaction analysis suggests that it is just the other way around: in the beryllium surface the areal density of retained deuterium is only about 68% of the deuterium amount detected in the nitrogen saturated surface. In the un-ordered nitrogen saturated surface, lattice displacements induced by the preceding nitrogen bombardment might serve as

additional trapping sites for implanted deuterium. All in all, this effect seems to exceed any differences in the layer thickness of the deuterium saturated surface zone due to unequal projectile ranges.

From a comparison of the mass change observed in steady state, the erosion rate of nitrogen saturated beryllium is apparently a bit higher than for pure beryllium (where essentially no surface erosion is observed in dynamic equilibrium). This is in line with the respective surface binding energies of the two surfaces. Usually the enthalpy of formation is considered to be a suitable measure for the surface binding energy of a solid, which is $\sim$ 4.9 eV/at for beryllium nitride compared to $\sim$ 3.4 eV/at for pure beryllium [193]. In table 4.1 the above comparison is summarized.

Deuterium Desorption

When the deuterium bombardment of the surface was interrupted at a fluence of $\sim 2.3 \cdot 10^{18}$ D per cm^2, overall a mass change of the surface was observed, as is shown in figure 4.42. Initially a negative mass loss, i.e. a dominant mass increase of the surface is found. For the first $\sim$ 1.5 hours, apparently the mass change due to surface oxidation exceeds any simultaneous mass loss due to thermal deuterium desorption. This is in clear contrast to the behavior observed for the nitrogen saturated surface, which is in accordance with the decreased surface oxidation rate previously found on nitrogen saturated surfaces (see section 4.4.3). The overall mass change observed in the case of pure beryllium therefore only represents a lower estimate for the actual deuterium release rate, as it is apparently superimposed by a counteracting mass increase due to surface oxidation.

After approximately $\sim$ 1500 s, the overall mass loss observed on the pure beryllium surface even exceeds the desorption rate observed on nitrogen saturated beryllium. Similarly, in previous studies [67] a shift of deuterium desorption towards higher surface temperatures was found. This was attributed to a reduced diffusivity of deuterium through the disordered nitrogen containing surface layer as compared to pure beryllium, which retards the release of deuterium from the surface.

After about 11,000 seconds until the end of the investigated time interval, the observed deuterium release rate on beryllium equals the mass change rate found for the nitrogen saturated surface.

Katharina Dobeš
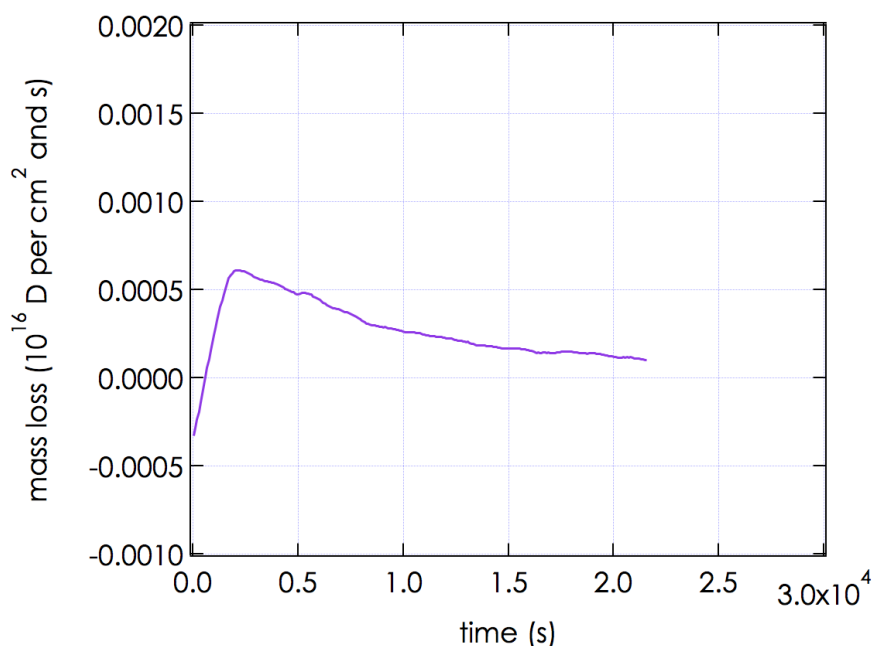
Figure 4.42: Observed mass loss rate of the beryllium surface as a function of the elapsed time after a cumulative D fluence of $2.3 \cdot 10^{18}$ D per cm^2. Initially a mass increase is detected, which is probably due to dominant surface oxidation. For longer waiting times, the D release from the surface can be observed.

4.5.4 Summary & Concluding Remarks

The dynamics of the deuterium saturation behavior of a previously nitrogen saturated surface was studied in real time and compared to the respective dynamics on pure beryllium. The presented measurements were performed at an elevated surface temperature of 460 K, where a continuous thermal desorption of deuterium has to be expected. Indeed a pronounced mass change implying a deuterium release from the surface was observed as soon as the deuterium bombardment of the surface was interrupted.

There are some distinct differences but also similarities in the deuterium saturation dynamics of the two surfaces. For low fluences, an about constant deuterium retention rate is observed on both surfaces. The overall retention rate on nitrogen saturated beryllium is a bit higher (~ 0.7) than on pure beryllium (~ 0.58). In the disordered nitrogen saturated surface, defects induced by the preceding nitrogen bombardment might serve as binding sites for implanted deuterium and might therefore be responsible for this slightly elevated deuterium retention rate

compared to the as-received beryllium surface. In the environment of a fusion reactor, this might eventually result in a higher overall D retention rate in disordered, nitrogen containing mixed material layers compared to as-received, pure beryllium surfaces.

On both surfaces, at a fluence of $\sim 2.5 \cdot 10^{17}$ D per cm^2 the deuterium retention rate starts to saturate, which in analogy to observations from the literature [67, 115, 215] can most likely be explained by a local saturation of the deuterium concentration at the ion implantation depth. Subsequently, the retention dynamics observed on the two surfaces becomes slightly dissimilar. On the nitrogen saturated surface a second regime of about constant retention rate is observed, where the retention probability of deuterium now is ~ 0.11. This second retention regime can most likely be ascribed to a thermally activated retention of deuterium in a beryllium-hydride phase [115] but probably also to the formation of ternary Be-N-D compounds [67]. At a fluence of $\sim 8 \cdot 10^{17}$ D per cm^2 a transition to net surface erosion is finally found. Steady state conditions are reached at a total fluence of $\Phi_{eq} \sim 1.2 \cdot 10^{18}$ D per cm^2 with a constant erosion yield of ~ 0.12 amu per D. On the pure beryllium surface on the other hand, establishing the local deuterium saturation concentration is followed by a slow, gradual decrease of the retention rate. Finally, only at a fluence of $\Phi_{eq} \sim 2.3 \cdot 10^{18}$ D per cm^2, steady state surface conditions are reached, which in this case are marked by a mass change of about zero, i.e. all involved processes balance each other.

The fluence at which dynamic equilibrium conditions are reached on the two surfaces, is about twice as high for pure beryllium than for the nitrogen saturated surface. This might be understood based on the higher implantation depth in pure beryllium compared to beryllium-nitride, which in turn might result in a thicker, deuterium saturated surface layer on pure beryllium and therefore in higher deuterium fluences needed to establish steady state surface conditions. The amount of retained deuterium as determined by post mortem nuclear reaction analysis is however noticeably higher on the nitrogen saturated surface, compared to pure beryllium. The increased number of deuterium trapping sites due to defects induced in the preceding nitrogen bombardment seems to overall exceed any differences in the thickness of the deuterium saturated surface.

The deuterium release behavior right after ceasing deuterium bombardment was investigated for both surfaces. On the previously nitrogen saturated surface, a pronounced mass loss is observed for the entire observation interval. The mass change due to deuterium release apparently at least exceeds any mass increase due to a possible surface oxidation. From oxidation rates observed for beryllium surfaces with varying nitrogen saturation levels it can be assumed that in this case,

the nitrogen content in the surface overall serves as a passivation towards oxidation. The kinetics of the observed deuterium desorption curve implies that initially the deuterium release rate from the surface is limited by D_2 recombination. Eventually a clear change in the desorption kinetics can be observed and the release rate is henceforward limited by other reaction steps like e.g. deuterium diffusion towards the surface layer.

On pure beryllium on the other hand the observed deuterium desorption dynamics has a markedly different shape. Immediately after stopping the deuterium irradiation, at first a mass increase is observed, which can probably be attributed to dominant surface oxidation. This is followed by a transition to dominant mass loss, which after about $\sim$ 1500 seconds already exceeds the respective mass increase detected for the nitrogen saturated surface. In accordance with previous findings [67] the disordered nitrogen containing surface layer might reduce the deuterium diffusivity towards the surface and by this might retard the deuterium release as compared to pure beryllium. After about some time, the desorption rate from the two surfaces becomes very similar.

In summary, the incorporation of nitrogen into beryllium plasma facing components might overall lead to slightly increased deuterium retention rates. The deuterium inventory in a beryllium-nitride surface saturates at about half the fluence needed to establish dynamic equilibrium conditions on pure beryllium. Although concealed by simultaneous surface oxidation in the experiment, the observed deuterium release rates imply that initially, deuterium will be desorbed faster from the pure beryllium surface than from nitrogen saturated beryllium. After about 3 hours the release rates on the two surfaces apparently become rather similar.

Chapter

5

Results II
Electron Emission Studies

When a highly charged ion approaches a solid surface it is neutralized and the potential energy, i.e. the sum of the ionization energies that has to be spent in its production, is released. The neutralization of the highly charged ion is marked by the formation of a transient, highly excited so-called hollow atom [80]. In the initial stages of the neutralization process, electrons are predominantly captured into higher energy levels of the projectile, while inner shells remain empty (see section 2.3.1). In this way a large part of the potential energy which is stored in the highly charged projectile is still available at the surface impact, were empty inner shells are filled rapidly by Auger-like processes [85, 221, 222]. The decay process of a hollow atom, both in front as well as below the surface, is accompanied by the emission of a large number of low energy electrons.

The above-sketched interaction of a highly charged projectile with a solid surface can be described within the 'classical over the barrier model' as outlined in section 2.3.1. For metallic surfaces, the fundamental underlying mechanisms are well understood to a large extend and have been studied extensively both in experimental as well as theoretical investigations (see e.g. [85, 131, 147] and references therein). Similar electron exchange and excitation processes at insulating and also semi-conducting surfaces are, however, much less understood. A substantially different behavior has to be expected however, as the neutralization process is governed by a variety of surface parameters, which are different for insulating surfaces compared to conducting targets. Among these are e.g. the dielectric response of the material, the target work function and band gap, the electron binding energy and also the reduced electrical conductivity in an insulator which might result in a local charging-up of the surface.

Katharina Dobeš

For metals, the determining parameter in the classical over the barrier model is the target work function, which determines both the critical distance at which the highly charged ion starts to capture electrons from the surface, R_C (see equation 2.21), as well as the projectile energy gain towards the surface due to its self-image attraction (and therefore the time available for electron exchange processes in front of the surface). For insulating targets on the other hand, the dielectric response of the surface has to be included in the classical over the barrier model (see e.g. [82, 150, 151]). As a consequence, the self-image interaction can be significantly reduced [82]. In addition, electron capture from the surface results in a local electron depletion due to the reduced charge mobility in the surface. The electron capture rate might hence be reduced and the de-excitation process in front of the surface might be hampered [223]. Moreover the electron binding energies within an insulator might well exceed the work function of metallic surfaces. Therefore it could be expected that the electrons that are able to cross the potential barrier between the surface and the projectile are captured into lower lying projectile states and less Auger processes are needed for the de-excitation of the hollow atom in front of the surface, which might severely influence the number of emitted electrons [149]. Although from the above-consideration a reduction of the electron yield for insulating targets could be expected, investigations for the electron emission from LiF and CaF_2 [224] revealed surprisingly large yields. These were attributed to a more efficient production of sub-surface contributions to the potential electron emission yield by cascade multiplication of sub-surface Auger electrons, which have a high surface escape probability due to the increased inelastic mean free path in these insulators.

For a more profound insight into the influence of the electronic structure of the target on the neutralization and decay dynamics of a highly charged ion impinging on a surface, electron emission yields on a variety of surfaces were investigated within the framework of this thesis. The presented data includes measurements for clean Au(111) surfaces (cf. section 5.1), a gold surface covered with 1 - 5 monolayer thin films of C_{60} (see section 5.2) and highly ordered pyrolytic graphite (HOPG, see section 5.3). Depositing thin films of C_{60} on a metallic substrate allows for an almost continuous variation of the surface properties (from the clean substrate to bulk film properties), whereas the exact electronic structure of the surface depends on the layer thickness of the film. Additionally, to better understand the individual contributions of electron emission from the projectile's potential (PE, see section 2.3.2) and the kinetic energy (KE, see section 2.3.3) respectively, total electron emission yields were determined in a wide range of projectile

Katharina Dobeš

charge states (corresponding to $E_{pot} \sim 140$ eV $- 12$ keV) and also kinetic energies ($E_{kin} \sim 3.9$ keV $- 328$ keV) for different impact angles.

The experimental results presented here were obtained at the *Zernike Leif* facility of the KVI in Groningen. A detailed description of the experimental setup is given in section 3.2.

5.1   Electron Emission from Clean Gold Surfaces

Part of the following has been published in [141]

To determine the contributions of kinetic and potential electron emission from a metallic target, the interaction of Ar^{13+} ions with a clean gold Au(100) surface was investigated at different impact angles and initial kinetic energies, ranging from 4 to 91 keV. The experiments were performed at the IISIS setup at KVI Groningen (see section 3.2 for a detailed description of the setup). Electron emission yields were studied under ultra high vacuum conditions in an UHV chamber pumped by a 360 l/s turbo pump, which is capable of maintaining the chamber at a base pressure in the low 10^{-10} mbar regime during the experiments. The projectile ions were produced in an 14 GHz electron cyclotron ion source at the KVI ZERNIKELEIF facility. Ions can be extracted from the ion source in an energy range from 3 keV/q up to 25 keV/q. They are mass over charge state separated by a 110° sector magnet and subsequently guided and focused onto the experimental setup by means of quadrupole magnets. Low impact energies can be attained by deceleration in a six-element lens system. In this case the setup, including the electronics and the pumps, is floated on the high, positive source potential.

A gold Au(100) single crystal is installed on a sample holder (cf. p. 68), which is designed in such a way that the supporting structure is not exposed to the ion beam. The gold target is cleaned by cycles of sputtering using 7 keV Ar^+ ions at grazing incidence angles and subsequent surface annealing to temperatures of up to 500 °C. The surface composition can be determined by means of time of flight low energy ion scattering (cf. section 3.2.3).

The electron statistics detector [180-182] is mounted under 90° with respect to the incoming ion beam. The sample is surrounded by a set of six electrodes to assure an optimal electron collection efficiency (cf. section 3.2.1). A highly transparent grid in front of the surface barrier detector is positively biased to attract the electrons towards the detector. The surface barrier detector is at a voltage of 30 kV. The detector output pulse height of one single ion impact event is a direct measure for the number of electrons emitted per impinging projectile. Total electron emission yields are determined by a pulse height analysis of the detector output signal from the electron number distribution (see section 3.2.2) [180].

Katharina Dobeš

5.1.1 Experimental Results & Discussion

Total Electron Emission Yields

Total electron emission yields from a clean Au(100) surface were determined for the impact of Ar^{13+} ions. The ion kinetic energy ranged from 4 up to 91 keV, resulting in impact velocities varying from $1.4 \cdot 10^5$ m/s to $6.6 \cdot 10^5$ m/s. This impact energy range covers both impact velocities below and above the threshold for kinetic electron emission v_{th}, which from equation 2.26 is determined to be $v_{th} \sim 2.4 \cdot 10^5$ m/s (corresponding to an Ar^{13+} impact energy of ~ 12 keV). In figure 5.1, the measured electron emission yields are shown as a function of the projectile velocity component perpendicular to the surface, $v_\perp$. For one single kinetic impact energy, the incidence angle of the impinging ions was varied between 20° and 80° with respect to the surface normal, thereby covering a wider range of $v_\perp$.
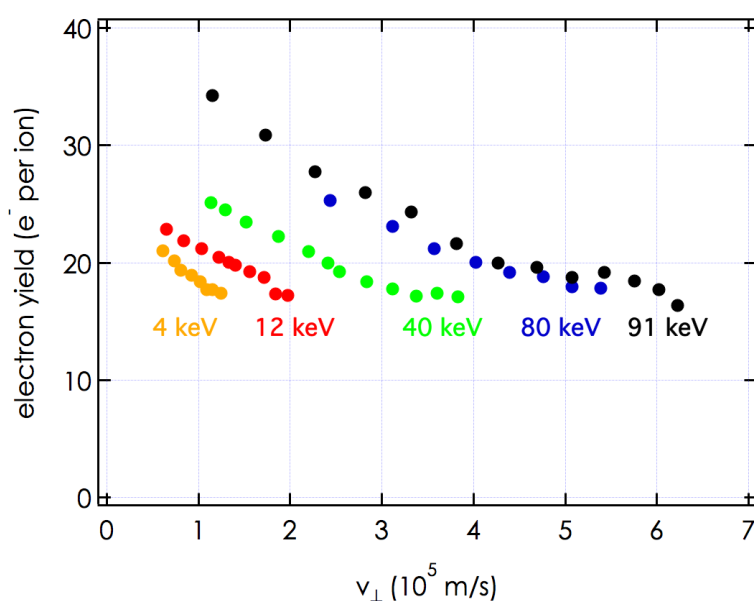
Figure 5.1: Total electron yield for Ar^{13+} ions impinging on an Au(100) surface as a function of the perpendicular projectile velocity. The kinetic energy of the projectiles are indicated in the graph.

As outlined in sections 2.3.2 and 2.3.3 the total electron emission yield is composed of both kinetically (KE) and potentially induced emission effects (PE). As the ion approaches the surface, low energy electrons are emitted in electron exchange processes involved in the neutralization of the projectile and the subse-
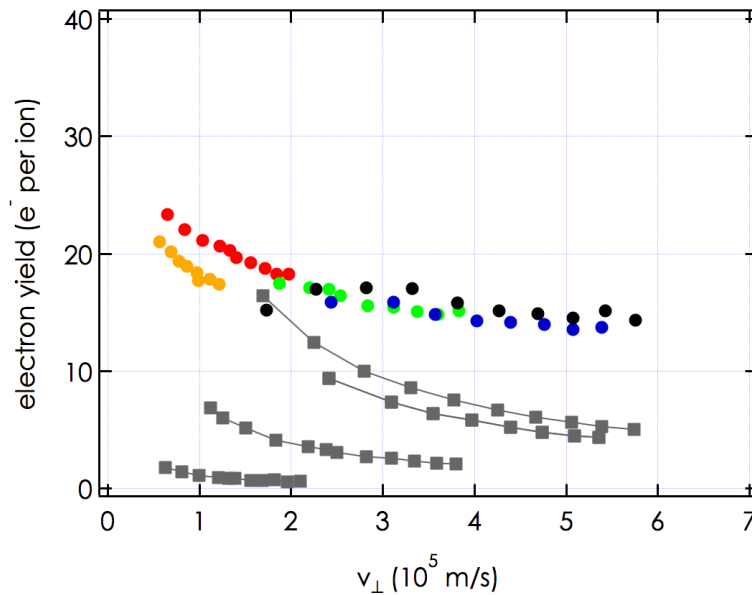
Figure 5.2: Potential electron emission yields for Ar^{13+} ions colliding with an Au(100) surface as a function of the perpendicular velocity. The presented data is derived from measurements at various impact energies. The color code of the data corresponds to the convention of figure 5.1. The presented yields are determined by subtracting the kinetic contribution to the electron yield (grey symbols) from the total yields of figure 5.1.

quent decay of the resulting hollow atom. This contribution (c_v) to the potential electron emission yield γ_{PE} depends on the interaction time of the ion in front of the surface, i.e. the square-root of the inverse velocity component towards the surface $1/\sqrt{v_\perp}$. Additionally electrons are emitted at and below the surface as the inner shells of the hollow atom are rapidly filled in Auger-type processes and weakly bound electrons are peeled off by the enhanced electronic screening upon entering the target (γ_∞).

Kinetic electron emission γ_{KE} on the other hand, originates from the collisional excitation of the electronic system of the solid induced by the ion impact. It is therefore dependent on the geometric path length of the projectile within the electron escape depth of the solid. Above the threshold velocity v_{th} (cf. equation 2.28), kinetic electron emission ($\gamma_{KE}(0) \cdot \cos^{-1}(\vartheta)$) increases approximately linearly with the ion impact velocity in accordance with the electronic stopping power.

Katharina Dobeš
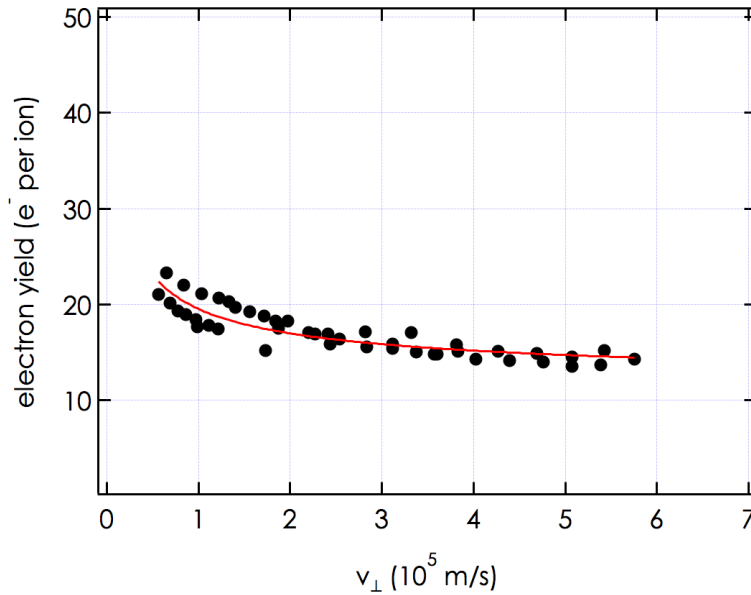
Figure 5.3: Potential electron emission yields for Ar^{13+} ions colliding with an Au(100) surface as a function of the perpendicular velocity (black solid symbols). The data can nicely be fitted to γ_{PE} from equation 5.1 (red solid line).

Putting the above together, the observed total electron yield can be represented by the following relation [131, 138, 158]:

$$\gamma = \underbrace{\gamma_\infty(q) + \frac{c_v}{\sqrt{v_\perp}}}_{\gamma_{PE}} + \underbrace{\frac{c_{KE}\,(v - v_{th})}{\cos\vartheta} \cdot \Theta\,(v - v_{th})}_{\gamma_{KE}} \qquad (5.1)$$

In this formula, the Heavisede step function $\Theta\,(v - v_{th})$ governs the onset of kinetic electron emission above the threshold velocity v_{th}. Above this threshold, the kinetic electron emission yield increases about linearly (proportionality factor c_{KE}) with increasing projectile impact energy (cf. section 2.3.3).

The fact that the data in figure 5.1 depends both on the impact energy and the velocity component perpendicular to the surface, i.e. that the individual curves in figure 5.1 do not coincide, therefore implies that the observed electron yields contain a distinct contribution from kinetic emission. To reduce the number of free parameters in equation 5.1, literature values can be used to subtract γ_{KE} from the measured values for the electron yield in figure 5.1. For this purpose, kinetic elec-

tron emission yields of Ar^+ ion impact are chosen [138], where the potential contribution to the total emission yield is considered to be negligible.

In figure 5.2, the resulting potential emission yields γ_{PE} are shown. In contrast to the total electron yields obtained in the measurement (cf. figure 5.1), the thus obtained potential emission yields coincide nicely for the investigated projectile energies. The resulting velocity dependence of the potential electron yield can then be fitted according to equation 5.1 (see figure 5.3), giving values for the two fitting parameters of $\gamma_\infty \sim 10.8$ e$^-$ per ion and $c_v \sim 8.7$ e$^-$ per ion.

Characteristics of the Electron Number Statistics

Further information on the nature of the involved processes can be obtained from the shape of the electron number statistics. In figure 5.4, two different electron number spectra obtained from Ar^{13+} impinging on an Au(100) surface at a kinetic energy of 91 keV are depicted . The spectrum to the left has been obtained at an impact angle of 30° to the surface normal, the spectrum on the right side at an impact angle of 75°.

As the electrons are emitted independently in an ion impact event, the observed number statistics should obey a Poisson distribution (cf. section 3.2.2). For large electron yields γ the Poisson distribution converges into a Gaussian function with its variance σ^2 being equal to the value of its center position, i.e. the mean number of emitted electrons: $\sigma = \sqrt{\gamma}$. As can be seen from figure 5.4 (right), for relatively low impact angles, a single Gaussian distribution fits the data well.
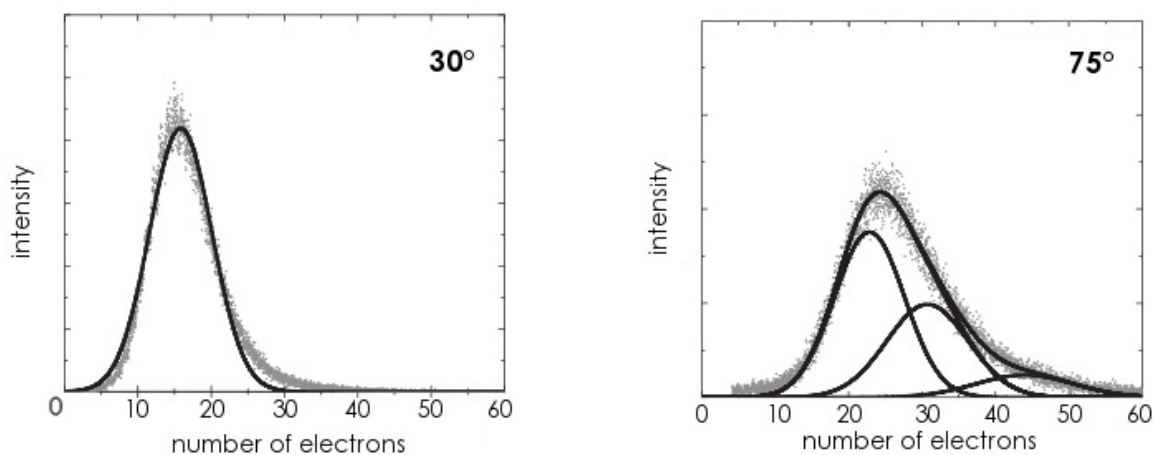
Figure 5.4: Measured data (grey) and fitted electron number distributions (black) for two different impact angles, i.e. 30° (left) and 75° (right).

Katharina Dobeš

For higher impact angles however, multiple Gaussian functions have to be used to fit the observed number statistics (see left graph in figure 5.4). Qualitatively this can be explained by the concept of different projectile trajectory classes (see [157]), which are involved in the interaction of the ion with the surface. Three different classes of trajectories are considered here:

1. Penetration of ions into the bulk before a hard collision takes place.

2. The first collision with a surface atom occurs in a near surface region (after which the projectile is either backscattered of deflected deeper into the bulk).

3. Impinging ions are scattered in a near surface plane resulting in a long geometric path within the electron escape depth.
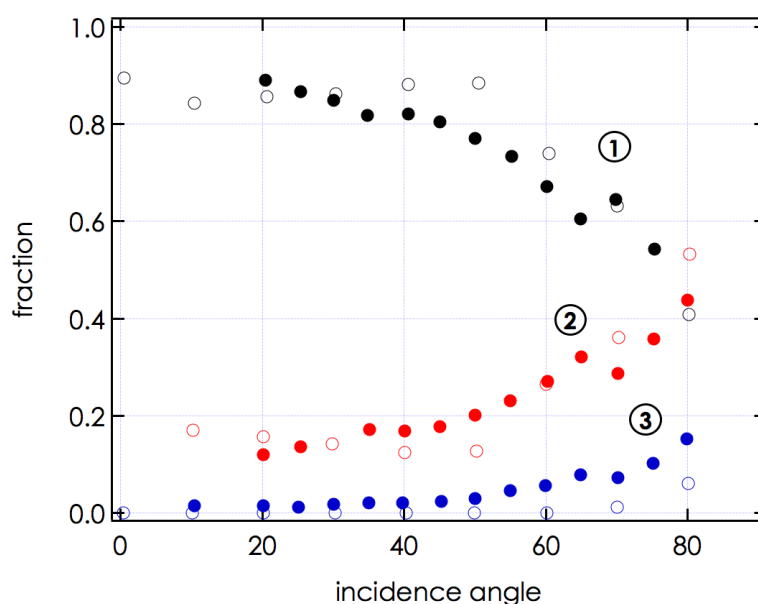
Figure 5.5: Normalized fractions of the contributions of the three trajectory classes (1-3) to the electron number statistics. The experimental data (full symbols) is compared to trajectory intensities obtained from SRIM simulations (open symbols). For details see text.

The validity of this simplified picture can be tested using SRIM [192]. Although SRIM does not take into account the neutralization and relaxation of the highly

charged ion in front of the surface, it is possible nonetheless to get an idea of the ion trajectories within the surface. To separate the penetrating ions (class 1) from the ions which are already scattered in a near surface region (class 2). 'Near surface collisions' were defined as collisions occurring within the first two atomic layers of the solid. The limiting condition for class 3 projectiles, was that the projectile undergoes not one but at least three collisions above the second atomic layer. Figure 5.5 compares the results of this simulation (open symbols) to the normalized contributions of the multiple Gaussians fitted to the experimental data (cf. figure 5.4). Here trajectory class number 1 (black markers) gives rise two the lowest emission yields, i.e. corresponds to the Gaussian fit with the lowest center position in the number statistics. The trajectory class number 3 on the other hand corresponds to the highest electron yield, reflecting the fact that electrons generated in a near surface region have the highest escape probability from the surface. The resemblance between the simulations and the experimentally obtained contributions is very good for processes one and two, i.e. for ions penetrating into the bulk and being scattered in a near surface region, respectively. For the third considered process, the agreement is somewhat poorer, but the trend is fairly well reproduced. From this it is concluded that it is reasonable that different trajectory classes contribute to the observed electron emission yield.

5.1.2 Summary & Concluding Remarks

Total electron yields for the impact of Ar^{13+} ions were determined at different impact energies and impact angles. Contributions of kinetic and potential electron emission could be distinguished using literature values for γ_{KE}. For the resulting potential emission the number of electrons originating from exchange processes in front and below the surface, respectively, could be estimated using an empirical formula for the angular dependency of the observed electron emission yield.

From the shape of the electron number statistics, it was concluded that different projectile trajectory classes contribute to the electron emission process. SRIM simulations were able to support this assumption. Ions penetrating deep into the bulk of the target are most probable and give rise to the lowest electron emission yield, while long near-surface trajectories are least probable but result in the highest emission yield.

Katharina Dobeš

5.2 Electron Emission from Gold Covered by Thin Films of C_{60}

Part of the following has been published in [225, 226]

The sheath potential plays an important role in plasma wall interaction of fusion machines (cf. section 2.3). It is influenced by particle induced electron emission [136]. For thermonuclear fusion reactors which use carbon as a plasma facing material, the formation of porous, flaky layers of graphite is observed as a result of plasma wall interaction. C_{60} films with their open structure may be valuable in experimentally modeling the effect of such graphite deposits on highly charged projectile induced electron emission. Additionally highly charged ions are also used as a gentle tool to fabricate nanostructures on surfaces without damaging the underlying bulk (see e.g. [86] and references therein). Both of the above triggers a general interest in studying C_{60} surfaces in more detail.

Highly charged ions can contain high amounts of potential energies (e.g. for an Ar^{13+} ion, the potential energy is already no less than 3.3. keV). Upon surface impact, this potential energy is dissipated within very short time scales. The general trends of the neutralization and relaxation mechanisms of such a highly charged ion interacting with a solid surface were successfully described within the hollow-atom scenario [80, 227, 228] (see section 2.3.1). The exact influence of the surface electronic structure and especially the target work function on the highly charged ion neutralization and the hollow atom decay is however still not fully understood. One possible way to vary the influencing surface parameters, is by depositing thin dielectric films onto metallic substrates. In this work, this was done by evaporating single layers of C_{60} on an Au(111) sample.

Up to now only a few pioneering experiments on hollow atom formation and decay at metallic surfaces covered with thin films have been performed. Meyer and co-workers [227] used thin films of Cs deposited on Au(011) to gradually lower the target work function by 3.3 eV. They observed an increase in the *KLL* Auger electron yield with decreasing work function, which is explained by the larger distances R_c in front of the surface at which the highly charged ion starts to capture electrons (cf. equation 2.21). The resulting increase in interaction time available for the hollow atom decay above the surface is further enhanced by a reduction of the image charge acceleration.

Using electron spectroscopy, Khemliche and co-workers [228, 229] measured *KLL* electrons from O^{7+} and N^{6+} ions interacting with a LiF-covered Au(111) target.

They investigated LiF deposits up to film thicknesses of 1 monolayer. In contrast to Cs, LiF deposition increases the binding energies of the surface electrons. It was found that for N^{7+} impact, the Auger intensity increased with LiF film thickness, amounting to about 30% for a single monolayer of LiF coverage. For the impact of O^{7+} ions, no change in the *KLL* spectrum was found, however. From their studies the authors conclude that a single monolayer of LiF coverage is able to completely shield the gold substrate as far as the neutralization of the highly charged projectile is concerned and that the wide band gap introduced by the LiF coverage does not play any role in the suppression of the above-surface inner-shell filling of the projectile [228].

KLL Auger decays represent (one of) the final steps in the relaxation of hollow atoms. The initial steps in which low-energy electrons are emitted should be influenced more directly by changes of the target work function. Low-energy electrons constitute by far the largest fraction of all electrons which are emitted, when a highly charged ion impinges on a solid surface. Therefore, total electron yields for the impact of highly charged Ar^{q+} (q = 7 - 13) and Xe^{q+} (q = 10 - 26) ions on Au samples covered with thin films of C_{60} were determined. The film thickness was varied between zero and five monolayers. Over this thickness range, the electronic structure of the surface changes from Au-like to bulk C_{60}. By this the work function was gradually changed from 5.3 to 7.5 eV, and the conductivity from metallic to semiconducting and insulating.

The experiments presented in this section were performed with the IISIS setup at the KVI in Groningen. The setup is thoroughly described in section 3.2. During ion bombardment, the base pressure in the experimental chamber is kept in the 10^{-10} mbar regime. The ions used in the presented investigations are extracted from a 14 GHz electron cyclotron ion source. They interact with a sample installed at a sample holder, which is designed to ensure minimum exposure of the supporting structure to the impinging ion beam (cf. figure 3.17).

The gold Au(111) single crystal target is prepared by cycles of sputter cleaning with 7 keV Ar^+ ions and subsequent annealing at temperatures of up to 500°C. The surface composition can be checked by means of time of flight low energy ion scattering (cf. section 3.2.3). Thin films of C_{60} are deposited using an Omicron EFM3 evaporator. To calibrate the deposition rate, a quartz crystal microbalance is used. By scanning the quartz crystal through the C_{60} beam prior to deposition, it is ensured that the size of the evaporated C_{60} beam (determined by its full width at half maximum) covers the entire Au(111) crystal (8 × 5.5 mm). The films are

Katharina Dobeš

deposited at an elevated target temperature of 180°C, which is maintained for a short while after deposition to ensure relaxation of the evaporated C_{60} surface.

5.2.1 Experimental Results & Discussion

Dependence of the Electron Yield on the Film Thickness

To study the effect of thin films on the hollow atom dynamics, C_{60} films with a thickness of 1 - 5 monolayers were deposited on an Au sample. The effect of film coverage on the total electron yield was studied for the impact of 7 keV Ar^{q+} ions (q = 7,9,11,13) and 70 keV Xe^{q+} ions (q = 10,12,14, ..., 24, 26). For reference, total electron yields obtained with similar projectiles on a clean gold surface are shown in figure 5.6. In this graph, electron yields for Ar^{q+} (open symbols) were obtained at an incidence angle of 50°, yields for Xe^{q+} impact at 45° with respect to the surface normal. The data shown in figure 5.6 serve as reference for the electron emission yields obtained on the C_{60} films.
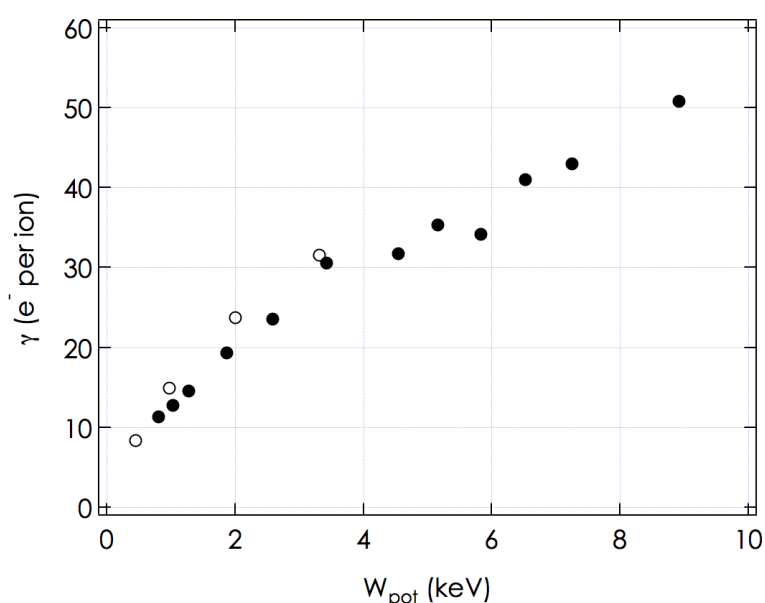
Figure 5.6: Total electron yield observed for Ar^{q+} (q = 7, 9, 11, 13; open symbols) and Xe^{q+} (q = 10, 12, 14, ...; full symbols) impact on clean Au(111) as a function of the projectile's potential energy. Ion impact angles were 50° for Ar^{q+} bombardment and 45° for Xe^{q+}, respectively.

The fact that the data shown in figure 5.6 connect nicely for both ion species, implies that possible contributions of kinetic electron emission to the observed total electron yield are small. The kinetic electron emission contribution can be estimated from measurements of Eder *et al.*, who investigated electron emission of clean gold under Ar^+ impact. It should be no more than 2 to 3 electrons [138].

To compare the electron yields γ obtained on C_{60} layers of variable thickness with electron emission from the clean gold substrate, the relative electron yield $\gamma_{rel}(\Theta)$ is introduced:

$$\gamma_{rel}(\Theta) = \frac{\gamma^{C_{60}}(\Theta)}{\gamma^{Au}(\Theta = 0)} \qquad (5.2)$$

In this equation γ^{Au} is the electron yield obtained on clean gold (cf. figure 5.6) and $\gamma^{C_{60}}(\Theta)$ the electron yield obtained after the deposition of Θ monolayers of C_{60}. Typical results obtained for γ_{rel} are shown in figure 5.7, where the relative electron yield for 70 keV Xe^{24+} ions impinging under 50° relative to the surface normal as a function of the C_{60} film thickness is shown. The C_{60} layers were deposited sequentially, i.e. C_{60} deposition was alternated with electron emission measurements. Typical electron emission spectra require a total ion fluence of about 10^5. The ions impinge onto the surface within an area of approximately 1 mm^2. From this it can be concluded that the surface damage to the thin films as a result of the ion bombardment is negligible.

The relative electron yield shown in figure 5.7 shows a distinct increase with the film thickness of C_{60} deposited onto the Au surface. The largest part of this increase already occurs after depositing a single monolayer onto the gold substrate. At a surface coverage of about five monolayers in thickness, the increase in the total electron yield saturates at approximately 1.35 times the value observed on the clean gold target. The fit to the data, which is also shown in figure 5.7 (red solid line) corresponds to an exponential gain curve, which is given by the equation:

$$\gamma_{rel}(\Theta) = \gamma_{rel}^{\infty} - \left(\gamma_{rel}^{\infty} - 1\right) e^{-\Theta/\Theta_{ch}} \qquad (5.3)$$

with Θ being the number of C_{60} monolayers and the parameter γ_{rel}^{∞} the relative yield for thick layes ($\Theta \mapsto \infty$), i.e. bulk C_{60}. In the above equation the fitting parameter Θ_{ch} denotes the characteristic layer thickness of the exponential function.

A series of experiments for the dependency of the total electron yield on the C_{60} layer thickness were performed for various charge states of Xe^{q+} and Ar^{q+} ion impact in order to investigate whether the increase in the relative electron yield depends on the potential energy of the projectile. The measured data were fitted

Katharina Dobeš
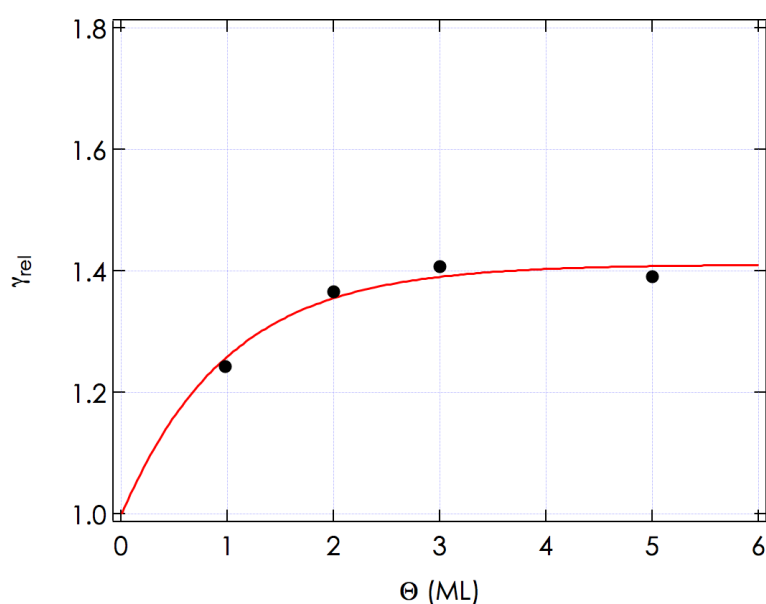
Figure 5.7: Relative electron yield per impinging 70 keV Xe^{24+} ion as a function of the layer thicknesses of C_{60} coverage. The incidence angle of the projectiles was 50°.

according to the gain function in equation 5.3. The thus obtained values for γ_{rel}^{∞} are shown in figure 5.8 for both Ar^{q+} (open symbols) and Xe^{q+} (full symbols) impact. Within the investigated range of W_{pot} the relative increase in electron yield does not vary much and corresponds to an increase of approximately 35% from clean gold to an Au surface covered by 5 monolayers of C_{60}. The sole exception to this behavior is found for Ar^{7+} ion impact, where the observed increase is twice as high.

At first glance the observed increase in the total electron emission yield with C_{60} coverage would seem surprising, as the binding energy of the electrons is ~ 2 eV larger for C_{60} than for a gold crystal. According to the classical over the barrier model [80] the distance above the surface, at which the highly charged projectile starts to first capture electrons R_c, scales inversely with the binding energy of the least bound electrons in the surface (see equation 2.21 in section 2.3.1). For a bulk C_{60} target it would therefore be expected that the distance of first electron capture is shorter than above a clean gold crystal. As a consequence for the C_{60} target, less time is available in front of the surface for the relaxation of the hollow atom. In addition, due to the resonant nature of the electron capture process, in this case, lower-lying, more tightly bound projectile states will be filled (cf. equa-
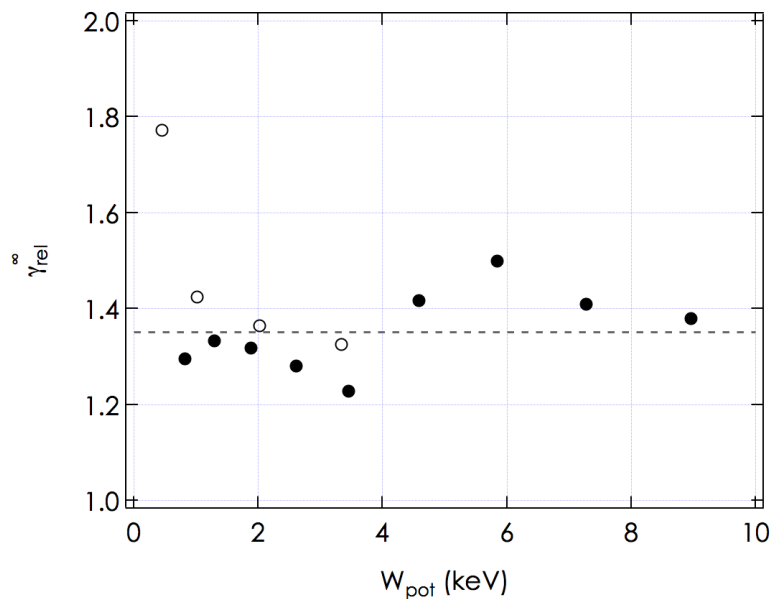
Figure 5.8: The relative yield γ_{rel}^{∞} as a function of the potential energy carried by the impinging projectile for Ar^{q+} (open symbols) and Xe^{q+} (full symbols) ion impact on C_{60} at 50° impact angle. The depicted values are obtained with equation 5.3.

tion 2.20) and fewer Auger de-excitation steps will therefore be necessary for the relaxation of the hollow atom. Both of the above would imply that a decrease in electron emission yield could be expected for C_{60} coverage compared to clean gold surfaces.

Recently Lake and co-workers extended the classical over the barrier model to thin dielectric films on top of metallic surfaces [150, 151]. The potential profile of a classical electron in a vacuum-dielectric-metal system was determined. It was found that the presence of the dielectric film can significantly influence the neutralization process of the highly charged ion in front of the surface. The distance of first electron capture critically depends on the thickness of the dielectric film, its permittivity and band gap and also on the charge state of the projectile. The authors in [151] determine three different regimes of electron capture (see also figure 5.9):

- A regime which is *limited by the vacuum barrier* and where electrons are first captured from the bulk metal.

Katharina Dobeš
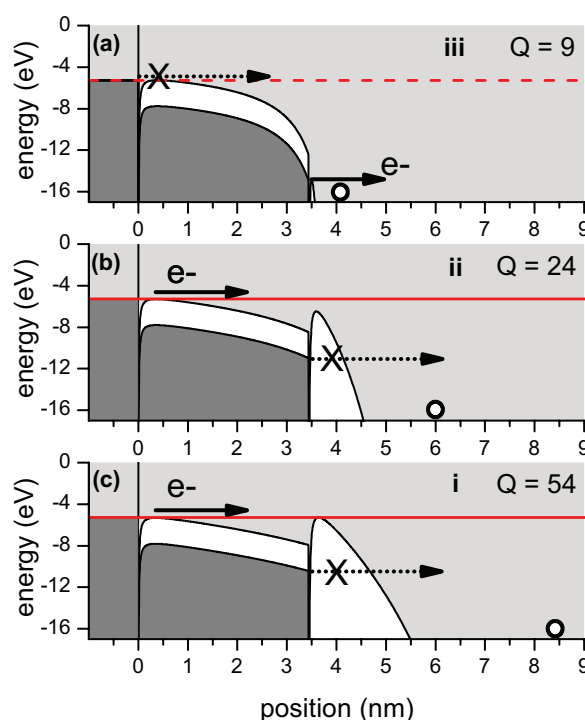
Figure 5.9: Electron potential energy plots for highly charged ions ($Q = 9, 24, 54$) approaching an Au(111) surface covered with 3.4 nm of C_{60}. The three plots represent (from bottom to top) (i) vacuum limited, (ii) thin film limited electron capture from the metal and (iii) capture from the dielectric. Picture from [151].

- A second so-called dielectric *film-limited* regime, where the first electron is still captured from the metal but the distance of first capture is determined by the potential barrier between the Fermi edge of the metal and the conduction band minimum of the dielectric film. This can either result in an enhancement or a suppression of the number of emitted electrons in front of the surface.

- A third regime of first electron *capture from the dielectric*, where the film completely shields the metal.

For thin films of C_{60} on a gold substrate, the authors in [151] were able to model both, the relative increase in experimentally observed electron emission yield γ_{rel}^{∞}, as well as the layer thickness, at which this increase is found to saturate (cf. figure 5.7). Their model predicts that for the investigated ion charge state and C_{60} layer thickness, the first captured electrons will originate from the gold substrate

and that the saturation observed in the experiments stems from a transition from the vacuum-limited to the dielectric film-limited regime (see above), which according to their model is expected to occur at approximately 4 monolayers of C_{60} coverage (in close agreement with our experimental results).

Another reason for the observed increase in electron emission yield might be the larger escape depth of electrons from C_{60} as compared to gold. An effect of the escape depth on the observed electron emission yield has been demonstrated for highly ordered pyrolytic graphite (HOPG) surfaces [160]. For ion impact parallel to the graphite planes (open geometry) the electron yield was found to be three times as high as for impact perpendicular to the graphite planes.

Finally, it is unlikely that the existence of a band gap in bulk or thick layers of C_{60} drives the enhancement of the electron yield by inhibiting resonant electron loss from the hollow atom back into empty states of the surface. The observed relative yield increase is realized to a large extend already by covering the gold substrate with a single monolayer of C_{60} (cf. figure 5.7). It is known from photoemission and atomic force microscopy studies on Au substrates covered with thin films of C_{60} that a film thickness of a single monolayer does not suffice for the development of the full band gap.

Influence of the Projectile Charge State and Incidence Angle on the Yield Change

A deeper insight into the involved processes can also be obtained from investigating the angular dependency of the electron emission yield for different projectile charge states. For this purpose measurements for Ar^{13+} and Ar^{4+} ion impact were performed and are presented here. The observed electron yields for gold surfaces covered with thin films of C_{60} of variable thickness are again compared to results from clean gold surfaces.

For reference the electron emission yield from a clean Au(111) surface as a function of the projectile impact angle with respect to the surface normal is shown in figure 5.10. The data is shown for three different projectile impact energies, i.e. 91 (squares), 28 (triangles) and 6.5 (circles) keV. Below the threshold for kinetic electron emission (for Ar ions the threshold energy is about 12 keV [138]), the observed electron yield is virtually independent of the kinetic energy of the projectile, as can be seen from the measured yields for 28 keV and 6.5 keV. In addition the electron yield is higher for grazing incidence angles, as in this case both the interaction time in front of the surface as well as the geometric path length of the projectile within the electron escape zone below the surface is increased (cf. section 2.3.3).

Katharina Dobeš
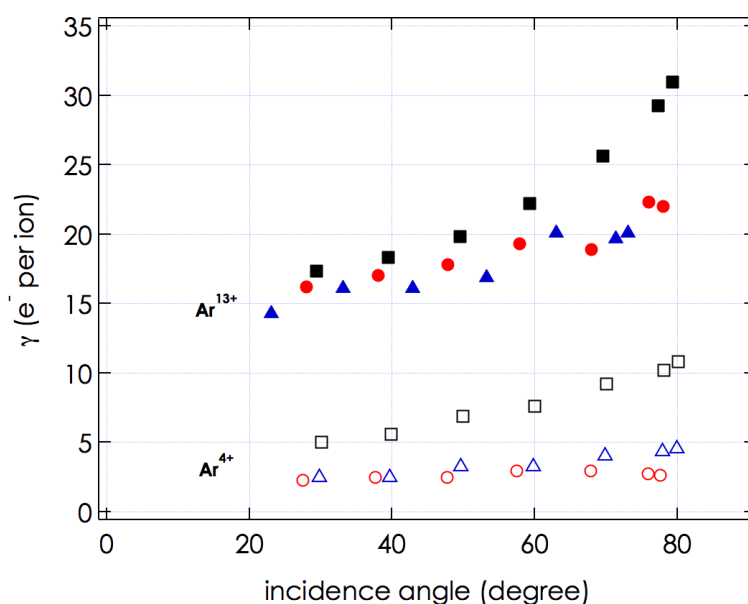
Figure 5.10: Total electron yield observed for Ar^{4+} (open symbols) and Ar^{13+} (full symbols) impact on clean Au(111) as a function of the projectile's incidence angle. The data was obtained at three different impact energies, i.e. 91 keV (■, □), 28 keV (▲, △) and 6.5 keV (●, ○).

The relative electron yield increase on C_{60}-covered surfaces according to equation 5.3 is shown in figure 5.11. Electron yields for four different incidence angles between 30° and 80° with respect to the surface normal are shown. Figure 5.11 compiles data for both the impact of Ar^{4+} (open symbols) as well as Ar^{13+} (full symbols) projectiles at an incidence energy of 28 keV. As can be seen from figure 5.11, the relative increase in electron emission yield is higher for Ar^{4+} impact than for Ar^{13+} projectiles. For gracing incidence angles this is most obvious.

All data presented in figure 5.11 is fitted according to the gain function in equation 5.3 (solid lines). The values of the fitting parameters γ_{rel}^{∞} and Θ_{ch} are shown in figure 5.12 for the full range of investigated impact angles for both projectile species (Ar^{4+} on the left side, Ar^{13+} on the right). Overall, the characteristic layer thickness Θ_{ch} seems to be independent from the angle of incidence (squares in figure 5.12). It is a bit higher for Ar^{4+} impact with approximately Θ_{ch} ~1.3 monolayers than for Ar^{13+} impact, where it falls slightly below 1 monolayer. For both projectile charge states however, the dominant contribution of the increase in electron yield stems from the deposition of the first C_{60} monolayer. The fitting parameter
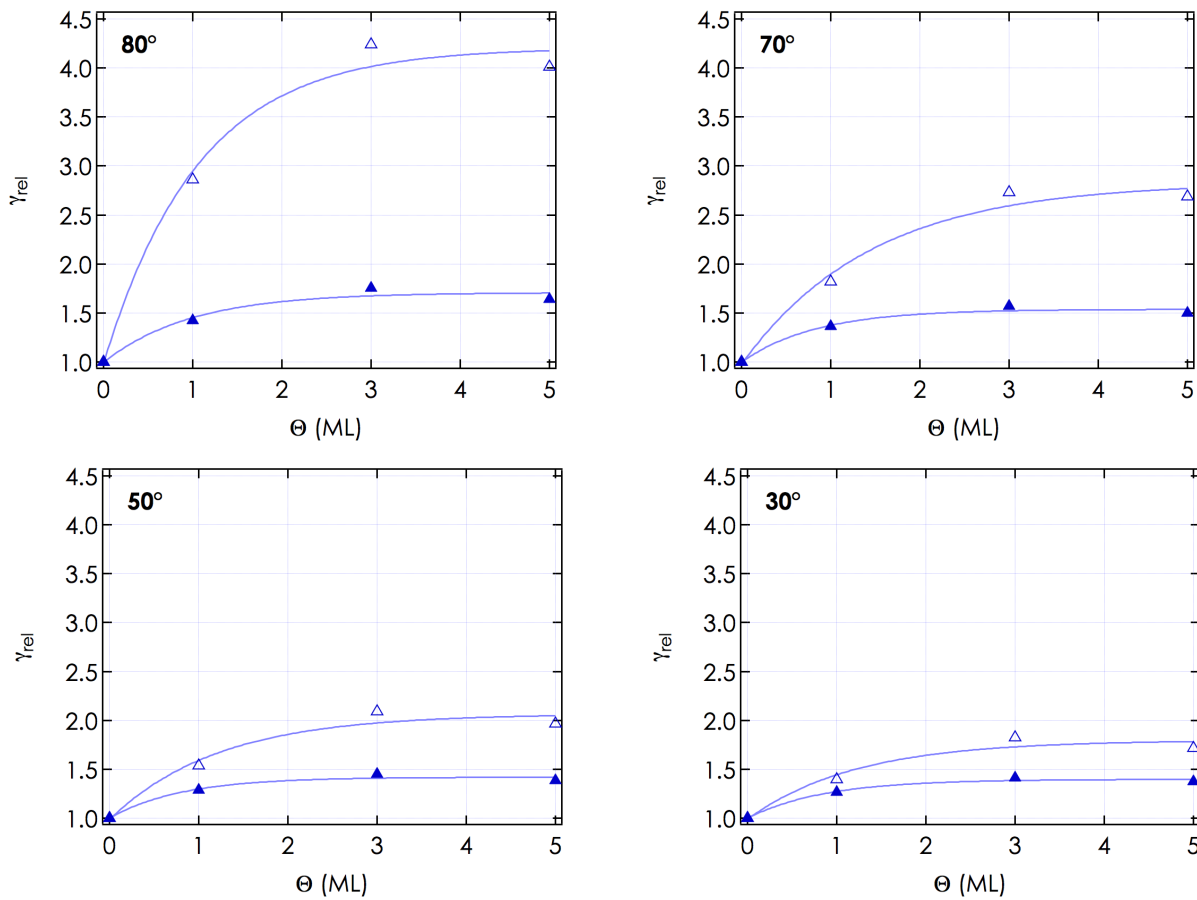
Figure 5.11: Relative electron yield γ_{rel} as a funtion of the of the C_{60} film thickness for Ar^{4+} (open symbols) and Ar^{13+} (full symbols) impact at different incidence angles. The fit to the data is derived with equation 5.3.

γ_{rel}^{∞} is almost independent from the impact angle for Ar^{13+} ions but shows a strong increase towards more gracing incidence angles for Ar^{4+} projectiles.

In order to asses the reason for the observed increase in electron yield, the difference in absolute electron yield $\Delta\gamma$ between a surface covered with 5 monolayers of C_{60} and a clean gold target was investigated for both ion species, i.e. Ar^{4+} and Ar^{13+}. As can be seen in figure 5.13, the difference in absolute yield is the same for Ar^{4+} and Ar^{13+} ion impact in contrast to the relative increase (cf. figure 5.11). This observation strongly suggests that the observed increase in electron yield is not due to the potential energy introduced by the impinging ion but rather gov-
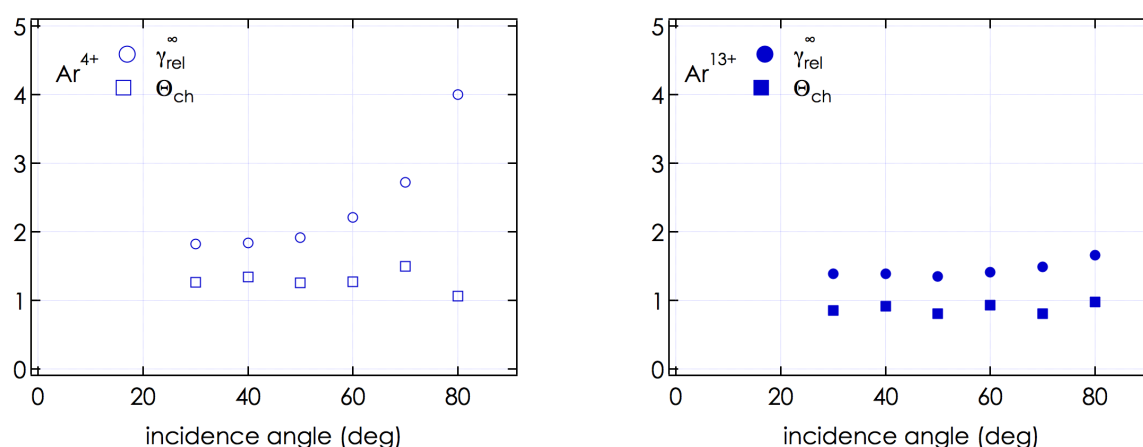
Figure 5.12: Values for the fitting parameters γ_{rel}^{∞} and Θ_{ch} according to equation 5.3 for the impact of Ar^{4+} and Ar^{13+} as a function of the impact angle with respect to the surface normal.

erned by the kinetic energy of the projectile. This is supported by the functional behavior of the angular dependency of $\Delta\gamma$, which can be fitted nicely to a cos^{-1} -dependency (solid line in figure 5.13), which is in accordance with the angular dependency generally observed for kinetic electron emission (cf. section 2.3.3).

For gold the threshold for kinetic electron emission lies at an impact energy of ~ 12 keV. The contribution to the total electron yield from kinetic emission at the investigated impact energy is therefore expected to be rather small (about 1 electron per ion at normal incidence [138]). No information is available on the threshold for kinetic electron emission neither for thin films of C_{60} nor for bulk C_{60}. However, to realize the observed enhancement in electron emission when covering a clean surface with thin films of C_{60}, the threshold energy must be lower for C_{60} than for clean gold.
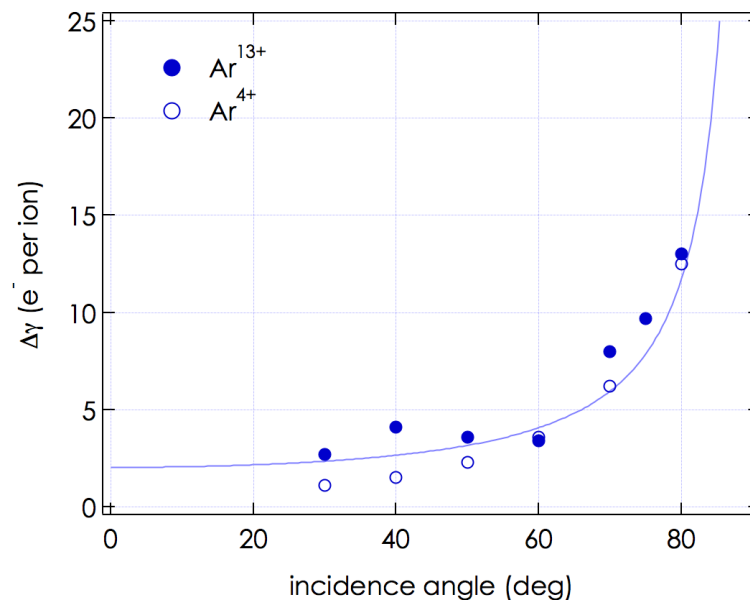
Figure 5.13: Difference in absolute electron yield between a surface covered by 5 monolayers of C_{60} and clean Au for Ar^{13+} impact (full symbols) and Ar^{4+} impact (open symbols). The fit to the data follows a $\cos^{-1}$ - dependency.

5.2.2 Summary & Concluding Remarks

Electron emission yields from highly charged ion impact were determined for clean gold surfaces as well as thin films of C_{60} deposited onto a gold substrate. The influence of the C_{60} layer thickness on the electron yield was investigated as a function of the C_{60} layer thickness, for various projectile charge states, impact angles and energies. It was found that the *relative* electron yield (from C_{60} covered surfaces compared to clean gold) increases with C_{60} coverage and that the observed enhancement saturates at about 35%, when five monolayers of C_{60} are deposited onto the Au substrate. This yield increase can be understood on the basis of an adapted classical over the barrier model [150, 151] for thin dielectric films on top of metallic surfaces, in which the presence of the dielectric film causes an enhancement of the distance of first electron capture R_c. The model also predicts that for the experimental parameters of this sturdy, the first captured electrons will originate from the gold bulk beneath the C_{60} film.

An exponential gain function has been successfully used to describe the yield enhancement for various projectile charge states and impact angles. It was found that the characteristic layer thickness is about constant for all investigated inci-

dence angles and does not differ much for Ar^{4+} and Ar^{13+} bombardment. On the other hand the relative enhancement in yield is found to increase towards lower charge states. This is most prominent for gracing incidence ions.

The difference in *absolute* yield from gold and C_{60} is the same for Ar^{4+} and Ar^{13+} bombardment. From this it was concluded that the observed yield increase is not due to the projectile's potential energy but driven by the kinetic energy of the impinging ion. It is suggested that this increase can be explained by the different kinetic electron emission thresholds for gold and C_{60}.

To assess how the deposition of thin dielectric films on metallic substrates influences the hollow atom formation and decay dynamics in front of the surface, lower impact velocities and higher projectile charge states would be required.

5.3 Electron Emission from Highly Ordered Pyrolytic Graphite

Studying electron emission yields from slow and medium energy, highly charged ions can help to elucidate their neutralization dynamics upon surface impact. In addition the interaction of highly charged ions with graphite surfaces is also of interest for plasma wall interaction in fusion experiments (cf. section 2.3). Particle induced electron emission will determine the plasma sheath potential, which accelerates particles emerging from the confined plasma onto the vessel walls [134-136].

Generally, ion-induced processes depend both on the kinetic (KE, cf. section 2.3.3) as well as the potential energy (PE, cf. section 2.3.2), which the projectile carries towards the surface. In the production of a highly charged ion Z^{q+}, the sum of the ionization energies, which have to be spent to remove q electrons from the initially neutral atom, is stored in the highly charged ion (cf. figure 2.16). For high charge states this potential energy can add up to several keV and might therefore exceed the kinetic energy of the projectile. The release of this internally stored energy upon surface impact of the highly charged ion will give rise to several ion induced phenomena such as potential sputtering [83, 84] and potential electron emission [81, 131] (see section 2.3.2).

The neutralization of a highly charged ion sets in well above the surface (see section 2.3.1), by quasi resonant capture of electrons into highly excited Rydberg states of the projectile, while lower lying energy levels remain empty [83, 85]. The so-formed transient 'hollow atom' [80, 131, 142] will rapidly start to decay in an auto-ionization cascade by electron exchange processes with the surface. The number of electrons thus emitted above the surface will depend on the interaction time above the surface [80, 184], i.e. scale inversely with the velocity component towards the surface $\propto 1/\sqrt{v \cdot \cos \vartheta}$ (cf. equation 2.24), if ϑ is the impact angle with respect to the surface normal. When the highly charged ion arrives at the surface, the de-excitation will be accelerated, as outer electrons are peeled-off due to the electronic screening at the surface [80]. The corresponding contribution to the observed electron emission yield, $\gamma_\infty(q)$ (cf. equation 2.24), will to a first approximation not depend on the impact velocity [138]. Just below the surface, inner shell vacancies will finally recombine by emission of fast Auger electrons and/or x-rays.

The angular and velocity dependency of the potential electron emission yield can therefore be summed up to (cf. equation 2.24) [138, 158]:

$$\gamma_{PE}(v, \vartheta) = \gamma_\infty + \frac{c_v}{\sqrt{v \cdot \cos \vartheta}} \tag{5.4}$$

Apart from potential electron emission, kinetic emission of electrons will increasingly become important above a certain threshold impact velocity v_{th} (cf. equation 2.26). Kinetic electron emission is related to an energy transfer from the projectile to the electronic system of the solid and therefore occurs as the ion finally penetrates the target bulk [133, 159, 160]. Kinetic electron emission involves a sequence of several mechanisms, i.e. energy transfer from the projectile to the electronic system of the solid in a collisional excitation, transport of generated electrons to the surface and finally the escape of electrons through the surface-vacuum boundary [132, 133].

There will be a velocity threshold v_{th}, below which kinetic electron emission is impossible due to insufficient energy transfer in a collision with the electronic system of the solid. Above it, the kinetic electron emission yield will follow the energy dependency of the electronic stopping power S_e (cf. equation 2.25). As the energy deposited into the electronic system of the solid gradually increases with the projectile energy, the kinetic electron emission yield will increase approximately linearly with the impact velocity [133, 161]. Overall, the number of emitted electrons will be proportional to the geometric path-length of the projectile within the near surface electron escape depth [133] and therefore scale with $\propto \cos\vartheta^{-1}$. For heavy particle impact, sometimes deviations from this inverse cosine law are observed [133, 165, 166] due to e.g. recoil ionization, deviations from the straight line approximation of the ion path through the surface but also variations of the electronic stopping power as the projectile is gradually slowed down in the surface [167].

In summary the total electron emission yield including both contributions from potential as well as kinetic emission can thus be approximated by the relation (cf. equation 5.1) [131, 138, 158]:

$$\gamma = \gamma_{PE} + \gamma_{KE} = \underbrace{\left(\frac{c_v(q)}{\sqrt{v \cdot \cos\vartheta}} + \gamma_\infty(q) \right)}_{\gamma_{PE}} + \underbrace{\Theta\left(v - v_{th}\right) \frac{c_{KE}(0)\left(v - v_{th}\right)}{\cos\vartheta}}_{\gamma_{KE}} \qquad (5.5)$$

if ϑ is again the impact angle with respect to the surface normal. Here, the Heaviside step function $\Theta\left(v - v_{th}\right)$ governs the onset of kinetic electron emission above the velocity threshold v_{th}.

In this section, systematic investigations of electron emission yields from highly ordered pyrolytic graphite surfaces (HOPG) during highly charged ion impact will be presented. Total electron emission yields were determined for Xe^{q+} (q = 7, ... 28) projectiles, for incidence angles between 40° and 10° with respect to the surface normal. The projectile impact energies ranged from 0.5 - 5 keV/amu, thereby

Katharina Dobeš

covering energies above and just below the threshold energy for kinetic electron emission, which for HOPG is $v_{th} \sim 1.5 \cdot 10^5$ m/s [230]. For particle velocities above this threshold, the relative importance of potential and kinetic electron emission are generally not easy to assess [158]. Varying the projectile impact angle, charge state and velocity might however aid in disentangling their respective contributions following equation 5.5.

The experiments were preformed at the IISIS setup at KVI Groningen (cf. section 3.2 for details on the experimental setup). During experiments, the ultra high vacuum chamber was kept at a base pressure in the 10^{-10} mbar regime by a turbomolecular pump. Projectile ions are produced in a 14 GHz ECR ion source and then selected and focused by a sector and quadrupole magnets. For low impact energies, the extracted ion beam can be decelerated in a six-element lens system, which eventually results in a slight deflection due to the high positive potential at the target (cf. figure 3.16). For the lowest impact energies, the effective incidence angle is therefore corrected in the data evaluation in accordance with SimIon [179] simulations for the deflection. An HOPG sample with a graphite layer orientation parallel to the surface plane is cleaved with an adhesive tape just before installation in the vacuum chamber (cf. section 3.2.3).

The electron statistics setup [180-182] used to determine total electron emission yields, is mounted under 90° with respect to the impinging ion beam (cf. section 3.2.1). A set of six electrodes surrounding the target is used to optimize the electron collection efficiency onto the detector. The electrons are accelerated towards the detector by a high positive potential of 30 kV. From the pulse height at the detector output, both the mean number of electrons emitted in a single ion impact event as well as the respective electron number statistics can be determined (cf. sections 3.2.2).

5.3.1 Experimental Results & Discussion

Total electron emission yields of HOPG were determined at various impact energies, ranging from 7.2 keV ($\sim 1 \cdot 10^5$ m/s) to 328 keV ($\sim 7 \cdot 10^5$ m/s). In the selected impact energy range, both velocities below as well as beyond the threshold for kinetic electron emission at $v_{th} \sim 1.5 \cdot 10^5$ m/s are covered. In figure 5.14 the total electron emission yields for the impact of Xe^{24+} ions is shown as a function of the velocity component towards the surface $v_{\perp}$. For obtaining the data in figure 5.14, the impact energy was kept constant (as labeled for the individual data sets in the graph) and the impact angle was varied between 30° and 80° to cover a wider range of impact velocities.

Katharina Dobeš
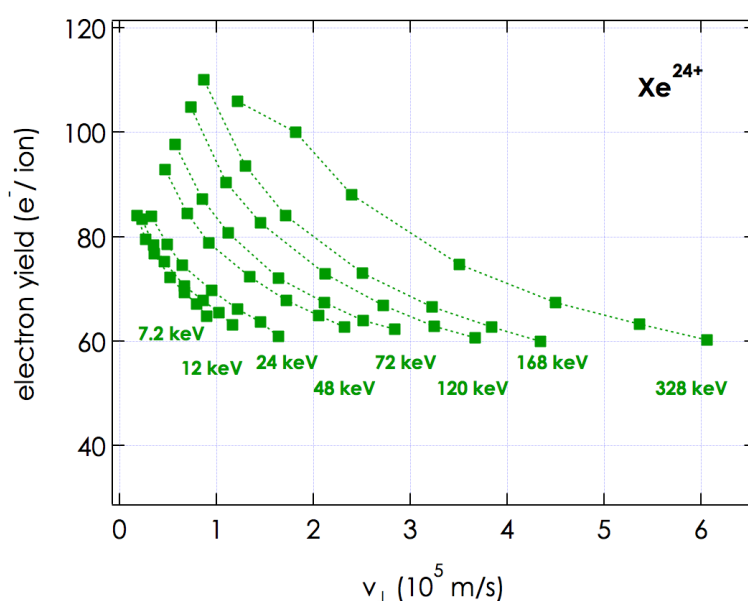
Figure 5.14: Total electron emission yield from HOPG as a function of the impact velocity towards the surface $v_\perp$. The graph comprises data for different impact energies of Xe^{24+} ions both below as well as above the threshold for kinetic electron emission ($v_{th} \sim 1.5 \cdot 10^5$ m/s).

At impact energies below ~ 12 keV ($\sim 1.3 \cdot 10^5$ m/s), the observed electron emission yield is independent from the impact energy and becomes only a function of the velocity component towards the surface $v_\perp$. As a result, in figure 5.14 the data sets below this impact energy coincide. From the fact that the observed electron yield only depends on $v_\perp$ but not on the impact energy, it can be inferred that any contribution from kinetic electron emission can be neglected here (cf. equation 5.5). The observed electron emission yield is solely due to potential emission. This is additionally supported by the fact that for the respective impact energies, the velocity towards the surface $v_\perp$ lies below the threshold velocity for kinetic electron emission, i.e. $v_{th} \sim 1.5 \cdot 10^5$ m/s.

The electron yields observed for 7.2 keV and 12 keV should therefore be adequately represented by the expression for potential electron emission in equation 5.4. The two data sets can be used to obtain the respective fitting parameters $\gamma_\infty(q)$ and $c_v(q)$. Subsequently keeping the thus determined fitting parameters for PE constant for the entire data set, the angular dependency of the kinetic contribution to the electron yields above the threshold energy can now be fitted

Katharina Dobeš
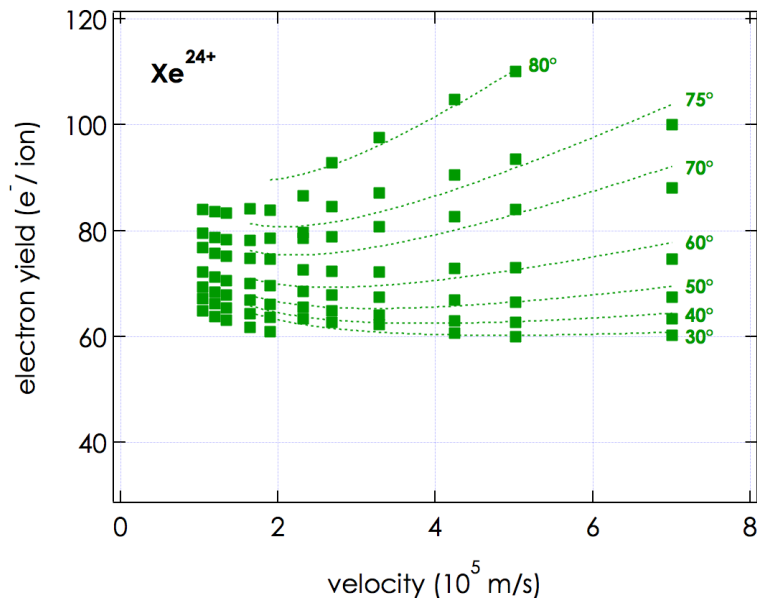
Figure 5.15: Total electron emission yield from HOPG as a function of the impact velocity. A wider range of impact velocities is covered by varying the impact angle of the of Xe^{24+} ions as indicated in the graph. The dashed lines are fits to the expression for γ_{KE} in equation 5.5 for a constant threshold velocity of $v_{th} = 1.5 \cdot 10^5$ m/s [230]. For details see text.

according to equation 5.5. In doing so, a threshold velocity of $\sim 1.5 \cdot 10^5$ m/s was assumed in accordance with the classical estimation. The result of this fitting procedure is shown in figure 5.15, where the entire set of measured electron yields for Xe^{24+} is shown again, including fits to the expression for the total electron emission yield according to equation 5.5 (dashed lines).

From the fitting procedure in figure 5.15, a value for the angular dependency of the kinetic electron emission yield, i.e. for the expression $\gamma_{KE}(0) \cos \vartheta^{-1}$ is obtained for each impact angle. To actually determine the fitting parameter $\gamma_{KE}(0)$, the thus obtained angular dependency of γ_{KE} is at first fitted to a $\cos^{-1}$ - dependency. This is shown in figure 5.16, where the angular dependency of the kinetic contribution to the electron yield as obtained from the fits in figure 5.15 is shown as green symbols, and the respective $\cos^{-1}$ fit as a black dashed line. Obviously fitting the angular dependency of the kinetic electron emission yield by a $\cos^{-1}$ dependency is a rather insufficient representation of the experimentally obtained data. A much better fit is obtained by replacing the $\cos^{-1}$ fit by a $\cos^{-\beta}$ dependency, where the

Katharina Dobeš
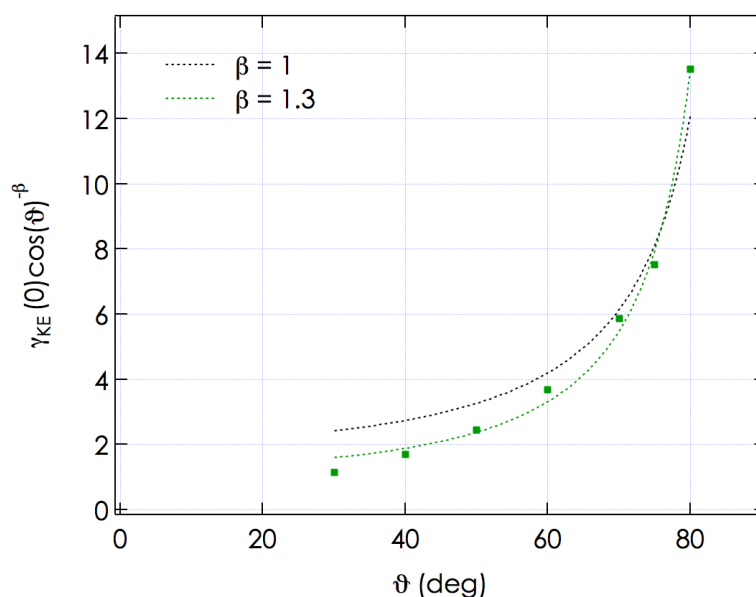
Figure 5.16: Results for the kinetic electron emission fitting parameter $\gamma_{KE}(0)\cos(\vartheta)^{-1}$ for all investigated impact angles (squares) obtained from the data set in figure 5.15. To obtain $\gamma_{KE}(0)$, a $\cos^{-1}$ dependency can be fitted (black dashed line). An even better fit is obtained with a $\cos^{-\beta}$ dependency, with β as a free fitting parameter. For details see text.

exponent β is a free fitting parameter. This is demonstrated by the green dashed line in figure 5.16, which corresponds to a β of ~ 1.3.

Deviations from a plain $\cos^{-1}$ angular dependency of the kinetic electron emission yield γ_{KE} were reported for various target projectile combinations in the literature [133, 165, 166, 231, 232]. In a series of experiments it was found empirically that the experimental data for the variation of the kinetic electron emission yield with the projectile impact angle, can best be fitted to a relation of the form $\gamma_{KE} \sim \gamma_{KE}(0) \cdot \cos^{-\beta}$. Here the free fitting parameter β varies between $0.5 \leq \beta \leq 1.5$ [133]. Experimental observations revealed that it increases with the projectile mass and decreases with the projectile impact energy [165, 231].

As kinetic electron emission is based on a collisional energy transfer from the impinging projectile to the electronic system of the solid (cf. section 2.3.3), it is generally expected that the electron emission yield is proportional to the energy transfer to target electrons in electronic collisions, i.e. the electronic stopping power (cf. equation 2.27). For heavy particle impact however, a non-negligible contribution
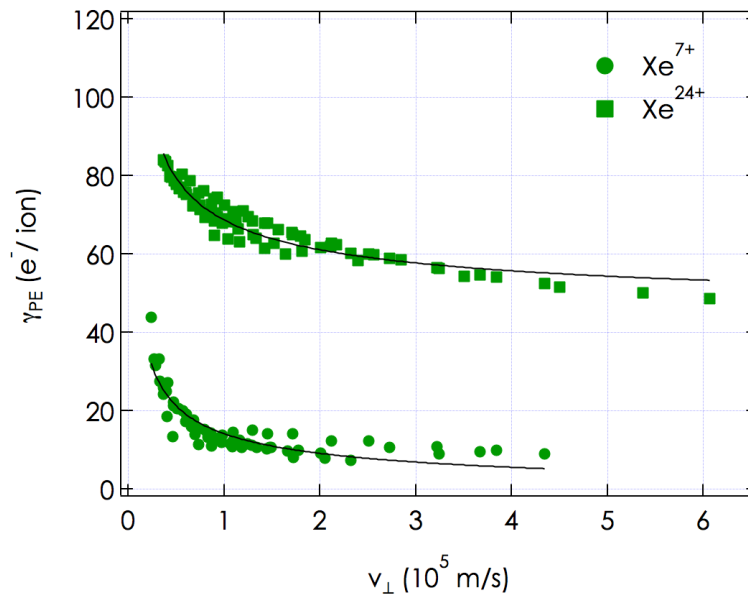
Figure 5.17: Potential electron emission yield obtained by subtracting the respective kinetic contributions. For both investigated charge states (i.e. ● Xe^{7+} and ■ Xe^{24+}) the data now coincides on one single curve and follows the general trend expected for potential electron emission (cf. equation 5.5), which is indicated by the fit (black line). For details see text.

to the energy deposited in the electronic excitation of the solid may originate from recoiling target atoms of the collision cascade, which is initiated by the particle impact [165]. This contribution from ionizing collisions with recoiling atoms will introduce a relation of the kinetic electron emission yield to the nuclear stopping power, i.e. in fact a second term in the simple relation of equation 2.27. It was shown [165] that this results in a variation of the kinetic electron emission yield which is faster than $1/\cos\vartheta$, i.e. a fitting parameter $\beta > 1$. In addition a $\beta \neq 1$ will consider deviations from the straight line approximation of the ion path through the electron escape depth in the solid, but also any slowing down of the projectile, which will result in a variation of the electronic stopping power [167].

With the fitting parameter $\gamma_{KE}(0)$ thus obtained from the data in figure 5.15, the kinetic contribution can be subtracted from the observed total electron yield in figure 5.15. The remaining yield can now be attributed to sole potential electron emission and should therefore only depend on the velocity component normal to the surface $v_\perp$ (cf. equation 5.5) but not the projectile impact energy. This is
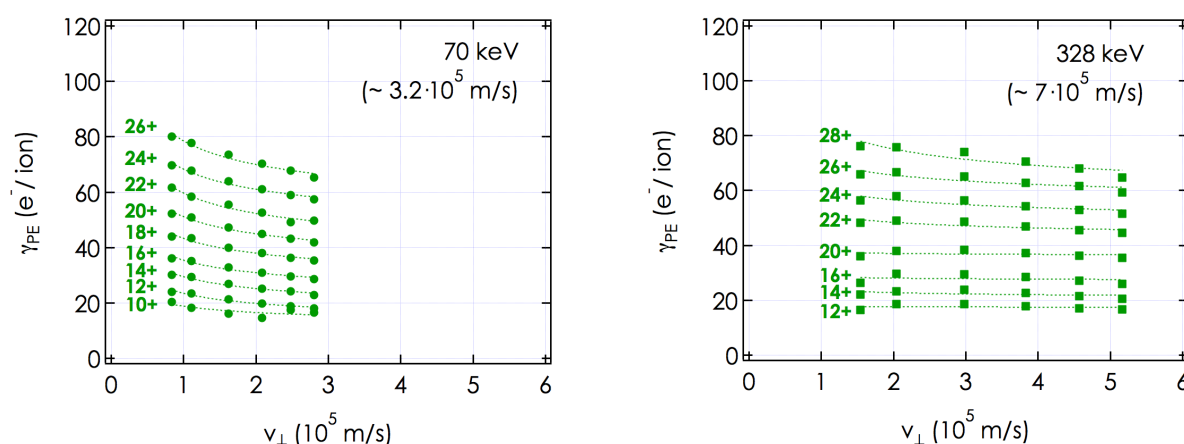
Figure 5.18: Potential electron emission yield γ_{PE} after subtraction of the kinetic contribution for various Xe charge states (q= 10, ..., 28) at two different impact energies, i.e. 70 keV (left) and 328 keV (right). The dashed lines represent a fit to the measured data according to equation 5.4.

demonstrated in figure 5.17, where the respective potential contributions of the observed electron emission yield indeed coincide onto one single curve for both, Xe^{24+} projectiles but in a similar way also for Xe^{7+} ion impact. In addition the remaining potential electron emission yield in figure 5.17 nicely follows the general trend expected for potential electron emission as indicated by a fit according to equation 5.4 (black line).

In a similar way the kinetic electron emission contribution to the total electron yield can be eliminated for various charge states. This has been done in figure 5.18 for two different impact energies, i.e. 70 keV (left) and 328 keV (right). The dashed lines represent fits to relation for the potential electron emission according to equation 5.4. As can be seen from figure 5.18 the potential electron emission yield depends only weakly on the velocity component towards the surface, i.e. $V_{\perp}$. This is in contrast to conducting targets like e.g. Au, were a much stronger dependency on the impact angle was found [158]. It was argued [224] that this is due to an increased binding energy of valence electrons in the case of HOPG (~ 7.5 eV) compared to those from the conduction band of a e.g. gold (~ 5 eV). As a result the critical distance at which electron capture sets in upon the approach of the highly charged ion towards the surface, is smaller and therefore less time is available for de-excitation processes resulting in the emission of electrons in front of the surface.

Katharina Dobeš

5.3.2 Summary & Concluding Remarks

Total electron emission yields from a HOPG surface under the impact of xenon ions of various charge states were studied. The impact energies of the ions ranged from below to well above the threshold for kinetic electron emission. By a thorough examination of the experimental data, contributions from kinetic and potential electron emission could be distinguished.

It was demonstrated that for the lowest investigated impact energies, kinetic electron emission is indeed negligible and the observed electron emission is solely driven by the potential energy stored in the projectile. This is in agreement with the threshold velocity for kinetic electron emission determined from classical considerations. Below this threshold velocity, for a given projectile charge state the potential electron emission yield could be fitted successfully to an empirically derived formula. The thus obtained fitting parameters were then used to determine the angular dependency of the kinetic electron emission yield over a wide range of impact energies above the threshold for kinetic emission.

Although it is commonly assumed that kinetic electron emission scales with an inverse cosine law for the impact angle with respect to the surface normal, it was found in the studies presented here, that in the case of xenon projectiles, the data could be best reproduced using a $\cos^{-\beta}$- fit instead, with $\beta > 1$. This implies that in the observed electron emission yield, a non-negligible contribution of emitted electrons originates from ionizing collisions with recoiling target atoms in the collision cascade initiated by the projectile impact.

In the following, the thus obtained fitting parameter for kinetic electron emission was used to eliminate the KE contribution from the experimental data. The resulting potential electron emission yields γ_{PE} showed only a very weak dependency on the velocity component towards the surface $v_\perp$. This is in contrast to the potential emission yield from conducting surfaces and has been observed in the past for various insulating target materials such as LiF and CaF_2.

Katharina Dobeš

5.4 Comparison of the Electron Yield from Au, C_{60} and HOPG

*Part of the following has been published in [226]*
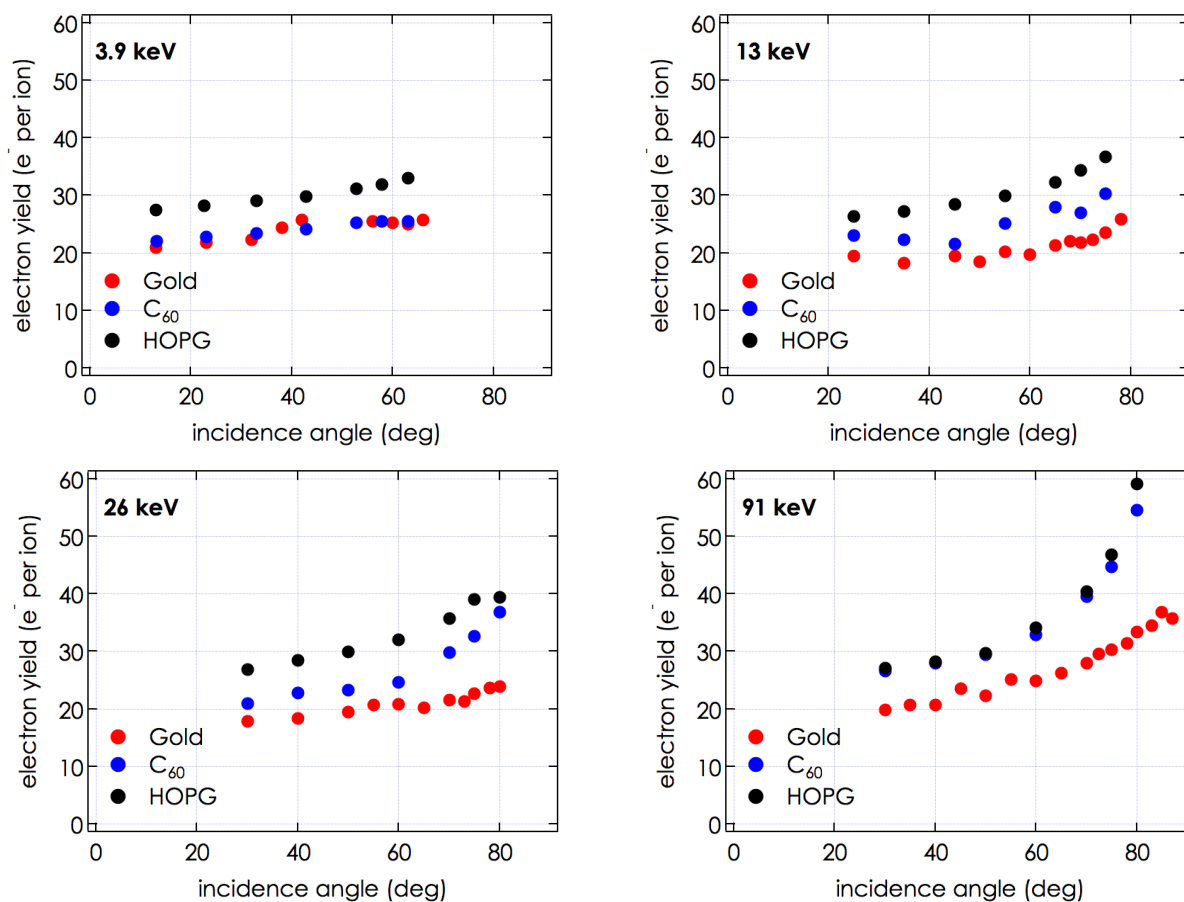
Figure 5.19: Comparison of the electron yield observed for Ar^{13+} ion impact on clean gold (red symbols), 5 monolayer thin films of C_{60} (blue symbols) and HOPG (black symbols) as a function of the impact angle with respect to the surface normal. The data are shown for four different impact energies.

Figure 5.19 shows a comparison for the total electron yield obtained on the three investigated surfaces, i.e. gold (in red), 5 monolayers of C_{60} on a gold substrate (in blue) and HOPG (in back). Measured electron yields are shown for four

Katharina Dobeš

different impact energies ranging from 3.9 keV to 91 keV. The presented energy range covers the threshold energy for kinetic electron emission of both HOPG (at $\sim$ 4 keV) and gold ($\sim$ 12 keV). The threshold energy for kinetic electron emission from thin layers of C_{60} is not known.

For an impact energy of 3.9 keV (upper left panel in figure 5.19) the electron emission yield for gold and a gold surface covered by five monolayers of C_{60} are the same, suggesting that the potential electron emission yield is the same for these two surfaces at this impact energy (as kinetic electron emission is not expected to play a significant role at energies that low). This probably points to the fact that the thin C_{60} film is not limiting the onset of potential emission (cf. the model of Lake et al., see page 171).

With increasing projectile impact energy the observed total electron yield of C_{60} and gold start to differ, whereas the difference increases as the kinetic energy is increased. Finally, for 91 keV impact energy, the observed electron yield of C_{60} is equal to the yield from the HOPG surface. Above its threshold velocity, the kinetic electron emission yield is known to increase about linearly with the impact velocity of the projectiles (cf. section 2.3.3). From the presented data it seems as if this increase was steeper for thin C_{60} layers than for HOPG and gold. This might also be due to effects from a variation in the ion penetration depth with the kinetic energy of the projectile: as the kinetic energy of the projectiles is increased, they penetrate deeper into the bulk of the surface, eventually entering deep into the gold substrate beneath the C_{60} film. This might result in a gradual change of the contribution of kinetic electron emission from the gold substrate to the observed electron yield for increasing impact energies. Additionally, the open structure of the C_{60} film might lead to an enhanced electron escape depth for electrons being generated below the surface.

Katharina Dobeš

6

Conclusion & Outlook

When ions impinge on solid surfaces, a variety of interaction phenomena is observed. These depend on the one hand on the properties of the projectiles, i.e. their kinetic and also internally stored (potential) energy. On the other hand also surface parameters such as the composition, the chemical reactivity, the topography, the electronic structure, the previous bombardment history, and many more are determinant. In this work, diverse aspects of ion-surface interaction processes were studied and analyzed.

One of the greatest challenges in the successful implementation of fusion energy for electricity production, will be the interaction of the very hot fusion plasma, with the walls of the containing vacuum vessel. A profound knowledge on plasma material interaction issues is hence very desirable. Therefore, the interaction of fusion relevant projectiles with materials considered to be used in the international fusion experimental reactor ITER were thoroughly studied within the framework of this thesis. The unique sensitivity and accuracy of the experimental setup used in the presented investigations allowed for studying ion surface interaction phenomena in-situ and in real-time. Experiments were performed under controlled laboratory conditions.

A wide range of projectiles including on the one hand seeding impurities such as Ar, Ne, and N but also fueling species such as D were investigated. Detailed studies were performed on their interaction with all of the three materials, which were originally planned to be used as plasma facing components in ITER, i.e. carbon, tungsten and beryllium. In the complex environment of a fusion reactor, mixed material layers will build-up during operation as a result of particle implantation, erosion and subsequent re-deposition as well as material migration. The incor-

poration of seeding impurities such as nitrogen but also the retention of the fusion fuel will have a severe influence on the operation of the fusion reactor. Hence, in this work a special emphasis was put on investigating multi-component systems.

While the vast majority of experiments on plasma wall interaction is restricted to analyzing surfaces post mortem, the studies presented in this thesis aimed at determining the individual reaction rates for the involved processes in situ, which can be a valuable contribution for understanding the basic mechanisms. With the experimental approach exploited in this thesis, a unique insight into the dynamics and built-up of mixed material layers could be gained. The presented data may aid in modeling and quantifying the respective plasma wall interaction processes.

The evolution of an amorphous, hydrogenated carbon layer under nitrogen impact was studied. Both the transient and the steady state sputtering behavior of the surface could be successfully modeled based on a simple set of rate equations. At first, hydrogen is preferentially sputtered from the surface, resulting in a hydrogen depleted, harder surface layer. This is apparently accompanied by a decrease in the molecule size of eroded hydrocarbons with increasing fluence. Additionally impinging nitrogen projectiles are implanted at the ion penetration depth. Steady state surface conditions are obtained, when the surface recession is of the order of the ion range and the nitrogen containing, hydrogen depleted layer has emerged to the surface.

On tungsten surfaces, an unexpected molecular effect for the erosion with nitrogen projectiles was found. The sputtering yield for di-molecular nitrogen projectiles at low energies (below 500 eV/at) is about 25% higher than the respective erosion rate for atomic ions. A qualitative explanation for this could be given based on a simple energy transfer model for direct collisions between target atoms and the two projectile species. For high nitrogen fluences, the built up of a tungsten-nitride phase within the ion penetration depth was reported in the literature. When saturating a tungsten surface with nitrogen, the change in total sputtering yield was found to be insignificant, with the partial nitrogen sputtering yield apparently balancing the reduced tungsten erosion. Although previously observed for other non-conducting targets (such as e.g. LiF), no enhancement of the sputtering yield for highly charged ion impact, i.e. so-called 'potential sputtering' could be observed on these nitrogen saturated surfaces.

The saturation dynamics of beryllium surfaces under nitrogen impact was studied. It was found to be composed mainly of three individual regimes: at first the interaction of the energetic nitrogen projectiles with the beryllium surface is marked by dominant projectile implantation. As the nitrogen content saturates at the ion implantation depth, a transition to net erosion is observed. Finally only when the

Katharina Dobeš

nitrogen saturated layer has emerged to the surface, dynamic equilibrium conditions are obtained with a constant nitrogen content in the surface and a surface erosion rate furthermore independent from the applied ion fluence. It was also observed that the oxidation rate of the beryllium surface decreases with increasing nitrogen saturation level and falls below any detectable limit for nitrogen saturated surfaces.

Subsequently the deuterium retention behavior of the resulting nitrogen saturated beryllium surface was studied and compared to the dynamics on pure beryllium. Initially the retention rate is similar for both surfaces and the local deuterium saturation concentration is reached at comparable fluences. On the nitrogen saturated beryllium surface, steady state conditions are reached at only about half the fluence that is needed to establish a dynamic equilibrium on pure beryllium. Post mortem NRA revealed that the areal density of retained deuterium is about twice as high for nitrogen saturated beryllium compared to pure beryllium. In the nitrogen saturated surface, defects created by the preceding nitrogen bombardment might serve as additional trapping sites and are probably responsible for this increased deuterium inventory. In steady state, only a very small erosion rate is observed for both surfaces. In addition thermal desorption of implanted deuterium at an elevated surface temperature of 460 K was studied for both, pure and nitrogen saturated beryllium. An estimation of the desorption rate and dynamics could be made. At first the deuterium release rate is apparently limited by the recombination of D_2 molecules at the surface. For longer waiting times a clear change in the dynamics is observed and the desorption rate is then probably limited by deuterium diffusion to the surface.

In the near future the investigations so far performed on beryllium surfaces will be extended. Studies on the oxidation behavior of nitrogen saturated surfaces under more controlled conditions are planned. First results on estimating the oxidation rate of the surface as a function of the nitrogen content show great promise for a more quantitative determination. In addition, mixing of both nitrogen saturated as well as pure beryllium surfaces with helium will be studied, as helium is the end product of the fusion reaction exploited in ITER. Since surface defects are important trapping sites for hydrogen isotopes, it would also be interesting to expand the studies presented in this thesis to well defined, pre-damaged surfaces (both beryllium and tungsten).

A fundamental re-designing of the quartz-crystal microbalance setup is planned for the near future (refer to B. Bergers work [233]), where the quartz crystal shall serve as a catcher for sputtered particles. Placed in near vicinity of a surface, which is bombarded with energetic particles, erosion rates could then be deter-

mined independently from any restrictions regarding temperature control (for investigations with e.g. high particle and heat fluxes but also varying surface temperature) or adhesion of the surface of interest to the quartz. This would also allow investigations of e.g. single crystal targets and measurements of the angular distribution of eroded particles.

In the second part of this thesis, a series of measurements for the emission of electrons upon highly charged ion impact on solid surfaces was performed. The presented measurements include studies on clean gold, gold surfaces covered with single to a few monolayes of C_{60} and a bulk carbon surface, i.e. HOPG. These investigations aimed at a more profound insight into the influence of the electronic structure of the target material on the hollow atom formation and decay dynamics in front and at the surface.

As a gold surface is gradually covered by single monolayers of C_{60}, an increase of the electron emission yield is observed, which saturates at about 35% of the respective yield on the clean gold substrate. Most likely this yield enhancement is due to an increase in the critical distance for first electron capture of the highly charged ion as it approaches the surface. The neutralization dynamics of the highly charged ion in front of the C_{60} films can be understood on the basis of an adapted classical over the barrier model, extended to thin dielectric films deposited onto solid surfaces. Accordingly the first captured electron will likely still originate from the gold substrate underneath the C_{60} film, within the experimental parameter range of the here presented investigations.

For a bulk carbon (i.e. HOPG) surface, the contribution of kinetic and potential electron emission to the total observed electron emission yield could be distinguished from a wide scan of projectile charge states, impact energies and angles. For the kinetic electron emission yield, a deviation from the commonly expected angular dependency of the emission yield was observed, implying that a non-negligible fraction of emitted electrons is generated in ionizing collisions of recoiling target atoms. The potential emission yield on the other hand showed only a very weak dependency on the interaction time of the projectile in front of the surface. This can probably be explained by the fact that for the HOPG surface, the critical distance of first electron capture is generally reduced compared to e.g. clean gold, due to the higher binding energies of conduction band electrons.

All in all it was found that the difference in total electron yield observed on the three surfaces are mainly due to kinetic electron emission. For lower impact energies (3.9 keV Ar ions), the observed electron emission yield on thin C_{60} films resembles the values observed on clean gold. As the projectile impact energy is

gradually increased, the electron yield from the C_{60} films approximates the yield observed for the HOPG surface. This can be attributed to an increased contribution of kinetic electron emission and the fact, that the electron emission yield observed for the C_{60} films is still limited by the Au bulk in the here presented energy and charge state range.

To actually assess the influence of thin dielectric films on the hollow atom dynamics of a highly charged ion upon surface impact, investigations at lower impact velocities and with higher projectile charge states would be required.
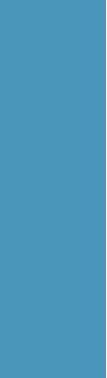
Danksagung

*Leider lässt sich eine wahrhafte Dankbarkeit
mit Worten nicht ausdrücken.*
(J. W. Goethe)

Tatsächlich fällt es schwer, die tiefe Dankbarkeit, die ich - endlich hier am Ende meiner Arbeit angelangt - empfinde, gebührend in Worte zu fassen. Ich will es dennoch versuchen ...

Zu allererst geht ein sehr großes Dankeschön an meinen Doktorvater Prof. Dr. Friedrich Aumayr. Nicht nur bist Du mir in Deiner Herangehensweise an wissenschaftliche Fragestellungen ein großes Vorbild gewesen, Du hast wahrhaft wie ein Vater über das Gelingen dieser Arbeit gewacht. Deine Anteilnahme übersteigt hierbei das rein Wissenschaftliche und selbst als wir Dir im Labor Deine Ionenquelle in Kleinstteile zerlegten, hattest Du aufmunternde Worte übrig (auch wenn in diesem Fall etwas Sorge mitschwang)!

Mit Deinem Dir eigenen, besonderen Geschick für Zwischenmenschliches hast Du mir im Laufe dieser Arbeit viele Türen und Tore geöffnet, mir eine Vielzahl an Messaufenthalten an den verschiedensten Forschungseinrichtungen quer durch Europa ermöglicht und mich dabei unterstützt, meine Arbeit auf internationalen Tagungen zu präsentieren und Kontakte zu knüpfen. Die Unterstützung die Du in dieser Hinsicht Deinen Doktoranden zu Teil werden lässt übersteigt bei weitem das Erwartbare und dafür möchte ich Dir danken!

Auch wenn meine Zeit hier am Institut von durchaus viel Arbeit geprägt war, sich mir immer wieder Herausforderungen in den Weg stellten, die sich zeitweilig auch

Katharina Dobeš

schon mal auf eine - zumindest subjektiv empfundene - mittelschwere persönliche Katastrophe aufblähen konnten, bin ich immer gerne hier gewesen und denke mit einem Lächeln an die vergangene Zeit zurück. Das verdanke ich vor allem einer Vielzahl an sehr lieben Kollegen.

Elisabeth, Du warst mir in all der Zeit sehr viel mehr als nur eine Kollegin! Mit Dir gemeinsam konnte es sogar Spaß machen, bis weit in den Abend hinein ratlos vor einem Problem zu stehen. Oft genug bist Du geblieben und hast geholfen, auch wenn es Dich persönlich nicht betraf. Die moralische Unterstützung, die Du mir damit geleistet hast, ist für mich unschätzbar. Viel konnte ich von Dir lernen auch wenn es darum geht, mit den Widrigkeiten des Lebens fertig zu werden und darüber nicht in Selbstmitleid zu vergehen! Darüber hinaus denke ich mit viel Freude an unsere gemeinsamen Auslandsaufenthalte zurück, an unsere Abendsonne in Russland, eine gemeinsame Achterbahnfahrt, einen Abend voller uralt-Werbespots, schwimmen auf der Donauinsel - kurz: eine schöne gemeinsame Zeit!

Valerie, Du bist zwar erst recht spät dazu gestoßen, aber Du warst dennoch eine unglaubliche Bereicherung für den Arbeitsalltag und auch weit darüber hinaus! Ich bin Dir dankbar, für die Farbe, die Du mitgebracht hast und schätze Dich sehr für Deine verquere Art zu Denken! Es macht nicht nur Spaß, mit Dir über physikalische Probleme zu diskutieren, sondern auch über die weite Welt da draußen zu philosophieren. Du hast mir bei Zeiten das Gefühl gegeben, dass ich zumindest in guter Gesellschaft bin, wenn ich auch manchmal aus der Norm fallen sollte! Dafür und, dass Du mir mit Sympathie begegnet bist, auch wenn ich mal nicht so gut drauf war, bin ich Dir sehr dankbar! Die Physik ist betrunken und das ist manchmal gut so ...

Gregor, wir hatten es wahrlich nicht immer leicht miteinander, aber ich denke dennoch eigentlich durchwegs gut an unsere gemeinsame Zeit zurück. Ich konnte wirklich sehr viel von Dir lernen, wenn es darum geht, wie man ein Problem, das sich im wissenschaftlichen Alltag so stellt, anpacken soll. Es war stets spannend, wenn auch manchmal hitzig, sich mit Dir auszutauschen! Auf unseren gemeinsamen Messaufenthalten hätten wir zwar vielleicht manchmal jemanden gebraucht, der uns ein wenig einbremst, aber wir hatten trotz allem Spaß zusammen und wussten auch, es uns gutgehen zu lassen.

Paulus, es war immer sehr angenehm mit Dir zusammen zu arbeiten. Von Deiner Ruhe und Ausgeglichenheit, mit der Du an Probleme herangegangen bist, kann ich mir noch viel abschauen! Katha, Du hast mir sehr gefehlt, seit Du hier weggegangen bist! Nicht nur, dass ich mich blind darauf verlassen konnte, dass Du Dich darum kümmerst, dass ich auch ins Bett gehe, wenn ich über dem Lesen einschlafe, ich vermisse auch Deinen Einfluss auf das allgemeine Temperament unserer

Katharina Dobeš

Arbeitsgruppe! Alex, es war eine Bereicherung Dich in unserer Arbeitsgruppe zu haben! Ich hoffe, Du nimmst mir meine Zweifel über die Ungerechtigkeiten dieser Welt nicht persönlich! Robert, wir sind uns zwar nur selten über den Weg gelaufen, wenn Du aus Deiner Klausur des AFM Kammerls aufgetaucht bist, aber Du hast mich trotzdem oft mal zum Lachen gebracht und das ist gar nicht zu unterschätzen. Matthias, Du warst dahingegen ja eher der Nörgler vom Dienst, aber in Deiner trocken ehrlichen Art, die Du dabei an den Tag gelegt hast, war auch das oft erheiternd. Florian (P.) bei Dir möchte ich mich vor allem entschuldigen, dass ich über die eine oder andere Diskussion im Labor die Nerven verloren habe! Ich hoffe Du bist den restlichen Teil Deiner Arbeit hier vom Glück verfolgt! Florian (L.) Du bist zweifellos die Diva der Arbeitsgruppe (bitte verzeih!) und hast sie mit sehr viel Lebendigkeit bereichert! Bernhard, auch Du bist gerade erst aufgetaucht ... Dir wünsche ich vor allem alles Gute bei der Fortführung meiner Arbeit. Sei ein bisserl geduldig und nachsichtig mit der QCM, dann wird's schon gehen!

Damit sich so ein Doktorand auf seine Arbeit konzentrieren kann, braucht es eine Hand voll Leute, die beinahe unbemerkt im Hintergrund das Ihre dazu beitragen. Auch das soll hier Erwähnung und Dank finden!

Zu diesen gehören einmal Rainer Gärtner und Herbert Schmidt, die die Werkstatt betreuen. Danke für all die guten Ideen, die ihr zu so mancher, vielleicht etwas suboptimal gestalteten Konstruktionszeichnung von mir beigesteuert habt! Auch wenn viel zu tun war, oder ich mal spät dran war und etwas dringend brauchte, konnte ich mich stets darauf verlassen, dass ihr alles rechtzeitig fertig bekommt!

Ein herzlicher Dank geht auch an unseren Elektroniker, Paul Berlinger, zu dem man wirklich mit jedem Problem kommen konnte und der für alles eine schnelle und gute Lösung gefunden hat!

Manuela Marik, der gute Geist des ganzen Instituts, ist zwar über die immer wieder auf wundersame Weise auftauchenden Kaffeeheferln im Labor vielleicht mit mir (und der ganzen Arbeitsgruppe) am Verzweifeln gewesen, war dabei aber trotz ihrer manchmal etwas strengen und resoluten Art immer jemand, dem man gerne begegnet ist! Danke für Deinen unermüdlichen Einsatz, um allen hier die kleinen und großen Dinge des Alltags angenehm zu gestalten!

Bei den beiden Damen aus dem Sekretariat, Christine Toupal-Pinter und Erika Ebner, möchte ich mich herzlich bedanken für die Unterstützung mit all der Bürokratie, die so anfällt und auch für die eine oder andere Erinnerung, dass noch eine Reiseabrechnung aussteht!

Im Laufe meiner Arbeit war ich immer wieder an ausländischen Forschungseinrichtungen. Ich habe mich auf all diesen Aufenthalten stets wohl gefühlt und ein

Katharina Dobeš

sehr breites Maß an Unterstützung erfahren. Gerade während zeitlich sehr dicht gedrängter Messaufenthalte ist das eine sehr große Hilfe gewesen!

Martin Köppen möchte ich danken, dafür, dass er stets bemüht war, mir jeden noch so unmöglichen Wunsch zu erfüllen, Geräte aus dem halben Institut zusammen zu schnorren und somit in kürzester Zeit den Messaufbau in Garching zum Laufen zu bringen. Du hast dabei sehr viel Ausdauer an den Tag gelegt. Ich werde nie vergessen, wie wir Freitag Nacht, an der Beamline herum zu sägen angefangen haben! Mein Übereifer hat Dir vielleicht manchmal etwas zu schaffen gemacht. Umso mehr bin ich Dir auch dafür dankbar, dass Du mich nach der einen oder anderen durchwachten Nacht, der Apparatur geradezu entrissen und mich zu einem Morgenkaffee verschleppt hast!

Martin Oberkofler möchte ich danken für all die interessanten Denkanstöße und für die Begeisterung, die er für unsere Ergebnisse gezeigt hat. Auch wenn Du gerade viel zu tun hattest, eiltest Du mir so manches Mal zur Hilfe, wenn das Interlock an der Apparatur sich selbstständig machte oder um die eine oder andere Ionenspezies dingfest zu machen!

Auch wenn Christian Linsmeir und ich uns irgendwie stets verpassten, wenn ich in Garching war, möchte ich ihm für seine Unterstützung danken, die er mir dennoch zu Teil werden ließ!

Erwin Bodewits is surely one of the kind that too, does not know when to let go and get some sleep! This is probably why my memory of Groningen is somehow restricted to the KVI in the middle of nowhere ('keep straight ahead until you pass the windmill and then go even further') and to bicycle rides to and from the guest house at the strangest times of the day. We still had a lot of fun climbing around the lab and having our own private Hawaiian party, when there was no-one around on holidays and thankfully even survived getting electrocuted (sorry for that)! So thank you for all your effort that in the end turned out to be quite fruitful and above that also for making me feel really welcome!

I would also like to thank Ronnie Hoekstra, who frequently visited us in the lab at KVI to give us some input in passing by or just see how we were.

Although none of the results collected there finally made it into my thesis, I also spent some time at the Ganil facility in Caen. I would like to thank Arek Lawicky for his endurance and enthusiasm in getting things going, Jimmy Rangama for trying to make the best out of our constant lack of time and Bernd Huber for finally shedding some light onto the mass spectra we obtained.

Um gut 'funktionieren' zu können, den Frust, an dem man bei Zeiten schon mal zu kiefeln hat, nicht überhand gewinnen zu lassen, um Energie zu tanken und Aus-

Katharina Dobeš

gleich zu gewinnen - für all das liebe Menschen, die einen umgeben! Ich war sicher im Laufe der Zeit nicht immer leicht zu ertragen, aber ihr wusstet mir mit einer guten Mischung aus Aufmerksamkeit und Ablenkung sehr viel Rückhalt zu geben! Das war und ist von unschätzbarem Wert für mich und dafür möchte ich mich herzlich bei Euch bedanken!

Besonders geht mein Dank in diesem Zusammenhang an Roland! Du warst gleich in einer Hand voll Situationen für mich da, als ich wirklich dringend einen Freund brauchte! Die beinahe bedingungslose Unterstützung und Zuneigung, die Du mir im Laufe der Jahre entgegen gebracht hast, weiß ich sehr zu schätzen. Ich möchte mich hier auch ganz besonders dafür bedanken, dass Du so geduldig mir Dein Ohr geschenkt hast, mir den Rücken gestärkt hast, immer wieder einmal gegen meine Selbstzweifel angekämpft hast!

Nicht weniger sollen auch Hannes und Iva hier noch einmal Erwähnung finden. Ihr ward und seid für mich zwei große Vorbilder dafür, wie man es vielleicht schaffen könnte und das hat in vielen Situationen sehr gut getan. Eure unkonventionelle, herzerwärmende Art, Euer Gespür für das Wichtige, hat mir viel Auftrieb gegeben. Ihr seid mir Familie, wenn alles um mich zu zerfallen beginnt. Ich weiß dass ich mich auf Euch und Euer Wohlwollen verlassen kann und dafür bin ich Euch zutiefst dankbar!

Meinen Schwestern möchte ich ganz herzlich dafür danken, dass sie mich mit so viel Anteilnahme bis hierher begleitet haben. Genau in den Momenten, als ich es am nötigsten brauchte, wusstet ihr, ein Stückchen näher zu rücken, für mich da zu sein, ohne zu fragen und ohne dafür eine Gegenleistung zu erwarten. Ihr versteht mich, ohne viele Worte, könnt nachvollziehen, wie es ist, in meiner Haut zu stecken und seid damit eine große Bereicherung in meinem Leben! Barbara, danke für Dein Interesse und Deine Begeisterung für Dinge, die mich beschäftigen! Ich schätze unsere Gesprächsbasis sehr. Bernadette, danke, dass Du mir so viel moralische Unterstützung vor allem (aber nicht nur) während der letzten Monate gegeben hast! Ich bewundere Deine kompromisslose Ehrlichkeit, mit der Du - trotz Deiner Zurückhaltung - Dinge beim Namen nennst! Stephanie, danke für Deine Zuneigung und dafür, dass wir mit einander Spaß haben können!

Dir, Martin, vielen Dank dafür, dass Du, wann immer ich Unterstützung brauchte, einer der ersten warst, der fragte, was er tun könne. Dir, Daniel, ein Dankeschön dafür, dass Du mir vorlebst, wie man ohne viel Aufhebens, viele Dinge sehr richtig machen kann! Euch, Jakob und Benjamin, möchte ich danken, dafür dass ihr mein Kuschelbedürfnis ertragt und für Euer unvoreingenommenes, freundliches Lächeln!

Katharina Dobeš

Vielen Dank, Andrea, für all die Geborgenheit, die Du mir im Laufe meines Lebens gegeben hast und die vielen Geschichten und Unternehmungen, mit denen Du meine Kindheit erfüllt hast. Omi, Du bist mir ein großes Vorbild, wie man sein Leben immer wieder neu erfinden kann, sich nicht unterkriegen lässt und vor allem auch, was es heißt, sein Herz auf dem rechten Fleck zu haben!

Liebe Eltern, Euch zu aller erst einen Dank dafür, dass ihr nie gefragt habt, wann ich denn endlich fertig bin! Danke auch, dass ihr mir stets die Freiheit gegeben habt, zu tun, was ich für richtig halte. Meine Kindertage haben viel dazu beigetragen, dass ich zu einem wissbegierigen und kritisch denkenden Menschen geworden bin und das geht sicherlich auch auf Eure Rechnung!

Lieber Stephan, was für eine Erleichterung muss es auch für Dich sein, dass ich endlich fertig bin! Du hättest Dir dafür, wie sehr Du letztendlich zum Gelingen dieser Arbeit beigetragen hast, einen eigenen Titel verdient. Du warst mir mein Ritter in der glänzenden Rüstung, der mir mehr als einmal tatkräftig zur Hilfe eilte, um mich vor dem Verzweifeln zu retten. Danke für spätnächtliche Schraubaktionen im Labor, danke für gemeinsam verbrachte Messnächte (Oscarübertragung inklusive), danke, dass Du Dich für meine langweiligen und schier nie enden wollenden Problemchen interessiert hast, danke für Deine Geduld, mit der Du meinen Launen begegnest, danke, dass Du mir ein zu Hause gibst und an mich glaubst! Mit Dir gemeinsam denke ich sogar manchmal, dass ich die Welt erobern könnte!

Und wer bis hierher noch nicht aufgegeben hat, dem ist tatsächlich nicht zu helfen!

Bildung ist das, was übrig bleibt, wenn man alles vergessen hat, was man gelernt hat.
(W. Heisenberg)

Katharina Dobeš

Bibliography

[1]   IEA, `World Energy Outlook 2012', *OECD Publishing* (2012)

[2]   Clarke L., Edmonds J., Krey V., Richels R., Rose S. and Tavoni M., `International climate policy architectures: Overview of the EMF 22 International Scenarios', *Energy Economics*, **31**, S64 (2009)

[3]   IEA, `Co-Generation and Renewables', *OECD Publishing* (2011)

[4]   `Wikipedia', URL www.wikipedia.org

[5]   Maisonnier D., Campbell D., Cook I., Pace L.D., Giancarli L., Hayward J., Puma A.L., Medrano M., Norajitra P., Roccella M., Sardain P., Tran M.Q. and Ward D., `Power Plant Conceptual Studies in Europe', *Nuclear Fusion*, **47**, 1524 (2007)

[6]   `European Fusion Development Agreement', URL www.efda.org

[7]   Cook I., Marbach G., Pace L.D., Girard C., Rocco P. and Taylor N.P., `Results, Conclusions, and Implications of the SEAFP-2 Programme', *Fusion Engineering and Design*, **51 - 52**, 409 (2000)

[8]   IAEA, `Agreement on the Establishment of the ITER International Fusion Energy Organization for the Joint Implementation of the ITER project', *ITER EDA Documentation Series* (2006)

[9]   Jacquinot J. and the JET team, `Deuterium - Tritium Operation in Magnetic Confinement Experiments: Results and Underlying Physics', *Plasma Physics and Controlled Fusion*, **41**, A13 (1999)

[10]   `ITER organization', URL www.iter.org

[11]   Lawson J.D., `Some Criteria for a Power Producing Thermonuclear Reactor', *Proceedings of the Physical Society B*, **70**, 6 (1957)

[12]   `National Ignition Facility', URL https://lasers.llnl.gov/programs/ife/

[13]   Fowler T.K., `A Look at a Possible Energy Choice for the Future', *Nuclear Fu-*

sion, **8**, 7 (1989)

[14] Federici G., Skinner C.H., Brooks J.N., Coad J.P., Grisola C., Haasz A.A., Hassanein A., Philipps V., Pitcher C.S., Roth J., Wampler W.R. and Whyte D.G., `Plasma-Material Interactions in Current Tokamaks and their Implications for Next Step Fusion Reactors', *Nuclear Fusion*, **41**, 1967 (2001)

[15] Gasparotto M., Andreani R., Boccaccini L.V., Cardella A., Federici G., Giancarli L., Marois G.L., Maisonnier D., Malang S., Moeslang A., Poitevin Y., van der Schaaf B. and Victoria M., `Survey of in-Vessel Candidate Materials for Fusion Power Plants - the European Materials R&D Programme', *Fusion Engineering and Design*, **66 - 68**, 129 (2003)

[16] Shimada M., Costley A.E., Federici G., Ioki K., Kukushkin A.S., Mukhovatov V., Polevoi A. and Sugihara M., `Overview of Goals and Performance of ITER and Strategy for Plasma-Wall Interaction Investigation', *Journal of Nuclear Materials*, **337 - 339**, 808 (2005)

[17] Federici G., `Plasma Wall Interactions in ITER', *Physica Scripta*, **T124**, 1 (2006)

[18] Loarte A., Saibene G., Sartori R., Riccardo V., Andrew P., Paley J., Fundamenski W., Eich T., Herrmann A., Pautasso G., Kirk A., Counsell G., Federici G., Strohmayer G., Whyte D., Leonard A., Pitts R.A., Landman I., Bazylev B. and Petschanyi S., `Transient Heat Loads in Current Experiments, Extrapolation to ITER and Consequences for its Operation', *Physica Scripta*, **T128**, 222 (2007)

[19] Eich T., Herrmann A., Pautasso G., Andrew P., Asakura N., Boedo J.A., Corre Y., Fenstermacher M.E., Fuchs J.C., Fundamenski W., Federici G., Gauthier E., Goncalves B., Gruber O., Kirk A., Leonard A.W., Loarte A., Matthews G.F., Neuhauser J., Pitts R.A., Riccardo V. and Silva C., `Power Deposition onto Plasma Facing Components in Poloidal Divertor Tokamaks During Type-I ELMs and Disruptions', *Journal of Nuclear Materials*, **337 - 339**, 669 (2005)

[20] Loarte A., Saibene G., Sartori R., Becoulet M., Horton L., Eich T., Herrmann A., Laux M., Matthews G., Jachmich S., Asakura N., Chankin A., Leonard A., Porter G., Federici G., Shimada M., Sugihara M. and Janeschitz G., `ELM Energy and Particle Losses and their Extrapolation to Burning Plasma Experiments', *Journal of Nuclear Materials*, **313 - 316**, 962 (2003)

[21] Federici G., Loarte A. and Strohmayer G., `Assessment of Erosion of the ITER Divertor Targets During Type I ELMs', *Plasma Physics and Controlled Fusion*, **45**, 1523 (2003)

[22] Valovic M., Cunningham G., Garzotti L., Gurl C., Kirk A., Naylor G., Patel A., Scannell R., Thornton A.J. and the MAST team, `Pellet Fuelling of Plasmas with Edge Localized Modes Mitigation by Resonant Magnetic Perturbations in MAST', *Plasma Physics and Controlled Fusion*, **55**, 025009 (2013)

[23] Bolt H., Barabash V., Federici G., Linke J., Loarte A., Roth J. and Sato K., `Plasma Facing and High Heat Flux Materials - Needs for ITER and Beyond',

Katharina Dobeš

Journal of Nuclear Materials, **307 - 311**, 43 (2002)

[24] Behrisch R., Federici G., Kukushkin A. and Reiter D., `Material Erosion at the Vessel Walls of Future Fusion Devices', *Journal of Nuclear Materials*, **313 - 316**, 388 (2003)

[25] Loarte A., Saibene G., Sartori R., Campbell D., Becoulet M., Horton L., Eich T., Herrmann A., Matthews G., Asakura N., Chankin A., Leonard A., Porter G., Federici G., Janeschitz G., Shimada M. and Sugihara M., `Characteristics of type I ELM Energy and Particle Losses in Existing Devices and their Extrapolation to ITER', *Plasma Physics and Controlled Fusion*, **45**, 1549 (2003)

[26] Neu R., Kallenbach A., Balden M., Bobkov V., Coenen J.W., Drube R., Dux R., Greuner H., Herrmann A., Hobrik J., Höhnle H., Krieger K., Kocan M., Lang P., Lunt T., Maier H., Mayer M., Müller H.W., Potzel S., Pütterich T., Rapp J., Rhode V., Ryter F., Schneider P.A., Schweinzer J., Sertoli M., Strober J., Suttrop W., Sugiyama K., van Rooij G., Wischmeier M. and the ASDEX Upgrade Team, `Overview on Plasma Operation with a Full Tungsten Wall in ASDEX Upgrade', *Journal of Nuclear Materials*, **438**, S34 (2013)

[27] Pitcher C.S. and Stangeby P.C., `Experimental Divertor Physics', *Plasma Physics and Controlled Fusion*, **39**, 779 (1997)

[28] Keim A., Rasul B., Endstrasser N., Scheier P., Märk T.D. and Herman Z., `Interaction of Small Hydrocarbon Ions and Ar^+ with Carbon-Fibre-Composite Surfaces at Room Temperature', *Journal of Mass Spectrometry*, **306**, 204 (2011)

[29] Roth J., Tsitrone E., Loarer T., Philipps V., Brezinsek S., Loarte A., Counsell G.F., Doerner R.P., Schmid K., Ogorodnikova O.V. and Causey R.A., `Tritium Inventory in ITER Plasma-Facing Materials and Tritium Removal Procedures', *Plasma Physics and Controlled Fusion*, **50**, 103001 (2008)

[30] Janeschitz G., ITER JCT and HTs, `Plasma-Wall Interaction Issues in ITER', *Journal of Nuclear Materials*, **290 - 293**, 1 (2001)

[31] Günter S., et al., `Overview of ASDEX Upgrade Results - Development of Integrated Operating Scenarios for ITER', *Nuclear Fusion*, **45**, S93 (2005)

[32] Neu R., Hopf C., Kallenbach A., Pütterich T., Dux R., Greuner H., Gruber O., Herrmann A., Krieger K., Maier H., Rhode V. and the ASDEX Upgrade Team, `Operational Conditions in a W-Clad Tokamak', *Journal of Nuclear Materials*, **367 - 370**, 1497 (2007)

[33] Matthews G., Beurskens M., Brezinsek S., Groth M., Joffrin E., Loving A., Kear M., Mayoral M.L., Neu R., Prior P., Riccardo V., Rimini F., Rubel M., Sips S., Villedieu E., de Vries P., Watkins M.L. and EFDA-JET contributors, `JET ITER-Like Wall - Overview and Experimental Programme', *Physica Scripta*, **145**, 014001 (2011)

[34] Neu R., Arnoux G., Beurskens M., Bobkov V., Brezinsek S., Bucalossi J., Calabro G., Challis C., Coenen J.W., de la Luna E., de Vries P.C., Dux R., Frassinetti

L., Giroud C., Groth M., Hobrik J., Joffrin E., Lang P., Lehnen M., Lerche E., Loarer T., Lomas P., Maddison G., Maggi C., Matthews G., Marsen S., Mayoral M.L., Meigs A., Mertens P., Nunes I., Philipps V., Pütterich T., Rimini F., Sertoli M., Sieglin B., Sips A.C.C., van Eester D., van Rooij G. and JET-EFDA contributors, `First Operation with the JET International Thermonuclear Experimental Reactor-Like Wall', *Physics of Plasmas*, **20**, 056111 (2013)

[35] Kallenbach A., Dux R., Mayer M., Neu R., Pütterich T., Bobkov V., Fuchs J.C., Eich T., Giannone L., Gruber O., Herrmann A., Horton L.D., Maggi C.F., Meister H., Müller H.W., Rohde V., Sips A., Stäbler A., Stober J. and the ASDEX Upgrade Team, `Non-Boronized Compared with Boronized Operation of ASDEX Upgrade with Full-Tungsten Plasma Facing Components', *Nuclear Fusion*, **49**, 045007 (2009)

[36] Loarte A., Lipschultz B., Kukushkin A.S., Matthews G.F., Stangeby P.C., ASakura N., Counsell G.F., Federici G., Kallenbach A., Krieger K., Mahdavi A., Philipps V., Reiter D., Roth J., Strachan J., Whyte D., Doerner R., Eich T., Fundamenski W., Herrmann A., Fenstermacher M., Ghendrih P., Groth M., Kirschner A., Konoshima S., LaBombard B., Lang P., Leonard A.W., Monier-Garbet P., Neu R., Pacher H., Pegourie B., Pitts R.A., Takamura S., Terry J., Tsitrone E. and the ITPA Scrape-off Layer and Divertor Physics Topical Group, `Progress in the ITER Physics Basis, Chapter 4: Power and Particle Control', *Nuclear Fusion*, **45**, S203 (2007)

[37] Kallenbach A., Balden M., Dux R., Eich T., Girard C., Huber A., Maddison G.P., Mayer M., McCormick K., Neu R., Petrie T.W., Pütterich T., Rapp J., Reinke M.L., Schmid K., Schweinzer J., Wolfe S., the ASDEX-Upgrade Team, DIII-D Team, Alcator Team and JET-EFDA contributors, `Plasma Surface Interactions in Impurity Seeded Plasmas', *Journal of Nuclear Materials*, **415**, S19 (2011)

[38] Kallenbach A., Dux R., Fuchs J.C., Fischer R., Geiger B., Giannone L., Herrmann A., Lunt T., Mertens V., McDermott R., Neu R., Pütterich T., Rathgeber S., Rohde V., Schmid K., Schweinzer J., Treutterer W. and the ASDEX Upgrade Team, `Divertor Power Load Feedback with Nitrogen Seeding in ASDEX Upgrade', *Plasma Physics and Controlled Fusion*, **52**, 055002 (2010)

[39] Neu R., Kallenbach A., Sertoli M., Dux R., Fischer R., Fuchs J.C., Janzer A., Müller H.W., Potzel S., Pütterich T., van Rooij G. and the ASDEX Upgrade Team, `Tungsten Behaviour in Radiatively Cooled Plasma Discharges in ASDEX Upgrade', *Journal of Nuclear Materials*, **415**, S322 (2011)

[40] Dux R., Bobkov V., Herrmann A., Janzer A., Neu R., Mayer M., Müller H.W., Pugno R., Pütterich T., Rhode V., Sips A.C.C. and the ASDEX Upgrade Team, `Plasma-Wall Interaction and Plasma Behaviour in the Boronised All Tungsten Wall', *Journal of Nuclear Materials*, **390 - 391**, 858 (2009)

[41] Pitts R.A., Coad J.P., Coster D.P., Federici G., Fundamenski W., Horacek J.,

Krieger K., Kukushkin A., Likonen J., Matthews G.F., Rubel M., Strachan J.D. and JET-EFDA contributors, `Material Erosion and Migration in Tokamaks', *Plasma Physics and Controlled Fusion*, **47**, B303 (2005)

[42] Naujoks D. and Eckstein W., `Non-Linear Erosion Effects in Plasma Experiments', *Journal of Nuclear Materials*, **230**, 93 (1996)

[43] Sigmund P., `Theory of Sputtering, I. Sputtering Yield of Amorphous and Polycrystalline Targets', *Physical Review*, **184**, 383 (1969)

[44] Bohdansky J., `A Universal Relation for the Sputtering Yield of Monoatomic Solids at Normal Ion Incidence', *Nuclear Instruments and Methods in Physics Research B*, **2**, 587 (1984)

[45] Eckstein W. and Preuss R., `New Fit Formulae for the Sputtering Yield', *Journal of Nuclear Materials*, **320**, 209 (2003)

[46] Sigmund P., `Recollections of Fifty Years with Sputtering', *Thin Solid Films*, **520**, 6031 (2012)

[47] Sigmund P., *Sputtering by Particle Bombardment I*, chapter Sputtering by Ion Bombardment Theoretical Concepts, 9, Topics of Applied Physics, Springer Berlin, Heidelberg (1981)

[48] Eckstein W., *Computer Simulation of Ion - Solid Interactions*, volume 10 of *Springer Series in Materials Sience*, Springer Berlin, Heidelberg (1991)

[49] Langley R.A., Bohdansky J., Eckstein W., Mioduszewski P., Roth J., Thomas E.W., Verbeek H. and Wilson K.L., `Data Compendium for Plasma-Surface Interactions', *Nuclear Fusion*, **24**, S9 (1984)

[50] Lindhard J. and Scharff M., `Energy Dissipation by Ions in the keV Region', *Physical Review*, **124**, 128 (1961)

[51] Lindhard J., Nielsen V. and Scharff M., `Approximation Method in Classical Scattering by Screened Coulomb Fields', *Kongelige Danske Videnskabernes Selskab, Matematisk-Fysike Meddelelser*, **36**, 10 (1968)

[52] Bohdansky J., Roth J. and Bay H.L., `An Analytical Formula and Important Parameters for Low-Energy Ion Sputtering', *Journal of Applied Physics*, **51**, 2861 (1980)

[53] Eckstein W., *Sputtering by Particle Bombardment*, volume 110 of *Topics in Applied Physics*, chapter Sputtering Yields, 33 -- 189, Springer Berlin, Heidelberg (2007)

[54] García-Rosales C., Eckstein W. and Roth J., `Revised Formulae for Sputtering Data', *Journal of Nuclear Materials*, **218**, 8 (1994)

[55] Wilson W.D., Haggmark L.G. and Biersack J.P., `Calculations of Nuclear Stopping, Ranges, and Straggling in the Low-Energy Region', *Physical Review B*, **15**, 2458 (1977)

[56] Oen O.S. and Robinson M.T., `Computer Studies of the Reflection of Light Ions From Solids', *Nuclear Instruments and Methods*, **132**, 647 (1976)

[57] Biersack J.P. and Eckstein W., `Sputtering Studies with the Monte Carlo Program TRIM.SP', *Applied Physics A: Materials Science and Processing*, **34**, 73 (1984)

[58] Möller W. and Eckstein W., `TRIDYN - A TRIM Simulation Code Including Dynamic Changes', *Nuclear Instruments and Methods in Physics Research B*, **2**, 814 (1984)

[59] Jacob W. and Roth J., *Sputtering by Particle Bombardment*, volume 110 of *Topics in Applied Physics*, chapter Chemical Sputtering, Springer Berlin, Heidelberg, 329 - 401 (2007)

[60] Horn A., Schenk A., Biener J., Winter B., Lutterloh C., Wittmann M. and Küppers J., `H Atom Impact Induced Chemical Erosion Reaction at C:H Film Surfaces', *Chemical Physics Letters*, **231**, 193 (1994)

[61] Roth J., *Nuclear Fusion Research*, volume 78 of *Springer Series in Chemical Physics*, chapter Review and Status of Physical Sputtering and Chemical Erosion of Plasma Facing Materials, 203 -- 225, Springer Berlin, Heidelberg (2005)

[62] Refke A., Philipps V. and Vietzke W., `Chemical Erosion Behavior of Graphite Due to Energetic Oxygen Impact', *Journal of Nuclear Materials*, **250**, 13 (1997)

[63] Grigull S., Behrisch R. and Parascandola S., `Nitrogen Implantation into Carbon: Retention, Release and Target Erosion Processes', *Journal of Nuclear Materials*, **275**, 158 (1999)

[64] Roth J., Bohdansky J., Blewer R.S., Ottenberger W. and Borders J., `Sputtering of Be and BeO by Light Ions', *Journal of Nuclear Materials*, **85 - 86**, 1077 (1979)

[65] Hechtl E., Eckstein W., Roth J. and Laszlo J., `Sputtering of Tungsten by Oxygen at Temperatures up to 1900 K', *Journal of Nuclear Materials*, **179 - 181**, 290 (1991)

[66] Schmid K., Manhard A., Linsmeier C., Wiltner A., Schwarz-Selinger T., Jacob W. and Mändl S., `Interaction of Nitrogen Plasmas with Tungsten', *Nuclear Fusion*, **50**, 025006 (2010)

[67] Oberkofler M. and Linsmeier C., `Properties of Nitrogen-Implanted Beryllium and its Interaction with Energetic Deuterium', *Nuclear Fusion*, **50**, 125001 (2010)

[68] Keim A., Harnisch M., Scheier P. and Herman Z., `Collisions of Low-Energy Ions Ar^+ and N_2^+ with Room Temperature and Heated Surfaces of Tungsten, Beryllium and a Mixed Beryllium-Tungsten Thin Film', *International Journal of Mass Spectrometry*, **354 - 355**, 78 (2013)

[69] Linsmeier C., Reinelt M. and Schmid K., `Surface Chemistry of First Wall Materials - From Fundamental Data to Modelling', *Journal of Nuclear Materials*, **415**, S512 (2011)

[70] Balden M. and Roth J., `New Weight-Loss Measurements of the Chemical Ero-

sion Yields of Carbon Based Materials under Hydrogen Ion Bombardment', *Journal of Nuclear Materials*, **280**, 39 (2000)

[71] Roth J. and García-Rosales C., `Analytic Description of the Chemical Erosion of Graphite by Hydrogen Ions', *Nuclear Fusion*, **36**, 1647 (1996)

[72] Roth J., `Chemical Erosion of Carbon Based Materials in Fusion Devices', *Journal of Nuclear Materials*, **266 - 269**, 51 (1999)

[73] Wittmann M. and Küppers J., `A Model of Hydrogen Impact Induced Chemical Erosion of Carbon Based on Elementary Reaction Steps', *Journal of Nuclear Materials*, **227**, 186 (1996)

[74] Hopf C. and Jacob W., `Bombardment of Graphite with Hydrogen Isotopes: A Model for the Energy Dependence of the Chemical Sputtering Yield', *Journal of Nuclear Materials*, **342**, 141 (2005)

[75] Roth J. and Bohdansky J., `Mechanism of Hydrocarbon Formation upon Interaction of Energetic Hydrogen Ions with Graphite', *Applied Physics Letters*, **51**, 964 (1987)

[76] Erents S.K., Braganza C.M. and McCracken G.M., `Methane Formation During the Interaction of Energetic Protons and Deuterons with Carbon', *Journal of Nuclear Materials*, **63**, 399 (1976)

[77] Hopf C., von Keudell A. and Jacob W., `Chemical Sputtering of Hydrocarbon Films', *Journal of Applied Physics*, **94**, 2373 (2003)

[78] Vietzke E., Flaskamp K. and Phillips V., `Hydrocarbon Formation in the Reaction of Atomic Hydrogen with Pyrolytic Graphite and the Synergistic Effect of Argon Ion Bombardment', *Journal of Nuclear Materials*, **111 - 112**, 763 (1982)

[79] Haasz A.A., Franzen P., Davis J.W., Chiu S. and Pitcher C.S., `Two-Region Model for Hydrogen Trapping in and Release from Graphite', *Journal of Applied Physics*, **77**, 66 (1995)

[80] Burgdörfer J., Lerner P. and Meyer F.W., `Above-Surface Neutralization of Highly Charged Ions: The Classical Over-the-Barrier Model', *Physical Review A*, **44**, 5674 (1991)

[81] Aumayr F., Kurz H., Schneider D., Briere M., McDonald M.A., Cunningham J.W., Winter C.E. and Winter H.P., `Emission of Electrons from a Clean Gold Surface Induced by Slow Highly Charged Ions at the Image Charge Acceleration Limit', *Physical Review Letters*, **71**, 1943 (1993)

[82] Bárány A. and Setterlind C.J., `Interaction of Slow Highly Charged Ions with Atoms, Clusters and Solids: a Unified Classical Barrier Approach', *Nuclear Instruments and Methods in Physics Research B*, **98**, 184 (1995)

[83] Aumayr F. and Winter H.P., `Potential Sputtering', *Philosophical Transactions of the Royal Society*, **362**, 77 (2004)

[84] Schneider D.H.G. and Briere M.A., `Investigations of the Interactions of Highest Charge State Ions with Surfaces', *Physica Scripta*, **53**, 228 (1996)

[85]   Arnau A., Aumayr F., Echinique P.M., Grether M., Heiland W., Limburg J., Morgenstern R., Roncin P., Schippers S., Schuch R., Stolterfoht N., Varga P., Zouros T.J.M. and Winter H.P., `Interaction of Slow Multicharged Ions with Solid Surfaces', *Surface Science Reports*, **27**, 113 (1997)

[86]   Aumayr F., Facsko S., El-Said A., Trautmann C. and Schleberger M., `Single Ion Induced Surface Nanostructures: a Comparison between Slow Highly Charged and Swift Heavy Ions', *Journal of Physics: Condensed Matter*, **23**, 393001 (2011)

[87]   Neidhart T., Pichler F., Aumayr F., Winter H.P., Schmid M. and Varga P., `Potential Sputtering of Lithium-Fluoride under Impact of Slow Multicharged Ions', *Physical Review Letters*, **74**, 5280 (1995)

[88]   Sporn M., Libiseller G., Neidhart T., Schmid M., Aumayr F., Winter H.P., Varga P., Grether M. and Stolterfohrt N., `Potential Sputtering of Clean SiO_2 by Slow Highly Charged Ions', *Physical Review Letters*, **79**, 945 (1997)

[89]   Varga P., Neidhart T., Sporn M., Libiseller G., Schmid M., Aumayr F. and Winter H.P., `Sputter Yields of Insulators Bombarded with Hyperthermal Multiply Charged Ions', *Physica Scripta*, **T73**, 307 (1997)

[90]   Hayderer G., Cernusca S., Hoffmann V., Niemann D., Stolterfoht N., Schmid M., Varga P., Winter H.P. and Aumayr F., `Sputtering of Au and Al_2O_3 Surfaces by Slow Highly Charged Ions', *Nuclear Instruments and Methods in Physics Research B*, 143 (2001)

[91]   Aumayr F., Burgdörfer J., Varga P. and Winter H.P., `Sputtering of Insulator Surfaces by Slow Highly Charged Ions: Coulomb Explosion or Defect Mediated Desorption', *Comments on Atomic and Molecular Physics*, **34**, 201 (1999)

[92]   Vana M., Aumayr F., Winter H.P., Drexel H., Grill V., Scheier P. and Märk T.D., `Electron Emission for Impact of Slow Fullerene Ions on Clean Gold', *Physica Scripta*, **T73**, 318 (1997)

[93]   Hayderer G., Schmid M., Varga P., Winter H.P., Aumayr F., Wirtz L., Lemell C., Burgdörfer J., Hägg L. and Reinhold C.O., `Threshold for Potential Sputtering of LiF', *Physical Review Letters*, **83**, 3948 (1999)

[94]   Hayderer G., Cernusca S., Schmid M., Varga P., Winter H.P., Aumayr F., Niemann D., Hoffmann V., Stolterfoht N., Lemell C., Wirtz L. and Burgdörfer J., `Kinetically Assisted Potential Sputtering of Insulators by Highly Charged Ions', *Physical Review Letters*, **86**, 3530 (2001)

[95]   Kakutani N., Azuma T., Yamazaki Y., Komaki K. and Kuroki K., `Strong Charge State Dependence of H^+ and H_2^+ Sputtering Induced by Slow Highly Charged Ions', *Nuclear Instruments and Methods in Physics Research B*, **96**, 541 (1995)

[96]   Williams R.T., Song K.S., Faust W.F. and Leung C.H., `Off-Center Self-Trapped Excitons and Creation of Lattice Defects in Alkali-Halide Crystals', *Physical Review B*, **33**, 7232 (1986)

Katharina Dobeš

[97]   Bitensky I.S., Murakhmetov M.N. and Parilis É.S., `Sputtering of Nonmetals by Intermediate-Energy Multiply Charged Ions Through a Coulomb 'Explosion'', *Soviet Physics - Technical Physics*, **24**, 618 (1979)

[98]   Bitensky I.S. and Parilis É.S., `The Sputtering of Non-Metals Under Slow Multiply Charged Ions', *Journal de Physique Colloques*, **2**, 227 (1989)

[99]   Schenkel T., Hamza A.V., Barnes A.V. and Schneider D.H., `Interaction of Slow, Very Highly Charged Ions with Surfaces', *Progress in Surface Science*, **61**, 23 (1999)

[100]   Schenkel T., Hamza A.V., Barnes A.V., Schneider D.H., Banks J.C. and Doyle B.L., `Ablation of GaAs by Intense, Ultrafast Electronic Excitation from Highly Charged Ions', *Physical Review Letters*, **81**, 2590 (1998)

[101]   Stampfli P., `Electronic Excitation and Structural Stability of Solids', *Nuclear Instruments and Methods in Physics Research B*, **107**, 138 (1996)

[102]   Loarer T., `Fuel Retention in Tokamaks', *Journal of Nuclear Materials*, **390 - 391**, 20 (2009)

[103]   Skinner C.H., Bekris N., Coad J.P., Gentile C.A. and Glugla M., `Tritium Removal from JET and TFTR Tiles by a Scanning Laser', *Journal of Nuclear Materials*, **313 - 316**, 496 (2003)

[104]   Counsell G., Coad P., Grisola C., Hopf C., Jacob W., Kirschner A., Kreter A., Krieger K., Likonen J., Philipps V., Roth J., Rubel M., Salancon E., Semerok A., Tabarés F.L., Widdowson A. and JET-EFDA contributors, `Tritium Retention in Next Step Devices and the Requirements for Mitigation and Removal Techniques', *Plasma Physics and Controlled Fusion*, **48**, B189 (2006)

[105]   Tabarés F.L., `Tritium Inventory Control During ITER Operation Under Carbon Plasma-Facing Components by Nitrogen-Based Plasma Chemistry: a Review', *Plasma Sources Science and Technology*, **22**, 033001 (2013)

[106]   Skinner C.H. and Federici G., `Is Carbon a Realistic Choice for ITER's Divertor', *Physica Scripta*, **T124**, 18 (2006)

[107]   Myers S.M., Richards R.M. and Wampler W.R., `Ion-Beam Studies of Hydrogen-Metal Interactions', *Journal of Nuclear Materials*, **165**, 9 (1989)

[108]   Serra E., Benamati G. and Ogorodnikova O.V., `Hydrogen Isotopes Transport Parameters in Fusion Reactor Materials', *Journal of Nuclear Materials*, **255**, 105 (1998)

[109]   Rhode V., Maier H., Krieger K., Neu R. and Perchermaier J., `Carbon Layers in the Divertor of ASDEX Upgrade', *Journal of Nuclear Materials*, **290 - 293**, 317 (2001)

[110]   Kirschner A., Borodin D., Droste S., Philipps V., Samm U., Federici G., Kukushkin A. and Loarte A., `Modelling of Tritium Retention and Target Lifetime of the ITER Divertor Using the ERO code', *Journal of Nuclear Materials*, **363 - 365**, 91 (2007)

[111] Anderl R.A., Causey R.A., Davis J.W., Doerner R.P., Federici G., Haasz A.A., Longhurst G.R., Wampler W.R. and Wilson K.L., `Hydrogen Isotope Retention in Beryllium for Tokamak Plasma-Facing Applications', *Journal of Nuclear Materials*, **273**, 1 (1999)

[112] Causey R., Wilson K., Venaus T. and Wampler W.R., `Tritium Retention on Tungsten Exposed to Intense Fluxes of 100 eV Tritons', *Journal of Nuclear Materials*, **266 - 269**, 467 (1999)

[113] Jones P.M.S. and Gibson R., `Hydrogen in Beryllium', *Journal of Vacuum Science and Technology A*, **21**, 353 (1967)

[114] Schwasinger W.A., `Summary Abstract: Tritium Solubility in High Purity Beryllium', *Journal of Vacuum Science and Technology A*, **4**, 1216 (1986)

[115] Reinelt M., Allouche A., Oberkofler M. and Linsmeier C., `Retention Mechanisms and Binding States of Deuterium Implanted into Beryllium', *New Journal of Physics*, **11**, 043023 (2009)

[116] Causey R.A., Longhurst G.R. and Harbin W., `Tritium Retention in S-65 Beryllium after 100 eV Plasma Exposure', *Journal of Nuclear Materials*, **241 - 243**, 1041 (1997)

[117] Mayer M., Behrisch R., Plank H., Roth J., Dollinger G. and Frey C.M., `Codeposition of Hydrogen with Beryllium, Carbon and Tungsten', *Journal of Nuclear Materials*, **230**, 67 (1996)

[118] Frauenfelder R., `Solution and Diffusion of Hydrogen in Tungsten', *Journal of Vacuum Science and Technology6*, **6**, 388 (1969)

[119] Skinner C.H., Haasz A.A., Alimov V.K., Bekris N., Causey R.A., Clark R.E.H., Coad J.P., Davis J.W., Doerner R.P., Mayer M., Pisarev A., Roth J. and Tanabe T., `Recent Advanecs on Hydrogen Retention in ITER's Plasma Facing Materials: Beryllium, Carbon and Tungsten', *Fusion Science and Technology*, **54**, 891 (2008)

[120] Alimov V.K. and Roth J., `Hydrogen Isotope Retention in Plasma-Facing-Materials: Review of Recent Experimental Results', *Physica Scripta*, **T128**, 6 (2007)

[121] Sattel S., Robertson J. and Ehrhardt H., `Effects of Deposition Temperature on the Properties of Hydrogenated Tetrahedral Amorphous Carbon', *Journal of Applied Physics*, **82**, 4566 (1997)

[122] Jacob W., `Surface Reactions During Growth and Erosion of Hydrocarbon Films', *Thin Solid Films*, **326**, 1 (1998)

[123] Schwarz-Selinger T., von Keudell A. and Jacob W., `Plasma Chemical Vapor Deposition of Hydrocarbon Films: The Influence of Hydrocarbon Source Gas on the Film Properties', *Journal of Applied Physics*, **86**, 3988 (1999)

[124] Davis J.W., Haasz A.A. and Walsh D.S., `Flux and Fluence Dependence of H^+ Trapping in Graphite', *Journal of Nuclear Materials*, **176 - 177**, 992 (1990)

Katharina Dobeš

[125] Chiu S. and Haasz A.A., `Molecule Formation Due to Sequential and Simultaneous Exposure of Graphite to H^+ and D^+', *Journal of Nuclear Materials*, **196 - 198**, 972 (1992)

[126] Naujoks D., `Criterion for Zero Net Erosion at Divertor Plates in Fusion Experiments', *Nuclear Fusion*, **37**, 1193 (1997)

[127] Betz G. and Wehner G.K., *Sputtering by Particle Bombardment II*, volume 52 of *Topics in Applied Physics*, chapter Sputtering of Multicomponent Materials, 11 -- 90, Springer Berlin, Heidelberg (1983)

[128] Liau Z.I., Brown W.L., Homer R. and Poate J.M., `Surface-Layer Composition Changes in Sputtered Alloys and Compounds', *Applied Physics Letters*, **30**, 626 (1977)

[129] Taglauer E., Heiland W. and Onsgaard J., `Ion Beam Induced Desorption of Surface Layers', *Nuclear Instruments and Methods*, **168**, 571 (1980)

[130] Nastasi M., Mayer J.W. and Hirvonen J.K., *Ion-Solid Interactions: Fundamentals and Applications*, chapter Sputtering, Cambridge Solid State Science Series, Cambridge University Press (1996)

[131] Aumayr F. and Winter H.P., *Slow Heavy-Particle Induced Electron Emission from Solid Surfaces*, volume 225 of *Springer Tracts in Modern Physics*, chapter Potential Electron Emission from Metal and Insulator Surfaces, Springer Berlin, Heidelberg (2007)

[132] Winter H., *Slow Heavy-Particle Induced Electron Emission from Solid Surfaces*, volume 225 of *Springer Tracts in Modern Physics*, chapter Kinetic Electron Emission for Grazing Scattering of Atoms and Ions from Surfaces, Springer Berlin, Heidelberg (2007)

[133] Hasselkamp D., Rothard H., Groeneveld K.O., Kemmler J., Varga P. and Winter H., *Particle Induced Electron Emission II*, volume 123 of *Springer Tracts in Modern Physics*, Springer Berlin, Heidelberg (1992)

[134] Fuchs G. and Nicolai A., `Computer Modelling of the Tokamak Scrape-Off Layer Including Secondary-Electron Emission and Sheath Potential at the Limiter', *Nuclear Fusion*, **52**, 1247 (1980)

[135] Hofer W.O., `Plasma-Surface Interactions: The Role of Charged Particle Emission', *Journal of Vacuum Science and Technology A*, **5**, 2213 (1987)

[136] Schupfer N., Tskhakaya sr. D.D., Khanal R., Kuhn S., Aumayr F., Figueira da Silva S. and Winter H.P., `Effect of Particle-Induced Electron Emission (PIEE) on the Plasma Sheath Voltage', *Plasma Physics and Controlled Fusion*, **48**, 1093 (2006)

[137] Thomas E.W., *Particle-Impact Induced Electron Ejection from Surfaces*, International Nuclear Data Report, International Atomic Energy Agency (1995)

[138] Eder H., Aumayr F. and Winter H.P., `Search for Projectile Charge Dependence of Kinetic Electron Emission from Clean Polycrystalline Gold', *Nuclear*

Instruments and Methods in Physics Research B, **154**, 185 (1999)

[139] Aumayr F., Lakits G. and Winter H.P., `On the Measurement of Statistics for Particle-Induced Electron Emission from a Clean Metal Surface', *Applied Surface Science*, **47**, 139 (1991)

[140] Vana M., Aumayr F., Lemell C. and Winter H.P., `Ion-Induced Electron emission from Solid Surfaces: Information Content of the Electron Number Statistics', *International Journal of Mass Spectrometry and Ion Processes*, **149/150**, 45 (1995)

[141] Bodewits E., Bekker H., de Nijs A.J., Hoekstra R., Winklehner D., Daniel B., Kowarik G., Dobes K. and Aumayr F., `Electron Emission Yields from Boron-Like Ar Ions Impinging on Au(100)', *Nuclear Instruments and Methods in Physics Research B*, **269**, 1203 (2011)

[142] Briand J.P., de Billy L., Charles P., Essabaa S., Briand P., Geller R., Desclaux J.P., Bliman S. and Ristori C., `Production of Hollow Atoms by the Excitation of Highly Charged Ions in Interaction with a Metallic Surface', *Physical Review Letters*, **65**, 159 (1990)

[143] Ritter R., `Nanostructures Formed on Surfaces Due to the Impact of Slow Highly Charged Ions', Ph.D. thesis, Vienna University of Technoliogy (2013)

[144] Hagstrum H.D., `Auger Ejection of Electrons from Tungsten by Noble Gas Ions', *Physical Review*, **96**, 325 (1954)

[145] Hagstrum H.D., `Theory of Auger Ejection of Electrons from Metals by Ions', *Physical Review*, **96**, 336 (1954)

[146] Bethe H.A. and Salpeter E.E., `Quantum Mechanics of One- and Two-Electron Systems', *Encyclopedia of Phyiscs*, **7**, 88 (1957)

[147] Burgdörfer J. and Lemell C., *Slow Heavy-Particle Induced Electron Emission from Solid Surfaces*, volume 225 of *Springer Tracts in Modern Physics*, chapter Theoretical Concepts and Methods for Electron Emission from Solid Surfaces, Springer Berlin, Heidelberg (2007)

[148] Ducrée J.J., Casali F. and Thumm U., `Extended Classical Over-Barrier Model for Collisions of Highly Charged Ions with Conducting and Insulating Surfaces', *Physical Review A*, **577**, 338 (1998)

[149] Wirtz L., Reinhold C.O., Lemell C. and Burgdörfer J., `Liouville Master Equation for Multielectron Dynamics: Neutralization of Highly Charged Ions Near a LiF Surface', *Physical Review A*, **67**, 012903 (2003)

[150] Lake R.E., Pomeroy J.M. and Sosolik C.E., `Critical Capture Distances for Highly Charged Ions Above Dielectric Covered Metal Surfaces', *Nuclear Instruments and Methods in Physics Research B*, **269**, 1199 (2011)

[151] Lake R.E., Sosolik C.E. and Pomeroy J.M., `Classical Over the Barrier Model for Neutralization of Highly Charged Ions above Thin Dielectric Films', *Physical Review A*, **87**, 062901 (2013)

Katharina Dobeš

[152] Aumayr F. and Winter H.P., `Slow Highly Charged Ions - A New Tool for Surface Nanostructuring', *e-Journal of Science and Nanotechnology*, **1**, 171 (2003)

[153] Delaunay M., Fehringer M., Geller R., Hitz D., Varga P. and Winter H.P., `Electron Emission from a Metal Surface Bombarded by Slow Highly Charged Ions', *Physical Review B*, **35**, 4232 (1987)

[154] Kurz H., Töglhofer K., Winter H.P. and Aumayr F., `Electron Emission from Slow Hollow Atoms at a Clean Metal Surface', *Physical Review Letters*, **69**, 1140 (1992)

[155] Kurz H., Aumayr F., Winter H.P., Schneider D., Briere M.A. and McDonald J.W., `Electron Emission and Image-Charge Acceleration for the Impact of Very Highly Charged Ions on Clean Gold', *Physical Review A*, **49**, 4693 (1994)

[156] Hughes I.G., Burgdörfer J., Folkerts L., Havener C.C., Overbury S.H., Robinson M.T., Zehner D.M., Zeijlmans van Emmichoven P.A. and Meyer F.W., `Separation of Kinetic and Potential Electron Emission Arising from Slow Multicharged Ion-Surface Interaction', *Physical Review Letters*, **71**, 291 (1993)

[157] Lemell C., Stöckl J., Burgdörfer J., Betz G., Winter H.P. and Aumayr F., `Multicharged Ion Impact on Clean Au(111): Suppression of Kinetic Electron Emission at Glancing Angle Scattering', *Physical Review Letters*, **81**, 1965 (1998)

[158] Meissl W., Simon M.C., Crespo López-Urrutia J.R., Tawara H., Ulrich J., Winter H.P. and Aumayr F., `Highly Charged Ion-Induced Potential Electron Emission from Clean Au(111): Dependence on the Projectile Angle of Incidence', *Nuclear Instruments and Methods in Physics Research B*, **256**, 520 (2007)

[159] Schou J., `Transport Theory for Kinetic Emission of Secondary Electrons from Solids', *Physical Review B*, **22**, 2141 (1980)

[160] Cernusca S., Fürsatz M., Winter H.P. and Aumayr F., `Ion-Induced Kinetic Electron Emission from HOPG with Different Surface Orientation', *Europhysics Letters*, **70**, 768 (2005)

[161] Baragiola R.A., Alonso E.V. and Oliva Florio A., `Electron Emission from Clean Metal Surfaces Induced by Low-Energy Light Ions', *Physical Review B*, **19**, 121 (1979)

[162] Baragiola R.A., Alonso E.V., Ferron J. and Oliva Florio A., `Ion-Induced Electron Emission from Clean Metals', *Surface Science*, **90**, 240 (1979)

[163] Holmén G., Svensson B., Schou J. and Sigmund P., `Direct and Recoil-Induced Electron Emission from Ion-Bombarded Solids', *Physical Review B*, **20**, 2247 (1979)

[164] Hasselkamp D., Lang K.G., Scharmann A. and Stiller N., `Ion Induced Electron Emission from Metal Surfaces', *Nuclear Instruments and Methods in Physics Research B*, **180**, 349 (1981)

[165] Svensson B. and Holmén G., `Electron Emission from Ion-Bombarded Aluminium', *Journal of Applied Physics*, **52**, 6928 (1981)

[166] Veje E., `Study of Secondary Electron Emission from Be, B, Mg and Au as a Function of the Projectile Incidence Angle', *Nuclear Instruments and Methods in Physics Research B*, **2**, 536 (1984)

[167] Ferrón J., Alonso A.V., Baragiola R.A. and Oliva Florio A., `Dependence of Ion-Electron Emission from Clean Metals on the Incidence Angle of the Projectile', *Physical Review B*, **24**, 4412 (1981)

[168] Neidhart T., Toth Z., Schmid M. and Varga P., `Total Sputter Yield of LiF Induced by Hyperthermal Ions Measured by a Quartz Microbalance', *Nuclear Instruments and Methods in Physics Research B*, **90**, 496 (1994)

[169] Hayderer G., Schmid M., Varga P., Winter H.P. and Aumayr F., `A Highly Sensitive Quartz-Crystal Microbalance for Sputtering Investigations in Slow Ion-Surface Collisions', *Review of Scientific Instruments*, **70**, 3696 (1999)

[170] Golczewski A., Dobes K., Wachter G., Schmid M. and Aumayr F., `A Quartz-Crystal-Microbalance Technique to Investigate Ion-Induced Erosion of Fusion Relevant Surfaces', *Nuclear Instruments and Methods in Physics Research B*, **267**, 695 (2009)

[171] Sauerbrey G., `Verwendung von Schwingquarzen zur Wägung dünner Schichten und zur Mikrowägung', *Zeitschrift für Physik*, **155**, 206 (1959)

[172] Neidhart T., `Zerstäubung dünner Isolatorschichten durch hyperthermische, hochgeladene Ionen', Ph.D. thesis, Technical University Vienna (1995)

[173] Hayderer G., `Projectile Charge State Dependent Sputtering of Solid Surfaces', Ph.D. thesis, Technical University Vienna (2000)

[174] Galutschek E., `Development of a 14.5 GHz All-Permanent Magnet Multicharged ECR Source for Remote Operation', Ph.D. thesis, Technical University Vienna (2005)

[175] Galutschek E., Trassl R., Salzborn E., Aumayr F. and Winter H.P., `Compact 14.5 GHz All-Permanent Magnet ECRIS for Experiments with Slow Multicharged Ions', *Journal of Physics Conference Series*, **58**, 395 (2007)

[176] Lungu C.P., Mustata I., Zaroschi V., Lungu A.M., Anghel A., Chiru P., Rubel M., Coad P. and Matthews G.F., `Beryllium Coatings on Metals for Marker Tiles at JET: Development of Process and Characterization Layers', *Physica Scripta*, **T128**, 157 (2007)

[177] Landkammer B., von Keudell A. and Jacob W., `Erosion of Thin Hydrogenated Carbon Films in Oxygen, Oxygen/Hydrogen and Water Plasmas', *Journal of Nuclear Materials*, **264**, 48 (1999)

[178] Bodewits E., `Dynamics of Highly Charged Ions Interacting with Surfaces', Ph.D. thesis, Rijksuniversiteit Groningen (2010)

[179] Manura D. and Dahl D., *SIMION (R) 8.0 User Manual*, Scientific Instrument Services Inc. (2008), URL http://simion.com

[180] Lakits G., Aumayr F. and Winter H.P., `Statistics of Ion-Induced Electron Emis-

sion from a Clean Metal Surface', *Review of Scientific Instruments*, **60**, 3151 (1989)

[181] Töglhofer K., Aumayr F. and Winter H.P., `Ion-Induced Electron Emission from Metal Surfaces - Insights from the Emission Statistics', *Surface Science*, **281**, 143 (1993)

[182] Eder H., Vana M., Aumayr F. and Winter H.P., `Precise Total Electron Yield Measurements for Impact of Singly or Multiply Chagred Ions on Clean Solid Surfaces', *Review of Scientific Instruments*, **68**, 165 (1997)

[183] Winter H.P., Vana M., Lemell C. and Aumayr F., `Interaction of Slow Multi-charged Ions with Solid Surfaces: Current Concepts and New Information on Slow Electron Emission', *Nuclear Instruments and Methods in Physics Research B*, **115**, 224 (1996)

[184] Kurz H., Aumayr F., Lemell C., Töglhofer K. and Winter H.P., `Neutralization of Slow Multicharged Ions at a Clean Gold Surface: Total Electron Yields', *Physical Review A*, **48**, 2182 (1993)

[185] Tjeng L.H., `Development of the Electronic Structure in a K-Doped C_{60} Monolayer on a Ag (111) Surface', *Solid State Communications*, **103**, 1 (1997)

[186] Möller W. and Eckstein W., *TRIDYN - Binary Collision Simulation of Atomic Collisions and Dynamic Composition Changes in Solids*, IPP Garching (1988)

[187] Lindhard J. and Scharff M., `Energy Loss in Matter by Fast Particles of Low Charge State', *Kongelige Danske Videnskabernes Selskab, Matematisk-Fysike Meddelelser*, **27**, 1 (1953)

[188] Ziegler J.F., *Ion Implantation; Science and Technology*, chapter Stopping and Range of Ions in Solids, Academic Press, Inc. (1988)

[189] Jacob W., Hopf C. and Schlüter M., `Chemical Sputtering of Carbon by Nitrogen Ions', *Applied Physics Letters*, **86**, 24103 (2005)

[190] Schlüter M., Hopf C. and Jacob W., `Chemical Sputtering of Carbon by Combined Exposure to Nitrogen Ions and Atomic Hydrogen', *New Journal of Physics*, **10**, 053037 (2008)

[191] Lide D.R., ed., *CRC Handbook of Chemistry and Physics*, volume 76, CRC Press (1995)

[192] Ziegler J.F., Biersack J.P. and Ziegler M.D., *The Stopping and Range of Ions in Matter*, SRIM Co. (2008), URL www.SRIM.org

[193] Eckerlin P. and Rabenau A., `Zur Kenntnis des Systems Be_3N_2-Si_3N_4 Die Struktur einer neuen Modifikation von Be_3N_2', *Zeitschrift für anorganische und allgemeine Chemie*, **304**, 218 (1960)

[194] Dobes K., Hinterhofer M., Tichmann K., Golczewski A., Schwarz-Selinger T., Jacob W. and Aumayr F., `The Evolution of a Hydrogen-Depleted Surface Layer on a-C:H During Bombardment with N_2^+ Ions', Book of Abstracts of the

37th EPS Conference on Plasma Physics (2010)

[195] Dobes K., Naderer P., Hopf C., Schwarz-Selinger T. and Aumayr F., `Transient Effects During Sputtering of a-C:H Surfaces by Nitrogen Ions', *Nuclear Instruments and Methods in Physics Research B*, **288**, 20 (2012)

[196] Rapp J., Matthews G.F., Monier-Garbet P., Sartori R., Corre Y., Eich T., Felton R., Fundamenski W., Giroud C., Huber A., Jachmich S., Morgan P., O'Mullane M., Koslowski H.R., Stamp M. and EFDA-JET work programme, `Strongly Radiating Type-III ELMy H-Mode in JET - an Integrated Scenario for ITER', *Journal of Nuclear Materials*, **337 - 339**, 826 (2005)

[197] Maya P.N., von Toussaint U. and Hopf C., `Synergistic Erosion Process of Hydrocarbon Films: a Molecular Dynamics Study', *New Journal of Physics*, **10**, 023002 (2008)

[198] Hammer P. and Gissler W., `Chemical Sputtering of Carbon Films by Low Energy N_2^+ Ion Bombardment', *Diamond and Related Materials*, **5**, 1152 (1996)

[199] Zekonyte J., Zaporojtchenko V. and Faupel F., `Investigation of the Drastic Change in the Sputter Rate of Polymers at Low Ion Fluence', *Nuclear Instruments and Methods in Physics Research B*, **236**, 241 (2005)

[200] Briggs D. and Wooton A.B., `Analysis of Polymer Surfaces by SIMS - An Investigation of Practical Problems', *Surface and Interface Analysis*, **4**, 109 (1982)

[201] von Keudell A., Jacob W. and Fukarek W., `Role of Hydorgen Ions in Plamsa-Enhanced Chemical Vapor Deposition of Hydrogen Films, Investigated by in Situ Ellipsometry', *Applied Physics Letters*, **66**, 1322 (1995)

[202] Dobes K., Naderer P., Lachaud N., Eisenmenger-Sittner C. and Aumayr F., `Sputtering of Tungsten by N^+ and N_2^+ Ions: Investigations of Molecular Effects', *Physica Scripta*, **T145**, 014017 (2011)

[203] Bader M., Witteborn F.C. and Snouse T.W., *Sputtering of Metals by Mass-Analyzed N_2^+ and N^+*, volume NASA-TR-R-105, NASA Technical Report (1961)

[204] Andersen H.H. and Bay H.L., `Nonlinear Effects in Heavy-Ion Sputtering', *Journal of Applied Physics*, **45**, 953 (1974)

[205] Andersen H.H. and Bay H.L., `Heavy-Ion Sputtering Yields of Gold: Further Evidence of Nonlinear Effects', *Journal of Applied Physics*, **46**, 2416 (1975)

[206] Andersen H.H., *Fundamental Processes in Sputtering of Atoms and Molecules*, chapter Nonlinear Effects in Collsional Sputtering under Cluster Impact, 127, Royal Danish Academy of Science and Letters (1993)

[207] Yao Y., Hargitai Z., Albert M., Albridge R.G., Barnes A.V., Gilligan J.M., Ferguson B.P., Lüpke G., Gordon V.D., Tolk N.H., Tully J.C., Betz G. and Husinsky W., `New Molecular Collisional Interaction Effect in Low-Energy Sputtering', *Physical Review Letters*, **81**, 550 (1998)

[208] Meyer F.W., Zhang H., Lance M.J. and Krause H.F., `Chemical Sputtering and Surface Damage of Graphite by Low-Energy Atomic and Molecular Hydro-

Katharina Dobeš

gen and Deuterium Projectiles', *Vacuum*, **82**, 880 (2008)

[209] Harris P.R., Meyer F.W., Jacob W., Schwarz-Selinger T. and von Toussaint U., `Molecular Size Effect in the Chemical Sputtering of a-C.H Thin Films by Low Energy H^+, H_2^+ and H_3^+ Ions', *Nuclear Instruments and Methods in Physics Research B*, **269**, 1276 (2011)

[210] Dobes K., Smejkal V., Schäfer T. and Aumayr F., `Interaction of Seeding Gas Ions with Nitrogen Saturated Tungsten Surfaces', *International Journal of Mass Spectrometry (accepted for publication)*, doi: 10.1016/j.ijms.2013.11.015 (2014)

[211] Lin J., Tsukune A., Suzuki T. and Yamada M., `Different Effect of Annealing Temperature on Resistivity for Stoichiometric, W Rich, and N Rich Tungsten Nitride Films', *Journal of Vacuum Science and Technology A*, **17**, 936 (1999)

[212] Oberkofler M., Douai D., Brezinsek S., Coenen J.W., Dittmar T., Drenik A., Romanelli S.G., Joffrin E., McCormick K., Brix M., Calabro G., Clever M., Giroud C., Kruezi U., Lawson K., Linsmeier C., Rojo A.M., Meigs A., Marsen S., Neu R., Reinelt M., Sieglin B., Sips G., Stamp M., Tabarés F.L. and the EFDA-JET contributors, `First Nitrogen-Seeding Experiments in JET with the ITER-like Wall', *Journal of Nuclear Materials*, **438**, S258 (2013)

[213] Oberkofler M., private communication

[214] Zalkind S., Polak M. and Shamir N., `The absorption of H_2O vs O_2 on Beryllium', *Surface Science*, **385**, 318 (1997)

[215] Yoshida N., Mizusawa S., Sakamoto R. and Muroga T., `Radiation Damage and Deuterium Trapping in Deuterium Ion Injected Beryllium', *Journal of Nuclear Materials*, **233 - 237** (1996)

[216] Haasz A.A. and Davis J.W., `Deuterium Retention in Beryllium, Molybdenum and Tungsten at High Fluences', *Journal of Nuclear Materials*, **241 - 243**, 1076 (1997)

[217] Reinelt M. and Linsmeier C., `Ion Implanted Deuterium Retention and Release from Clean and Oxidized Beryllium', *Journal of Nuclear Materials*, **390 - 391**, 568 (2009)

[218] Chernikov V.N., Alimov V.K., Markin A.N. and Zakharov Q.P., `Gas Swelling and Related Phenomena in Beryllium Implanted with Deuterium Ions', *Journal of Nuclear Materials*, **228**, 47 (1996)

[219] Sugiyama K., Roth J., Anghel A., Porosnicu C., Baldwin M., Doerner R., Krieger K. and Lungu C.P., `Consequences of Deuterium Retention and Release from Be-Containing Mixed Materials for ITER Tritium Inventory Control', *Journal of Nuclear Materials*, **415**, S731 (2011)

[220] Federici G., Anderl R.A., Brooks J.N., Causey R., Coad J.P., Cowgill D., Doerner R., Haasz A.A., Longhurst G., Luckhardt S., Mueller D., Peacock A., Pick M., Skinner C.H., Wampler W.W., Wilson K., Wong C., Wu C. and Youchison D.,

`Tritium Inventory in the ITER PFC's: Predictions, Uncertainties, R&D Status and Priority Needs', *Fusion Engineering and Design*, **39 - 40**, 445 (1998)

[221] Stolterfoht N., Arnau A., Grether M., Köhrbrück R., Spieler A., Page R., Saal A., Thomaschewskia J. and Bleck-Neuhaus J., `Multiple-Cascade Model for the Filling of Hollow Ne Atoms Moving Below an Al Surface', *Physical Review A*, **52**, 445 (1995)

[222] Winter H., `Scattering of Atoms and Ions from Insulator Surfaces', *Progress in Surface Science*, **63**, 177 (2000)

[223] Limburg J., Schnippers S., Hoekstra R., Morgenstern R., Kurz H., Aumayr F. and Winter H.P., `Do Hollow Atoms Exist in Front of an Insulating LiF(100) Surface', *Physical Review Letters*, **75**, 217 (1995)

[224] Meissl W., Winklehner D., Aumayr F., Simon M.C., Ginzel R., Crespo López-Urrutia J.R., Ulrich J., Solleder B., Lemell C. and Burgdörfer J., `Electron Emission from Insulators Irradiated by Slow Highly Charrged Ions', *e-Journal of Surface Science and Nanotechnology*, **6**, 54 (2008)

[225] Bodewits E., Hoekstra R., Kowarik G., Dobes K. and Aumayr F., `Highly-Charged-Ion-Induced Electron Emission from C_{60} Thin Films', *Physical Review A*, **84**, 042901 (2011)

[226] Bodewits E., Hoekstra R., Dobes K. and Aumayr F., `Kinetic-Energy-Driven Enhancement of Secondary-Electron Yields of Highly Charged Ions Impinging on Thin Films of C_{60} on Au', *Physical Review A*, **86**, 062904 (2012)

[227] Meyer F.W., Folkerts L., Hughes I.G., Zehner D.M., Zeijlmans van Emmichoven P.A. and Burgdörfer J., `Work-Function Dependence of Above-Surface Neutralization of Multicharged Ions', *Physical Review A*, **48**, 4479 (1993)

[228] Khemliche H., Schlathölter T., Hoekstra R., Morgenstern R. and Schippers S., `Hollow Atom Dynamics on LiF Covered Au(111): Role of Surface Electronic Structure', *Physical Review Letters*, **81**, 1219 (1998)

[229] Khemliche H., Schlathölter T., Hoekstra R. and Morgenstern R., `L-Shell Filling of N^{6+} and O^{7+} Ions from a Clean and LiF-Covered Au(111) Surface', *Physcial Review A*, **60**, 3800 (1999)

[230] Cernusca S., Diem A., Winter H.P., Aumayr F., Lörincik J. and Sroubek Z., `Kinetic Electron Emission from Highly Oriented Pyrolytic Graphite Surfaces Induced by Singly Charged Ions', *Nuclear Instruments and Methods in Physics Research B*, **193**, 616 (2002)

[231] Svensson B., Holmén G. and Burén A., `Angular Dependence of the Ion-Induced Secondary-Electron Yield from Solids', *Physical Review B*, **24**, 3749 (1981)

[232] Jacobsson H. and Holmén G., `The Dependence of Si and SiO_2 Electron Emission on the Angle of Ion Incidence', *Journal of Applied Physics*, **74**, 6397 (1993)

Katharina Dobeš

[233] Berger B., Technical University Vienna, PhD thesis, ongoing

List of Figures

Katharina Dobeš

Katharina Dobeš

List of Tables